中国科学技术大学

博士学位论文

钌核-钌核与锆核-锆核对撞中粒子谱的实验研究及重子结寻找

作者姓名： 李洋

学科专业： 粒子物理与原子核物理

导师姓名： 唐泽波 教授 阮丽娟 研究员 马荣荣 研究员

完成时间： 二〇二三年八月十五日

University of Science and Technology of China

A dissertation for doctor's degree

Measurement of identified particle spectra and tracking the baryon number in $^{96}_{44}$Ru+$^{96}_{44}$Ru and $^{96}_{40}$Zr+$^{96}_{40}$Zr collisions at $\sqrt{s_{\mathrm{NN}}}$ = 200 GeV

Author: Yang Li

Speciality: Particle Physics and Nuclear Physics

Supervisors: Zebo Tang, Lijuan Ruan, Rongrong Ma

Finished time: August 15, 2023

中国科学技术大学学位论文原创性声明

本人声明所呈交的学位论文，是本人在导师指导下进行研究工作所取得的成果。除已特别加以标注和致谢的地方外，论文中不包含任何他人已经发表或撰写过的研究成果。与我一同工作的同志对本研究所做的贡献均已在论文中作了明确的说明。

作者签名：李洋　　签字日期：2023/9/21

中国科学技术大学学位论文授权使用声明

作为申请学位的条件之一，学位论文著作权拥有者授权中国科学技术大学拥有学位论文的部分使用权，即：学校有权按有关规定向国家有关部门或机构送交论文的复印件和电子版，允许论文被查阅和借阅，可以将学位论文编入《中国学位论文全文数据库》等有关数据库进行检索，可以采用影印、缩印或扫描等复制手段保存、汇编学位论文。本人提交的电子文档的内容和纸质论文的内容相一致。

控阅的学位论文在解密后也遵守此规定。

☑ 公开　☐ 控阅（____ 年）

作者签名：李洋　　导师签名：

签字日期：2023/9/21　　签字日期：2023/09/25

Dedicated to my family

&

In memory of my father

摘　要

格点量子色动力学（Lattice QCD）的计算表明核物质在极端高温高密的条件下会达到夸克解禁闭，形成具有部分子自由度的夸克胶子等离子体（Quark Gluon Plasma，简称 QGP）。这一极端条件可以通过相对论重离子碰撞实现。QGP 成为研究强相互作用特别是非微扰区强相互作用的理想平台。通过对 QGP 性质的深入研究，也可以帮助人们理解宇宙的早期演化。

2018 年，位于相对论重离子对撞机（RHIC）上的 STAR 实验收集了大量同重异位素 ${}^{96}_{44}$Ru+${}^{96}_{44}$Ru 和 ${}^{96}_{40}$Zr+${}^{96}_{40}$Zr 对撞数据，其平均每核子-核子对质心系能量为 $\sqrt{s_{\mathrm{NN}}}$ = 200 GeV。这一数据为 QGP 特性研究提供了独特的机遇。主要在于：1）极高的统计量可以很大程度改善各种测量的精度，对 QGP 特性进行精确研究；2）碰撞系统的尺寸介于 Cu+Cu 和 Au+Au 之间，可以研究 QGP 对碰撞系统的尺寸和几何形状的依赖关系；3）两种对撞系统具有同样的质量数和不同的质子数，可以在相同强作用的情形下研究不同质子数导致的差异，如寻找手征磁效应 (Chiral Magnetic Effect, CME) 和重子结 (Baryon junction) 等。

本论文通过联合 STAR 时间投影室和飞行时间探测器对带电粒子进行粒子种类识别，经过探测效率、弱衰变贡献、Knock-out 贡献等修正，分别测量了 ${}^{96}_{44}$Ru+${}^{96}_{44}$Ru 和 ${}^{96}_{40}$Zr+${}^{96}_{40}$Zr 对撞中 $\pi^{\pm}$，$K^{\pm}$，质子和反质子在中间快度区（$|y| < 0.5$）的横动量谱。该结果覆盖了 9 个中心度区间和大的横动量区间（$0.2 < p_T < 2.5$ GeV/c）。并通过这些数据研究了 QGP 中的粒子产生机制、热力学性质以及寻找重子结等。

论文对不同对撞中心度下 $\pi^{\pm}$，$K^{\pm}$，质子和反质子的横动量谱进行了爆炸波模型 (Blast-Wave Model）拟合，提取了径向流平均速度（$\langle\beta\rangle$) 与动力学冻结温度 (T_{kin})，并利用模型拟合得到的谱的形状将横动量谱测量外推到没有覆盖到的横动量区域，计算了这六种带电强子的多重数密度 $\mathrm{d}N/\mathrm{d}y$、正反粒子比、平均横向动量 $\langle p_{\mathrm{T}}\rangle$ 等。研究发现，在 Ru+Ru 和 Zr+Zr 中测量到的粒子 $\mathrm{d}N/\mathrm{d}y$ 随参与碰撞核子数（N_{part}）的变化与之前发表的 Cu+Cu 和 Au+Au 对撞中的结果具有相同的趋势。在相同的 N_{part} 下，不同尺寸的原子核对撞产生的重叠区具有很不一样的形状，然而实验观测发现在这四个对撞系统中，平均每 N_{part} 的粒子 $\mathrm{d}N/\mathrm{d}y$ 在误差范围内一致。这表明火球的体积（或 N_{part}）是主导碰撞动力学的主要因素，火球的几何形状对粒子产额没有明显的影响。实验还发现 π^-/π^+ 比率在所有碰撞系统中接近于 1，碰撞系统同位旋的影响可以忽略。K^-/K^+ 比率约为 0.95，这可能是与 Λ 超子相关的 K^+ 伴随产生所导致的。$\bar{p}/p$ 比率约为 0.8，且随着 N_{part} 的增加呈现下降趋势，反映了不同对撞中心度下的重子阻止本领的差别。爆炸波

模型拟合给出的 T_{kin} 与 $\langle\beta\rangle$ 之间的关联与 Au+Au 和 Cu+Cu 碰撞的结果相符。但与 Zr+Zr 碰撞相比，Ru+Ru 碰撞系统地具有更大的 $\langle\beta\rangle$ 和更低的 T_{kin}。这可以从 Ru+Ru 和 Zr+Zr 碰撞中同种粒子的横动量谱的比值更好地体现。这两种碰撞系统中粒子的比值均大于 1，并且对撞越偏心该比值越大。在所有的碰撞中心度下，该比值随着横动量的增加而增加，而且越重的粒子变化具有越大的斜率。这些可能是因为 Ru 和 Zr 两种核具有不同的核尺寸和结构。这些测量为 QGP 中的粒子产生机制、重子阻止本领、热力学性质、原子核的结构以及 QGP 演化与火球初始几何的关系的研究提供了重要数据。

论文还通过同重异位素对撞中带电粒子横动量谱的测量对重子数携带者进行了研究。重子数是物理学中最为人所熟知并严格测试的守恒量之一。传统观点认为重子数是由价夸克携带，但并没有严格的实验证据支持这一观点。而相对论重离子碰撞中中心快度区域的净重子数测量结果对这一传统观点提出了挑战。有理论认为重子的重子数不是由夸克携带，而是由连接三个价夸克的非微扰 Y 型胶子拓扑结构（胶子结或重子结）所携带。这一理论并不与标准模型相违背。重子数的携带者到底是什么，是一个非常基本但是极其重要的问题。论文认为通过同重异位素对撞中中心快度区净电荷数与净重子数的关联可以确定重子数的携带者。考虑到在单个碰撞系统中精确测量净电荷数的困难，论文提出了一种全新的方法，对 Ru+Ru 和 Zr+Zr 碰撞之间的净电荷差进行了精确测量。结果显示，两种对撞系统中的净重子数 B 和净电荷数的差异 ΔQ 的比值大约为价夸克携带重子数的期望值 96/4 以及基于价夸克携带重子数理论的模型（UrQMD 等）计算结果的两倍。这一结果与价夸克携带重子数不相符，而与重子结携带重子数的预期一致。本文结合之前研究的 Au+Au 碰撞中中心快度区净质子数与束流的快度关系以及 γ+Au 碰撞中净质子数快度分布测量结果可以为重子数携带者的研究提供重要的实验证据，对重子内部结构的深入理解具有非常重要的物理意义。

关键词：量子色动力学，夸克胶子等离子体，动力学冻结温度，径向流，原子核结构，重子数，重子结

ABSTRACT

Calculations in Lattice Quantum Chromodynamics (Lattice QCD) indicate that under conditions of extremely high temperature and density, nuclear matter experiences quark deconfinement, leading to the formation of a Quark-Gluon Plasma (QGP) where particles have freedom to move. Relativistic heavy-ion collisions offer a practical method to recreate these extreme conditions. QGP has thus emerged as an invaluable tool for probing the properties of strong interactions, particularly in the non-perturbative domain. Moreover, a deeper understanding of QGP properties is instrumental in elucidating the early stages of the universe's evolution.

In 2018, the STAR experiment, conducted at the Relativistic Heavy Ion Collider (RHIC), collected a large sample from collision events involving isobars ${}^{96}_{44}$Ru+${}^{96}_{44}$Ru and ${}^{96}_{40}$Zr+${}^{96}_{40}$Zr, with the collisions characterized by an average center-of-mass energy per nucleon of $\sqrt{s_{\mathrm{NN}}}$ = 200 GeV. This dataset offers an unparalleled opportunity to delve into the properties of QGP for several compelling reasons. Firstly, the substantial statistical volume significantly enhances the precision of various measurements, facilitating more accurate assessments of QGP characteristics. Secondly, the intermediate collision system size, falling between that of Cu+Cu and Au+Au, provides an exceptional prospect to analyze how QGP properties are influenced by the size and geometry of the collision system. Lastly, by employing two collision systems with identical mass numbers but differing proton counts, the data allows for examination of how variance in proton number under the same strong interactions manifests in outcomes, such as searching for the Chiral Magnetic Effect (CME) and Baryon Junctions.

In this thesis, particle identification is carried out by employing a combination of the STAR Time Projection Chamber and Time of Flight detectors. Following corrections for detection efficiency, contributions from weak decays, knock-out proton background, and other factors, transverse momentum spectra for $\pi^{\pm}$, $K^{\pm}$, protons, and anti-protons at mid-rapidity ($|y| < 0.5$) are measured for collisions of ${}^{96}_{44}$Ru+${}^{96}_{44}$Ru and ${}^{96}_{40}$Zr+${}^{96}_{40}$Zr. The measurements span nine centrality bins and a broad range of transverse momentum ($0.2 < p_T < 2.5$ GeV/c). The thesis employs these measurements as a basis for an in-depth investigation into various aspects, including the particle production mechanisms within QGP, the thermodynamic properties that characterize QGP, and the search for Baryon Junctions.

We utilize the Blast-Wave Model to fit the transverse momentum spectra of $\pi^{\pm}$,

$K^{\pm}$, protons, and antiprotons across varying collision centrality intervals, which enables us to extract the average radial flow velocity ($\langle\beta\rangle$) and the kinetic freeze-out temperature (T_{kin}). Furthermore, these model fits are employed to extrapolate the spectra to the unmeasured p_{T} regions, thereby facilitating the calculation of the multiplicity density $\mathrm{d}N/\mathrm{d}y$, antiparticle-to-particle ratios, and average transverse momentum $\langle p_{\mathrm{T}}\rangle$ for this set of charged hadrons. The measurements reveal that the $\mathrm{d}N/\mathrm{d}y$ of particles observed in Ru+Ru and Zr+Zr collisions exhibit trends with respect to the number of participating nucleons (N_{part}) that are consistent with previously published results for Cu+Cu and Au+Au collisions. When the same N_{part} is considered, collisions involving nuclei of varying sizes yield overlap regions with distinct shapes. Nevertheless, the experimental data demonstrate that the average $\mathrm{d}N/\mathrm{d}y$ per N_{part} across these four collision systems aligns within the margin of error. This finding suggests that the volume of the fireball (or N_{part}) predominantly influences the collision dynamics, with the fireball's geometric shape exerting minimal impact on particle production. Furthermore, the results establish that the π^-/π^+ ratio approximates 1 across all collision systems, implying the marginal impact of isospin effects. The K^-/K^+ ratio is around 0.95, potentially attributable to the associated production of K^+ with Λ hyperons. The $\bar{p}/p$ ratio approximates 0.8 and exhibits a declining trend with the increase of N_{part}, reflecting the variance in baryon stopping capabilities across different collision centralities. The Blast-Wave Model fitting elucidates a correlation between T_{kin} and $\langle\beta\rangle$, which aligns with findings from Au+Au and Cu+Cu collisions. Intriguingly, in comparison to Zr+Zr collisions, the Ru+Ru collision is characterized by systematically higher $\langle\beta\rangle$ and lower T_{kin}. This phenomenon is more conspicuously manifested in the ratios of the transverse momentum spectra of identical particles across Ru+Ru and Zr+Zr collisions. In both collision systems, the particle ratios exceed 1, with larger ratios observed in peripheral collisions. Across all collision centralities, this ratio rises alongside increasing transverse momentum, and the slope is steeper for heavier particles. These observations might stem from the divergent sizes and structures of Ru and Zr nuclei. In summary, these measurements furnish critical data that can facilitate research on the mechanisms of particle production in QGP, baryon stopping capabilities, thermodynamic properties, nuclear structures, and the interplay between QGP evolution and the initial geometry of the fireball.

In this thesis, we also seek to study baryon number carriers through the measurement of charged particle transverse momentum spectra in isobar collisions. Baryon number conservation is one of the most familiar and rigorously tested principles in

physics. Traditionally, it is believed that the baryon number is carried by valence quarks, however, there is no robust experimental evidence to support this theory. The measurements of the net baryon number in the mid-rapidity region of relativistic heavy-ion collisions put this conventional understanding into question. Certain theories suggest that the baryon number in a baryon is not carried by the quarks themselves, but rather by a non-perturbative Y-shaped gluon topology, known as a gluon or baryon junction, which connects three valence quarks. Interestingly, this hypothesis does not conflict with the Standard Model. Identifying the true carrier of the baryon number is fundamental and of utmost importance. The thesis proposes that through examining the correlation between the net charge and net baryon number in the mid-rapidity region of isobar collisions, it is possible to discern what carries the baryon number. Given the challenge of accurately measuring the net charge in a single collision system, the thesis introduces a novel approach, meticulously measuring the net charge difference between Ru+Ru and Zr+Zr collisions. Remarkably, the findings reveal that the ratio of the net baryon number B to the difference in net charge ΔQ across the two collision systems is approximately twice the expected value of 96/4, which is the value expected if the baryon number is carried by valence quarks, as well as twice of the values predicted by models such as UrQMD that are based on valence quarks carrying the baryon number. These results are not consistent with the idea of valence quarks carrying the baryon number and instead align with the hypothesis of the baryon number being carried by a baryon junction. In conjunction with prior studies focusing on the relationship between net proton numbers in the mid-rapidity region of Au+Au collisions and beam rapidity, as well as measurements of the rapidity distributions of net proton numbers in γ+Au collisions, the thesis furnishes important experimental evidence supporting the study of baryon number carrier. These findings hold significant implications, propelling our understanding of the complex internal structure of baryons forward.

Key Words: QCD, QGP, kinetic freeze-out temperature, radial flow, nuclear structure, baryon number, baryon junction

Contents

List of Figures

Figure 5.8 The relationship between T_{kin} and $\langle\beta\rangle$ for different collision systems and centrality intervals. For a given system, the centrality increases from left to right. Data points, excluding isobar collisions, are obtained from references[9,47]. The uncertainties presented in the graph represent the combined systematic and statistical uncertainties. · · ·

Figure 5.16 Average net-baryon yield in Ru+Ru and Zr+Zr collisions as a function of $\langle N_{\text{part}} \rangle$. The solid circles with rectangular boxes depict data with box heights representing systematic uncertainties. The hatched band denotes predictions from UrQMD model. · · · · · · · 126

Figure 5.17 The variation of net-charge difference between Ru+Ru and Zr+Zr collisions as a function of $\langle N_{\text{part}} \rangle$. The solid circles with rectangular boxes represent data with box heights representing systematic uncertainties. The hatched band denotes predictions from UrQMD model. · · · · · · ·

List of Tables

Chapter 1 Introduction

1.1 The Standard Model and the Quantum Chromodynamics

Particle physics has been continuously shaped by the contributions of numerous physicists since the 1930s, leading to a deep understanding of the fundamental structure of matter. Everything in the universe is made up of a few basic building blocks known as fundamental particles, which are governed by four fundamental forces. The Standard Model of particle physics is the most comprehensive theory in this field, predicting a broad range of phenomena and explaining almost all experimental results. It has become a well-established and rigorously tested theory in physics.

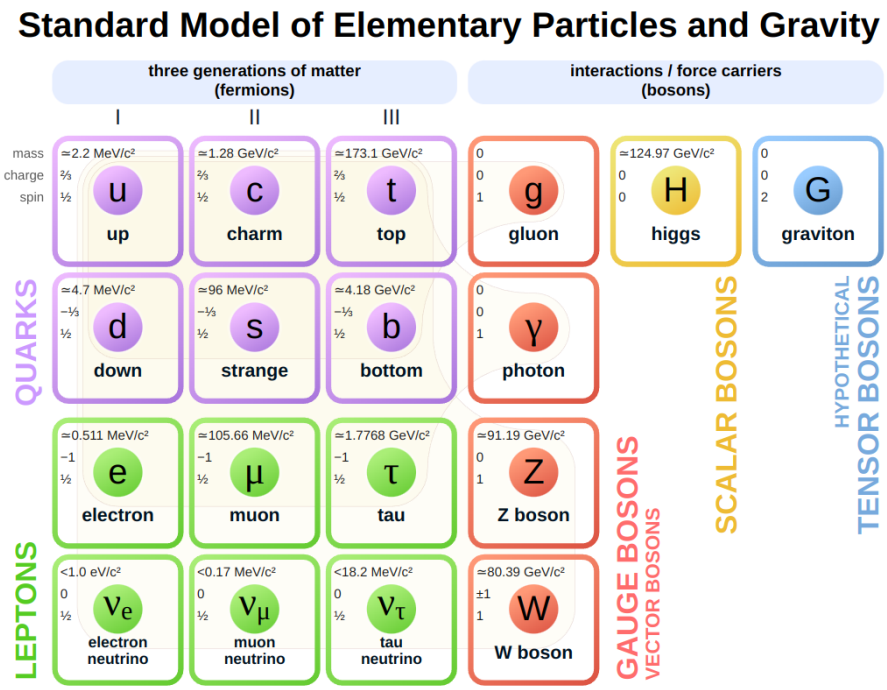

Figure 1.1 The Standard Model of elementary particles and hypothetical graviton. The figure is taken from Wikipedia[1].

Figure 1.1 presents the fundamental particles encompassed by the Standard Model, along with their associated properties such as mass, charge, and spin. The Standard Model categorizes particles into two primary classes: matter particles and force carriers. Matter particles, termed fermions, have a spin of 1/2 and contain six varieties of quarks, up (u), down (d), charm (c), strange (s), top (t), and bottom (b) and six types of leptons, electron (e), muon (μ), tauon (τ), and their corresponding neutrinos (ν_e, ν_μ and ν_τ). Quarks and leptons are classified into three generations each, with each generation comprised of a pair of them. Each particle has an antiparticle with the same mass, spin,

and isospin but opposite electric charge and lepton number. Charged leptons - specifically, electron, muon, and tauon - each carry a single unit of electric charge, while neutrinos are electrically neutral. In contrast, quarks carry fractional charges. Specifically, up, charm and top quarks carry a positive 2/3 charge, whereas down, strange, and bottom quarks carry a negative 1/3 electric charge. Quarks also come in three different colors (red (R), green (G), and blue (B)).

Conventionally, it is believed that each valence quark is also associated with a baryon number, and a hadron's baryon number is denoted as $B = \frac{1}{3}(n_q - n_{\bar{q}})$, where n_q represents the number of quarks and $n_{\bar{q}}$ signifies the number of antiquarks. The baryons, such as protons and neutrons, consist of three valence quarks carrying three different colors and exhibit a baryon number of $+1$. In contrast, mesons, such as pions and kaons, consist of a quark carrying one color and an antiquark carrying the corresponding anti-color, and have a baryon number of 0. Antibaryons, which consist of three antiquarks, bear a baryon number of -1. Moreover, exotic hadrons such as pentaquarks (four quarks and one antiquark) and tetraquarks (two quarks and two antiquarks) are classified as baryons and mesons based on their baryon number. Both the electric charge and the baryon number are conserved quantum numbers in the Standard Model.

The Standard Model incorporates three of the four fundamental forces known in the universe: the electromagnetic force, the strong force, and the weak force, each possessing distinct strengths and acting in varying ranges. The electromagnetic force enjoys infinite ranges, while the weak and strong forces operate at the subatomic level within limited ranges. The weak force is weaker than the other two forces, while the strong force emerges as the most potent fundamental interaction. These three fundamental forces in the Standard Model are realized via exchanges of force carrier particles, or bosons (spin 1), which mediate discrete energy transfers between matter particles. Photons, for instance, carry the electromagnetic force and interact with electric charge, while gluons carry the strong force for quarks and gluons. W and Z bosons, on the other hand, carry the weak force. Despite the comprehensive description of the electromagnetic, strong, and weak forces along with their carrier particles, the Standard Model fails to incorporate the most familiar force in our everyday lives, gravity. The challenge arises from the incompatibility between the quantum theory, describing the micro world, and the general theory of relativity, describing the macro world. However, the effect of gravity is so minuscule at the subatomic scale and only becomes dominant for matter in bulk, such as ourselves or planets. Consequently, the Standard Model remains a robust framework for understanding fundamental forces.

One crucial component of the Standard Model is the Higgs boson[2-3] which is essential for comprehending the origin of particle mass. In 2012, the A Toroidal LHC Apparatus (ATLAS)[4] and Compact Muon Solenoid (CMS)[5] experiments at the LHC revealed promising signs of a particle that corresponds to the Higgs boson. Work is ongoing for determining the exact nature of the particle and its role in our understanding of the universe.

Even though the Standard Model has been highly successful in predicting experimental results and is considered a self-consistent theory, it still fails to explain several key physical phenomena and is thus regarded incomplete. For example, it does not fully account for the baryon asymmetry, or incorporate the theory of gravitation mentioned above or explain the universe's accelerating expansion. Additionally, the Standard Model does not include any viable dark matter particle that possesses all the necessary properties as deduced from cosmological observations. Furthermore, it does not consider neutrino oscillations and their non-zero masses. All of these call for further development and possible expansion of the Standard Model.

1.1.1 Asymptotic freedom and confinement

Nambu introduced the concept of color degree of freedom and Quantum Chromodynamics (QCD) in 1966, which is an extension of Quantum Electrodynamics (QED). The color charge, a conserved quantum number in QCD, is analogous to the electric charge in QED. Both forces are mediated by massless vector particles, i.e., gluons for strong interactions and photons for electromagnetic interactions. Unlike in QED where photon does not carry electric charges themselves, in QCD, gluon also carries the color charge. As a result, QCD is a non-Abelian gauge theory that is described by the color SU(3) algebra and describes the strong force.

The Lagrangian of QCD, which is responsible for governing the behavior of quarks and gluons, is gauge invariant and given by Eq. 1.1[6].

$$\mathcal{L}_{QCD} = \bar{\Psi}_i(i\gamma^\mu(D_\mu)_{ij} - m\delta_{ij})\Psi_j - \frac{1}{4}F^\alpha_{\mu\nu}F^{\mu\nu}_\alpha. \tag{1.1}$$

The quark field, denoted by $\Psi_i(x)$, is a function of both time and space and is in the fundamental representation of the SU(3) gauge group. The indices i and j range from 1 to 3. Dirac matrices γ_μ connect the spinor representation to the vector representation of the Lorentz group. The gauge covariant derivative $(D_\mu)_{ij}$ is given by $\partial_\mu\delta_{ij} - ig(T_a)_{ij}A^a_\mu$, where g represents the coupling strength between the quark field and the gluon field. The quark field is coupled to the gluon field via the adjoint representations of the SU(3)

generator $T_a = \lambda_a/2$, where λ_a represents the Gell-Mann matrices and a ranges from 1 to 8. The gluon field strength tensor $F^{\alpha}_{\mu\nu}$ is defined as:

$$F^{\alpha}_{\mu\nu} = \partial_\mu A^a_\nu - \partial_\nu A^a_\mu + g f_{abc} A^a_\mu A^c_\nu. \tag{1.2}$$

The gluon fields $A^a_\mu(x)$ are functions of space-time and represented adjointly in the SU(3) gauge group, indexed by a, b, and c ranging from 1 to 8. The structure constants of SU(3) are denoted by f_{abc}. The quark mass and coupling, represented by m and g, respectively, are variables that are subject to renormalization.

Quarks and gluons, the fundamental particles carrying the color charge, have never been observed in isolation. Instead, they group to form color-neutral composite hadrons – a phenomenon referred to as color confinement. Although confinement has not been conclusively proven, it is widely accepted as a property of QCD due to numerous numerical simulations and experimental evidences. The confinement mechanism remains not fully understood but is believed to be linked to the QCD vacuum's behavior and the development of color flux tubes between quarks.

A crucial aspect of understanding confinement is the potential between a pair of quark and antiquark. At short distances, the interaction is expected to resemble the Coulomb force as for electromagnetic interactions. However, at larger distances, the potential must rise indefinitely to confine quarks within a hadron. This potential can be expressed by Eq. 1.3.

$$V = -\frac{4}{3}\frac{\alpha_s}{r} + \kappa r, \tag{1.3}$$

where α_s signifies the coupling constant in strong interactions, κ denotes the QCD string tension, and r represents the distance between color charges. As the distance between the pair expands, the potential increases. This results in the confinement of quarks within hadrons, as the energy required for their separation becomes infinite.

Another unique aspect of QCD is the asymptotic freedom, a phenomenon that the strong force between a pair of quark and antiquark weakens as their separation decreases. This behavior contrasts with other fundamental forces, such as electromagnetism. The root cause of asymptotic freedom lies in the behavior of the strong coupling constant, α_s, which depends on the self-interaction of gluons and results in a weaker strong force at shorter distances.

In QED, virtual electron-positron pairs can be excited by a propagating photon, partially screening the interaction between two electric charges. This screening effect causes the QED coupling constant to increase as electric charges drawn nearer. A similar screening effect occurs in QCD. As depicted in the Feynman diagram in Fig. 1.2

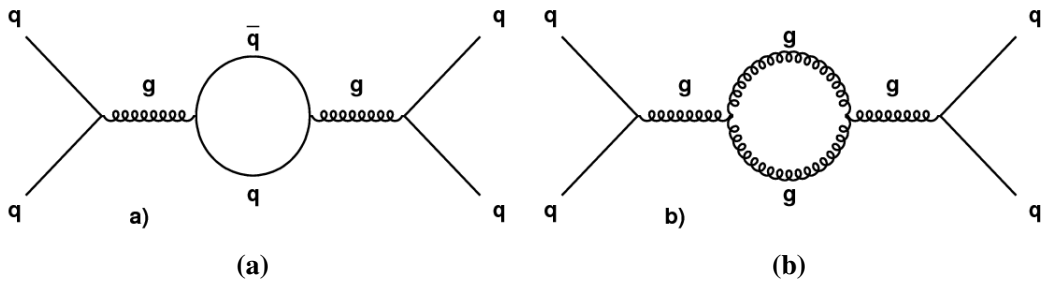

Figure 1.2 Feynman diagrams depicting the lowest order of screening (a) and anti-screening (b) between color charges.

(a), a quark-antiquark pair can also be excited in the vacuum, resulting in the screening of the strong force between color charges. However, as aforementioned, gluons possess color charges, allowing self-interaction, which is fundamentally different from photons in QED. As illustrated in Fig. 1.2 (b), gluons can scatter and absorb other gluons in the QCD vacuum, creating colored gluon clouds surrounding the two color charges and intensifying their interaction (anti-screening). Consequently, the strong interaction coupling α_s varies with the distance scale and decreases as the distance decreases[6].

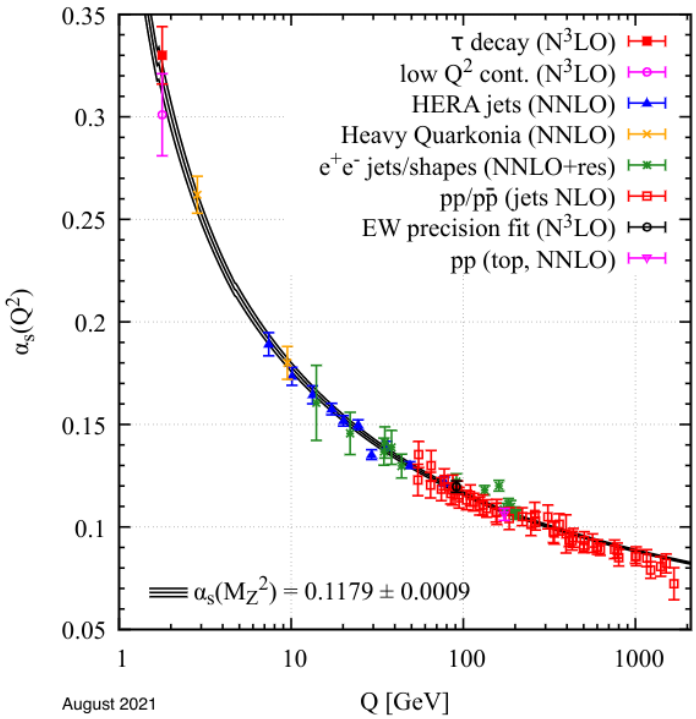

Figure 1.3 A summary of α_s measurements as a function of the energy scale Q is provided. The specific degree of QCD perturbation theory employed in extracting α_s is denoted in brackets. The abbreviations are as follows: NLO refers to next-to-leading order, NNLO is the next-to-next-to-leading order. NNLO+res signifies NNLO matched to a resummed calculation, and N^{3}LO represents the next-to-NNLO stage. Figure is taken from[6].

The running coupling constant can therefore be represented by Eq. 1.4.

$$\alpha_s(Q^2) = \frac{1}{4\pi\beta_0 ln(Q^2/\Lambda^2_{QCD})}, \tag{1.4}$$

where Q^2 is the amount of momentum transfer, β_0 is the first coefficient of the β function and Λ_{QCD} is the energy scale parameter of QCD. High momentum transfers correspond to small interaction distances. The values of α_s at different energy scales (Q), extracted from experimental measurements, are illustrated in Fig. 1.3 as data points. They show a clear decrease in α_s with increasing energy scale or decreasing distance, which is why it is referred to as asymptotic freedom.

One important consequence of the asymptotic freedom is the feasibility of carrying out QCD calculations perturbatively. One can expand a QCD calculation in a series of terms with an increasing order in α_s. When α_s is smaller which is the case at high energy or small distance, the contribution of each term in the series decays with a factor α_s, making higher-order terms less and less important. Therefore, QCD calculations can be done at fixed orders, with higher orders ignored and covered in systematic uncertainties. The perturbative QCD (pQCD) calculation of α_s at the next-to-leading order (NLO) is shown as the solid line in Fig. 1.3, which agrees well with experimental measurements. The expansion of the three solid lines indicates the world average of the calculation[6].

1.1.2 Lattice QCD

Experimental results in the high-energy regime align remarkably well with the predictions of pQCD. However, when Q^2 is small, which corresponds to the so-called soft physics regime, the applicability of perturbative calculations collapses. For example, explorations of the QCD phase diagram using high-energy heavy-ion collisions are limited in this aspect. In these collisions, the typical momentum transfer is small, and the perturbation theory is inadequate for elucidating the physics underpinning the phase transition as these phenomena are intrinsically non-perturbative. To overcome this difficulty, computational approaches, such as the lattice QCD, have been proposed.

Lattice QCD, initially proposed by Wilson in 1974[7], offers a powerful approach to achieve a comprehensive, first-principles understanding of QCD phenomena that cannot be studied using perturbative methods. The central idea is to define QCD on a space-time lattice, enabling gauge-invariant regularization of ultraviolet (UV) divergences to facilitate non-perturbative numerical simulations.

In lattice QCD, Euclidean space-time is discretized into a finite grid or lattice, with a spacing a between lattice points. It serves as a regularization tool, enabling the

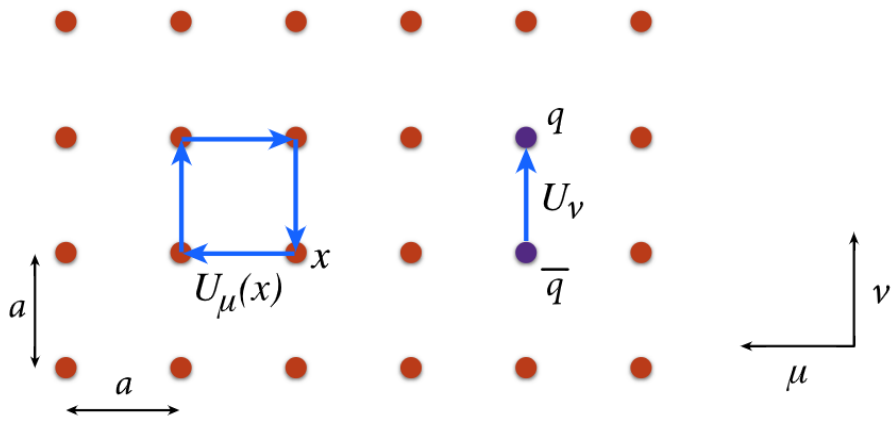

Figure 1.4 Illustration of a two-dimensional cross section of the $\mu - \nu$ plane within a lattice with gluon fields located on links. These gluon fields contribute to the formation of either the plaquette product present in the gauge action or a component of the covariant derivative connecting quark and antiquark fields. Figure is taken from[6].

calculation of various quantities of interest, such as the hadron mass, decay constant, and form factors. Quark fields, which occupy lattice sites, and gluon fields, which reside on the links between sites, represent the fundamental degrees of freedom on the lattice. The continuum theory can be recovered by taking the limit of vanishing lattice spacing, achievable by tuning the bare gauge coupling to zero according to the renormalization group.

Lattice quark field gauge transformations resemble those in the continuum: $q(x) \to V(x)q(x)$ and $\bar{q}(x) \to \bar{q}(x)V^\dagger(x)$, where $V(x)$ is an arbitrary element of SU(3). The only difference is that the Euclidean space-time positions x are limited to the lattice sites. Quark bilinears involving different lattice points can achieve gauge invariance by introducing the gluon field $U_\mu(x)$. For adjacent points, the bilinear is $\bar{q}(x)U_\mu(x)q(x + a\hat{\mu})$, with $\hat{\mu}$ representing the unit vector in the μ direction. This concept is illustrated in Fig. 1.4[6]. The formulation of lattice QCD is based on the path integral formalism, which expresses the QCD partition function as a sum over all possible field configurations. To make these calculations computationally tractable, a process called Monte Carlo integration is used to sample field configurations according to their importance in the path integral. This sampling is performed using a variety of algorithms, such as the Metropolis-Hastings algorithm, hybrid Monte Carlo, and others.

An important application of lattice QCD is to predict the properties of the QCD matter at the phase boundary. Figure 1.5 shows the temperature (T) vs. baryonic chemical potential (μ_B) of the QCD system at phase boundary calculated using lattice QCD[8]. The figure also shows the line of constant energy density $\epsilon(T, \mu_B) = \epsilon(T_c(0), 0) = 0.42(6)$ GeV/fm^3 and the line of constant entropy density $s(T, \mu_B) =$

$s(T_c(0), 0) = 3.7(5)\ \mathrm{fm}^{-3}$. Additionally, the chemical freeze-out parameters extracted from grand canonical ensemble-based fits to experimentally measured hadron yields[9] are also shown as markers, which are seen to coincide with the lattice QCD calculation.

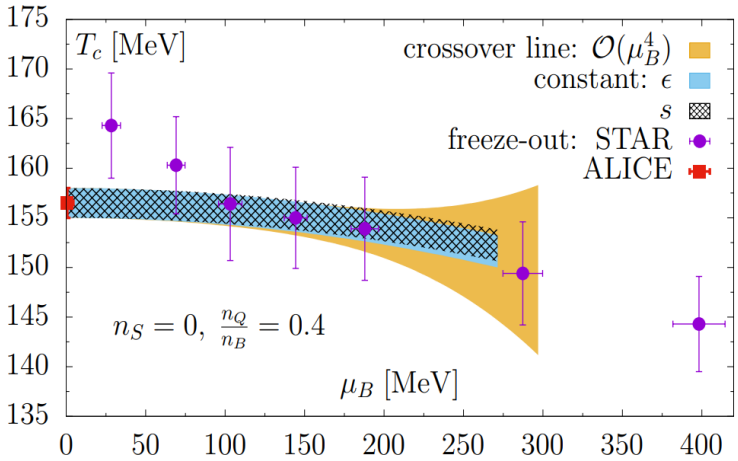

Figure 1.5 The phase boundary for (2+1)-flavor QCD within the temperature and baryonic chemical potential plane. Lines indicating constant energy and constant entropy density respectively are also displayed. Furthermore, the chemical freeze-out temperatures extracted based on experimental results are shown as markers. Figure is taken from[8].

While lattice QCD has been successful in providing first-principles predictions for many quantities, it is not without challenges. One major challenge is the computational cost. As the lattice spacing a decreases or the volume of the lattice increases, the number of degrees of freedom and the required computational resources grow substantially. Another challenge is the so-called sign problem, which arises when dealing with certain observables, such as those involving finite baryon density. The sign problem makes it difficult to perform Monte Carlo simulations, as it leads to a cancellation of contributions in the path integral, resulting in large statistical errors. Despite these challenges, lattice QCD has proven to be a powerful and indispensable tool in understanding the non-perturbative aspects of QCD, providing valuable insights into the behavior of quarks and gluons, for example at phase transitions, and making predictions that can be tested experimentally.

1.2 Quark Gluon Plasma (QGP)

1.2.1 QCD phase transition and QGP

The Quark-Gluon Plasma (QGP) is a theorized state of matter believed to have existed in the early universe momentarily after the Big Bang, when the temperature and energy density are exceptionally high. In this state, quarks and gluons, the basic

constituents of the strong nuclear force, are not confined within hadrons (like protons and neutrons) but roam freely in a hot, dense medium. As the universe expanded and cooled, it must have undergone a transition from QGP to the hadronic matter as we know it today. Figure 1.6 depicts the Big Bang and the evolution of the universe. The mechanisms governing the phase transition remain poorly understood, as does the structure of such nuclear matter at high energy densities and temperatures. This is also connected to dense astrophysical objects, such as neutron stars, where temperatures are low but densities are extremely high. Investigating QGP can shed light on the properties of neutron stars and

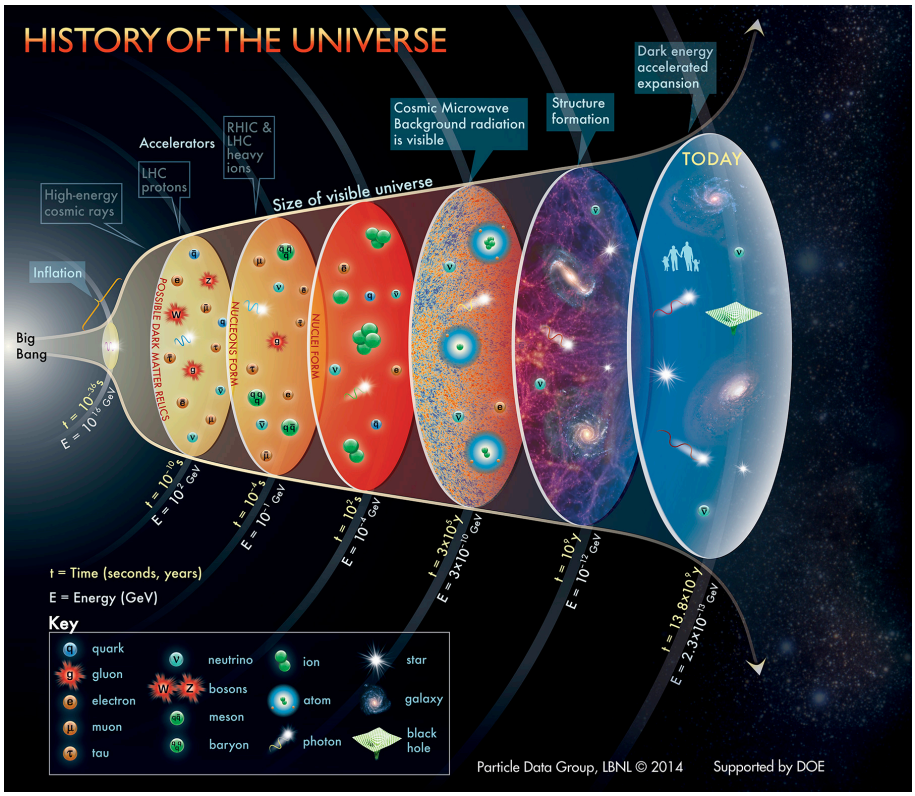

Figure 1.6 History of the universe. Figure is taken from[6].

provide valuable insights into the universe's evolution. Being a complex QCD system, the QGP also offers an invaluable means to probe the properties of QCD under extreme conditions.

In the 1970s, Nobel Prize-winning physicist T.D. Lee first suggested using relativistic heavy-ion collisions as a means of creating and studying the QGP[10]. This process involves accelerating two beams of charged heavy ions to nearly the speed of light using large particle accelerators and then colliding them. The kinetic energy lost by the colliding nuclei is concentrated in a space the size of an atomic nucleus, producing a high-temperature, high-density environment during a very brief time span. This environment alters the properties of the vacuum, causing particles to be excited. It also

allows quarks and gluons to escape confinement within hadrons, and ultimately form a QGP. The high-temperature, high-density conditions created by relativistic heavy-ion collisions bear a striking resemblance to the primordial fireball that emerged during the early stages of the Big Bang, leading to the nickname “Little Bang”.

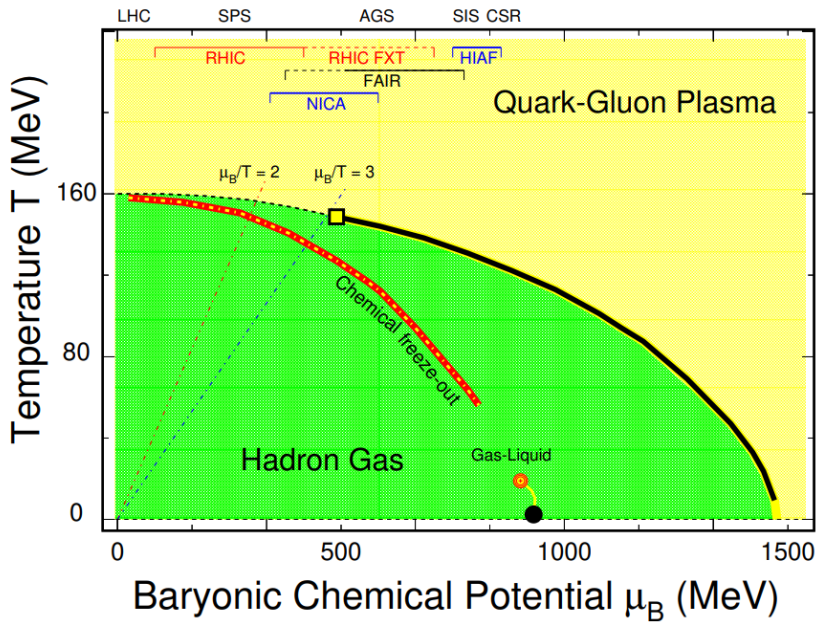

Figure 1.7 The schematic QCD phase diagram, depicted in the thermodynamic parameter space defined by temperature T and baryonic chemical potential μ_B. Chemical freeze-out parameters extracted from experiments are represented by the red line[11]. The dashed line near $\mu_B = 0$ indicates the crossover transition from the QGP to Hadron Gas[8,12-15]. The red circle and the yellow line denote the liquid-gas transition[16]. Phase spaces covered by physics programs of RHIC, NICA, FAIR, and HIAF are indicated at the top of the plot. Figure is taken from[17].

During the initial stage, nucleons break apart, releasing exciting quarks and gluons. As the mass-energy equation suggests, the higher the collision energy, the more and heavier particles are produced. The hot, dense system created is not static. Due to substantial kinetic energy and pressure gradients, it rapidly expands and cools. As the temperature falls below the critical threshold, quarks and gluons recombine into hadrons through intricate reactions, transitioning from the QGP phase to the hadronic phase. Finally, following interactions among hadrons and the decay of unstable hadrons, the final-state particles that can be detected experimentally are produced.

One of the main objectives of relativistic heavy-ion collisions is to investigate the phase transition between the QGP phase and the hadronic matter phase. The phase structure can be represented by a phase diagram, as shown in Fig. 1.7, that illustrates various states of the QCD matter in response to alterations in macroscopic thermodynamic variables, such as the temperature and the baryonic chemical potential[18-20].

The collision energies and their corresponding accelerator complexes are indicated at the top of the figure. At zero baryonic chemical potential or baryonic density, the transition from the QGP to the hadronic matter is a smooth crossover occurring at $T = 150 - 160$ MeV[8,12-15], as suggested by state-of-the-art lattice QCD calculations and shown as the dashed line in the figure. On the other hand, at high baryonic density, a first-order phase transition is expected, shown as the black solid line. Thermodynamically, the first-order phase boundary line must terminate at a finite baryonic density, which is the QCD critical point. Recent lattice calculations concluded that the QCD critical point is unfavored[21-22] when $\mu_B/T < 2.5$. The red line in the graph symbolizes the chemical freeze-out curve, derived from experimental measurements. The region beneath this curve signifies a state where inelastic scattering halts and the hadrochemistry is fixed.

1.2.2 QGP evolution and experimental observables

Figure 1.8 depicts the space-time evolution of a relativistic heavy-ion collision. If conditions for QGP formation aren't met, the system will follow a hydrodynamical evolution (as depicted on the left side of Figure 1.8). This initial phase, a pre-hadronic stage, sees elevated pressure and temperature without actual parton deconfinement. Nucleons can still recombine into new detectable hadrons after the hadron gas phase freeze-out. On the right side of the figure, we depict the collision's evolution in the case of formation when the critical temperature and energy density are achieved. The space-time progression can be described as follows:

- Initial stage
- Thermalization, hydrodynamical evolution and hadronization
- Chemical and kinetic freeze-out

In 2018, the STAR experiment at RHIC recorded collisions of Ruthenium (Ru+Ru) and Zirconium (Zr+Zr) isotopes, which provided a novel and unique research opportunity for investigation of the properties of the QGP in previously unexplored collision systems. The Ru+Ru and Zr+Zr collisions will be referred to as "isobar collisions" in subsequent chapters, due to the fact that the Ruthenium and Zirconium nuclei have the same number of nucleons, but different atomic numbers, making them isobars. In the rest of this chapter, measurements carried out to study the properties of the QGP produced in isobar collisions as well as other collision systems will be introduced.

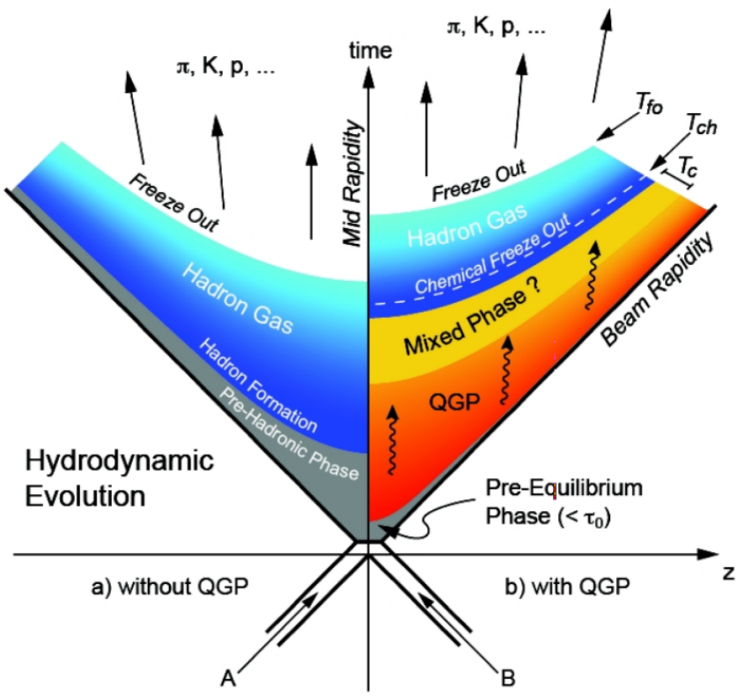

Figure 1.8 The diagram illustrates the progression of a heavy-ion collision. Two distinct scenarios – with and without the QGP formation – are depicted. The critical temperature for the transition to the QGP phase is denoted by T_c. Additionally, the temperatures at which kinetic freeze-out and chemical freeze-out occur are represented by T_{fo} and T_{ch}, respectively. Figure is taken from[23].

1. Initial stage ($\tau < 1$ fm/c)

During the initial stage of a heavy-ion collision at the time scale of < 1 fm/c, hard partonic scatterings with large momentum transfers occur, leading to the production of particles with either significant mass or substantial transverse momenta ($p_{\mathrm{T}} >$ a few GeV/c). These produced high-momentum or high-mass objects, usually referred to as hard probes, subsequently experience the entire evolution of the system and encode information on the QGP properties. Since the production of these particles involves high momentum transfers, pQCD is applicable and can be used to calculate their yields, making them well-calibrated probes to study the QGP. Two widely used hard probes of this kind are jets and quarkonium[24].

Jet measurements

Highly-energetic partons (quarks and gluons) travel through the medium and fragment into collimated sprays of hadrons, known as jets. Interactions with the QGP can cause penetrating partons to lose energy and have their shower structures modified, which are consequences of the phenomenon referred to as the jet quenching[25]. The leading-order hard scatterings are $2 \rightarrow 2$ processes, which lead to high-momentum par-

tons moving 180° apart in the plane transverse to the beam direction as depicted in Fig. 1.9. This specific event visualization represents a Au+Au event with a distinct back-to-back dijet signal. Lines represent tracks and the towers situated outside the depicted circumference indicate the energy deposits in the calorimeter. Tracks and towers proximate to the jet axes are illustrated in colors for distinction, while all other tracks and towers are depicted in grey.

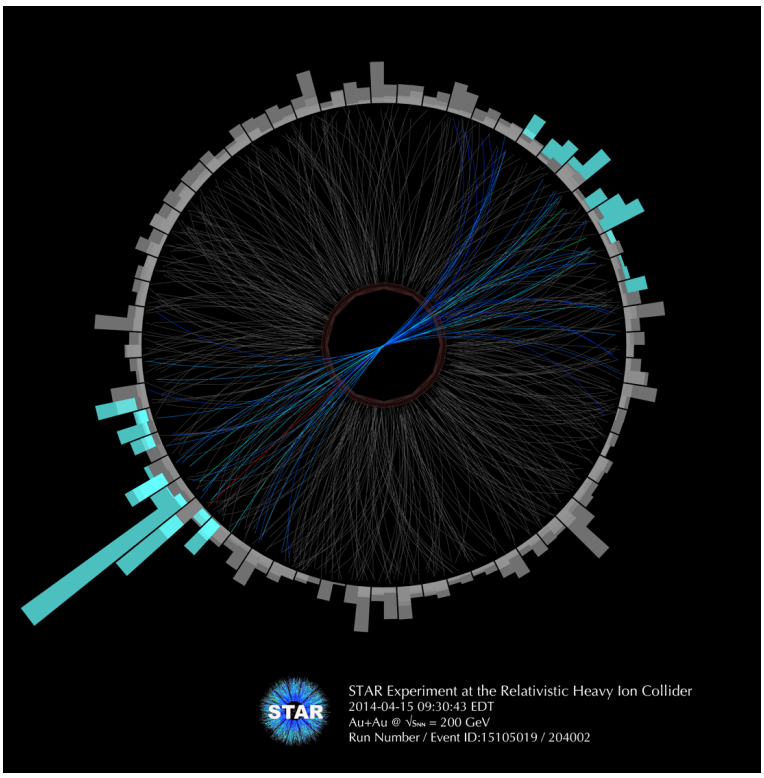

Figure 1.9 Event display depicting a dijet event in a Au+Au collision recorded by the STAR experiment.

High-momentum particles, primarily originating from hard scatterings, can be used as a proxy for jets to study jet quenching. In order to quantify alterations to the hadron spectra due to parton energy loss in nucleus-nucleus (A+A) collisions, the nuclear modification factor can be used, which is defined as:

$$R_{\mathrm{AA}} = \frac{\sigma_{\mathrm{NN}}}{\langle N_{\mathrm{coll}} \rangle} \frac{d^2 N_{\mathrm{AA}}/dp_T d\eta}{d^2\sigma_{pp}/dp_T d\eta}, \tag{1.5}$$

where $\langle N_{\mathrm{coll}} \rangle$ represents the average number of binary nucleon-nucleon collisions for A+A collisions within a specific range of impact parameters, and σ_{NN} is the nucleon-nucleon inelastic cross section. N_{AA} and σ_{pp} refer to the particle production yield in A+A collisions and the cross section in p+p collisions, respectively. If A+A collisions were merely a superposition of incoherent nucleon-nucleon collisions, the cross section of high-p_{T} particles is expected to scale with N_{coll}, resulting in $R_{\mathrm{AA}} = 1$. A value

of $R_{AA} < 1$ signifies suppression, while $R_{AA} > 1$ indicates enhancement. The term centrality in heavy-ion physics refers to the impact parameter of the collision. Central collisions are characterized by small impact parameters and typically result in the creation of a hotter and denser medium following the collision. On the other hand, peripheral collisions, which have larger impact parameters, generate a less dense and cooler post-collision environment.

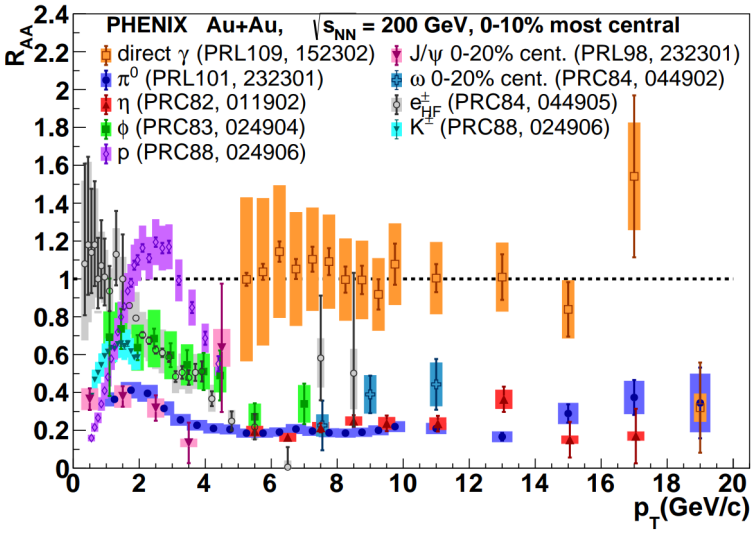

Figure 1.10 The R_{AA} values measured by the PHENIX experiment for various particles show that colored probes (high-p_T final-state hadrons) experience suppression, while electroweak probes (direct photons) do not exhibit suppression at RHIC. Figure is taken from [25].

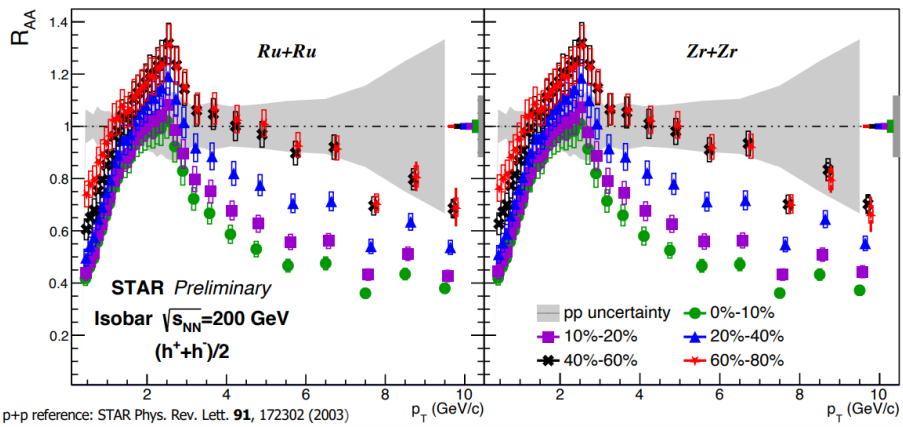

Figure 1.11 Charged hadron R_{AA} in Ru+Ru and Zr+Zr collisions at $\sqrt{s_{NN}}$ = 200 GeV. The grey bands represent the uncertainty for the p+p reference. Figure is taken from [26].

Figure 1.10 shows a range of R_{AA} measurements made by the PHENIX collaboration in Au+Au collisions at the center-of-mass energy per nucleon-nucleon pair ($\sqrt{s_{NN}}$) of 200 GeV for both color-charged probes (high-p_T final-state hadrons) and electroweak probes (direct photons). Remarkably, the R_{AA} values for direct photons, which do not interact with the QGP via strong force and thus are not expected to suffer from jet

quenching, are consistent with unity across all measured p_T ranges. This implies that the N_{coll} scaling is effective at high p_T. On the other hand, colored probes, such as π^0, η, are strongly suppressed with R_{AA} around 0.2 - 0.3 for $p_T > 5$ GeV/c. This is a direct consequence of the energy loss experienced by parent partons in the QGP medium.

Figure 1.11 shows a similar measurement but for charged hadrons as a function of p_T in Ru+Ru (left) and Zr+Zr (right) collisions at $\sqrt{s_{NN}}$ = 200 GeV by the STAR experiment. Substantial suppression is observed at high p_T with the suppression lessening from central to peripheral collisions, consistent with decreasing medium effects. Both Ru+Ru and Zr+Zr measurements indicate a similar degree of suppression, as the sizes of the Ru and Zr nuclei are similar and the collision energies are identical. These results clearly indicate the creation of the QGP in isobar collisions.

Quarkonium suppression

Quarkonia hold a unique position as probes of the QGP, as they enter the medium as bound states and are anticipated to dissociate due to the color-screening effect when the medium's Debye radius, inversely proportional to the medium temperature, becomes smaller than their sizes. In addition, dynamical processes, such as scatterings of quarkonia with partons in the medium can also lead to the breakup of quarkonium states[27]. Suppression of the J/ψ ($c\bar{c}$) meson yield in central Au+Au and Pb+Pb collisions at RHIC[28] and LHC[29] has been observed at high p_T. The suppression level exceeds what Cold Nuclear Matter (CNM) effects can account for, which include alterations to the parton distribution function in nuclei, nuclear absorption, etc. This implies that the reduction of the high-p_T J/ψ yield is, at least partially, due to the presence of the hot medium, with the medium-induced dissociation being the underlying mechanism. The newly recorded Ru+Ru and Zr+Zr collisions provided a unique opportunity to study whether it is the average energy density or the collision geometry that drives the J/ψ suppression.

Figure 1.12 illustrates the J/ψ R_{AA} against p_T in different centrality classes of isobar collisions at 200 GeV, where results from Ru+Ru and Zr+Zr collisions are found to be consistent and thus combined. A clear suppression from low to high p_T is evident in central collisions. At low p_T, it is probably due to a mix of CNM effects and QGP dissociation. R_{AA} rises with p_T, which could result from the interplay of several effects, including decreasing CNM effects with increasing p_T, less time spent in the medium for high p_T J/ψ, and rising contributions from b-hadron decays as p_T increases. The R_{AA} in Ru+Ru and Zr+Zr collisions are compared to the same results in smaller Cu+Cu[30] and

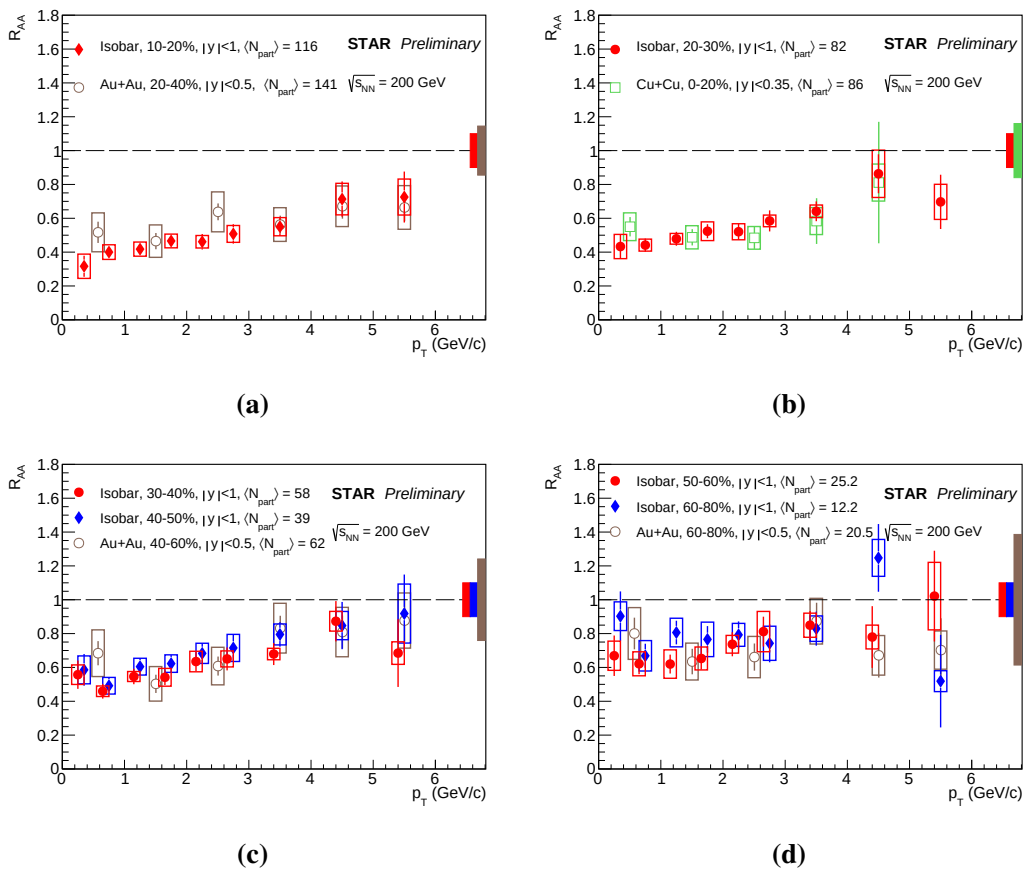

Figure 1.12 J/ψ R_{AA} **as a function of** p_T **in different centrality classes of isobar collisions at** $\sqrt{s_{NN}}$ **= 200 GeV. They are compared with results from Au+Au and Cu+Cu collisions of the same collision energy at similar** N_{part} **values.**

larger Au+Au[31] collision systems at similar N_{part} values, and the level of suppression is seen to be compatible. At similar N_{part}, the collision geometries in these systems are different, while the average energy densities, which roughly scale with N_{part}, are similar. The compatible R_{AA} values observed in Fig. 1.12 indicate that it is the energy density rather than the collision geometry that dictates the J/ψ suppression.

The N_{part} dependences of the J/ψ suppression are further explored in Fig. 1.13 for J/ψ $p_T > 0.2$ GeV/c in isobar (filled squares) and Au+Au (filled diamonds) collisions at $\sqrt{s_{NN}}$ = 200 GeV[28]. They are seen to follow a similar trend, confirming N_{part}-driven J/ψ suppression. The suppression also increases from peripheral to central collisions, as expected from the presence of a hotter and denser QGP in central collisions. When compared to results in Pb+Pb collisions at $\sqrt{s_{NN}}$ = 2.76 TeV[29] and $\sqrt{s_{NN}}$ = 5.02 TeV[32], J/ψ is more suppressed in central and semi-central collisions at RHIC than that at the LHC, likely due to the smaller charm quark production yield and thus less regeneration contribution[33-34] arising from deconfined charm-anticharm pairs combining to form J/ψ at RHIC.

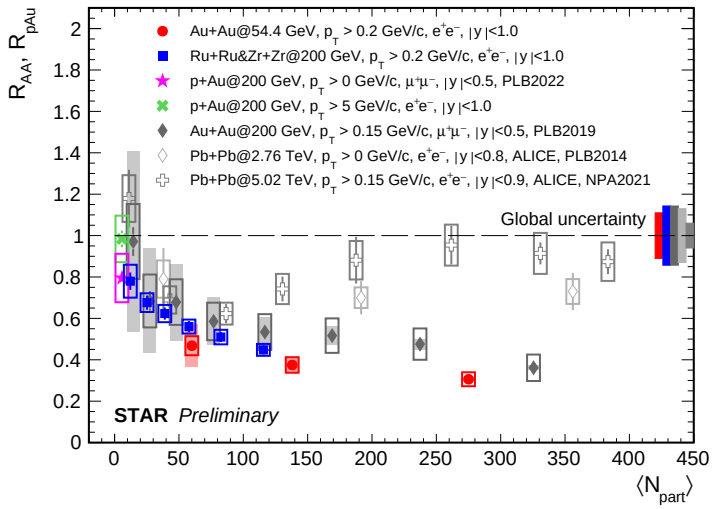

Figure 1.13 J/ψ R_{AA} **as a function of** N_{part} **for** p_{T} **above 0.2 GeV/**c **in isobar collisions at** $\sqrt{s_{\mathrm{NN}}}$ **= 200 GeV, compared to results from other collision systems.**

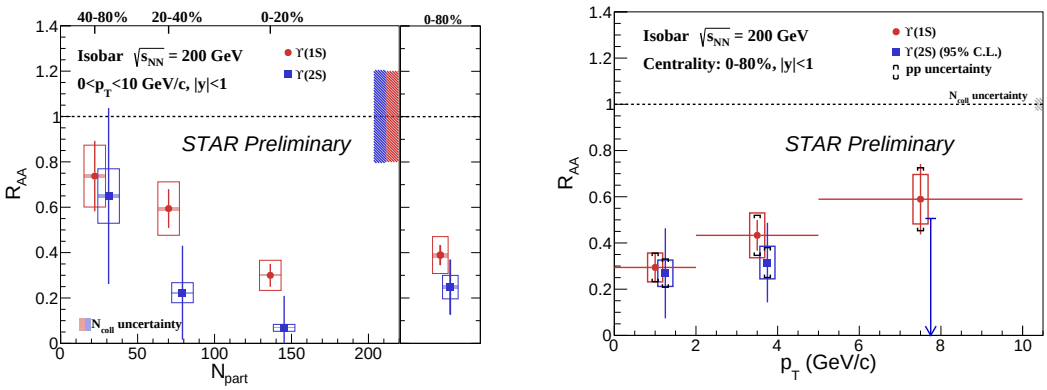

(a) **(b)**

Figure 1.14 **(a) The** R_{AA} **for** $\Upsilon(1S)$ **(red) and** $\Upsilon(2S)$ **(blue) as a function of** N_{part} **for** $p_{\mathrm{T}} <$ **10 GeV/**c **in isobar collisions at** $\sqrt{s_{\mathrm{NN}}}$ **= 200 GeV. The two bands at unity represent global uncertainties. (b) The** R_{AA} **for** $\Upsilon(1S)$ **(red) and** $\Upsilon(2S)$ **(blue) as a function of** p_{T} **in isobar collisions at** $\sqrt{s_{\mathrm{NN}}}$ **= 200 GeV. Figures are taken from[35].**

Furthermore, different quarkonium states of different sizes are expected to dissociate at different temperatures, resulting in a sequential suppression pattern. To observe this phenomenon, bottomonia ($\Upsilon(1S)$, $\Upsilon(2S)$, $\Upsilon(3S)$), mesons made up of bottom anti-bottom quark pairs, can be used. $\Upsilon(1S)$ is the smallest and thus should dissociate at the highest temperature, while $\Upsilon(3S)$ is the largest. Bottomonia are also cleaner probes compared to charmonia (J/ψ, $\psi(2S)$) due to the much smaller regeneration contribution[28] thanks to the lower production cross section for $b\bar{b}$ quarks.

Figure 1.14 (a) shows R_{AA} values for $\Upsilon(1S)$ and $\Upsilon(2S)$ as a function of N_{part} in isobar collisions. As observed for J/ψ, the R_{AA} decreases with increasing N_{part} indicating enhanced QGP effects in central collisions. When integrated over centrality

as shown in the right panel of Fig. 1.14 (a), a hint of sequential suppression is seen, i.e. $\Upsilon(2S)$ R_{AA} seems smaller than $\Upsilon(1S)$ R_{AA}. Due to a lack of statistics, $\Upsilon(3S)$ R_{AA} could not be measured. The p_{T} dependence of the $\Upsilon(1S)$ and $\Upsilon(2S)$ R_{AA} is shown in Fig. 1.14 (b), where a suggestive increasing trend is seen.

2. Thermalization, hydrodynamical evolution, and hadronization

Frequent elastic and inelastic interactions between partons in the QGP lead to a rapid thermalization of the system. Due to the internal pressure, the thermalized system expands quickly and the energy density decreases. The rapid expansion is typically modeled using relativistic hydrodynamics[36]. The hydrodynamic equation of motions is as follows:

$$\partial_\mu T^{\mu\nu} = 0, T^{\mu\nu}(x) = u^\mu u^\nu(\epsilon + P) - g^{\mu\nu} P, \tag{1.6}$$

$$\partial_\mu j_i^\mu = 0, j_i^\mu = n_i u^\mu. \tag{1.7}$$

In the local rest frame, ϵ, P, and n_i represent the proper energy density, pressure, and density of charge i, respectively, while u_μ denotes the four-velocity. The energy-momentum tensor is given by $T^{\mu\nu}$, and the charge current density is represented by j^μ. The equation of motion is derived from local charge conservation, expressed as $\partial_\mu j_i^\mu = 0$, and local conservation of energy and momentum, given by $\partial_\mu T^{\mu\nu} = 0$.

When the system reaches the critical energy density during cool-down, hadronization begins, and the system gradually evolves into interacting hadron resonance gas. There are two possible mechanisms for hadronization: fragmentation, which involves high-p_{T} partons breaking down into lower-p_{T} hadrons, and coalescence, which involves low-p_{T} partons combining to form higher-p_{T} hadrons. In this phase, the expansion and cooling of the system continue, as well as the elastic and inelastic interactions among the hadrons, which can alter their kinematics and species.

A variety of QGP signatures, such as strangeness production and collective flow[37], have been proposed to study the bulk properties of the QGP at this stage. By examining these aspects in conjunction, we can construct a more comprehensive understanding of the state and behavior of the QGP.

Collectivity

In semi-central heavy-ion collisions, the reaction zone of two colliding nuclei is non-spherical, as illustrated in the left panel of Fig. 1.15. The plane spanned by the impact parameter direction and the beam direction is called the reaction plane. As the

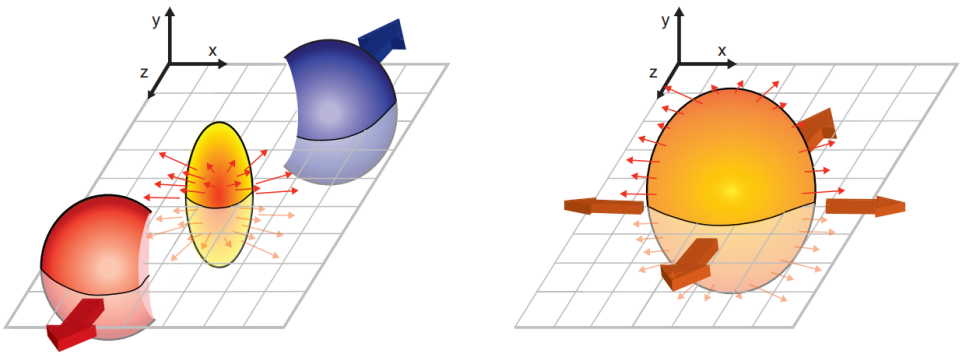

Figure 1.15 Schematic diagrams illustrating the initial overlap region (left) and the resulting momentum-space anisotropy. Figure is taken from[25].

pressure gradient is not azimuthally uniform, re-scatterings among the constituents of the system transform the initial coordinate-space anisotropy into the final momentum-space anisotropy (right panel of Fig. 1.15). The spatial anisotropy is most prominent during the early stages of the collision's evolution. As the system evolves, the anisotropy in the momentum space builds up over time and is expected to be the largest close to the phase boundary. The endurance of these anisotropies against the system's evolution suggests that the QGP possesses small viscosity to the entropy ratio, which turns out to be the smallest ever observed in nature. This is why the QGP is also referred as the "perfect fluid"[38]. Consequently, medium constituents share a common velocity distribution that is azimuthally asymmetric and move collectively, a phenomenon called "anisotropic flow".

Anisotropic flow is typically extracted via the Fourier expansion of the three-dimensional differential distribution of final-state particles[39].

$$E\frac{d^3N}{d^3p} = \frac{d^2N}{2\pi p_T dp_T dy}(1 + \sum_{n=1}^{\infty} 2v_n cos[n(\phi - \psi)]), \tag{1.8}$$

$$v_n = \langle cos[n(\phi - \psi)]\rangle, n = 1, 2, 3, \cdots \tag{1.9}$$

where ϕ denotes the azimuthal angle of an outgoing particle, ψ represents the angle of the reaction plane, and v_n is the nth order flow coefficient.

The second Fourier coefficient or elliptic flow (v_2) reflects the main feature of the initial geometric shape of the reaction region in the transverse plane, as shown in the left panel of Fig. 1.15. Large values of v_2 at low p_{T} are considered evidence of the hydrodynamic behavior of the system. At high p_{T}, v_2 could emerge from the jet quenching phenomenon that jets traveling perpendicular to the reaction plane have a longer path-length and experience more energy loss than those traveling along the reaction plane.

The origin of v_2 can be studied experimentally by checking v_2 scaled by the number

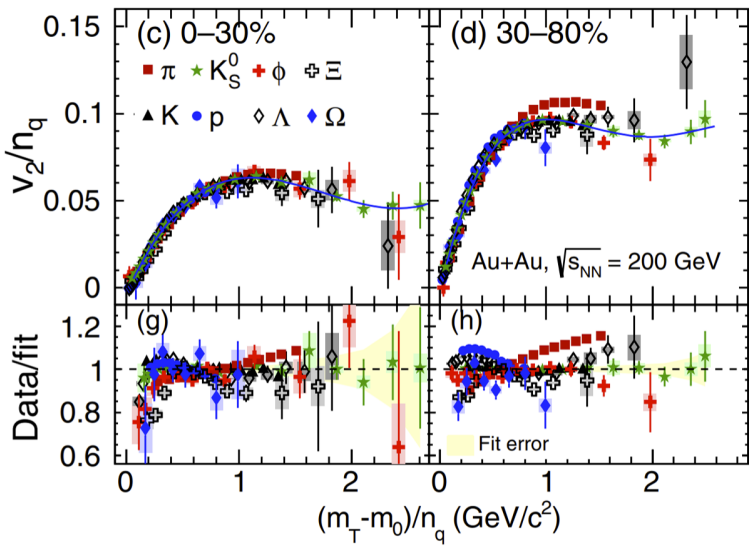

Figure 1.16 The elliptic anisotropy v_2, scaled by the number of constituent quarks, as a function of $(m_T$-$m_0)/n_q$ for identified hadrons from Au+Au collisions at $\sqrt{s_{NN}}$ = 200 GeV. The lower panels display ratios relative to a polynomial fit of the K^0_s v_2/n_q. Statistical uncertainties are indicated by vertical lines, while shaded boxes represent systematic uncertainties. Figure is taken from[40].

of constituent quarks (NCQ and denoted as n_q) for various particles. If v_2 is developed during the partonic phase and hadrons are formed mainly through parton recombination, one expects v_2/n_q of different particles to collapse to a common curve. Figure 1.16 displays v_2/n_q as a function of $(m_T$-$m_0)/n_q$ for eight different hadrons in Au+Au collisions at $\sqrt{s_{NN}}$ = 200 GeV. This is shown for 0 - 30% and 30 - 80% centrality classes, with m_T and m_0 representing the transverse and rest masses of the hadron, respectively. A distinct centrality dependence of v_2 is observed for all identified hadrons that the values of v_2 are larger in peripheral collisions (30% - 80% centrality) compared to those in central collisions (0% - 30% centrality). This observation aligns with the understanding that the final momentum anisotropy is largely influenced by the initial spatial anisotropy. The NCQ scaling is tested quantitatively by taking the ratios of v_2/n_q for measured particles to the third-order polynomial fit to the K^0_s v_2/n_q, as shown in the lower panels of Fig. 1.16. For both 0 - 30% and 30 - 80% centrality intervals, the scaling is approximately within 10%. The apparent deviation for pions from the NCQ scaling could arise from resonance decay and non-flow correlations[41]. Such a NCQ scaling is consistent with the existence of a partonic phase created in heavy-ion collisions where the anisotropic flow builds up, and the final-state hardons are produced mainly through the coalescence of constituent quarks.

Measurements of v_2 are also carried out in isobaric Ru+Ru and Zr+Zr collisions. The upper panel of Fig. 1.17 shows p_T-integrated charged hadron v_2 as a function of centrality using 5 different methods for the two collision systems, open symbols for Zr+Zr

and solid symbols for Ru+Ru. These methods mainly differ in the extent to which the

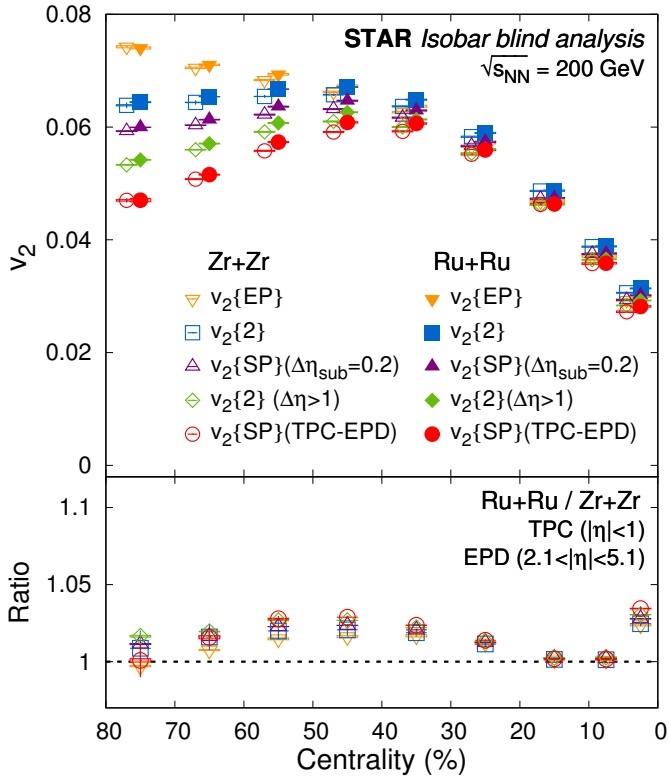

Figure 1.17 The elliptic anisotropy v_2 in isobar collisions at $\sqrt{s_{NN}}$ = 200 GeV is measured using different methods and depicted as a function of centrality. The upper panels feature both Ru+Ru (solid symbols) and Zr+Zr (open symbols) measurements. To improve clarity, data points are shifted along the x-axis. In the lower panels, the v_2 ratios are displayed for Ru+Ru over Zr+Zr collisions. Statistical uncertainties are delineated by lines, while boxes illustrate systematic uncertainties. Figure is taken from [42].

non-flow contribution is suppressed, which is why they are consistent in central collisions where the relative contribution of non-flow effect is small, but differ significantly in peripheral collisions. Taking $v_2\{\mathrm{SP}\}$ (TPC-EPD) results (red circles) as an example, its centrality dependence reflects the expected collision geometry, i.e., v_2 is the largest in mid-central collisions and decreases towards both central and peripheral collisions. The figure's lower panel displays the v_2 ratios between Ru+Ru and Zr+Zr collisions using different methods, and they follow a common trend. These ratios exceed unity by 2 - 3% in mid-central collisions and decrease towards peripheral and central collisions. However, an exception occurs in the top 5% centrality bin, where ratios also rise above unity by a few percent. The results from central collisions might be attributed to a larger quadrupole deformation in Ru compared to Zr. The above-unity ratio in mid-central collisions could stem from the different nuclear structures of the two isobars, as suggested by DFT calculations [42].

Another type of collectivity in heavy-ion collisions, known as the radial flow, arises

from the radial expansion of the system throughout the entire evolution, including both the partonic and hadronic phases. As a result, all the final-state particles experience a common transverse radial flow velocity field, which pushes heavier particles to larger transverse momenta[9]. The common radial velocity can be extracted by fitting the spectra of π, K, p, simultaneously with the Blast-Wave model[43-44]. The Blast-Wave model provides a framework for understanding the hydrodynamic evolution in heavy-ion collisions. Given the collision's geometry, it operates under the assumption of a cylindrically symmetric system. It is important to note that this model is merely a parameterization of the ideal, non-viscous hydrodynamic equations and does not address particle production directly. Instead, it focuses on how particles propagate within the expanding hydrodynamic system. The Blast-Wave model operates under the assumption of local thermal equilibrium. This equilibrium is anticipated to be established early in the heavy-ion collision process, implying that within this model, system evolution commences from a pre-thermalized state.

Figure 1.18 shows the average transverse radial flow velocity, $\langle\beta\rangle$, against the event multiplicity in Au+Au collisions of different energies. It can be seen that $\langle\beta\rangle$ increases dramatically with rising centrality in Au+Au collisions, indicating faster expansion in central collisions than that in peripheral collisions. Such a rising trend does not depend on the collision energy examined here.

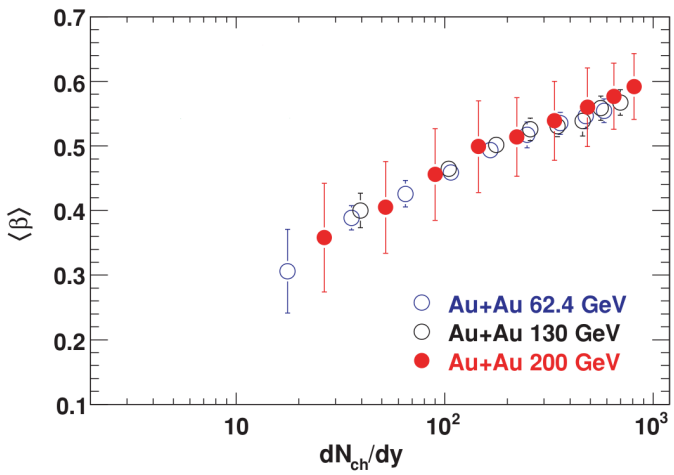

Figure 1.18 The average radial flow velocity derived from the Blast-Wave model fit for Au+Au collisions at 62.4, 130, and 200 GeV. The flow velocity is presented as a function of the charged-hadron multiplicity. The error bars indicate the total statistical and systematic uncertainties. Figure is taken from[9].

Strangeness enhancement

In heavy-ion collisions, hadrons containing strange quarks exhibit enhanced pro-

duction compared to expectations from p+p collisions. This observed enhancement is attributed to the QGP's efficient production and equilibration of strange quarks, driven by a large gluon density and a low energy threshold for $s\bar{s}$ production. In contrast, due to its higher threshold for strangeness production, a hadronic system is expected to yield considerably smaller amounts of strangeness with a significantly longer equilibration time. Therefore, strange hadrons can serve as excellent probes for studying the QGP dynamics.

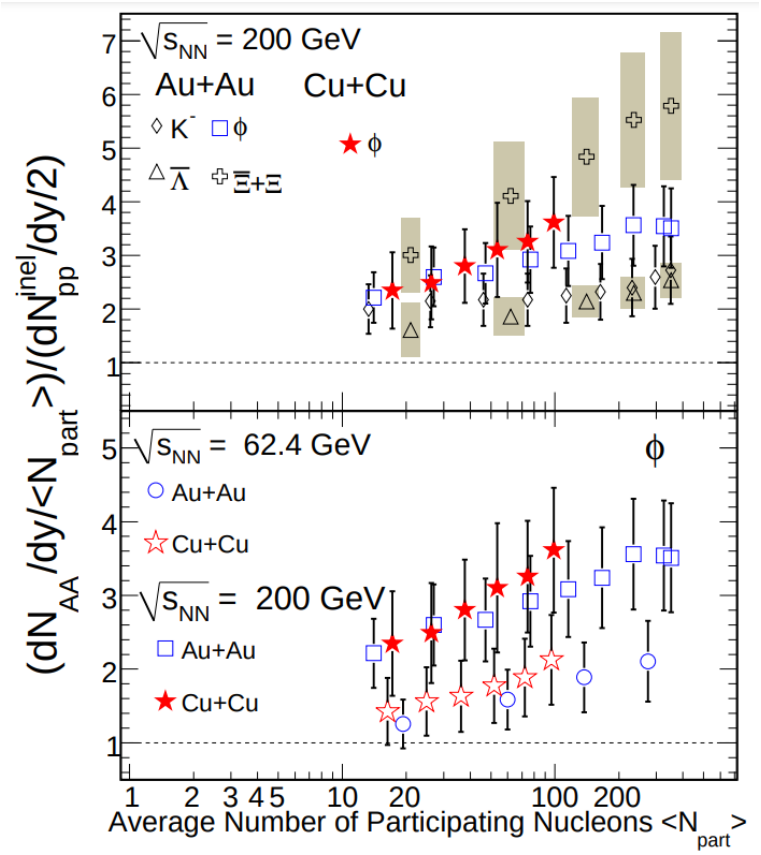

Figure 1.19 Upper panel: Ratio of yields for K^-, ϕ, $\bar{\Lambda}$, and $\Xi + \bar{\Xi}$ in Cu+Cu and Au+Au collisions, normalized to $\langle N_{\text{part}}\rangle$, to the corresponding yields in inelastic p+p collisions as a function of $\langle N_{\text{part}}\rangle$ at 200 GeV. Lower panel: The same for ϕ mesons in Cu+Cu and Au+Au collisions at 200 and 62.4 GeV. Figure is taken from[45].

The ratio of $\langle N_{\text{part}}\rangle$-normalized strange hadron production in Cu+Cu and Au+Au collisions to corresponding results from p+p collisions at 200 GeV is shown in the upper panel of Fig. 1.19. The results are plotted as a function of $\langle N_{\text{part}}\rangle$. K^-, $\bar{\Lambda}$, and $\Xi + \bar{\Xi}$ display an enhancement (ratio > 1) that increases with the particle's strange number. Moreover, the enhancement of these open-strange hadrons rises with collision centrality, peaking in the most central collisions, in line with the expected increase of QGP effects with collision centrality.

In the upper panel of Fig. 1.19, the ϕ meson production is also observed to be

enhanced. Interestingly, the production of ϕ mesons does not follow the strange quark ordering observed for other strange hadrons. The enhancement in ϕ meson production, related to the medium density, is further supported by the energy dependence shown in the lower panel of Fig. 1.19. The ϕ meson enhancement relative to p+p collisions is more significant at higher beam energy.

3. Chemical and kinetic freeze-out ($\tau \sim 10$ fm/c)[46]

The expansion of the QGP results in a decline in temperature, and the relative abundances of the emitted particle species become fixed at the chemical freeze-out temperature when inelastic scatterings among particles cease. However, these particles continue to interact elastically until all hadronic interactions cease, and kinetic freeze-out is reached at which point the kinematic distributions of the particles are frozen. No further hadronic interactions occur until the particles, now free-streaming, are detected experimentally. Therefore, measuring particle yield and spectrum can provide insights into the QGP properties at the chemical and kinetic freeze-out stages. Additionally, bulk characteristics such as rapidity density (dN/dy), average transverse momentum ($\langle p_{\mathrm{T}} \rangle$), and particle ratios, can offer further insights into the mechanisms responsible for particle production. Moreover, comparing bulk properties of the systems created in heavy-ion collisions of different sizes and energies can shed light on the underlying dynamics driving the evolution of the system.

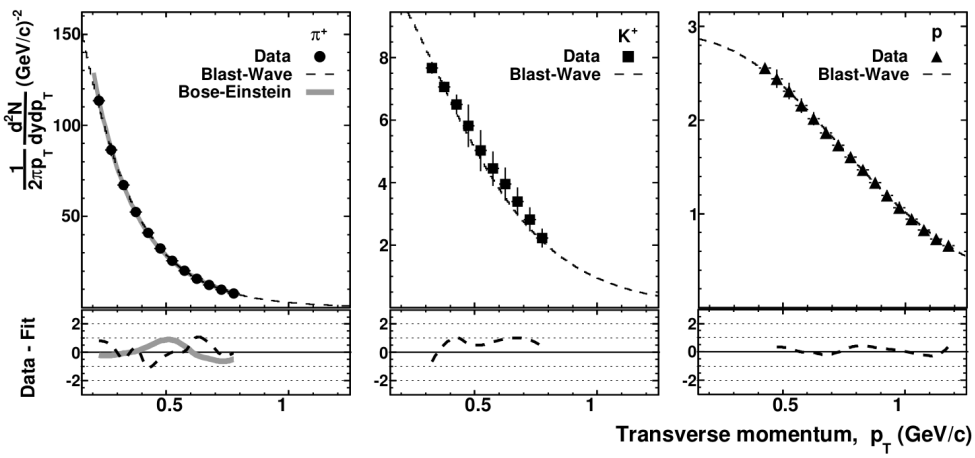

Figure 1.20 Spectra of π^+ (left), K^+ (center), and protons (right) in 0-10% central Cu+Cu collisions at $\sqrt{s_{\mathrm{NN}}}$ = 200 GeV, along with Blast-Wave model fit (dashed lines). The fit is performed across all species simultaneously. To mitigate the effect of resonance decays, pion data below p_{T} = 0.5 GeV/c are not included in the Blast-Wave fits. In addition, a Bose-Einstein fit to the pion spectra over the entire p_{T} range is displayed. The lower panels show the quality of the fits via the discrepancies between the measured points and the fit in terms of the number of standard deviations. Figure is taken from[47].

As an example to illustrate how the bulk properties are obtained, Fig. 1.20 presents measured p_T distributions for π^+ (left), K^+ (middle) and proton (right) in 0-10% central Cu+Cu collisions at $\sqrt{s_{NN}}$ = 200 GeV. The freeze-out properties are extracted through a simultaneous Blast-Wave fit to the π^+, K^+, and p spectra, shown as dashed lines overlapped with data points. The fit provides an accurate representation of the spectra, demonstrated by the differences between data and fit results in terms of the number of standard deviations in the lower panels. To minimize the impact of resonance decay contributions, π^+ data points for $p_T < 0.5$ GeV/c are excluded from the Blast-Wave fit. Fig. 1.20 also features the Bose-Einstein fit (grey band) to the π^+ spectra, which offers a slightly better interpretation of the data.

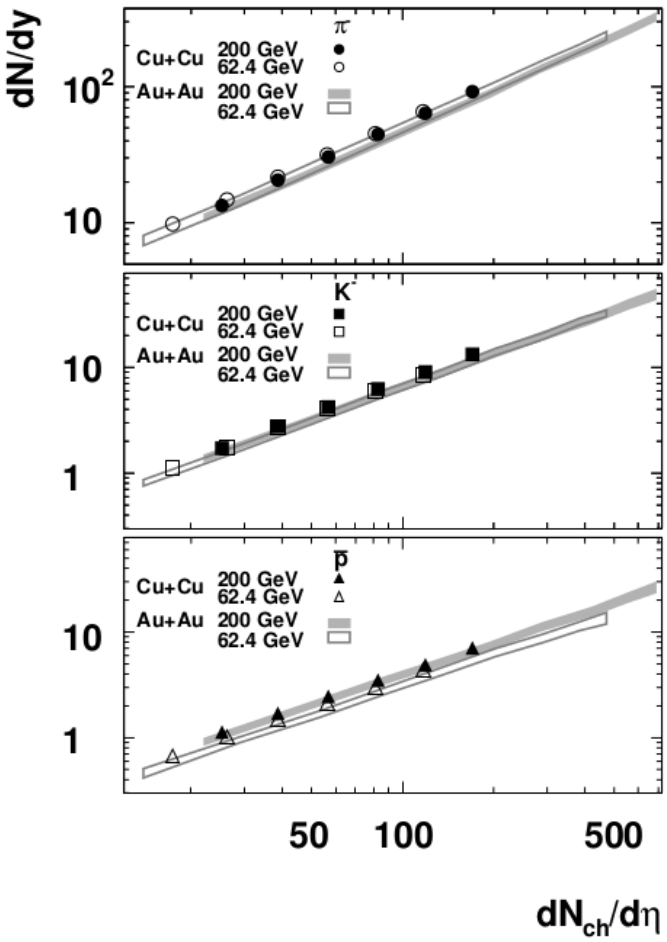

Figure 1.21 The integrated yields ($\mathrm{d}N/\mathrm{d}y$) **at mid-rapidity for pions, kaons, and anti-protons, plotted against the charged particle multiplicity** ($\mathrm{d}N_{ch}/\mathrm{d}\eta$)**. Filled and open points (bands) correspond to data in Cu+Cu (Au+Au) collisions at** $\sqrt{s_{NN}}$ **= 200 GeV and 62.4 GeV, respectively. The error bars indicate combined statistical and systematic uncertainties in quadrature. Figure is taken from[47].**

Figure 1.21 illustrates the relationship between integrated yields ($\mathrm{d}N/\mathrm{d}y$) and charged particle multiplicity ($\mathrm{d}N_{ch}/\mathrm{d}\eta$) for π^-, K^-, and $\bar{p}$ at mid-rapidity. $\mathrm{d}N/\mathrm{d}y$ for

each species exhibit a linear increase with multiplicity in this logarithmic representation, with Cu+Cu data aligning with Au+Au data at comparable values of $dN_{ch}/d\eta$. In cases where the $dN_{ch}/d\eta$ values are similar, higher collision energy results in increased yields. The scaling of dN/dy with $dN_{ch}/d\eta$ indicates that $dN_{ch}/d\eta$ dictates the bulk properties at mid-rapidity independent of the collision system at a given collision energy.

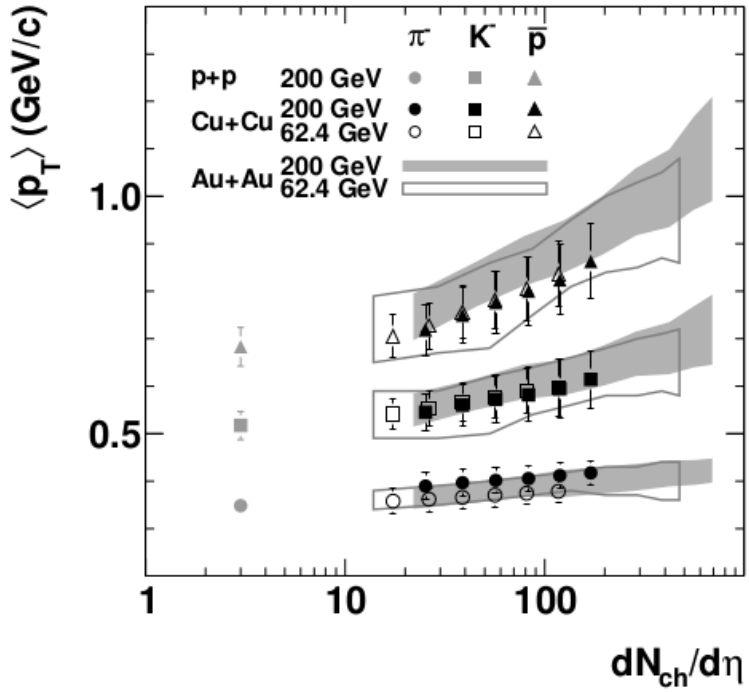

Figure 1.22 The mean transverse momentum plotted against mid-rapidity charged hadron multiplicity for pions, kaons, and anti-protons. Experimental data in Cu+Cu (Au+Au) collisions at $\sqrt{s_{NN}}$ = 200 GeV and 62.4 GeV are represented by open and closed symbols (bands) respectively. Error bars indicate the combined statistical and systematic uncertainties. Figure is taken from [47].

Figure 1.22 illustrates the relationship between $\langle p_T \rangle$ and $dN_{ch}/d\eta$ for π^-, K^- and $\bar{p}$ in Cu+Cu and Au+Au collisions at 62.4 and 200 GeV. An increase in the $\langle p_T \rangle$ slope is observed with an increase in hadron mass, implying a collective expansion along the radial direction. Notably, the $\langle p_T \rangle$ scales with $dN_{ch}/d\eta$, displaying minimal variation across different collision energies and systems.

Figure 1.23 (a) presents the ratios for negatively charged particles, $\bar{p}/\pi^-$ and K^-/π^-, plotted against $dN_{ch}/d\eta$. They exhibit a similar scaling behavior with respect to $dN_{ch}/d\eta$ for different collision systems. A minor decrease in the values for both ratios at the lower collision energy of 62.4 GeV is discernible, yet they fall within the bounds of experimental uncertainties. The ratios for positively charged particles, p/π^+ and K^+/π^+, are illustrated in Fig. 1.23 (b). These ratios similarly show a scaling behavior with $dN_{ch}/d\eta$ for the same collision energy. Interestingly, the energy effect observed

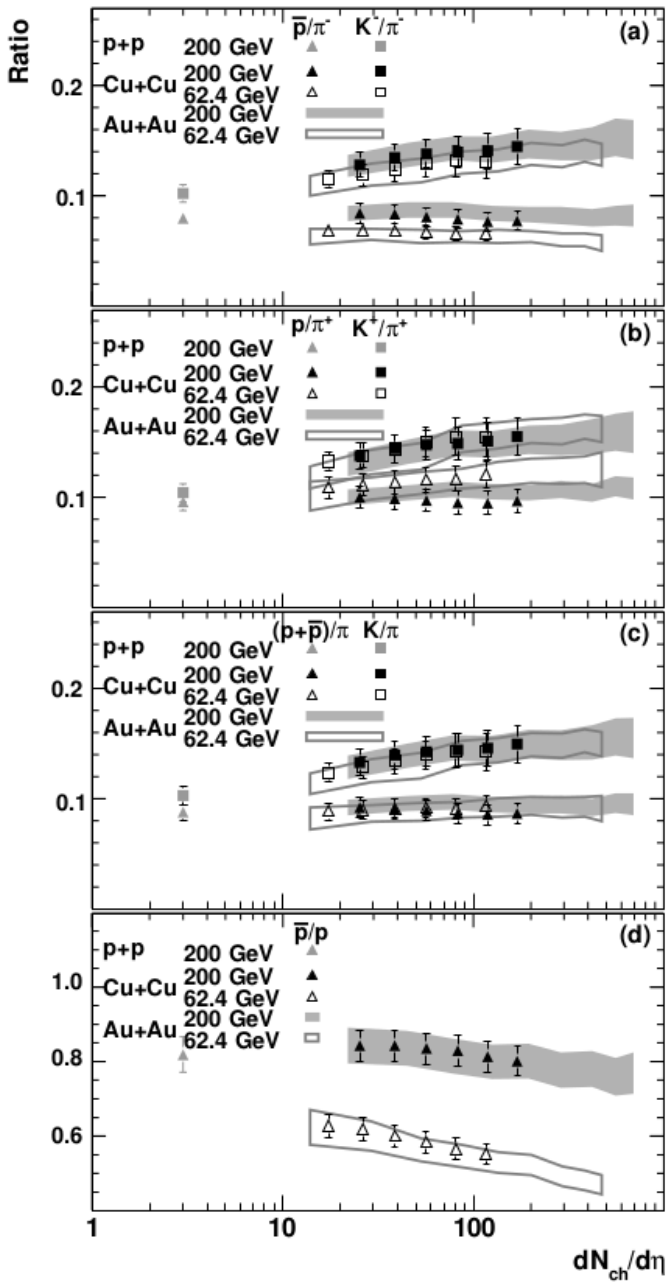

Figure 1.23 Integrated particle yield ratios at $\sqrt{s_{\mathrm{NN}}}$ =200 GeV (closed symbols) and 62.4 GeV (open) for Cu+Cu (black) and Au+Au collisions (grey bands) versus $\mathrm{d}N_{\mathrm{ch}}/\mathrm{d}\eta$ at mid- rapidity. Error bars represent statistical and systematic uncertainties added in quadrature. Figure is taken from[47].

here is reversed compared to that of negatively charged particles. When both charges are summed over, as shown in Fig. 1.23 (c), the resulting ratios show a scaling behavior with $\mathrm{d}N_{\mathrm{ch}}/\mathrm{d}\eta$, independent of the colliding system and collision energy. The separate consideration of the energy dependence of positive and negative particle ratios suggests the influence of baryon transport to mid-rapidity, which decreases with increasing energy. To study in detail the baryon transport, the anti-proton to proton ratios at 62.4 and 200 GeV are depicted in Fig. 1.23 (d). This ratio increases for higher energy collisions,

but decreases slightly with increasing charged particle multiplicity in both Cu+Cu and Au+Au collisions. It indicates that the effect of baryon stopping is more prominent in central collisions and at lower energies.

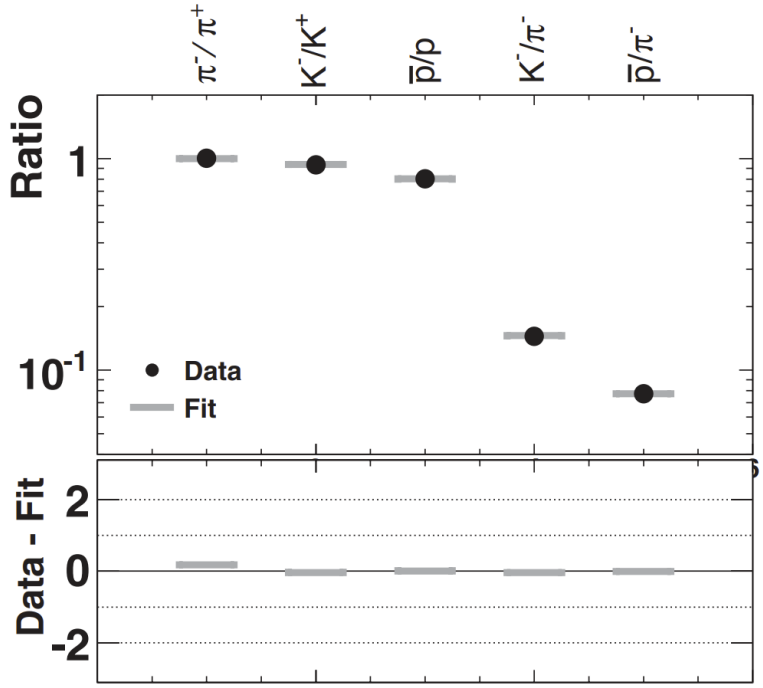

Figure 1.24 The upper panel presents measured particle yield ratios (solid circles) in 200 GeV central Cu+Cu collisions, along with statistical model fits (gray lines). The lower panel shows the difference between the measured data and the model fit, expressed as the number of standard deviations. Figure is taken from[47].

The system's chemical freeze-out parameters can be derived from statistical thermal model analyses of particle ratios, using the THERMUS package[48]. The Grand Canonical Ensemble (GCE) approach, which is commonly used in high-energy heavy-ion collisions, assumes that energy and quantum numbers, or particle numbers, are conserved on average through temperature and chemical potentials. This assumption is valid if the number of particles carrying the quantum number is large. An example of the thermal model fit to the identified hadron ratios from central $\sqrt{s_{\mathrm{NN}}}$ = 200 GeV Cu+Cu collisions is depicted in Fig. 1.24. The lower panel of this figure provides a visual representation of the fit's quality. While the model's successful description of the ratios does not necessarily prove chemical equilibrium, it does imply the statistical nature of particle production in these collisions. Figure 1.25 displays the trajectory of the derived chemical freeze-out temperature against the baryonic chemical potential in central heavy-ion collisions, encompassing data from the very low energy SIS through the AGS, the SPS, and up to the RHIC. The comprehensive evolution of T_{ch} is encapsulated by a phenomenological model fit applied to all the data points (dashed line).

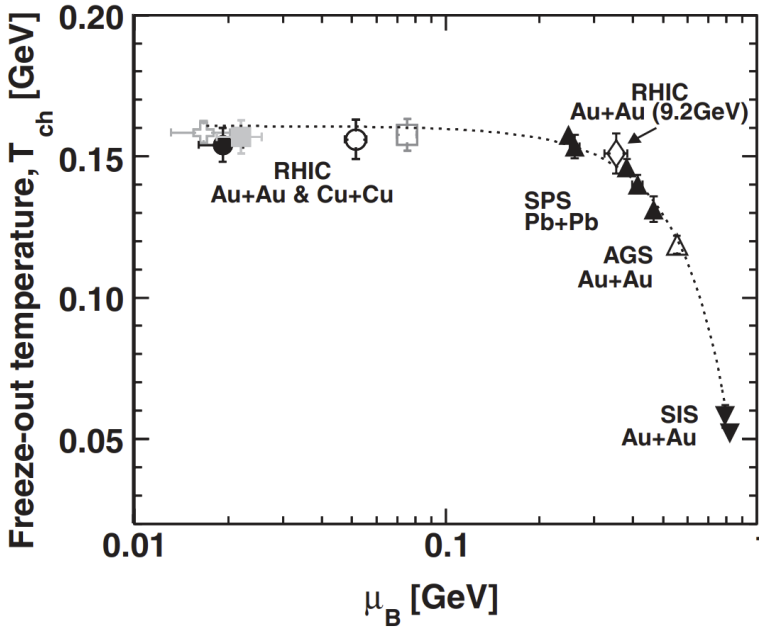

Figure 1.25 The chemical freeze-out temperature T_{ch} as a function of the baryonic chemical potential μ_B. Data points are derived from central Au+Au (0-5% for 200 and 62.4 GeV and 0-10% for 9.2 GeV) and Cu+Cu (0-10%) collisions. It also includes results for lower collision energies for comparison. The dashed line delineates a common fit to all available heavy-ion data. Figure is taken from[47].

An increasing trend in the freeze-out temperature is observed as the collision energy escalates, continuing up to SPS energies. This is followed by a plateau at RHIC energies, aligning closely with the expected hadronization temperature from lattice QCD calculations.

When the system reaches chemical freeze-out, inelastic scatterings between particles end, solidifying the relative abundance of final stable hadrons in the system. Despite this, hadrons continue to modify their momenta through elastic scattering until the system cools down to the kinematic freeze-out temperature T_{kin}. Kinematic freeze-out signifies a point where the momentum distribution of hadrons remains unaltered. Beyond this stage, the system can be treated as a non-interacting gas. Figure 1.26 demonstrates the relationship between T_{kin} and the average transverse radial flow velocity $\langle\beta\rangle$ across various collision energies and systems, extracted from the simultaneous fit of π, K, p spectra with the Blast-Wave model. An inverse relationship is observed that higher T_{kin} values correspond to lower $\langle\beta\rangle$ values and vice versa. This trend is similar for Cu+Cu and Au+Au collisions at both 200 GeV and 62.4 GeV.

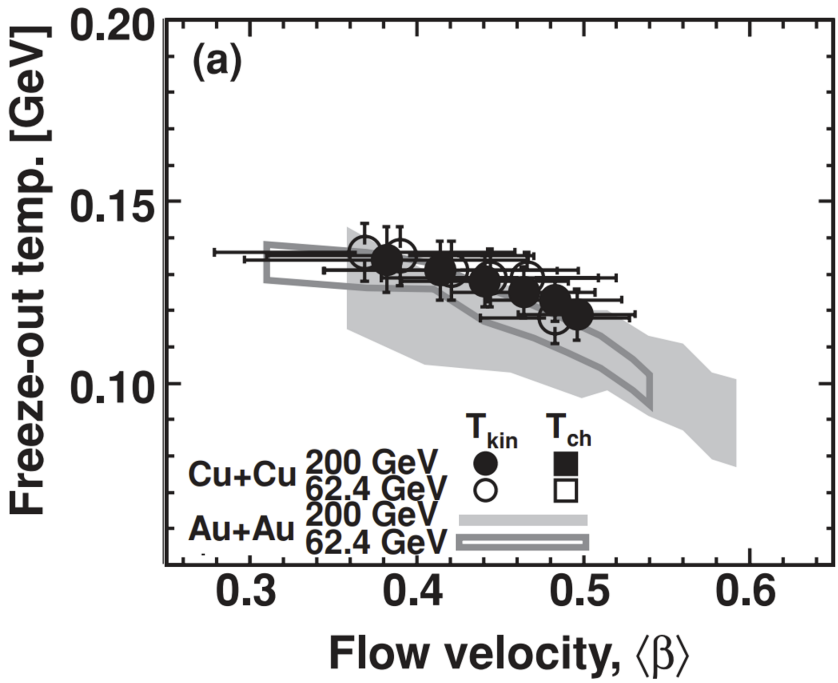

Figure 1.26 The kinetic freeze-out temperature (T_{kin}) as a function of the radial flow velocity (β) acquired from fits to Cu+Cu (symbols) and Au+Au (bands) collision data at $\sqrt{s_{\rm NN}}$ = 200 (closed) and 62.4 GeV (open). Figure is taken from[47].

1.2.3 Study QGP properties in Ru+Ru and Zr+Zr collisions

The large statistics Ru+Ru and Zr+Zr collisions recorded by the STAR experiment in 2018 provide a unique opportunity to study the QGP in unexplored collision systems. As aforementioned, measurements of high-$p_{\rm T}$ charged hadron suppression and elliptic flow have been carried out to study medium-induced energy loss and collectivity. These results are consistent with previous characterization of the QGP properties that it is opaque to colored objects and flows like a perfect fluid. Further explorations of the bulk properties of the medium created in isobar collisions, such as particle yields, freeze-out parameters, etc, are highly desirable to achieve a complete comprehension of the QCD matter.

Investigation of the QGP's properties in isobar collisions will bridge the gap in system size between Cu+Cu and Au+Au collisions. As demonstrated earlier, comparisons of bulk quantities between Cu+Cu and Au+Au collisions indicate that they are mainly driven by the system's entropy or particle multiplicity, rather than the collision geometry. Medium-sized Ru+Ru and Zr+Zr collisions can be used to further test the scaling behavior, and deepen our understanding of the system's evolution.

Furthermore, precisely characterizing the bulk properties of the medium in isobar collisions will provide invaluable inputs to the modeling of these collisions. An accurate representation of the collision dynamics in the modeling is needed for interpreting more

sophisticated measurements, such as the search for the CME.

1.3 Baryon stopping in heavy-ion collisions

A puzzling experimental finding in heavy-ion collisions is the notable baryon to anti-baryon asymmetry in the mid-rapidity region. This finding is noteworthy because the principle of baryon number conservation strictly prohibits the generation of such an asymmetry, suggesting that the extra baryons must originate from the colliding nuclei. Figure 1.27 shows the measurements of net-proton (proton minus anti-proton) yields, as a proxy for net-baryon, as a function of rapidity in the center-of-mass frame at AGS, SPS, and RHIC energies. The positive net-proton yields are clear evidence of the baryon number being transported from colliding beams to the mid-rapidity, also referred to as a "rapidity loss". In collisions at AGS energies ($\sqrt{s_{\mathrm{NN}}}$ = 6-10.8 GeV), the number of anti-protons is negligible, and the net-proton distribution is similar to that of protons. The net-proton rapidity distribution is centered around $y = 0$ and is relatively narrow. At CERN-SPS ($\sqrt{s_{\mathrm{NN}}}$ = 17.3 GeV, 158 AGeV Pb+Pb collisions), the rapidity loss is about 1.75 for a beam rapidity of 2.9, which is similar to the relative rapidity loss at AGS. Another feature visible at SPS is that the net-proton rapidity distribution exhibits a double-hump shape with a dip around $y = 0$. This shape is due to the finite rapidity loss of both colliding nuclei and the finite width of each of the humps reflecting the rapidity distributions of the protons after the collisions.

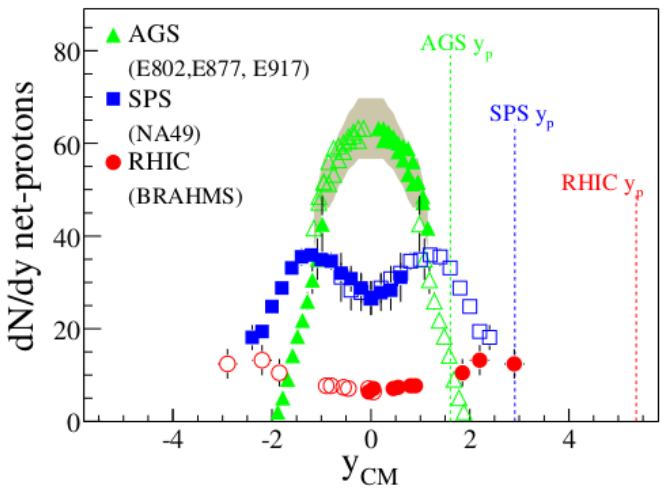

Figure 1.27 The net-proton rapidity distributions at AGS, SPS (Pb+Pb at $\sqrt{s_{\mathrm{NN}}}$ = 17.3 GeV), and RHIC (Au+Au at $\sqrt{s_{\mathrm{NN}}}$ = 200 GeV) energies. Data are taken from the top 5% most central collisions, and the errors include both statistical and systematic uncertainties (the light grey band displays the 10% overall normalization uncertainty for the E802 points). Weak decay corrections are negligible for AGS data and have been applied for SPS and RHIC data. Figure is taken from [49].

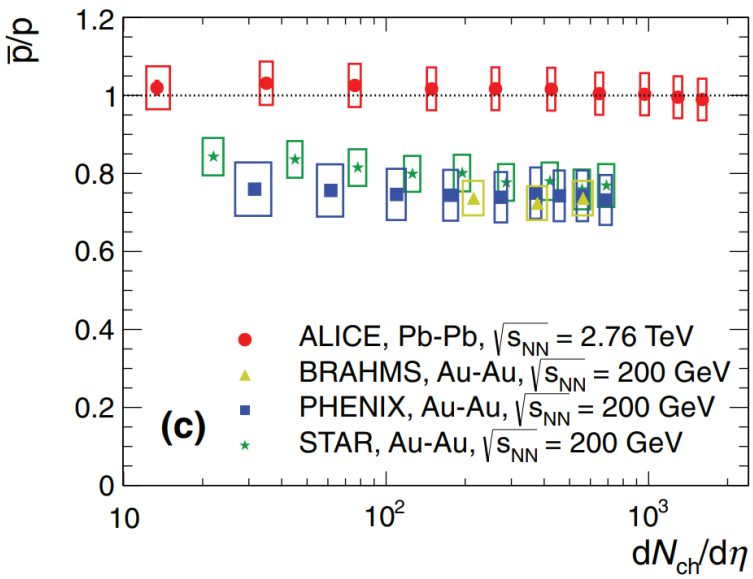

Figure 1.28 The $\bar{p}/p$ ratio as a function of $dN_{ch}/d\eta$ in Pb+Pb collisions at $\sqrt{s_{NN}}$ = 2.76 TeV measured by the ALICE experiment, along with similar measurements at 200 GeV for comparison. Figure is taken from [50].

The BRAHMS experiment measured the net-proton rapidity distribution at RHIC in the interval $y = 0 - 3$ for 0-10% central Au+Au collisions at $\sqrt{s_{NN}}$ = 200 GeV. The distribution at RHIC is qualitatively and quantitatively different from those at lower energies, indicating a different system formed near mid-rapidity. The net-proton number per unit rapidity around $y = 0$ is only about 7, almost a factor of 10 smaller than that at AGS energies, and the distribution is flat over at least ± 1 unit of rapidity. The distribution rises in the rapidity range $y = 2-3$, with an average yield of about 12. Compared to the net-proton distribution at SPS, the hump structure at RHIC has a smaller magnitude and peaks at larger rapidities.

Moving up in energy, the baryon asymmetry, quantified using the anti-proton to proton yield ratio, at the LHC is shown in Fig. 1.28 for Pb+Pb collisions at $\sqrt{s_{NN}}$ = 2.76 TeV, compared to similar measurements in 200 GeV Au+Au collision at RHIC. The $\bar{p}/p$ ratio at the LHC is found to be consistent with unity across all event multiplicity values, indicating negligible baryon transport to mid-rapidity at the LHC which could be due to the very large beam rapidity. This observation contrasts with findings from the RHIC energy regime, where the $\bar{p}/p$ ratio is approximately 0.7 - 0.8 at $\sqrt{s_{NN}}$ = 200 GeV [9].

Understanding the underlying mechanism responsible for the significant baryon transport from colliding nuclei to mid-rapidity is an actively pursued topic in the heavy-ion field. According to the conventional picture, the baryon number in a nucleon is carried equally by the three valence quarks, as illustrated in the left panel of Fig. 1.29.

However, the incoming nuclei are greatly Lorentz-contracted already at the RHIC energy, and thus the passing time of those nuclei is extremely short (< 1 fm/c), making it very difficult to stop baryons at mid-rapidity by the collision. Furthermore, there is no direct experimental evidence that it is the valence quarks that carry the baryon number. All of these observations raise the question: what carries the baryon number in a nucleon?

An alternative concept, formulated during the early development of QCD theory, postulates that the baryon number is conveyed by a baryon junction. This junction is a non-perturbative Y-shaped gluon configuration connected to all three valence quarks[51-54]. Figure 1.29 contrasts the traditional scenario (a), where each valence quark carries 1/3 of the baryon number, with the baryon junction model (b). To date, neither of these models has been experimentally validated.

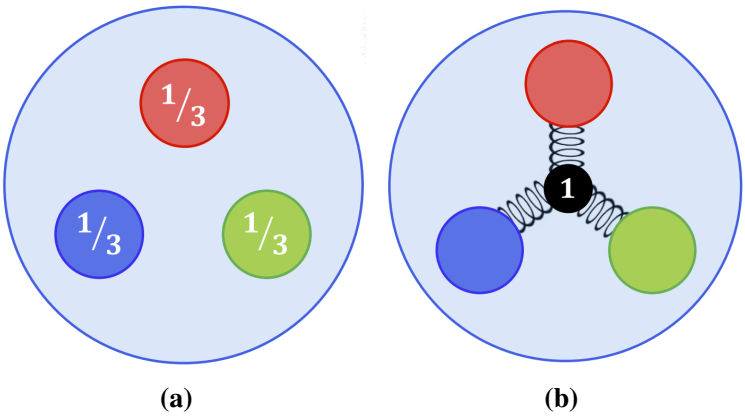

Figure 1.29 The quark content of a proton, the forces between these quarks are mediated by gluons. The circles in green, red, and blue signify valence quarks of corresponding color charges. (a) depicts the traditional understanding where each valence quark carries 1/3 of the baryon number. On the other hand, (b) illustrates the baryon junction concept, which posits a non-perturbative Y-shaped topology of gluons, connecting all three valence quarks, as the carrier of the baryon number. Figures are taken from[55].

Although the baryon junction model also attributes the baryon's electric charge to valence quarks as the traditional view, it predicts distinct interaction cross sections and distribution functions for the baryon junction than valence quarks. The soft parton field of the projectile can stop the junctions from a target hadron/nucleus in the mid-rapidity region, even in high-energy collisions, which is not the case for valence quarks[56]. When a baryon junction is halted at a specific rapidity y, the valence quarks can separate, producing a $q\bar{q}$ pair in the region between y and the fragmentation region, defined by the beam rapidity Y_{beam}. The baryon junction stopping is expected to follow an exponential decrease ($\sim exp(-\alpha_J \delta y)$) with the rapidity loss ($\delta y = Y_{beam} - y$), and the slope (α_J) is determined by the Regge intercepts of the baryon junction. It is predicted that $\alpha_J =$

$2 - 2\alpha_0^J = 1$ for double-baryon stopping and $\alpha_J = 2 - \alpha_0^J - \alpha_P(0) = 0.42$ for single-baryon stopping, using $\alpha \simeq 0.5$, and $\alpha_P(0) = 1.08$.

1.3.1 Current tests of baryon junction hypothesis

Currently, two approaches have been employed to test the baryon junction hypothesis, i.e., measuring net-proton yields in heavy-ion and γ+A events.

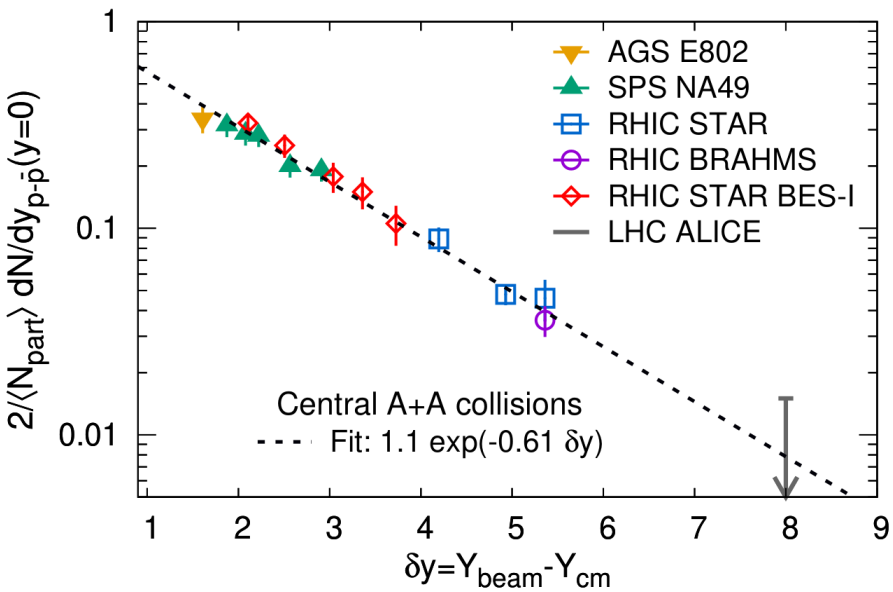

Figure 1.30 The net-proton yield per participant pair in central heavy-ion collisions at mid-rapidity ($y \approx 0$) as a function of the rapidity difference (δy) between the beam and center-of-mass rapidity. Figure is taken from[56].

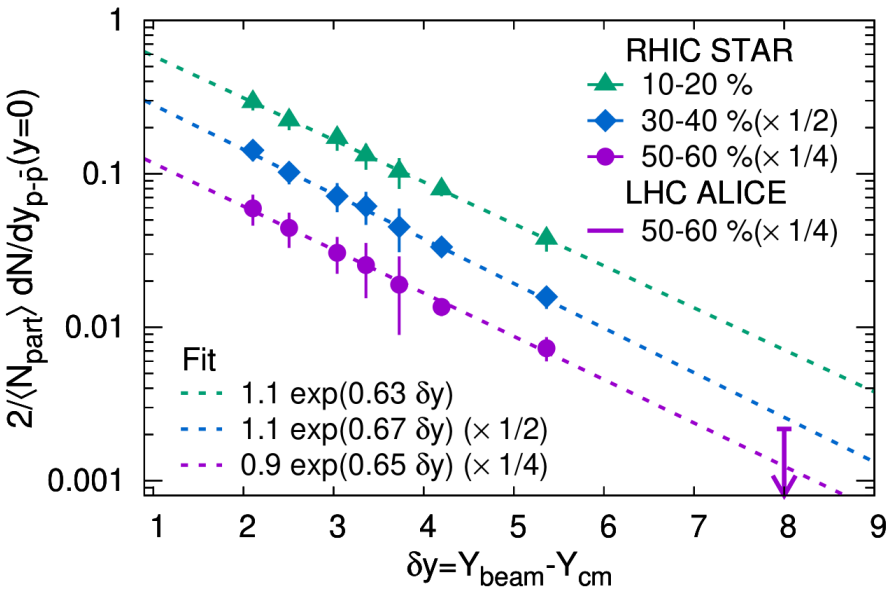

Figure 1.31 Same as Fig. 1.30, but for different collisions energies and centrality intervals. Figure is taken from[56].

Firstly, authors of Ref.[56] explored the rapidity dependence of the net-proton yield.

Figure 1.30 shows measurements of net-proton densities, scaled by the number of participating nucleons, at mid-rapidity from experiments at AGS, SPS, RHIC, and LHC[49]. The density is plotted against the rapidity loss $\delta y = Y_{beam} - Y_{cm}$, where Y_{cm} denotes the center-of-mass rapidity. For protons produced in a collision with $Y_{cm} = 0$, δy equals the beam rapidity: $\delta y = Y_{beam}$. Inspired by the baryon junction picture, the rapidity distribution is fit with an exponential function (Eq. 1.10), which is shown as the dashed line in Fig. 1.30. The resulting slope is $\alpha_B = 0.61$, which is consistent with the baryon junction prediction[54].

$$\frac{dN_{net-p}/dy}{N_{part}/2} = N_B exp(-\alpha_B \delta y), \tag{1.10}$$

Furthermore, Fig. 1.31 displays the measurement of the same net-proton density at mid-rapidity for various centrality intervals using data obtained from the RHIC Beam Energy Scan program[9,11] and the LHC[57-58]. The dotted lines illustrate the exponential fits to the data using the same function as for Fig. 1.30. The qualitative behavior of the net-proton distributions with rapidity loss δy does not vary with centrality, and the exponents α_B obtained from the fits are consistent across all centrality intervals. This invariance with centrality is hard to be coped with within the scenario of valence quarks carrying the baryon number since multi-parton interactions occurring more in central collisions are expected to result in a stronger transporting power and thus a decreasing slope with centrality[56].

Secondly, one can use the photon-induced interactions on nuclei (γ+A) to study what carries the baryon number. This is because the photon is the simplest entity that can undergo a single dipole fluctuation and interact with a gluon, quark, or baryon junction, making it the cleanest process possible. If valence quarks carry the baryon number, it would be challenging for a photon to stop all three quarks together to produce noticeable baryon asymmetry at mid-rapidity. Moreover, the characteristic exponential shape predicted by the baryon junction picture may be visible in γ+A interactions due to the absence of baryons in the photon. Such γ+A processes can be selected in ultra-peripheral collisions (UPCs) at RHIC, where the impact parameter of the collisions is larger than twice the nucleus radius, and thus hadronic interactions do not occur.

The STAR Collaboration has released preliminary results on proton and anti-proton production in γ+A processes selected from Au+Au collisions at $\sqrt{s_{\mathrm{NN}}}$ = 54 GeV. The feasibility of utilizing the STAR detector for selecting such processes is well-analyzed. The left panel of Fig. 1.32 demonstrates a scenario for studying baryon transport in UPCs. This situation involves an incoming baryon (B) from the target ion, which gets

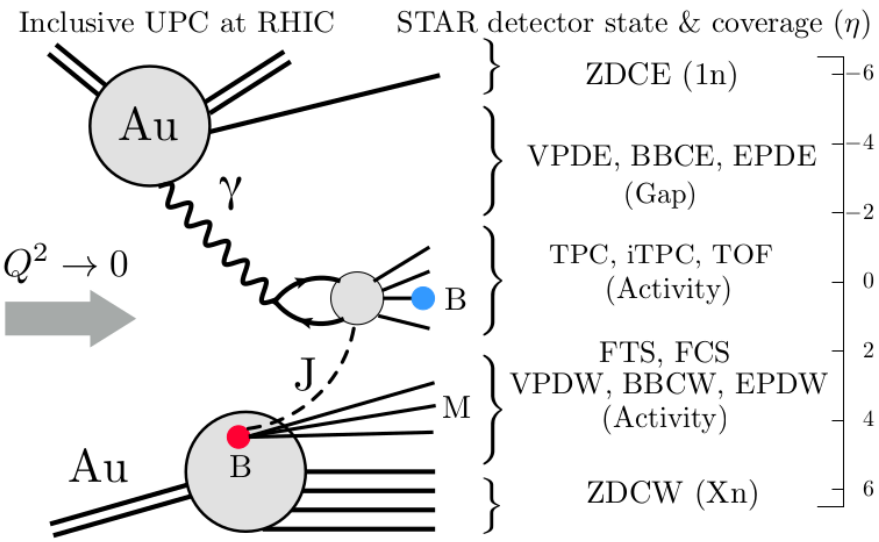

Figure 1.32 (Left) Inelastic scattering at low virtuality can be studied by triggering ultra-peripheral collisions at RHIC. (Right) The different detector systems in STAR have varying acceptance and will either be active or see no activity in these processes. Figure is taken from [56].

stopped near mid-rapidity by the incoming photon through the exchange of a baryon junction (J). The quarks attached to the junction fragment into mesons (M). These mesons then fill the gap between mid-rapidity and the target. The right panel illustrates the various detector systems in STAR, their acceptance ranges, and their activity during these processes. The photon-emitting ion might undergo Coulomb excitation, resulting in the ejection of a single neutron that can be detected by one side of the Zero Degree Calorimeters (ZDCs). Simultaneously, the target ion will fragment into several neutrons, detected by the ZDC on the other side. There are also significant activities on one side of the Beam Beam Counter (BBC) due to nucleus fragments, while almost no activity is seen on the other side. The combined asymmetric cuts on the ZDCs and BBCs are employed to select γ+Au interactions [56].

The resulting $\bar{p}/p$ ratio in γ+Au relative to peripheral Au+Au collisions as a function of p_{T} is depicted in Fig. 1.33. The double ratio of $\bar{p}/p$ is less than 1 for p_{T} values below 1 GeV/c, indicating that there is a greater proton to anti-proton asymmetry in γ+Au collisions compared to Au+Au collisions [59]. As a baseline, double ratios of π^-/π^+ and K^-/K^+ are also shown in Fig. 1.33, where no deviation between γ+Au and peripheral Au+Au collisions is seen. This corroborates that the behavior of $\bar{p}/p$ double ratio is caused by significant baryon transport in γ+Au events.

To investigate the rapidity dependence of the net-proton yield in γ+Au processes as predicted by the baryon junction picture, Fig. 1.34 displays the p (left) and $\bar{p}$ (right) spectra for various rapidity intervals. Those spectra are fitted with a Lévy function, indicated by dashed lines, for extrapolating the measured yields to the full p_{T} range. The

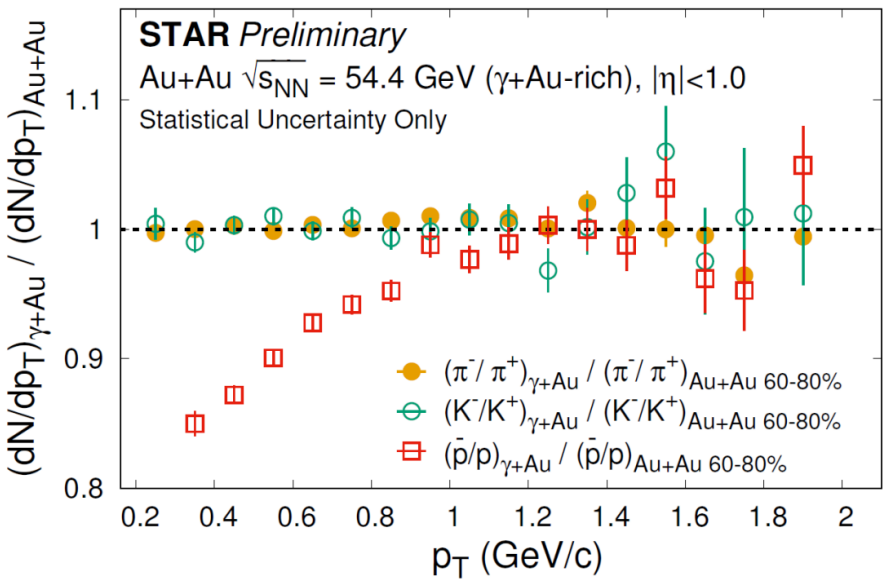

Figure 1.33 Double ratio: anti-particle/particle ratio in γ+Au/Au+Au collisions. Figure is taken from[59].

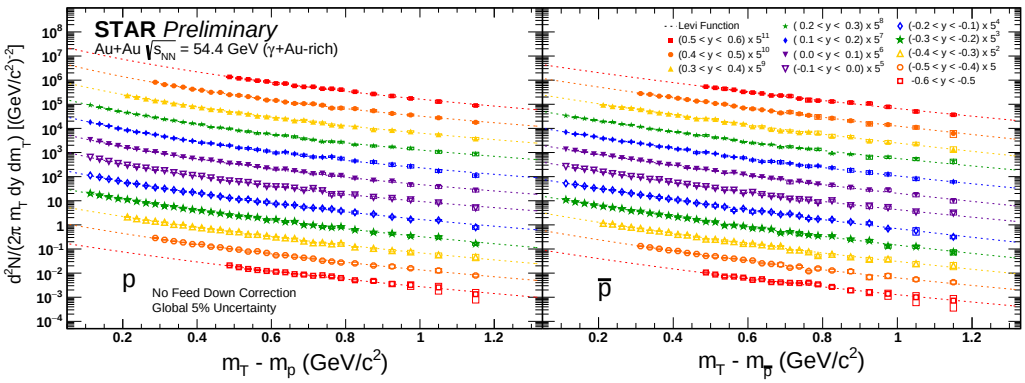

Figure 1.34 p (left) and $\bar{p}$ (right) spectra in γ+Au events. Different colors of markers represent different rapidity intervals, and the dashed lines indicate fits to the spectra using a Lévy function. Figure is taken from[59].

resulting dN/dy distributions for p (green), $\bar{p}$ (blue), and net-proton (red) as a function of rapidity are shown in Fig. 1.35. The dN/dy distributions of protons and net-protons exhibit an increase with rapidity, consistent with the baryon junction mechanism. Conversely, the dN/dy distribution for $\bar{p}$ remains flat across the measured rapidity range. This observation could be attributed to the counterbalancing of two effects: firstly, the positive slope resulting from the asymmetric particle production in γ+A collisions; and secondly, the negative slope from the $p\bar{p}$ pairs by the baryon junction mechanism, which exhibits a contrasting rapidity dependence as predicted by Regge theory.

Figure 1.36 compares net-proton dN/dy as a function of δy between γ+Au (red markers) and Au+Au collisions in different centrality intervals, indicated by black markers. The dN/dy distribution in γ+Au collisions is fitted with an exponential function,

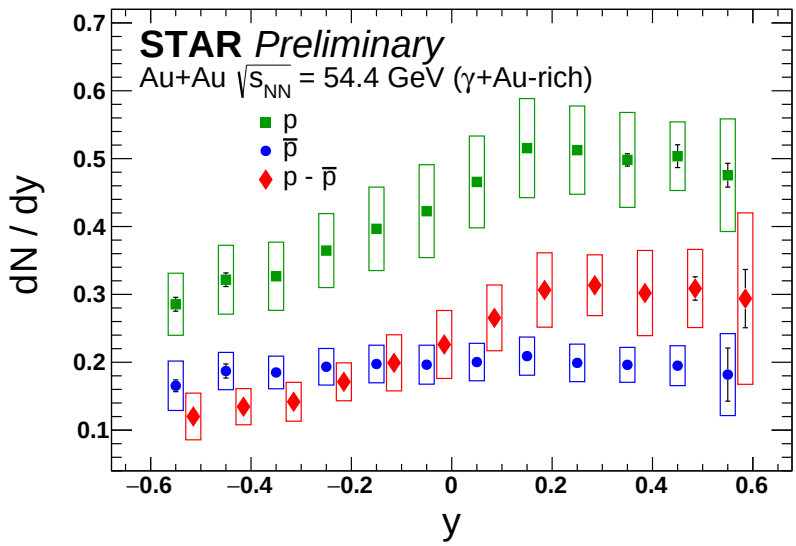

Figure 1.35 Distributions of $\mathrm{d}N/\mathrm{d}y$ for p (green), $\bar{p}$ (blue), and net-proton (red) as a function of rapidity in γ+Au events. Figure is taken from[59].

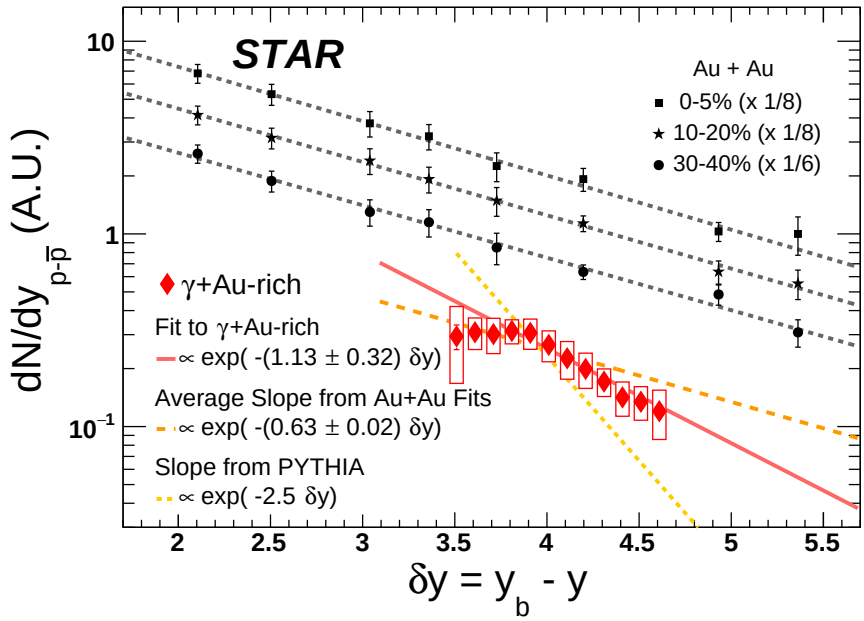

Figure 1.36 Rapidity dependences of net-proton yield in Au+Au and +Au events along with exponential fits. The Au+Au data points are from previous STAR publications for collision energies ranging from $\sqrt{s_{\mathrm{NN}}}$ = 7.7 to 200 GeV. Figure is taken from[59].

which is represented by the red solid line in the plot. The slope ($\alpha_B \approx 1.13 \pm 0.32$) is consistent with, but possibly slightly larger than, the slope observed in Au+Au collisions, which is represented by the orange dashed line on the plot with a slope of $\alpha_B \approx 0.63 \pm 0.02$. The extracted slope from γ+Au events is consistent with the baryon junction prediction, but significantly smaller than that from PYTHIA simulation of $\gamma + p$ collisions ($\alpha_B \approx 2.5$) where no baryon junction is present in the colliding proton.

1.3.2 Study the baryon number carrier in Ru+Ru and Zr+Zr collisions

The baryon junction typically carries lower momentum than the valence quarks and is more likely to be stopped by incoming projectiles[54]. Given that the electric charge is carried by quarks, baryons (B) are expected to experience more stopping than charges (Q) at mid-rapidity in the baryon junction mechanism. To test what carries the baryon number, a third approach would be to compare the net-baryon and net-charge numbers at mid-rapidity. If the baryon number is carried by the valence quarks, it is anticipated that the ratio of baryon stopping to charge stopping (B/Q) scales with A/Z where A is the mass number of the colliding nuclei and Z is the atomic number. On the other hand, if the baryon number is carried by the baryon junction, B/Q will be larger than A/Z.

However, measuring the charge stopping at mid-rapidity with the precision needed to distinguish between the two scenarios (baryon junction vs. valence quarks) is extremely difficult in hadronic collisions. The limiting factor arises from the uncertainties associated with the extrapolation of measured particle yields down to $p_{\mathrm{T}} = 0$ GeV/c because of the limited detector acceptance. While such uncertainties in the particle yields are usually acceptable, their contribution to the net-charge number, which is the difference between positively and negatively charged particle yields, becomes overwhelming since the difference is much smaller than the individual yields themselves. Given this difficulty, an alternative approach is proposed. Exploiting the unique operational procedure of isobar data-taking, including fill-by-fill switching and luminosity leveling, this approach suggests measuring the net-charge difference (ΔQ) between Ru+Ru and Zr+Zr collisions based on double ratios of particle yields and checking the relation between $B/\Delta Q$ and $A/\Delta Z$. Such double ratios, despite their small values, can be measured with high precision since the detector effects mostly cancel. Specifically, we propose to use the spectra of $\pi^{\pm}$, $K^{\pm}$ and $p\bar{p}$ at mid-rapidity ($|y| < 0.5$) to determine the net-charge difference (ΔQ), and compare it with the net-baryon number (B).

1.4 Scope of this thesis

This thesis will investigate the properties of the QGP and its dynamics by employing a pioneering set of measurements. Specifically, it will utilize the first measurements of identified particle spectra, including positively and negatively charged pions, kaons, and protons, at mid-rapidity ($|y| < 0.5$) in Ru+Ru and Zr+Zr collisions at $\sqrt{s_{NN}} =$ 200 GeV. The Ru+Ru and Zr+Zr collisions are particularly interesting as they bridge

the gap in system size between Cu+Cu and Au+Au collisions. They provide a unique opportunity to study the system size dependence of QGP's freeze-out properties, shedding light on the collision dynamics. In particular, the mean transverse momenta of different particles, anti-particle to particle ratios as well as kinetic freeze-out parameters will be measured, and compared to similar results in Cu+Cu and Au+Au collisions at the same energy. These results are highly desirable as they will provide the crucial data needed to analyze collision geometry. Moreover, they will serve as a cornerstone for attaining a complete understanding of the QGP. Through these findings, we can delve into the underlying structures and behaviors of QGP in unprecedented detail.

Additionally, this thesis will delve into the puzzling observation of baryon asymmetry at mid-rapidity in heavy-ion collisions, which suggests intriguing implications for baryon number carriers and challenges conventional perspectives on the roles of valence quarks. There exists an interesting theoretical proposition - the baryon junction, a non-perturbative Y-shaped gluon topology that binds all three valence quarks together and could potentially carry the baryon number. However, these provocative theories have yet to gain solid experimental confirmation. To test different theories, net-charge and net-baryon numbers at mid-rapidity are compared, and checked against theoretical predictions. In particular, a novel approach to measuring the net-charge difference between Ru+Ru and Zr+Zr collisions is proposed in light of the difficulties in measuring the absolute net-charge number in one collision system. The research presented in this thesis complements earlier investigations on this topic using Au+Au collisions at different energies and γ+Au processes. Any correct theory should be able to explain all three measurements simultaneously, placing stringent tests on different theoretical approaches.

Chapter 2 Experimental set-up

2.1 The Relativistic Heavy Ion Collider

The Relativistic Heavy Ion Collider (RHIC) is a unique research facility located at Brookhaven National Laboratory (BNL) in Upton, New York. Its primary objective is to accelerate beams of nuclei, ranging from protons to Uranium, to nearly the speed of light and collide them to study a diverse range of physics. In particular, heavy-ion collisions are used to recreate and analyze the QGP. RHIC is the only operating heavy-ion and particle collider in the United States, and the only spin-polarized proton collider ever built[60-61]. The four original large detectors, Broad RAnge Hadron Magnetic Spectrometers (BRAHMS), Pioneering High Energy Nuclear Interaction eXperiment (PHENIX), PHOBOS, and the Solenoidal Tracker at RHIC (STAR), situated along the 2.4-mile accelerator, recorded collisions at the beginning of RHIC's operation to reveal properties of the QGP[62-65]. Currently, STAR is one of the two operational detectors at RHIC, with sPHENIX starting its data collection in 2023. PHOBOS ceased operations in 2005, BRAHMS in 2006, and PHENIX stopped data gathering in 2016. The hall that formerly housed the PHENIX experiment is now repurposed for the new detector, sPHENIX. The "s" in sPHENIX signifies its focus on strongly interacting particles. The data set analyzed in this work was recorded by the STAR experiment.

RHIC can also be used to study the origin of the proton spin from the quark and gluon constituents by colliding polarized protons. In Jan. 2020, the United States Department of Energy announced that the RHIC will be transformed into the Electron Ion collider (EIC)[66] over the next ten years, at an estimated cost of 1.6 to 2.6 billion US dollars. The EIC allows 3D imaging of the structure of nucleons and nuclei by using high-energy electrons. In particular, scientists are hoping to learn how nuclear properties like mass and spin emerge from the dynamics of quarks and gluons, how the gluon saturation, if exists, sets in, etc.

Figure 2.1 shows a bird's eye view of RHIC, the locations of the STAR and PHENIX detectors, and various facilities corresponding to the various processes of heavy ion production, acceleration, and ultimate collision. At present, ions are generated by Electron Beam Ion Source (EBIS)[68], instead of the Tandem Strippers. The EBIS is composed of an electron beam particle source, a radio frequency quadrupole linear accelerator, and an interdigital-H linac. The EBIS is located in the region of the 200 MeV proton linear accelerator (Linac) and is capable of producing all stable ion

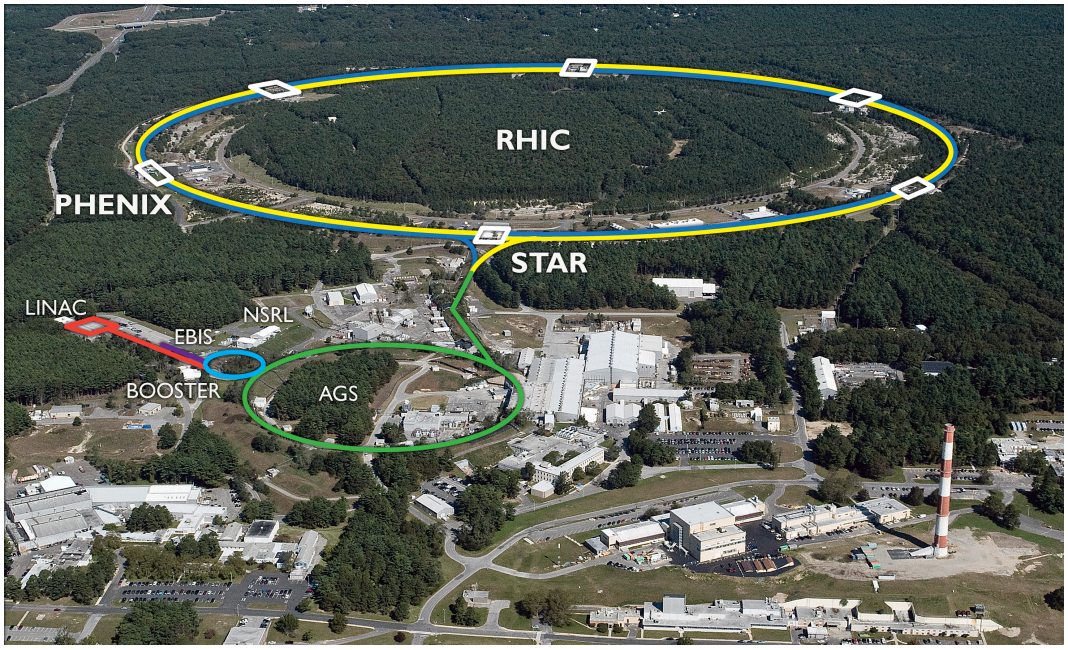

Figure 2.1 A bird's eye view of the Relativistic Heavy Ion Collider. The picture is taken from[67].

species from deuteron to uranium. Additionally, EBIS can quickly switch between different ion beams and send them to the Booster within a second. The Au^{32+} ions are created from gold atoms using the EBIS. The ion beams are then accelerated in Linac and delivered to the Booster, a powerful circular accelerator that further accelerates injected particles using radio frequency electromagnetic waves. In the Booster, the gold ions are accelerated to 95 MeV/u and stripped again into Au^{77+} before entering the Alternating Gradient Synchrotron (AGS). The AGS serves as the next-level accelerator and can accelerate particles from 0.37 times the speed of light to approximately 0.997 times the speed of light (10.9 GeV/u). The gold ions are fully stripped to Au^{79+} upon exiting the AGS and transferred to the RHIC ring through the AGS-to-RHIC transfer line. The particles are then transported to RHIC, where they undergo final acceleration to attain a speed of 99.9999% of the speed of light. This is the origin of the term "relativistic" in the name "Relativistic Heavy Ion Collider". RHIC is composed of two beam-circulating rings (noted as "yellow" and "blue" rings) with opposite directions of motion and six collision points[60-61]. The STAR detector which is located at the six o'clock position on RHIC, is the detector we use for this analysis.

2.2 The STAR detector

STAR is named for its solenoidal magnet[69] with a large cylindrical Time Projec-

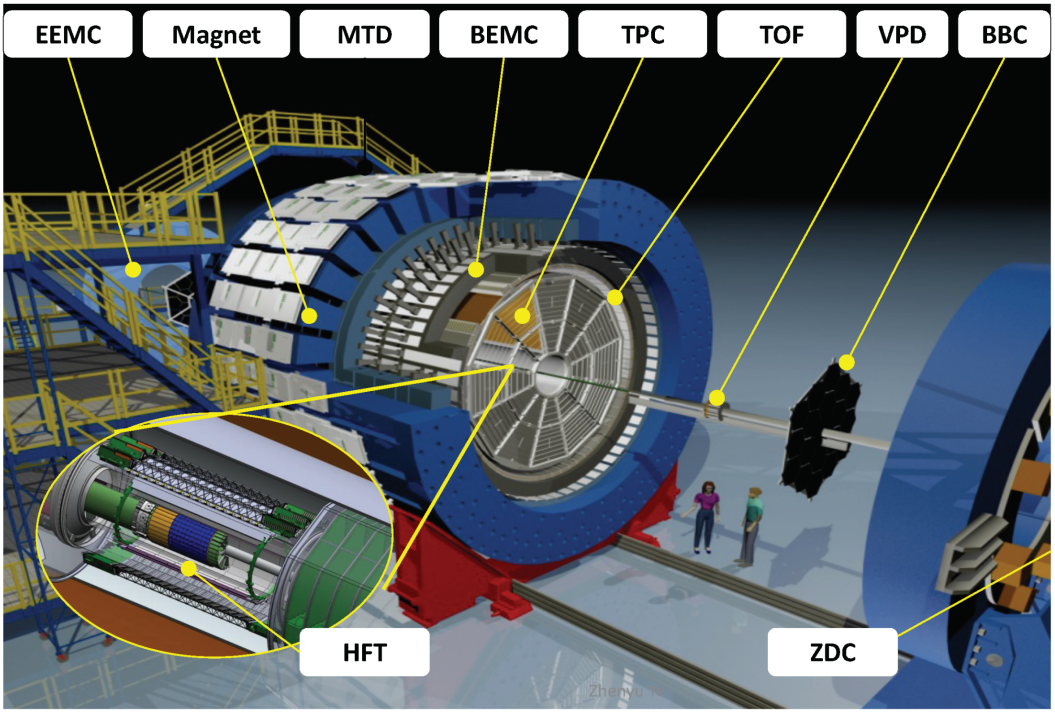

Figure 2.2 Overview of STAR detector system.

tion Chamber (TPC)[70] wrapped in the middle. This design allows for full azimuthal coverage ($0 < \phi < 2\pi$) and high precision tracking capability for charged particles. STAR is the general-purpose detector designed to search for the evidence of the QGP formation and study its properties[71].

The configuration of the STAR detector system is shown in Fig. 2.2. The main tracking device is the TPC, a gaseous detector that extends 4.2 m long and 2 m in radius and covers full azimuthal angle ($0 < \phi < 2\pi$) within a pseudo-rapidity acceptance $|\eta| < 1.0$. It also provides particle identification (PID) through the measurement of ionization energy loss by the traversing particle in the TPC gas. The Heavy Flavor Tracker (HFT) ($0 < \phi < 2\pi$, $|\eta| < 1.0$)[72] was located inside the TPC and operated from 2014 to 2016, designed to reconstruct secondary vertices for the charm and bottom hadron decays thanks to its excellent tracking pointing resolution[73-76]. Another important PID device is the Time of Flight (TOF) detector ($0 < \phi < 2\pi$, $|\eta| < 0.9$)[77], which identifies particles based on measurements of their arrival time. Situated outside the TOF, the Barrel Electromagnetic Calorimeter (BEMC)[78] covers the full azimuthal range ($0 < \phi < 2\pi$) and a pseudorapidity range of $|\eta| < 1.0$. The BEMC measures the energy and shape of the showers induced by incident particles to differentiate between electrons, photons, and hadrons. The STAR magnet system, positioned outside the BEMC, generates a near-uniform magnetic field parallel to the beam direction. The field strength varies from 0.25 T to 0.5 T, with the magnetic field strength set to 0.5 T for

this analysis. The outermost component of the detector system is the Muon Telescope Detector (MTD)[79-80], which was installed in 2014. This detector provides approximately 45% azimuthal coverage within $|\eta| < 0.5$. Its primary function is to trigger on and identify muons from quarkonium decays[28,81].

The STAR trigger system is composed of three types of detectors that work together to select desired events from collisions delivered by RHIC. The trigger detectors, which include the Zero Degree Calorimeter (ZDC) ($|\eta| > 6.3$)[82], the Beam-Beam Counter (BBC) ($3.3 < |\eta| < 5.0$)[83], and the Vertex Position Detector (VPD)[84], are responsible for providing Minimum-Bias (MB) trigger, whose efficiency decreases towards peripheral collisions due to low event activity and needs to be corrected for in the analysis. The VPD detectors, covering pseudo-rapidity of $4.24 < |\eta| < 5.1$, also provide the event start time for TOF and MTD as well as measure the primary vertex position along the beam direction (Z-direction). The forward-rapidity detectors, including the Forward Meson Spectrometer (FMS) and Roman Pot (RP) ($4.3 < |\eta| < 5.3$)[85], are used to select high-rapidity electromagnetic particles and scattered protons, respectively. The FMS is a high-resolution electromagnetic calorimeter designed for detecting photons and neutral mesons in the forward rapidity region ($2.5 < |\eta| < 4.0$)[86-88]. The RP comprises four planes of silicon microstrip detectors (SSDs) - two vertical and two horizontal - that can detect scattered protons for tagging elastic events[89].

The STAR trigger system can operate at a rate of around 10 MHz[90]. This system uses inputs from fast detectors, such as ZDC, BBC, and VPD, to select events for slower tracking detectors. It consists of four layers, with level 0 being the fastest and levels 1 and 2 applying more advanced constraints on event selection, but operating at a lower rate. The trigger system allows to efficiently select specific events for further analysis. The level 3 trigger system performs detailed online reconstruction of events using a dedicated network of CPUs[91]. This system can process central Au+Au collisions at a rate of 50 Hz and includes a simple analysis of particle momentum and energy loss. The level 3 trigger system also includes an online display that allows individual events to be viewed in real-time. Figure 2.3 displays a side view of a central Au+Au event at $\sqrt{s_{\mathrm{NN}}} = 200$ GeV inside STAR TPC. To keep up with the increasingly fast data acquisition of the STAR detector and meet the requirements of selecting rare events, an advanced High-Level Trigger (HLT) was developed. The HLT system is comprised of computer hardware and software capable of online event reconstruction and TPC track reconstruction. It reduces the data volume by selecting events with rare physics characteristics like high transverse momentum, di-leptons, and light nuclei while maintaining a high sampling rate for a

wide range of triggers. This enables offline processing and analysis to be conducted at a faster pace. In 2010, HLT was deployed and proved essential in the discovery of the antimatter ^{4}He nucleus and the initial study of J/Ψ elliptic flow. Additionally, HLT monitored the beam quality and kept track of the number of good events taken by STAR during the BES program[89,92].

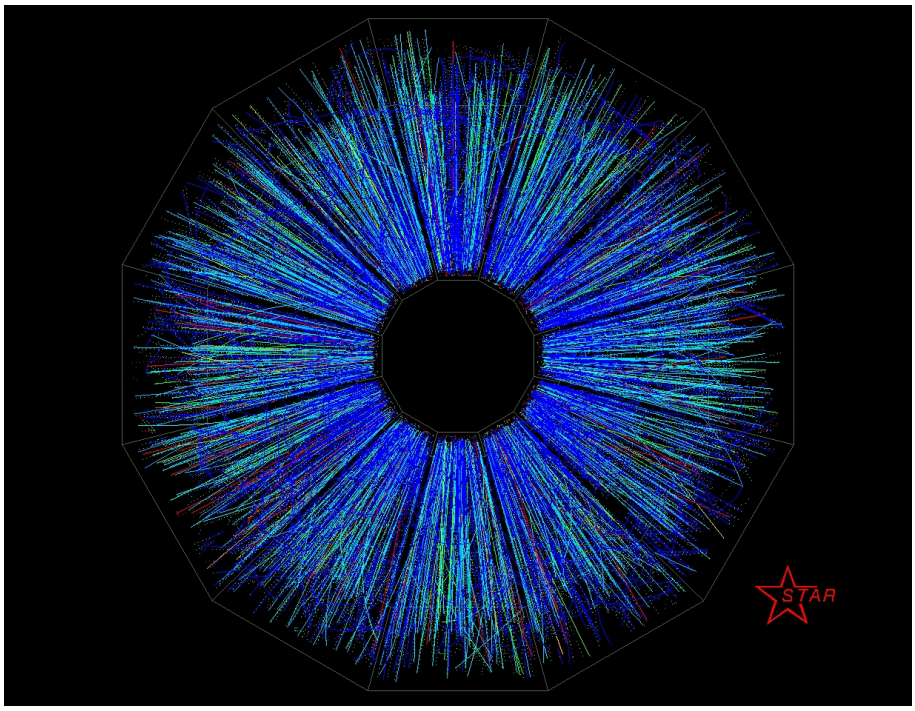

Figure 2.3 Side view of a central Au+Au event at $\sqrt{s_{\mathrm{NN}}}$ = 200 GeV in the STAR TPC. This event is drawn by the STAR level-3 online display.

The STAR collaboration conducted the BES phase I (BES-I)[20,93] program from 2010 to 2014, which contributed to initial explorations of the QCD phase diagram at RHIC. However, some of the crucial measurements made during BES-I required higher statistics to draw more definitive conclusions. In order to meet the precision requirements, STAR proposed a second phase of the BES (BES-II)[94-96] which was conducted in 2019-2021. BES-II covered the collision energy range of 3.0 to 19.6 GeV, which was guided by BES-I results in the search for a critical point and first-order phase transition. To improve the detector acceptance and particle identification capabilities, STAR installed three upgrades, namely the inner TPC sectors (iTPC)[97-99], the Event Plane Detector (EPD)[100-101], and the end-cap Time-of-Flight (eTOF)[102] in 2019.

Completed in 2019, the iTPC upgrades involved enhancing the inner pad plane's segmentation and refurbishing the inner sector wire chambers. This enhanced the TPC's performance, notably by refining tracking at narrow angles to the beamline, extending the acceptance to pseudo-rapidity $|\eta| < 1.5$, and boosting the resolution and acceptance

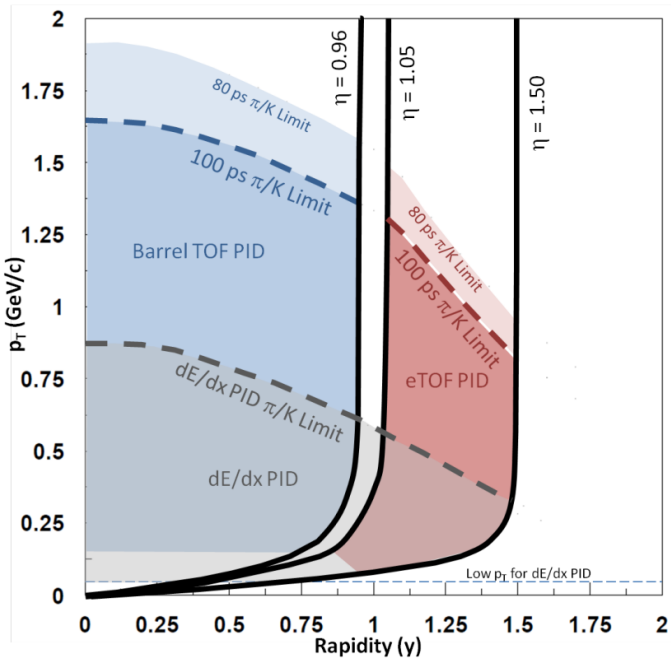

Figure 2.4 The $p_T - y$ acceptance map for pions showing the limits due to tracking coverage and PID. Figure is taken from[102].

for tracks across all momenta, particularly low-momentum ones. The eTOF upgrade is crucial for high-precision studies of bulk properties and mid-rapidity PID between 4.5 and 7.7 GeV in fixed-target mode, extending pseudo-rapidity coverage to $1.05 < \eta < 1.5$ as shown in Fig. 2.4 and enhancing particle identification for pions, kaons, and protons up to rapidity of 1.2 in collider mode. With a time resolution of around 80 ps, it pairs well with the iTPC upgrade's forward tracking. The EPD which is made of scintillators, measures charged particle distribution at angles between 0.7° and 13.5° (pseudo-rapidity range of $2.14 < |\eta| < 5.09$). It consists of two wheels with 12 supersectors each, further split into 31 tiles. Light from tiles is transferred to a silicon photomultiplier via optical fibers, amplifying the signals before digitizing and acquisition by the STAR system[103].

STAR has added a Forward Calorimeter System (FCS) that integrates an electromagnetic and hadronic calorimeter, a Forward Silicon Tracker (FST) with 3 Silicon mini-strip disks, and 4 Small-Strip Thin Gap Chamber (sTGC) wheels, all with pseudo-rapidity coverage of $2.5 < \eta < 4.0$. FCS is situated around 7 m from the interaction point, with the electromagnetic calorimeter using refurbished PHENIX towers and a hadronic calorimeter comprising iron-scintillator sandwiches. The sTGC, inspired by ATLAS design, has four identical planes with pentagonal gas chambers. The FST includes three stations of silicon mini-strip sensors within the STAR magnetic field. These upgrades aim to study the initial state of nucleons and nuclei, and cold QCD physics with extended particle identification and acceptance, with FCS anticipated to deliver

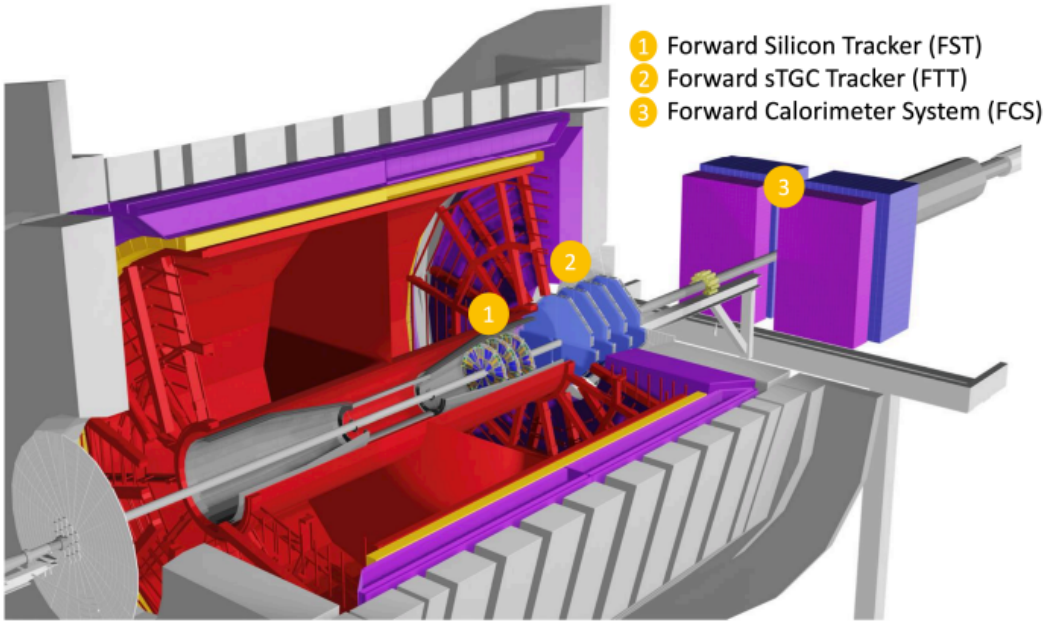

Figure 2.5 Side view of the STAR detector with forward rapidity upgrades. Figure is taken from STAR cold QCD White Paper[104].

high energy resolutions for electromagnetic and hadronic particles, and the FST capable of measuring charged particle transverse momenta with 20-30% resolution in heavy ion collisions[96,104-108].

2.2.1 The Time Projection Chamber

As the main tracking device, the TPC is able to record the trajectories of the charged particles, determine their charge signs and momenta, and identify their species based on the amount of energy ($\mathrm{d}E/\mathrm{d}x$) they lose while passing through and ionizing the TPC gas. The TPC is a cylindrical chamber located within a solenoidal magnet that operates at a field strength of 0.5 T. The TPC is filled with P10 gas (10% methane, 90% argon)[109] which is maintained at a pressure of 2 mbar above the atmospheric pressure, and has an electric field of approximately 135 V/cm. When particles pass through the gas, they ionize the gas atoms and leave a trail of electron clusters that drift toward the ends of the chamber before being captured by the end caps.

Figure 2.6 displays a schematic view of the TPC. As shown in the figure, the TPC has a cathode at its center, pushing ionized electrons moving toward the anode at the ends. The TPC uses a thin, conductive Central Membrane (CM), concentric field-cage cylinders, and the readout end caps to create a uniform electric field for drifting the electrons. The CM cathode is operated at -28 kV, while the end caps are at the ground acting as the anode. It is important for the electric field to be uniform for high track reconstruction precision given that the electron drift path can be as long as 2.1 m. The

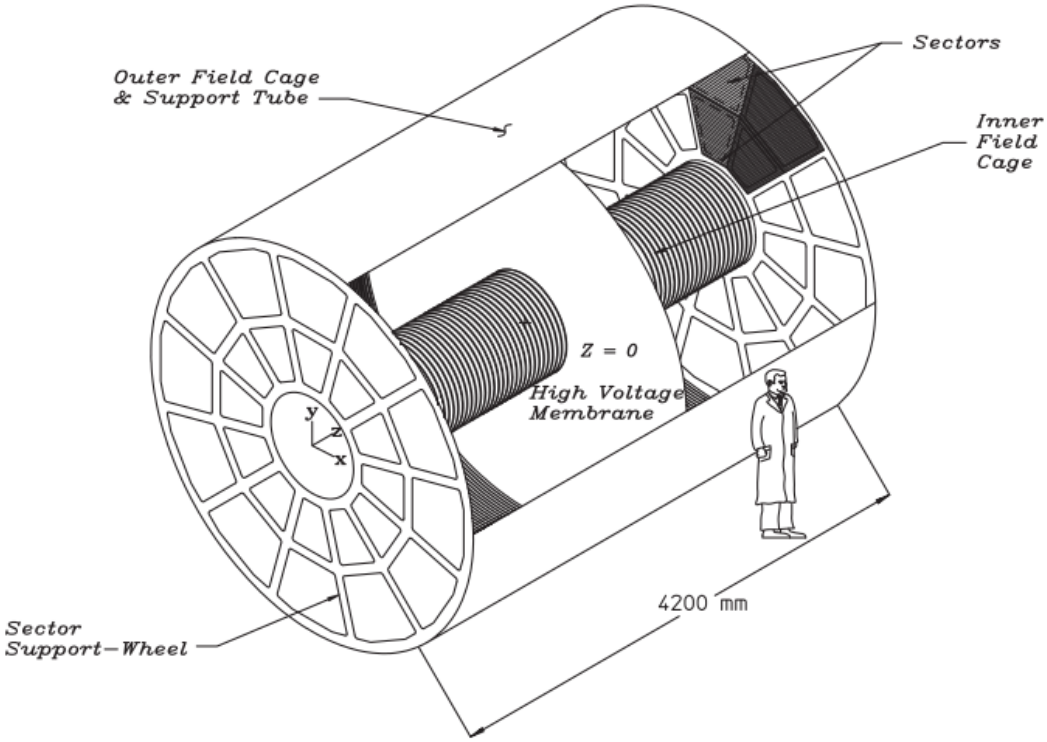

Figure 2.6 The schematic view of the STAR TPC. Figure is taken from[110].

readout system is made of Multi-Wire Proportional Chambers (MWPC) with readout pads that amplify the drifting electrons through avalanches and measure their arrival time and position with high precision. The readout planes, which are mounted on aluminum support wheels, resemble a clock, with 12 sectors arranged in a circle at each end. Figure 2.7 shows the configuration of one TPC sector. There are 13 and 32 pad rows in the inner and outer parts of the sector (45 in total), respectively[110]. Each chamber comprises four components: a pad plane and three wire planes (anode, ground, and gating grid). The amplification/readout layer features an anode wire plane composed of 20 μm wires. This layer is flanked by the pad plane on one side and the ground wire plane on the other. The anode wire plane is a solitary plane of 20 μm wires spaced on a 4 mm pitch, without any interspersed field wires. Such a design enhances the wire chamber's stability and virtually eliminates the need for initial voltage conditioning time.

The ground wire plane, composed of 75 μm wires, is a crucial part of the MWPC. Its primary functions include terminating the field in the avalanche region and offering additional radio frequency shielding for the pads. The outermost wire plane, the gating grid, is situated 6 mm from the ground plane. This grid serves as a gate, regulating the influx of electrons from the TPC drift volume into the MWPC and preventing the positive ions produced in the MWPC from entering the drift volume, where they could disrupt the drift field. The gating grid plane's unique feature is its ability to have different

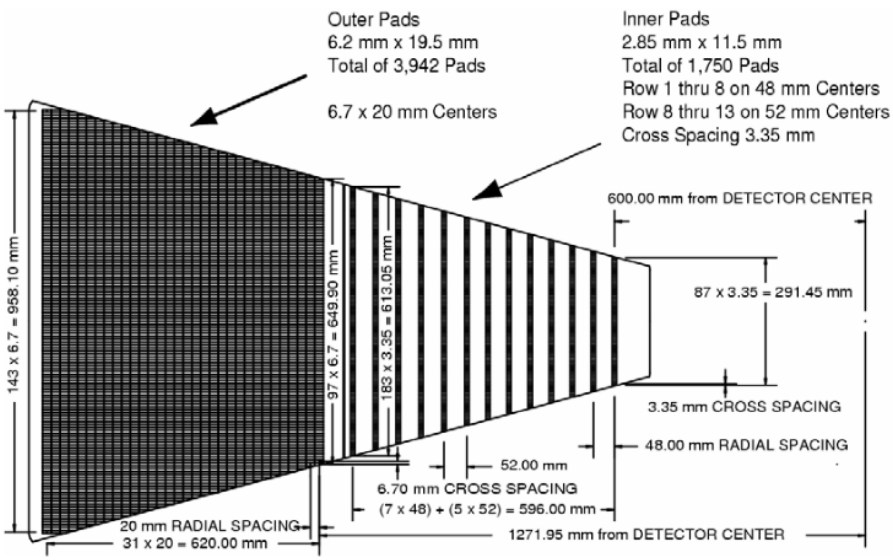

Figure 2.7 One TPC sector on anode pad plane. The inner part has small pads arranged in widely spaced rows while the outer part is densely packed with larger pads. Figure is taken from[110].

voltages on alternate wires. When recording an event, it allows the drift of electrons but remains closed otherwise. When all of the wires are biased to the same potential (typically 110 V), the grid is considered 'open'. It is deemed 'closed' when the voltages alternate by ± 75 V from the nominal value. Positive ions, which are too slow to escape during the open period, are trapped during the closed period.

When a particle traverses through the TPC volume, it ionizes the gas, leaving behind clusters of electrons and positive ions. A primary particle's track is reconstructed by locating these ionization clusters along its path. These clusters are identified separately in the X, Y, and Z dimensions. The local X-axis aligns with the direction of the pad row, while the local Y-axis extends perpendicularly from the beam line through the middle of the pad rows. The Z-axis runs along the beam line. The X and Y coordinates of a cluster are determined by the charge distribution measured on adjacent pad rows. The Z coordinate is calculated by measuring the drift time of an electron cluster from the point of origin to the anodes on the end cap and then dividing it by the average drift velocity. In order to precisely convert the measured time into position, the drift velocity needs to be measured with an accuracy of 0.1%. To reach this goal, two steps are taken. First, the cathode voltage is set to match the electric field in the TPC such that the peak of the drift velocity distribution is achieved. This peak is broad and flat, and minor pressure changes do not significantly affect the drift velocity at the peak. Second, the drift velocity is measured independently every few hours using artificial tracks created by laser beams[111]. Finally, these clusters with X, Y, and Z coordinates are then

reconstructed as TPC hits.

Track trajectories are reconstructed using TPC hits through a combination of Kalman filtering and track finding algorithms[112]. The algorithm starts by selecting a seed track, which is a set of TPC hits likely originating from a common particle. The Kalman filter predicts the expected trajectory of the particle and estimates the likelihood of each TPC hit corresponding to that trajectory. The hits with the highest likelihood are added to the track. Quality cuts are then applied to remove unlikely tracks. The 3D momentum of a track is determined by the curvature of the track. The magnetic field is homogeneous at the central region of the STAR TPC, and the radius of the track's curvature in the transverse plane is proportional to p_{T} of the particle, while the orientation of the curvature can be used to determine the particle's charge sign. When a charged particle passes through the TPC, the measured hits may not be sufficient for reconstructing the complete trajectory due to factors such as tracks falling in the gaps between sectors. The overall detection efficiency of the TPC is about 80-90%.

Energy loss is a crucial measurement provided by the TPC for identifying particle species. The energy loss ($\mathrm{d}E/\mathrm{d}x$) is calculated from the total charge collected by the TPC pads along the particle's path. The length over which the energy loss is measured is usually too short to average out fluctuations in ionization. Therefore, it's not feasible to accurately measure the average $\mathrm{d}E/\mathrm{d}x$. Instead, the most probable energy loss is measured by discarding the largest ionization clusters. This is achieved using the truncated mean method, in which a certain fraction (usually about 30%) of the clusters with the highest signals are removed. This method effectively measures the most probable $\mathrm{d}E/\mathrm{d}x$.

The resolution of the measured $\mathrm{d}E/\mathrm{d}x$ is influenced by the gas gain, which in turn is dependent on the pressure within the TPC. As the TPC is maintained at a constant pressure of 2 mbar above atmospheric pressure, the internal pressure varies over time in correspondence to the external pressure. Local gas gain fluctuations are calibrated by calculating the average signal measured on one row of pads on the pad plane and assuming that all pad rows register the same signal. This correction is carried out at the pad row level because the anode wires are situated directly above and span the full length of the pad row. The readout electronics also introduce uncertainties in the $\mathrm{d}E/\mathrm{d}x$ signals. Small variations in individual pads could arise from the different responses of each readout board. These variations are monitored by sending pulses to the ground plane and pad plane readout system, and it is assumed that the response will be consistent across all pads.

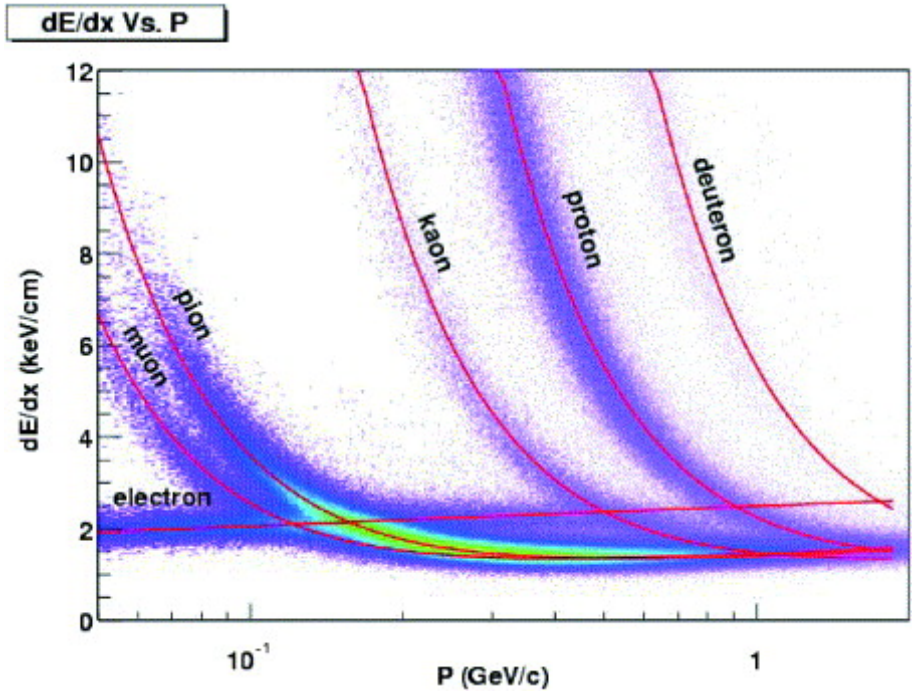

Figure 2.8 The energy loss distribution in the STAR TPC, plotted against the momentum of the traversing particle. These measurements were conducted under a magnetic field of 0.25 T. The figure is taken from[110].

Figure 2.8 presents the energy loss of particles in the TPC, plotted against the particle momentum. The data, corrected for signal and gain variations, utilizes a 70% truncated mean method, as mentioned earlier. The measurements were carried out under a magnetic field of 0.25 T, and the resolution was found to be 8% for a track crossing 40 pad rows. At a magnetic field of 0.5 T, the dE/dx resolution improves due to the decreased transverse diffusion, resulting in a better signal-to-noise ratio for each cluster. The dE/dx curves of pions and kaons converge around 0.7 GeV/c and the curve for protons merges around 1.0 GeV/c with others.

2.2.2 The Time of Flight detector

As mentioned above, the TPC can only identify pions and kaons up to 0.7 GeV/c and protons up to 1.0 GeV/c. This means that roughly half of the charged particles measured in the TPC in any given event cannot be directly identified, which motivated the construction of a large-area TOF detector.

The TOF detector[113] provides accurate particle identification for particles of p_{T} up to approximately 2.5 GeV/c. It is constructed using the Multi-gap Resistive Plate Chamber (MRPC) technology[114-115]. The TOF detector is made of 120 trays that form a cylindrical outer shell around the TPC. It covers the full azimuthal angle and the range $-1 < \eta < 1$ in pseudo-rapidity. Each tray covers 6 degrees in azimuthal angle

and one unit of pseudo-rapidity ($-1 < \eta < 0$ or $0 < \eta < 1$)[77]. The dimensions of a TOF tray box are 241.3 cm long, 21.6 cm wide, and 8.9 cm high. Each tray contains 32 MRPC modules (inside) and 17 electronic boards (outside). Trays are sealed and filled with R134a (freon) that flows during operation.

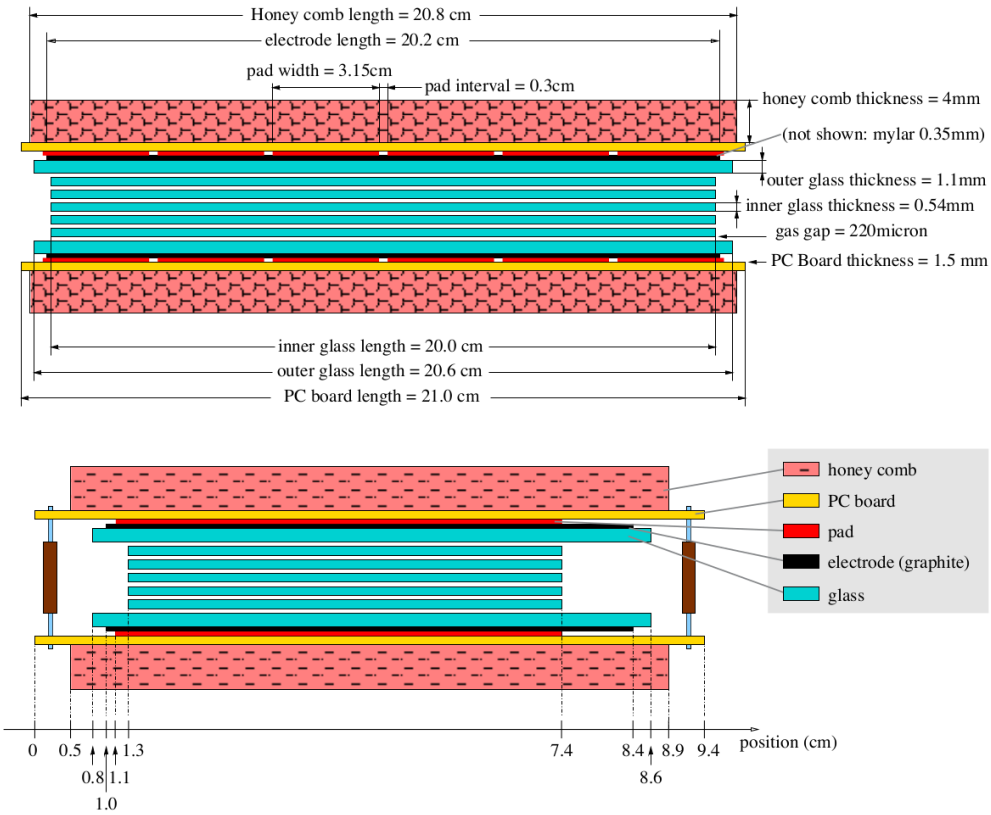

Figure 2.9 Side views of one TOF MRPC module. The figure is taken from[77].

The MRPC consists of a stack of resistive plates made from 0.54-mm-thick float glass, with uniform 220 μm gas gaps in between. Graphite electrodes are applied to the outer surface of the outer glass plates. By applying high voltage across these electrodes, a strong electric field is generated in each of these gaps. All the inner glass plates float electrically. When a charged particle travels through the glass stack, it generates primary ionization along its path within the gaps. The strong electric field within these gaps then produces Townsend amplification avalanches. Given that both the electrodes and the glass plates are resistive (with a volume resistivity of 10^{13} Ωcm and surface resistivity of 10^5 Ω/□, respectively), they are transparent to the avalanche charge. Therefore, the induced signal on the copper readout pads, which are located outside the electrodes on the Printed circuit board (PCB) board, is the sum of the avalanches occurring in all the gas gaps. Each pad layer is comprised of a single row of six pads, each with dimensions of 3.15×6.3 cm^2. The pads are read out on one edge through traces connected to

twisted-pair signal cables, which transport the signals to the electronics for amplification and digitization. The PCB boards are affixed to 4-mm-thick honeycomb panels on the outermost part of the detector. Considering that the MRPC's main body is made of delicate float glass, these honeycomb panels play a crucial role. They not only provide the necessary rigidity and flatness but also protect the detector and maintain the overall structure. The small size of the gaps in the MRPC reduces fluctuations in avalanche development time, thus enhancing its time resolution compared to a single-gap RPC. The typical time resolution of an MRPC module is around 65 ps, while the time resolution for the whole TOF system is 75 ps[77,115-116].

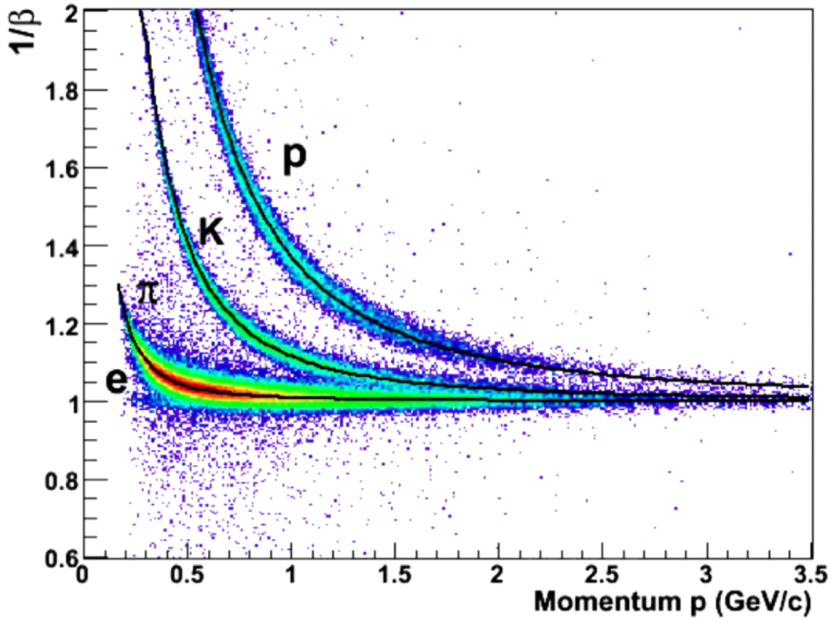

Figure 2.10 $1/\beta$ **plotted against momentum during Run 8 is based on a preliminary calibration of a very small fraction of the available dataset. The figure is taken from[113].**

The TOF system measures the arrival time or the stop time (t_{stop}) of a charged particle, from which the particle's flight time can be calculated ($\Delta t = t_{\text{stop}} - t_{\text{start}}$). The start time ($t_{\text{start}}$) is measured by the VPDs. Furthermore, one can match the hit left by the charged particle in the TOF to the track reconstructed in the TPC. Using the path length l of the matched track, it is possible to calculate the inverse velocity $1/\beta$:

$$\frac{1}{\beta} = c\frac{\Delta t}{l}, \tag{2.1}$$

where c is the speed of light. The quantity used in this analysis for PID is the square of the particle mass, which can be derived as follows:

$$m^2 = (\frac{p}{\gamma\beta c})^2 = \frac{p^2(1-\beta^2)}{\beta^2 c^2} = \frac{p^2}{c^2}[(\frac{1}{\beta})^2 - 1]. \tag{2.2}$$

2.2.3 Vertex Position Detector

The VPD[84] covering the pseudo-rapidity range of $4.24 < |\eta| < 5.1$ is a crucial part of the STAR trigger system, providing primary input for the MB trigger for heavy-ion collisions at top RHIC energy. The MB trigger typically includes constraints on the collision vertex ($V_{z,\mathrm{VPD}}$) calculated online using VPD timing information (Eq. 2.3) to select collisions near the center of STAR, which have the best detector acceptance and lowest background from particles produced in the support materials.

The VPD detectors have two identical assemblies which are installed at both the east and west sides of the STAR. The two assemblies are mounted symmetrically with respect to the center of STAR, at a distance of 5.7 m. Each VPD assembly consists of nineteen tubes, as shown in the left panel of Fig. 2.12. Each tube is made with a 0.25-inch-thick non-conductive spacer, followed by an active element composed of a 0.25-inch-thick lead converter (equivalent to 1.13 radiation lengths) and a 1-cm-thick scintillator. The lead layer serves as a photon converter, feeding the subsequent scintillator layer with electrons. The scintillator is coupled to a 1.5-inch-diameter Hamamatsu R-5946 fine mesh dynode PMT using RTV-615 optically transparent silicone adhesive. The photons produced in the scintillator result in significant Photomultiplier tube (PMT) signals, thereby providing excellent resolution for timing measurement. The entire tube is enclosed in a 2-in-outer-diameter and 0.049-inch-thick aluminum cylinder, with 3/8-inch-thick aluminum front and back caps. Figure 2.11 shows the structure of one tube in a VPD assembly.

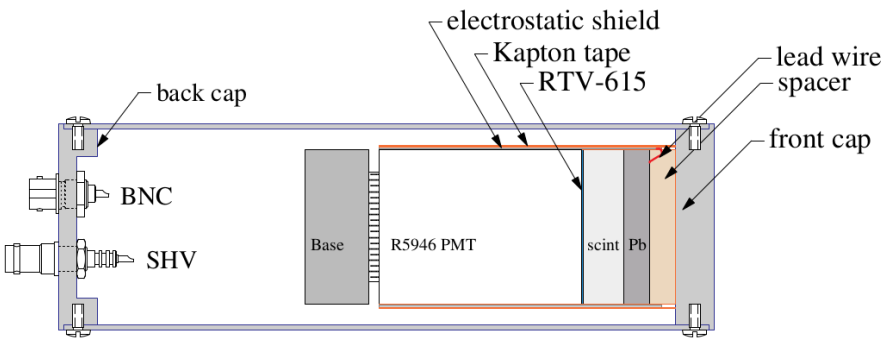

Figure 2.11 A schematic view of a single VPD tube. The figure is taken from[84].

In the left panel of Fig. 2.12, a front view of one VPD assembly shows that it consists of two semi-circular sections surrounding the beam pipe. The sections are fastened together and supported by Delrin blocks attached to a horizontal mount plate, which is clamped to the beam pipe support. As the beam pipe and the support are at a different electrical ground than the rest of the experiment, the Delrin blocks serve both to hold

the assembly in place and provide electrical isolation[84]. The right panel of Fig. 2.12 illustrates two rings of readout tubes, which are attached to the beam pipe support of each VPD assembly.

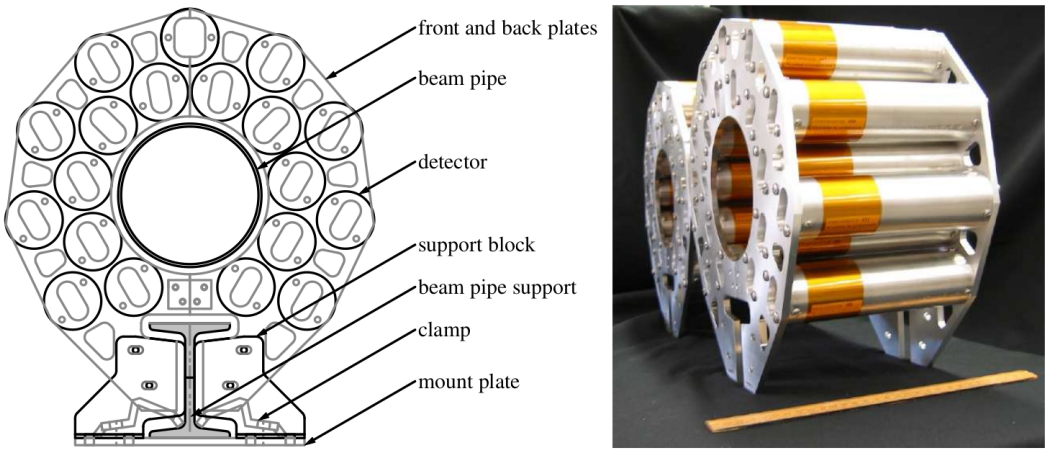

Figure 2.12 The left figure shows a schematic front view of one VPD assembly, while the right figure is a photo of both VPD assemblies. The figure is taken from[84].

In heavy-ion collisions, a significant number of forward-going, high-energy photons are produced. These photons effectively form a prompt pulse that travels away from the collision vertex. The VPD is a fast detector designed to measure the times when these forward pulses arrive. This information is used online to estimate the collision vertex's location along the beam pipe. Such a location ($V_{z,\mathrm{VPD}}$) can be determined using the time difference from the east and west VPDs as shown in Eq. 2.3,

$$V_{z,\mathrm{VPD}} = c(t_{\mathrm{east}} - t_{\mathrm{west}})/2, \tag{2.3}$$

where t_{east} and t_{west} represent the earliest timing signals over all channels in each VPD assembly, and c is the speed of light. The $V_{z,\mathrm{VPD}}$ can also be calculated offline using average timing signals from each VPD assembly. Its correlation with the vertex position calculated with TPC ($V_{z,\mathrm{TPC}}$) can be used to reject pile-up events.

The timing measured in the VPD can also help determine the event start time, which is fed to other timing detectors, such as TOF and MTD, to calculate particles' flight time for PID. The event start time can be obtained by Eq. 2.4.

$$t_{\mathrm{start}} = (t_{\mathrm{east}} + t_{\mathrm{west}})/2 - l/c, \tag{2.4}$$

where l represents the distance from the center of STAR to either one of the VPDs.

The VPD's timing resolution for each assembly is around 95 ps in 200 GeV Au+Au collisions, but it worsens to roughly 150 ps in p+p and lower-energy Au+Au collisions.

The start time resolution varies from 20-30 ps in 200 GeV Au+Au collisions to approximately 80 ps in p+p collisions. In 200 GeV p+p and Au+Au collisions, the VPD can measure the location of the primary vertex with a resolution of around 2.5 cm and 1 cm, respectively.

Chapter 3 Dataset and data quality assurance

The data used in this thesis is the collisions of Ru+Ru and Zr+Zr recorded by STAR in 2018. The main goal is searching for the Chiral Magnetic Effect (CME). The Ru nucleus has 44 protons while the Zr nucleus has 40. The 10% charge difference between the two isobars is expected to generate an approximately 15% difference in the CME signal while the background is expected to be similar[42]. While the anticipated CME signal was not observed unfortunately[42], the large-statistics isobar data open the door for many other research topics.

The isobar data-taking was conducted in a special way to minimize the differences between the run conditions for the two species, i.e., the $^{96}_{44}$Ru beam was injected and kept for a period of time, and then the $^{96}_{40}$Zr beam was injected right after dumping of the $^{96}_{44}$Ru beam. The beam luminosities for both species were maintained at the same level. Additionally, long stores were maintained for each species with constant luminosity, adjusted to ensure that the hadronic interaction rate at STAR approached 10 kHz[117]. In this way, the running conditions and detector performance were almost identical between the isobar collisions, so most systematic uncertainties can be canceled out if one takes ratios of observables in these two colliding systems. Benefiting further from the large statistics of 1.7B good events for each collision system, one can measure the identified particle spectra, the baryon, and charge stopping with great precision.

3.1 Run-by-run QA

At STAR, collision data is recorded continuously for a certain period of time and then saved as a single "run". An essential aspect of ensuring data quality is to identify and eliminate bad runs. We study run-by-run variations in the mean values of quantities, including track azimuthal angle $\langle\phi\rangle$ and $\langle p_{\mathrm{T}}\rangle$, the distance of the closest approach between track and the primary vertex $\langle\mathrm{DCA}\rangle$, other track variables introduced in Sec. 3.5 as well as the Particle IDentification (PID) variables to be introduced in Sec. 4.1. The Quality Assurance (QA) procedure is performed over the entire Ru+Ru and Zr+Zr data samples, calculating the average values and standard deviations for all run-by-run variables. A run is considered an outlier or bad run if any of its QA quantity values deviate by more than five standard deviations from the mean. The removal of bad runs is conducted iteratively, with the whole process repeated until no additional bad run is

identified by the algorithm. Figure 3.1 shows the mean values of examined quantities for each run, where red points are the identified bad runs and blue ones are the good runs.

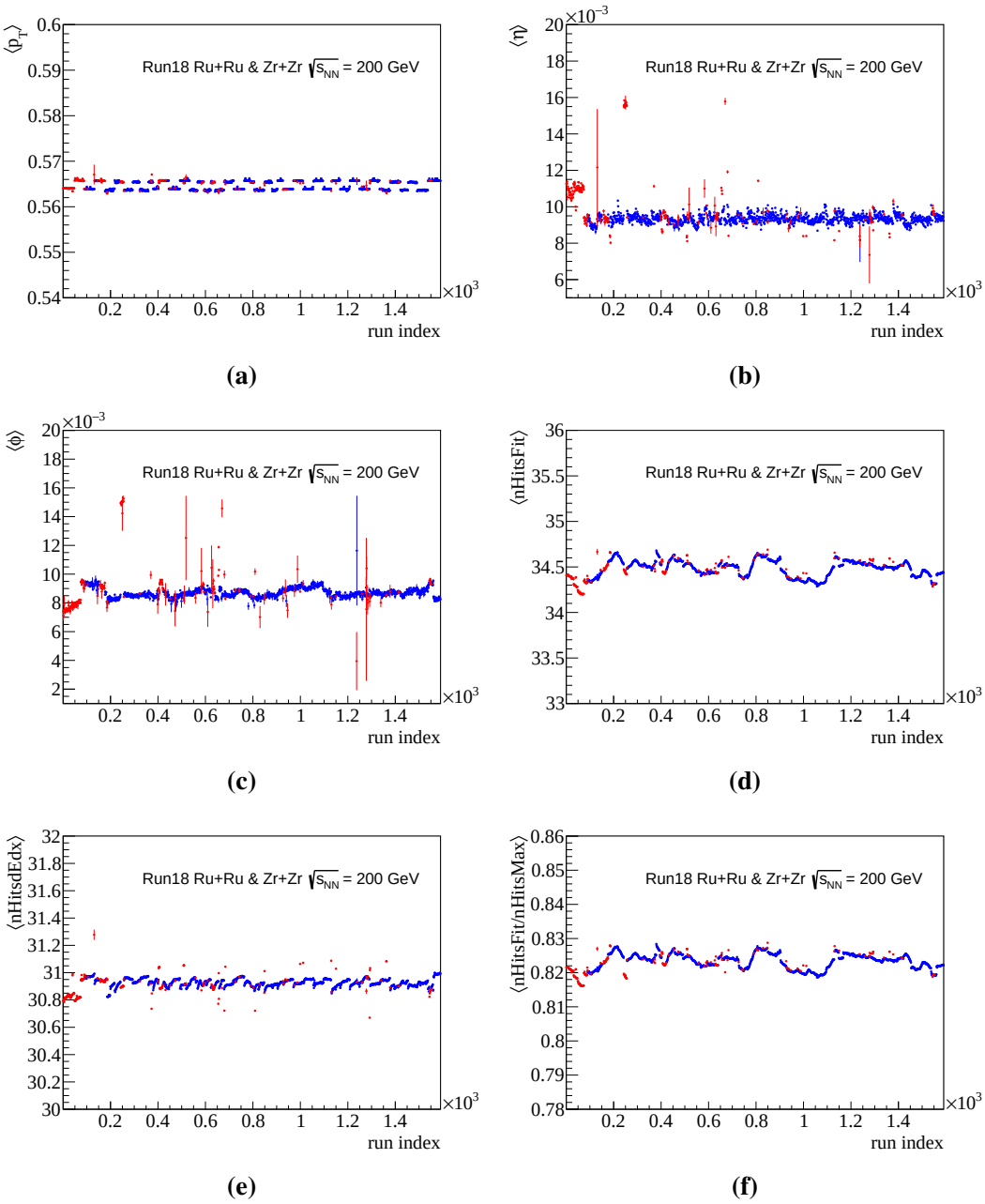

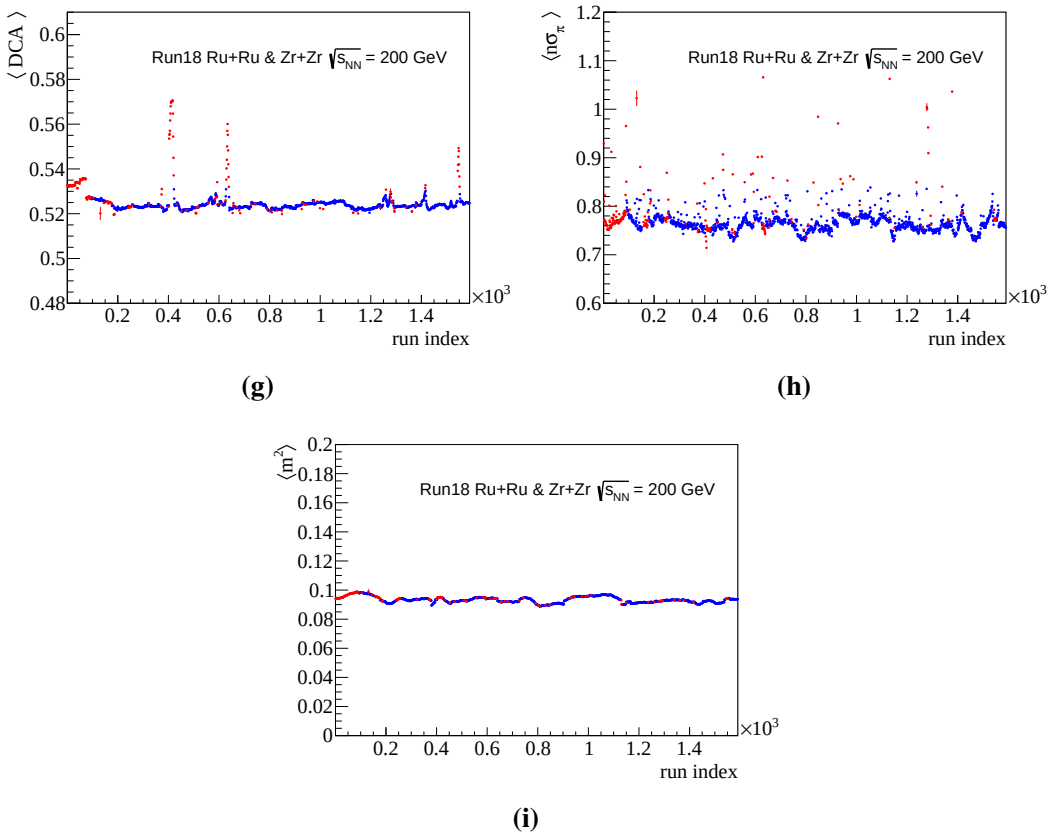

Figure 3.1 $\langle p_{\mathrm{T}} \rangle$ **(a),** $\langle \eta \rangle$ **(b),** $\langle \phi \rangle$ **(c),** $\langle nHitsFit \rangle$ **(d),** $\langle nHitsDedx \rangle$ **(e),** $\langle nHitsFit/nHitsMax \rangle$ **(f),** $\langle DCA \rangle$ **(g),** $\langle n\sigma_{\pi} \rangle$ **(h) and** $\langle m^2 \rangle$ **(i) as a function of run index. The red points represent the bad runs identified by the algorithm, while the blue data points are good runs.**

3.2 Pile-up rejection

The average drift time of primary ionized electrons in the STAR TPC is around 40 µs[118]. When coupled with the long integration time of the electronics, it results in a relatively large read-out time interval in the data acquisition system. If more than one collision occurs within the read-out time window, there could be tracks in the TPC from other events accidentally assigned to the primary vertex of the triggered collision, resulting in an unusually high event multiplicity. These events are regarded as pile-up events and should be rejected in data analysis.

Since the TOF is a fast detector that is not influenced by the pile-up effect, its data can be used for identifying pile-up events. Normally, pile-up events have larger multiplicities than good events. Therefore, the correlation between the event multiplicity, called "*refMult*", and the number tracks matched to TOF (*nBTOFMatch*) can be used to reject them. The *refMult* is determined by counting good TPC tracks with DCA < 3 cm

and within the pseudo-rapidity range of $|\eta| < 0.5$. Furthermore, employing the TOF as an additional detector can help to mitigate the impact of any false tracks. For an event to be classified as valid in this analysis, it is required to have at least one TPC track that matches with the TOF (*nBTOFMatch*).

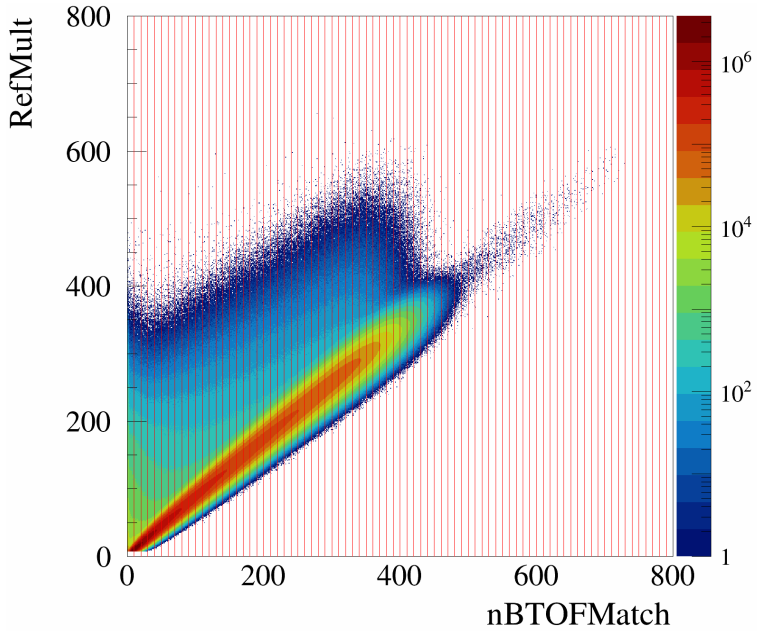

Figure 3.2 Correlation between *nBTOFMatch* and *refMult*. Vertical red lines divide the *nBTOFMatch* distribution into different slices.

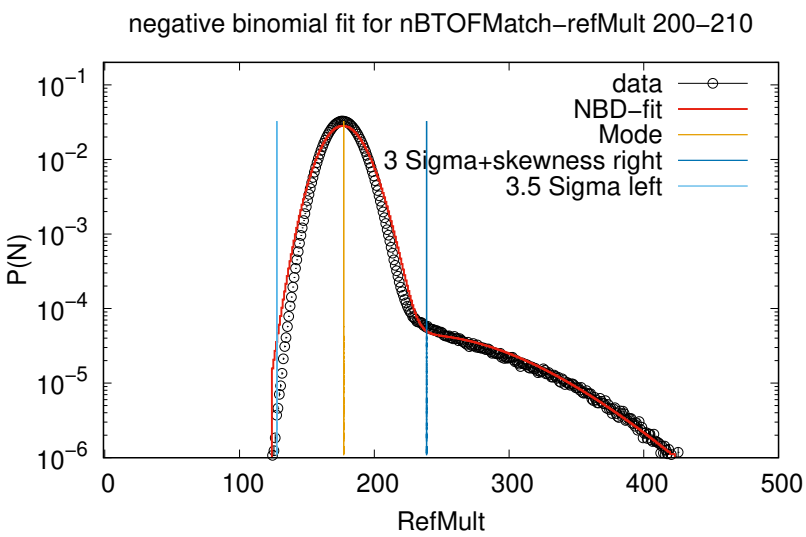

Figure 3.3 Double-NBD fit to the *refMult* distribution with *nBTOFMatch* from 200 to 210.

Figure 3.2 displays the *nBTOFMatch-refMult* correlation, with the pile-up effect showing up in a form of unusually high *refMult* values for a given *nBTOFMatch* bin. The vertical red lines in the plot divide the *nBTOFMatch* distribution into different slices. To determine the pile-up cuts, one projects the *refMult* distribution for each slice of

nBTOFMatch. An example of the *refMult* distribution for *nBTOFMatch* between 200 and 210 is shown in Fig. 3.3. It is fitted with a double Negative Binomial Distribution (NBD), shown as the red curve. The *refMult* distribution can be separated into two clear regions: 1) a peak region described by a narrow NBD and 2) a tail at large *refMult* resulting from pile-up events and described by a broader NBD. The yellow line indicates the position of the peak, while the two blue lines define the selection window for the signal peak.

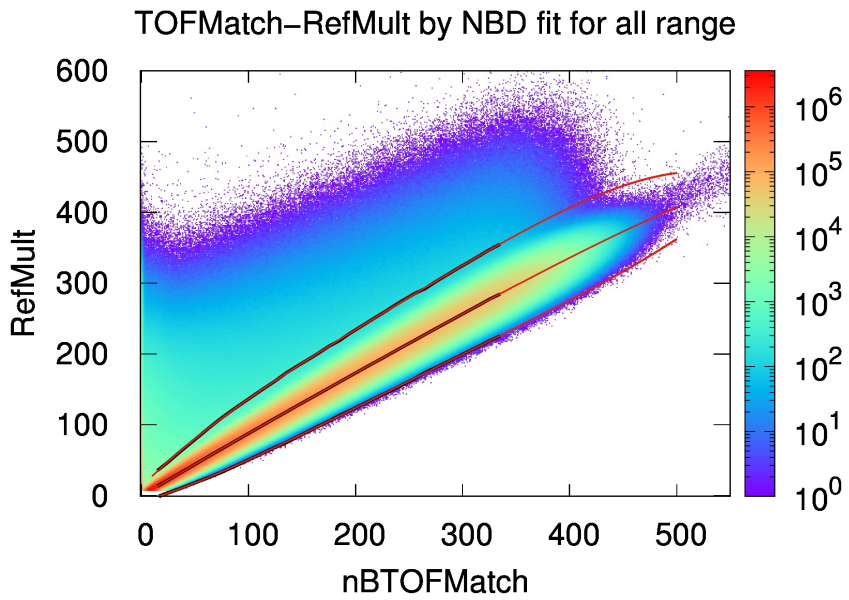

Figure 3.4 Correlation between *nBTOFMatch* and *refMult*. The entries beyond the upper red curve and those below bottom red curve are treated as pile-up events and rejected in the analysis.

Figure 3.4 shows again the correlation between *nBTOFMatch* and *refMult*. The three red curves represent the upper limit, mean value, and lower limit respectively. These mean values and the upper and lower limits are established through double-NBD fits and are fitted by fourth-order polynomial functions. Events that fall between the upper and lower curves are classified as good events, while the rest are discarded as pile-up events.

3.3 Centrality definition

Figure 3.5 provides a schematic representation of a heavy-ion collision. As the relativistic nuclei travel along the beam axis, they experience Lorentz contraction, rendering their transverse dimension larger compared to their longitudinal dimension. Therefore,

their collision can essentially be viewed as a superposition of several binary nucleon-nucleon collisions. Given the extended nature of nuclei, the interaction volume is contingent upon the impact parameter (b), which is defined as the distance between the centers of the two colliding nuclei in the transverse plane. As depicted in Fig. 3.5, the participating nucleons engage directly in the collision process. They contribute predominantly to particle production, potentially leading to the creation of a QGP. After the collision, produced particles may undergo numerous scattering interactions before the system reaches a freeze-out state, after which the final state hadrons are detected. On the contrary, spectators are the nucleons that typically originate from the peripheral areas of the colliding nuclei and pass by the collision zone without significantly contributing to particle production. Therefore, spectators predominantly continue on their initial trajectories with minor deviations, retaining a substantial portion of the initial energy of the nuclei. This residual energy often correlates with the particles detected at forward rapidities in such collision experiments.

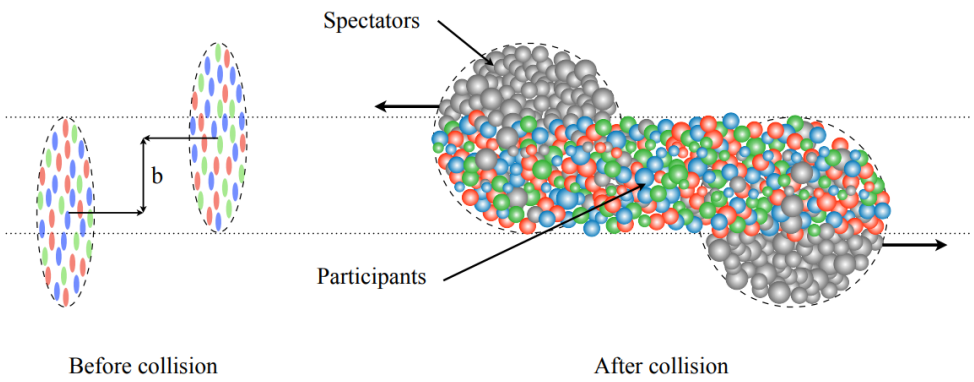

Figure 3.5 Illustration of an ultra-relativistic heavy-ion collision. Prior to the collision, the two nuclei are Lorentz contracted. Following the collision, a high-temperature and high-density region is formed, consisting of the participating nucleons (fireball), while the spectator nucleons continue their motion in the beam direction. Figure is taken from [119].

Since the properties of the medium created in heavy-ion collisions depend on the extent to which colliding nuclei overlap with each other, it is desirable to carry out measurements for different sizes of the overlapping region. Theoretically, one can quantify the overlapping region size using the impact parameter, which however could not be measured experimentally [120]. In heavy-ion physics, it is customary to introduce the concept of collision centrality, which is directly related to the impact parameter. Central collisions occur when the two nuclei collide nearly head-on, with almost all nucleons within the nucleus participating in the collision. These collisions are characterized by a small impact parameter and the largest particle multiplicity production. In contrast, peripheral collisions have a large impact parameter and only a few nucleons participate

in the collision.

At STAR, the uncorrected multiplicity (*refMult*) is used to define centrality. *RefMult* is affected by the TPC tracking efficiency which decreases with increasing luminosity, and by the TPC acceptance related to the primary vertex position. Therefore, its dependence on the collision vertex position ($V_{z,\mathrm{TPC}}$) and the beam luminosity has to be taken into account such that a single set of *refMult* cuts can be used to determine centrality for all the events.

Figure 3.6 displays the relationship between the ZDC coincidence rate, which is a measure of the beam luminosity, and the average *refMult* for isobar species 1 (Zr) and species 2 (Ru). The dark blue data points correspond to Ru+Ru, while the light blue data points correspond to Zr+Zr. The red lines represent linear fits to the data. The functional form $y = a \times x + b$ is used to perform the linear fit, where a and b are the fitting parameters. The values for these parameters obtained from the fit are provided in Table 3.1, and used to correct for luminosity dependence in the analysis.

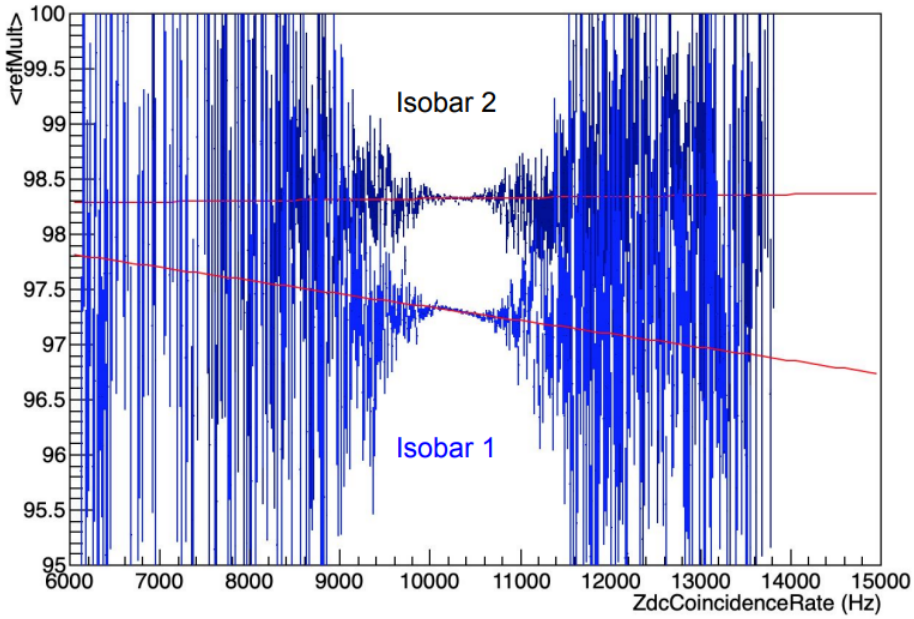

Figure 3.6 Correlation between $\langle refMult \rangle$ and ZDC coincidence rate for isobar species 1 (Zr+Zr) and 2 (Ru+Ru). Figure is taken from[121].

Table 3.1 The linear fitting parameters applied to the *refMult* dependence on the ZDC coincidence rate for both Ru+Ru and Zr+Zr collisions.

	a	b
Isobar 1 (Zr)	$(-1.4 \pm 0.1) \times 10^{-4}$	98.41 ±0.11
Isobar 2 (Ru)	$(-1.2 \pm 1.0) \times 10^{-5}$	98.11 ±0.11

The *refMult* undergoes further correction to account for the acceptance variation with respect to $V_{z,\mathrm{TPC}}$. To determine the correction factor, the *refMult* distributions are plotted in 2 cm intervals of $V_{z,\mathrm{TPC}}$ over the range of $-35 < V_{z,\mathrm{TPC}} < 25$ cm. In

heavy-ion collisions, the *refMult* distributions display a characteristic sharp decline at high values. The position of the half-maximum of this decline, defined as the high-end point, is obtained by fitting this region with an error function[42]. The distribution of high-end points as a function of $V_{z,\mathrm{TPC}}$ is then fitted using a sixth-degree polynomial function as shown in Fig. 3.7.

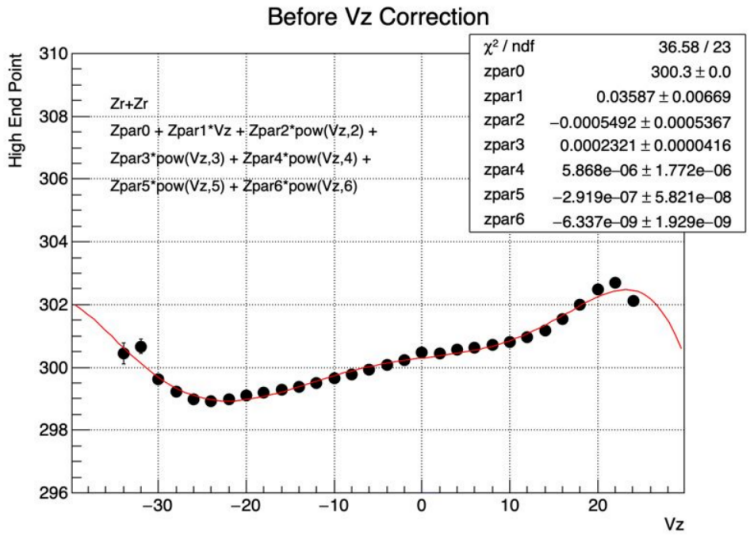

Figure 3.7 The high-end points of *refMult* distribution as a function of $V_{z,\mathrm{TPC}}$, with the red curve illustrating the sixth-degree polynomial fit function. Figure is taken from[121].

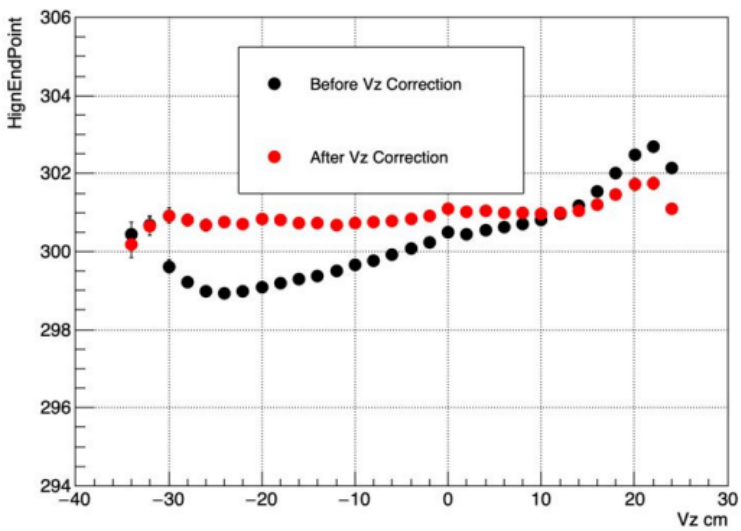

Figure 3.8 The high-end point as a function of $V_{z,\mathrm{TPC}}$ before (black circles) and after (red circles) corrections. Figure is taken from[121].

Figure 3.8 illustrates the distributions of high-end points as a function of $V_{z,\mathrm{TPC}}$ before and after correction in Zr+Zr collisions. The correction factor is calculated as the ratio of the high-end point for a specific $V_{z,\mathrm{TPC}}$ bin to the high-end point at $-1 < V_{z,\mathrm{TPC}} < 1$ cm, which is the center of the TPC[42]. Figure 3.9 displays the *refMult*

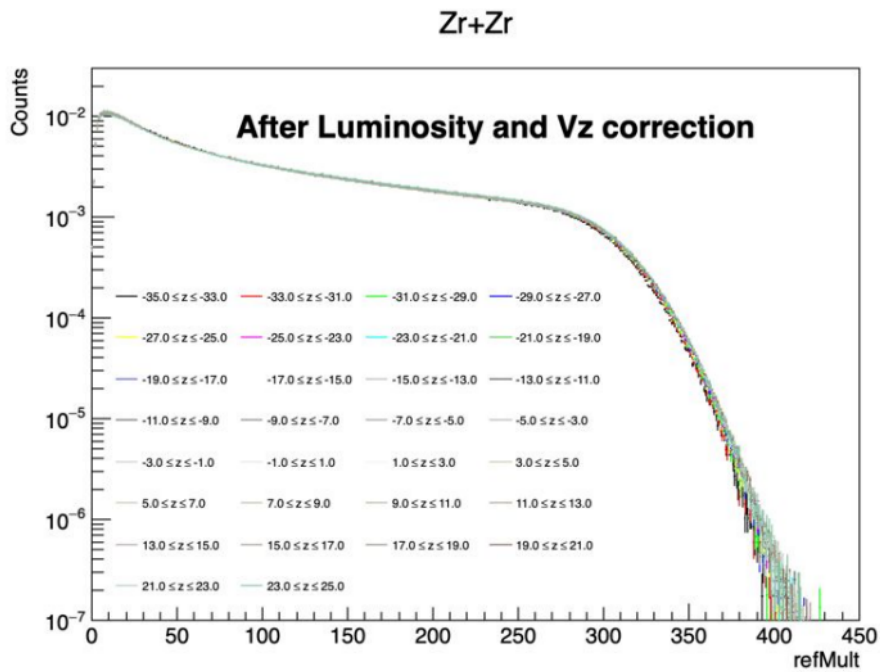

Figure 3.9 The *refMult* distributions in Zr+Zr collisions after corrections for both luminosity and $V_{z,\mathrm{TPC}}$ are shown in different $V_{z,\mathrm{TPC}}$ intervals. Figure is taken from[121].

distribution in Zr+Zr collisions following corrections for luminosity and $V_{z,\mathrm{TPC}}$. The *refMult* distributions are then fitted using the Monte-Carlo (MC) Glauber model[122] to define different centrality bins. In Glauber simulations, the probability of a collision at a specific impact parameter, along with the corresponding N_{part} and the number of binary nucleon-nucleon collisions (N_{coll}), are determined via Monte Carlo sampling. A binary collision occurs when two nucleons from different nuclei come close enough together to interact via strong interactions. The required inputs for the Glauber simulation include the nuclear thickness function and the inelastic nucleon-nucleon cross-section, which is set to be 42 *mb* for the current analysis of $\sqrt{s_{\mathrm{NN}}}$ = 200 GeV collisions. The nuclear thickness function represents the projection of the 3D nuclear density onto the transverse plane (perpendicular to the z axis). It is calculated by sampling nucleons from the incoming nuclei following the Woods-Saxon distribution defined in the rest frame of the nucleus using a spherical coordinate system (where r is the radial position and θ is the polar angle), as indicated in Eq. 3.1.

$$\rho(r,\theta) = \frac{\rho_0}{1 + exp[\frac{r - R(1+\beta_2 Y_0^2(\theta))}{a}]}, \tag{3.1}$$

where R is the nucleus radius, a is the diffuseness parameter of the nuclear surface, β_2 quantifies the quadrupole deformation, $Y_2^0(\theta) = \frac{1}{4}\sqrt{\frac{5}{\pi}}(3cos^2\theta - 1)$ is the spherical harmonic function, and ρ_0 acts as the normalization factor[123]. The particle multiplicity

at a given b is parameterized by the two-component model as:

$$N_{\text{trk}}^{\text{Glauber}} = n_{pp}[(1-x)N_{\text{part}}/2 + xN_{\text{coll}}], \tag{3.2}$$

where n_{pp} represents the average pseudo-rapidity multiplicity density in nucleon-nucleon (NN) collisions and x denotes the relative contribution of hard processes to the multiplicity.

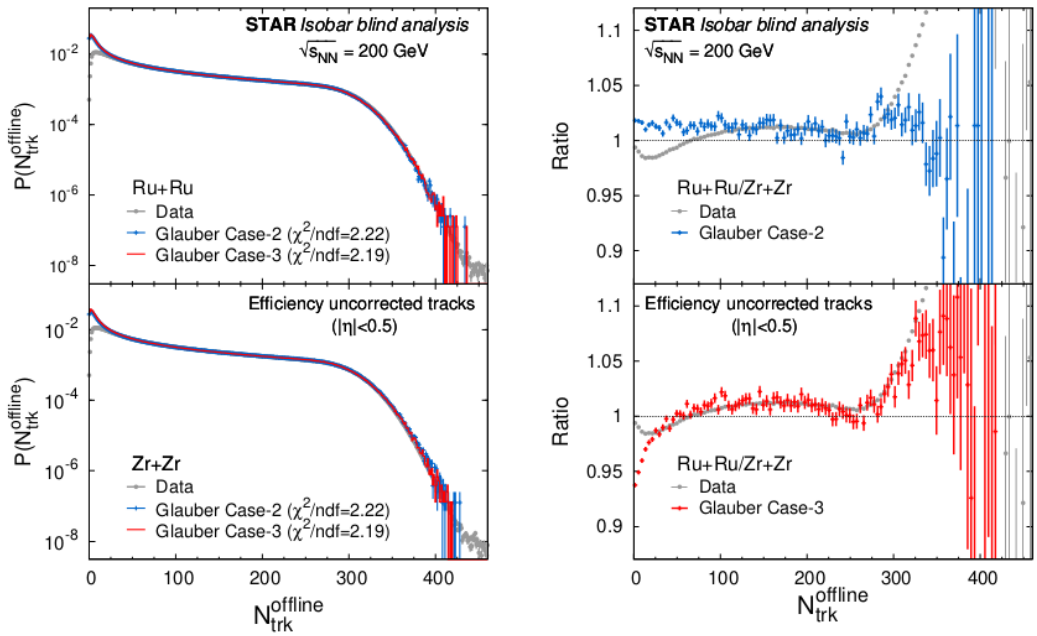

Figure 3.10 Distributions of the *refMult* (denoted as $N_{\text{trk}}^{\text{offline}}$) in Ru+Ru (upper left panel) and Zr+Zr (lower left panel) collisions, along with two Glauber fits with two different sets of nuclear shape parameters. The upper right and lower right panels display the ratio of $refMult$ between Ru+Ru and Zr+Zr in data and from the Glauber model fits. Figure is taken from [42].

Table 3.2 The Woods-Saxon parameters used in Glauber simulations.

	Case-1 [124]			Case-2 [124]			Case-3 [125]		
Nucleus	R (fm)	a (fm)	β_2	R (fm)	a (fm)	β_2	R (fm)	a (fm)	β_2
$^{96}_{44}$Ru	5.085	0.46	0.158	5.085	0.46	0.053	5.067	0.500	0
$^{96}_{40}$Zr	5.02	0.46	0.08	5.02	0.46	0.217	4.965	0.556	0

Figure 3.10 (left panels) shows the *refMult* distributions (denoted as $N_{\text{trk}}^{\text{offline}}$ on the plot) in Ru+Ru and Zr+Zr collisions. They are simultaneously fitted using the Glauber model with two sets of Woods-Saxon parameters (Case-2 and Case-3), represented by the blue and red histograms, respectively [42]. The Woods-Saxon parameters for these two cases are listed in Table 3.2. The right panels of Fig. 3.10 display a comparison between the ratio of the experimentally measured *refMult* for Ru+Ru to that for Zr+Zr and the corresponding ratio obtained from the MC Glauber fits. These results demonstrate that the nuclear density parameters used in Case-3 provide a better description of the experimental data. Therefore, Case-3 is selected for the final centrality determination.

As can be seen in the left panel of Fig. 3.10, while there is a good agreement

between data and Glauber model fit at large multiplicities, there is a clear discrepancy in the low-end part due to the STAR event trigger inefficiency. To correct this centrality bias in the measurement, an event weight proportional to the inverse trigger efficiency is applied. The weighting factors for events in various centrality intervals can be seen in Fig. 3.11. The plot indicates that in peripheral collisions, the weighting factors are greater than 1, caused by the trigger inefficiency at low *refMult*. Conversely, in central collisions, the weighting factors are closer to 1. However, for some events in the most central collisions (0-5%), the weights also deviate from 1, which accounts for the slight shape differences of the $refMult$ distributions in different $V_{z,\mathrm{TPC}}$ intervals after all the corrections.

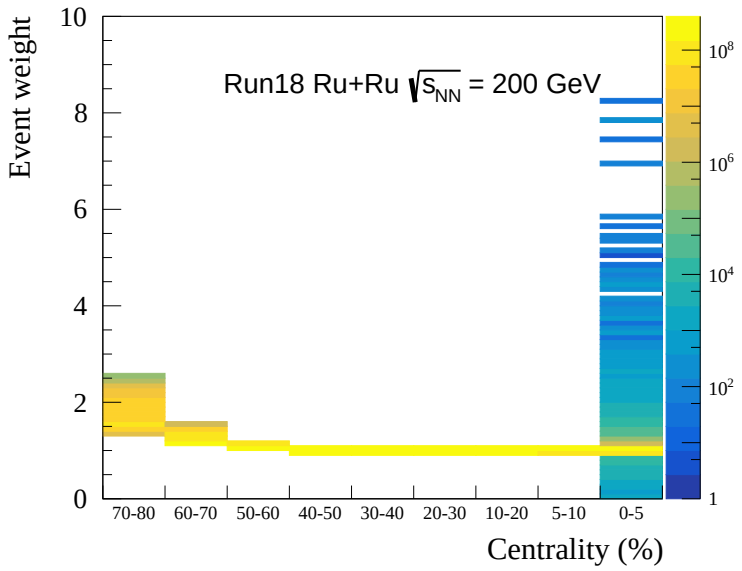

Figure 3.11 Event weighting factors in different centrality intervals of Ru+Ru collisions.

Tables 3.3 and 3.4 show the centrality intervals, $N_{\mathrm{trk}}^{\mathrm{offline}}$ cuts and the corresponding $\langle N_{\mathrm{trk}}^{\mathrm{offline}} \rangle$, $\langle N_{\mathrm{part}} \rangle$ and $\langle N_{\mathrm{coll}} \rangle$ values in Ru+Ru and Zr+Zr collisions at $\sqrt{s_{\mathrm{NN}}} = 200$ GeV. The uncertainties of $\langle N_{\mathrm{part}} \rangle$ and $\langle N_{\mathrm{coll}} \rangle$ are obtained by varying input parameters in the MC Glauber model.

3.4 Event selection

The MB trigger used in this analysis requires a coincidence between the signals from both the east and west VPD detectors and an online cut on the collision vertex ($V_{z,\mathrm{VPD}}$) to select events of interest. In other words, events are accepted only when there is a signal in both the east and west VPDs and the collision vertex falls within a predefined range along the beam direction. The trigger ids, designed to label events

Table 3.3 Centrality definition by $N_{\mathrm{trk}}^{\mathrm{offline}}$ ranges in Ru+Ru collisions at $\sqrt{s_{\mathrm{NN}}}$ = 200 GeV. The first column provides the labels for the centrality ranges defined. The centrality column indicates the actual centrality ranges, which may vary slightly due to the use of integer cuts for determining the centrality. The mean $\langle N_{\mathrm{trk}}^{\mathrm{offline}} \rangle$ values, the mean number of participants ($\langle N_{\mathrm{part}} \rangle$), and the mean number of binary collisions ($\langle N_{\mathrm{coll}} \rangle$) are also listed. The statistical uncertainties on $\langle N_{\mathrm{trk}}^{\mathrm{offline}} \rangle$ are all significantly smaller than 0.01.

Centrality label (%)	Ru+Ru Centrality(%)	$N_{\mathrm{trk}}^{\mathrm{offline}}$	$\langle N_{\mathrm{trk}}^{\mathrm{offline}} \rangle$	$\langle N_{\mathrm{part}} \rangle$	$\langle N_{\mathrm{coll}} \rangle$
0–5	0–5.01	258.–500.	289.32	166.8±0.1	389±10
5–10	5.01–9.94	216.–258.	236.30	147.5±1.0	323±5
10–20	9.94–19.96	151.–216.	181.76	116.5±0.8	232±3
20–30	19.96–30.08	103.–151.	125.84	83.3±0.5	146±2
30–40	30.08–39.89	69.–103.	85.22	58.8±0.3	89.4±0.9
40–50	39.89–49.86	44.–69.	55.91	40.0±0.1	53.0±0.5
50–60	49.86–60.29	26.–44.	34.58	25.8±0.1	29.4±0.2
60–70	60.29–70.04	15.–26.	20.34	15.83±0.03	15.6±0.1
70–80	70.04–79.93	8.–15.	11.47	9.34±0.02	8.03±0.04
20–50	19.96–49.86	44.–151.	89.50	60.9±0.3	96.7±1.0

Table 3.4 Same as Table 3.3 but for Zr+Zr collisions.

Centrality label (%)	Zr+Zr Centrality(%)	$N_{\mathrm{trk}}^{\mathrm{offline}}$	$\langle N_{\mathrm{trk}}^{\mathrm{offline}} \rangle$	$\langle N_{\mathrm{part}} \rangle$	$\langle N_{\mathrm{coll}} \rangle$
0–5	0–5.00	256.–500.	287.36	165.9±0.1	386±10
5–10	5.00–9.99	213.–256.	233.79	146.5±1.0	317±5
10–20	9.99–20.08	147.–213.	178.19	115.0±0.8	225±3
20–30	20.08–29.95	100.–147.	122.35	81.8±0.4	139±2
30–40	29.95–40.16	65.–100.	81.62	56.7±0.3	83.3±0.8
40–50	40.16–50.07	41.–65.	52.41	38.0±0.1	48.0±0.4
50–60	50.07–59.72	25.–41.	32.66	24.6±0.1	26.9±0.2
60–70	59.72–70.00	14.–25.	19.34	15.10±0.03	14.3±0.1
70–80	70.00–80.88	7.–14.	10.48	8.58±0.02	7.12±0.04
20–50	20.08–50.07	41.–147.	85.68	58.9±0.3	90.3±0.9

of desired trigger conditions, are summarized below. Multiple trigger ids due to slight changes in the trigger setup are included in the analysis since those changes do not impact the physics results.

- Trigger ID: 600001, 600011, 600021, and 600031

For each MB-triggered event, TPC tracks are used to reconstruct the primary collision vertex. Since collisions happening close to the center of the STAR detector can be better captured by the TPC, those events with vertices along the longitudinal beam direction ($V_{z,\mathrm{TPC}}$) ranging between -35 cm and 25 cm are selected for this analysis, as shown in the left panel of Fig. 3.12. The asymmetric $V_{z,\mathrm{TPC}}$ cut with respect to the center of STAR is a consequence of a timing offset that was not calibrated out for the online VPD trigger. The primary vertex location is further evaluated by comparing the VPD's measurement ($V_{z,\mathrm{VPD}}$) to the one obtained from TPC ($V_{z,\mathrm{TPC}}$). The relationship between these two quantities is shown in Fig. 3.13. The vertex resolution is determined

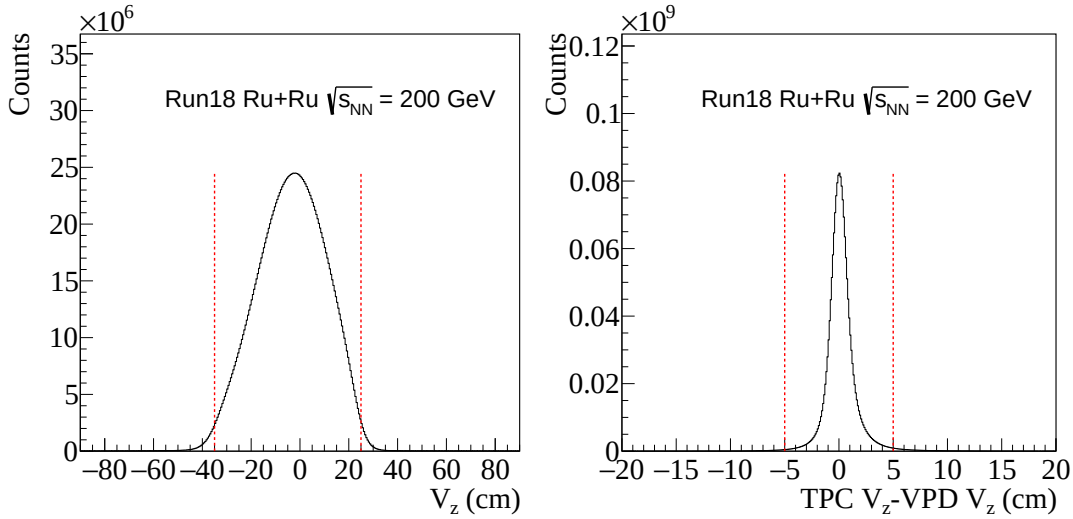

(a) **(b)**

Figure 3.12 $V_{z,\mathrm{TPC}}$ **(a) and** $V_{z,\mathrm{TPC}} - V_{z,\mathrm{VPD}}$ **(b) distributions in isobar collisions. The dashed red lines indicate the cut values.**

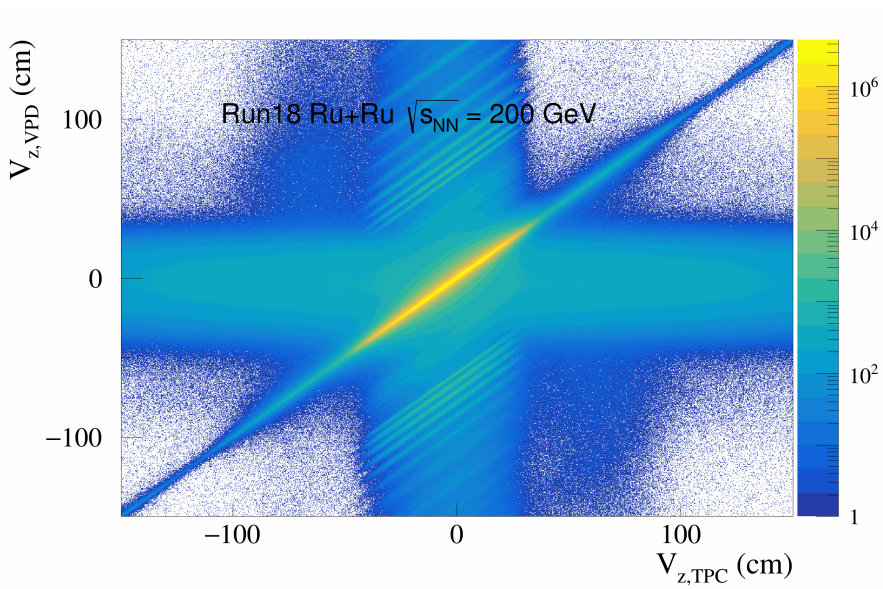

Figure 3.13 Correlation between $V_{z,\mathrm{TPC}}$ **and** $V_{z,\mathrm{VPD}}$**.**

by fitting the difference between $V_{z,\mathrm{VPD}}$ and $V_{z,\mathrm{TPC}}$ using a Gaussian function since the TPC vertex resolution is much better than that of VPD. The standard deviations obtained from these fits are typically 1 cm for 200 GeV isobar collisions. An additional $|V_{z,\mathrm{TPC}} - V_{z,\mathrm{VPD}}| < 5$ cm cut, as shown in the right panel of Fig. 3.12, is applied to reject out-of-time pile-up events which happen in different bunch crossings.

Pile-up events are further rejected by requiring at least one TPC track matched to a TOF hit for all selected events since TOF is a fast detector and thus resilient to pile-up events. In order to exclude the collisions occurring in the beam pipe or detector material, the vertex position in the radial plane is also constrained with a $V_{r,\mathrm{TPC}} < 2$ cm cut shown

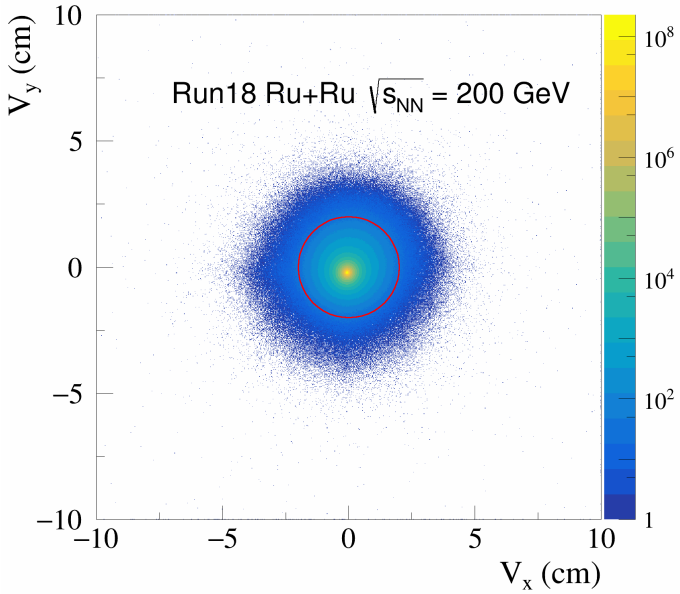

Figure 3.14 Correlation between V_x and V_y, and the red circle represents the cut.

as a red circle in Fig. 3.14. The selection criteria for good events are summarized here:

- Vertex-z position: $-35 < V_{z,\mathrm{TPC}} < 25$ cm
- Vertex-x vs. vertex-y position: $\sqrt{V_x^2 + V_y^2} < 2$ cm
- VPD V_z and TPC V_z difference: $|V_{z,\mathrm{TPC}} - V_{z,\mathrm{VPD}}| < 5$ cm
- Number of TOF matched tracks: $nBTOFMatch > 0$

3.5 Track selection

Tracks directly reconstructed from the hits in the TPC are called global tracks. For those global tracks whose DCA to the primary collision vertex is less than 3 cm, they are re-fitted with the primary vertex included. If the fit is successful, the resulting track is referred to as the primary track and used in this analysis since charged particles produced at the primary vertex are of interest. The inclusion of the primary vertex in the fitting significantly extends the lever arm of the track trajectory, resulting in a much better momentum resolution for primary tracks than that for the global tracks.

To ensure the quality of the primary tracks used in this analysis, we apply the following track quality cuts. We require the DCA to the primary vertex less than 3 cm. We also require that each track should have at least 16 TPC hits for reconstruction ($nHitsFit \geq 15$) and at least 11 hits for dE/dx calculation ($nHitsDedx \geq 10$). As introduced before, there are 45 pad rows in each TPC sector and therefore tracks passing through the TPC can have up to 45 maximum possible hits. The fraction of TPC hits used in the track reconstruction is required to be greater than 52% of the maximum possible num-

ber of hits along the track trajectory (*nHitsFit/nHitsMax* > 0.52) to remove split tracks. Furthermore, tracks are required to be within $p_{\mathrm{T}} > 0.2$ GeV/c and $|\eta| < 1$. The track selection criteria are listed below:

- Primary tracks
- Transverse momentum: $p_{\mathrm{T}} > 0.2$ GeV/c
- Pseudo-rapidity: $|\eta| < 1$
- Distance of the closest approach: DCA < 3 cm
- Number of TPC hits used for track reconstruction: *nHitsFit* ≥15
- Number of TPC hits used for specific energy loss calculation: *nHitsDedx* ≥10
- $\frac{nHitsFit}{nHitsMax} > 0.52$

Figure 3.14 displays the distributions of p_{T}, η, ϕ, DCA, *nHitsFit*, *nHitsDedx*, and *nHitsFit/nHitsMax* in Ru+Ru collisions. Distributions in Zr+Zr collisions are similar. The dashed red lines represent the cut values for each quantity.

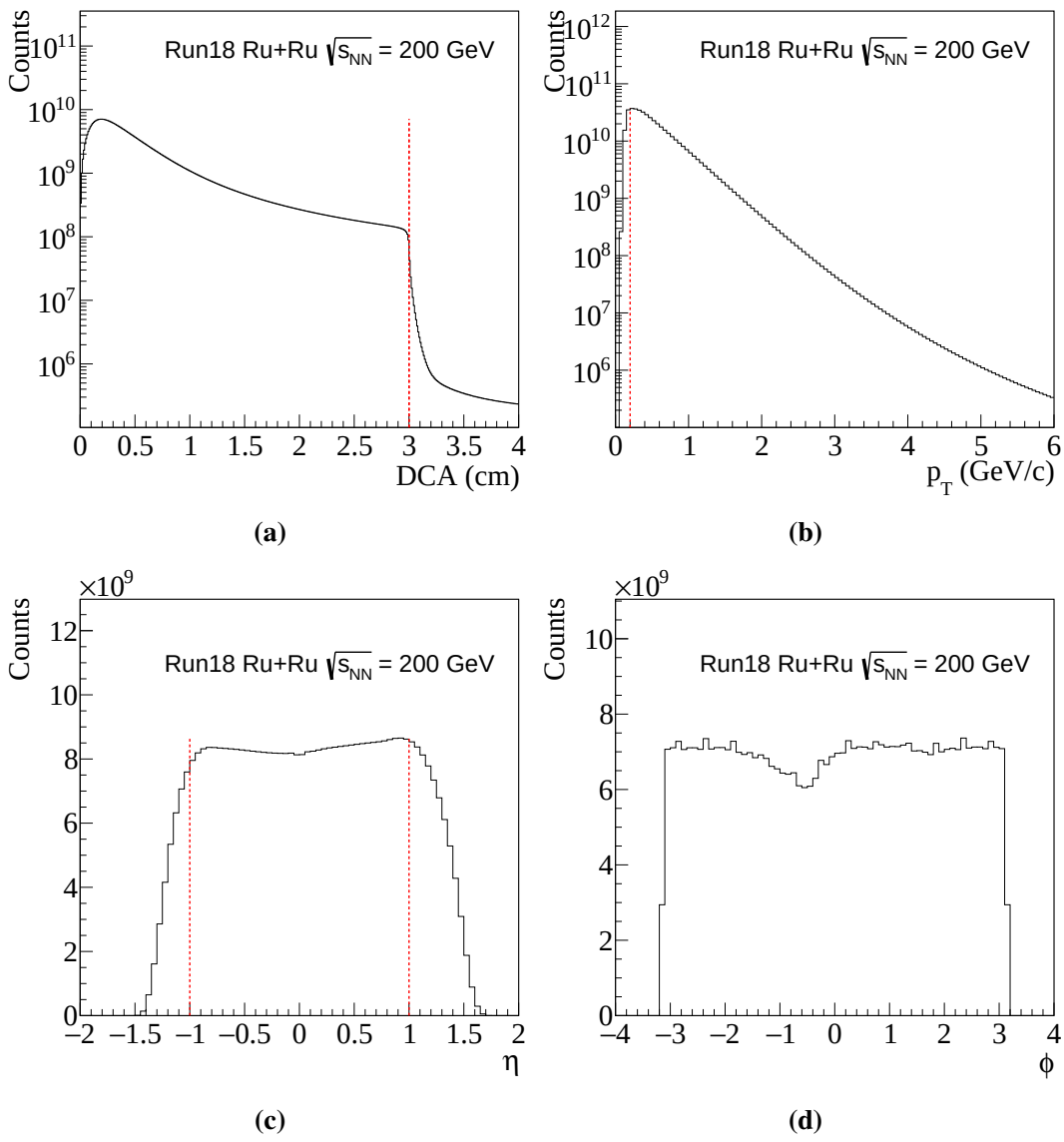
Counts
Run18 Ru+Ru $\sqrt{s_{NN}}$ = 200 GeV
DCA (cm)
(a)
Counts
Run18 Ru+Ru $\sqrt{s_{NN}}$ = 200 GeV
p_T (GeV/c)
(b)
$\times 10^9$
Counts
Run18 Ru+Ru $\sqrt{s_{NN}}$ = 200 GeV
η
(c)
$\times 10^9$
Counts
Run18 Ru+Ru $\sqrt{s_{NN}}$ = 200 GeV
ϕ
(d)

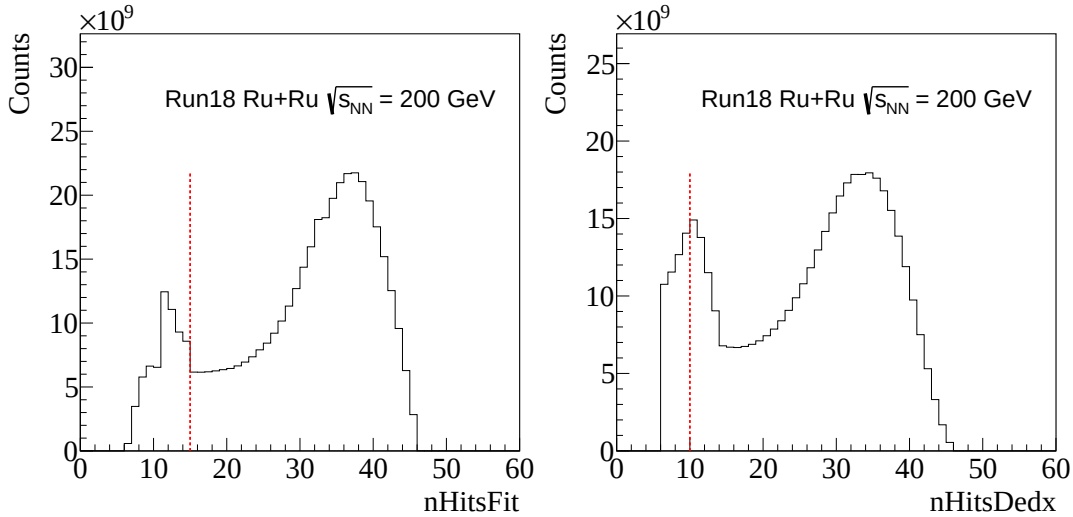

(e) **(f)**

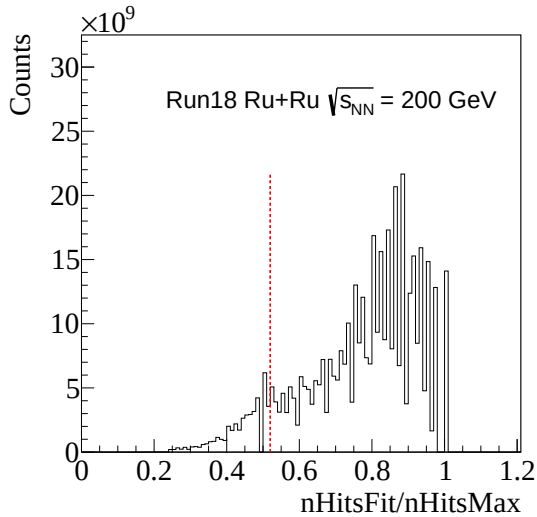

(g)

Figure 3.14 (a) DCA, (b) p_T, (c) η, (d) ϕ, (e) $nHitsFit$, (f) $nHitsDedx$ and (g) $nHitsFit/nHitsDedx$ distributions for primary tracks. Red dashed lines indicate track quality cut values.

Chapter 4 Particle identification and Yield calculation

4.1 Particle identification and signal extraction

To measure the identified particle spectra, one first needs to identify the particles of interest from all the other particles present. At STAR, the ionization energy loss ($\mathrm{d}E/\mathrm{d}x$) measured by TPC and the flight time measured by TOF are used for particle identification. The following sections detail the particle identification methodology utilizing these detectors.

4.1.1 Particle identification by $\mathrm{d}E/\mathrm{d}x$

As charged particles move through the TPC volume, they lose energy by ionizing the gas atoms they interact with. This specific energy loss, denoted as $\mathrm{d}E/\mathrm{d}x$, depends on the velocity of the particle. Consequently, particles of different masses exhibit distinct momentum-dependent behavior of $\mathrm{d}E/\mathrm{d}x$. This property can be used to identify different particle species. The Bethe-Bloch formula describes the ionization energy loss of charged particles in the material, while the more precise Bichsel formula[126] is used for thin materials. By measuring the particles' momenta and $\mathrm{d}E/\mathrm{d}x$, the particle species can be determined by comparing the $\mathrm{d}E/\mathrm{d}x$ to the Bichsel expectation.

Figure 4.1 shows the $\mathrm{d}E/\mathrm{d}x$ distribution vs. rigidity (momentum/charge). Different curves are the Bichsel predictions for various particles, including electrons, pions, kaons, and protons. As shown in the figure, different particles fall within a specific range (band) of $\mathrm{d}E/\mathrm{d}x$ values around their expected values based on the Bichsel function. At momentum around 0.5 GeV/c, the pion and kaon bands begin to overlap. This suggests that the TPC's ability to identify particles becomes limited in this momentum region. The analysis in this thesis identifies pions up to 0.5 GeV/c using TPC because of the overlapping $\mathrm{d}E/\mathrm{d}x$ bands. However, since the pion yield is significantly more than the kaon yield, the TPC alone does not provide sufficient precision for kaon identification even below 0.5 GeV/c and TOF is used starting at 0.25 GeV/c. TPC operates better for proton PID (up to 0.7 GeV/c) because of the proton's greater mass. In analyses, a new variable $n\sigma_x$ (where x denotes various particle kinds like π, K, p, etc.), which is expected to follow the Gaussian distribution, is frequently used. The normalized $n\sigma_x$ is defined in Eq. 4.1:

$$n\sigma_x = \frac{1}{R} \ln \frac{\langle dE/dx \rangle^{measured}}{\langle dE/dx \rangle_x^{Bichsel}}, \tag{4.1}$$

where $\langle dE/dx \rangle^{measured}$ is the measured energy loss, while $\langle dE/dx \rangle_x^{Bichsel}$ is the expected energy loss value predicted by the Bichsel function for a certain particle species x. The $ln(\mathrm{d}E/\mathrm{d}x)$ resolution R depends on the characteristics of each track, such as the number of TPC hits used for the $\mathrm{d}E/\mathrm{d}x$ measurement. The shape of a $n\sigma_x$ distribution for particle species x should be very close to that of a standard Gaussian distribution ($\mu = 0$, $\sigma = 1$).

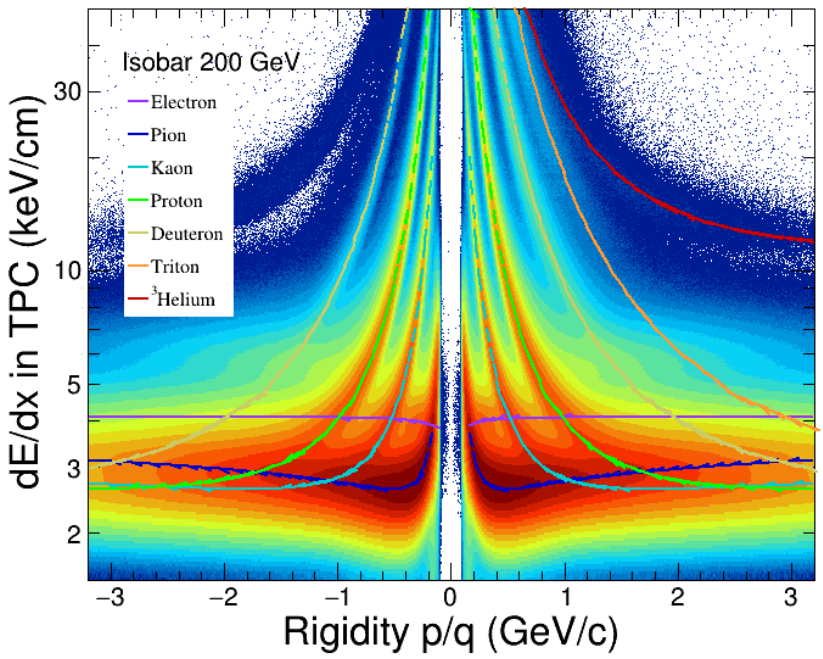

Figure 4.1 The $\mathrm{d}E/\mathrm{d}x$ of particles measured by the TPC vs. rigidity (momentum/electric charge) in isobar collisions at $\sqrt{s_{NN}}$ = 200 GeV. The solid curves are the Bichsel expectations for different particles.

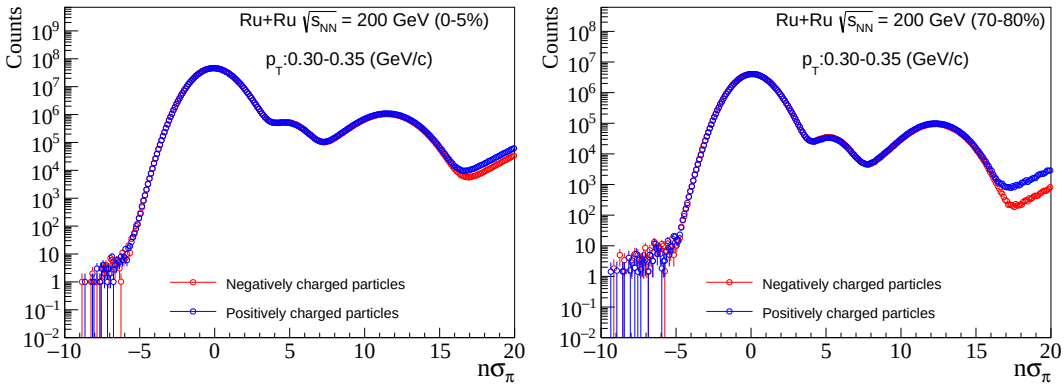

(a) **(b)**

Figure 4.2 (a) $n\sigma_\pi$ distributions for positively and negatively charged particles with $0.30 < p_T < 0.35$ GeV/c in 0-5% most central Ru+Ru collisions at $\sqrt{s_{NN}}$ = 200 GeV. (b) Same as (a) but for peripheral collisions (70-80%).

The μ and σ for each particle species usually deviate from 0 and 1, respectively

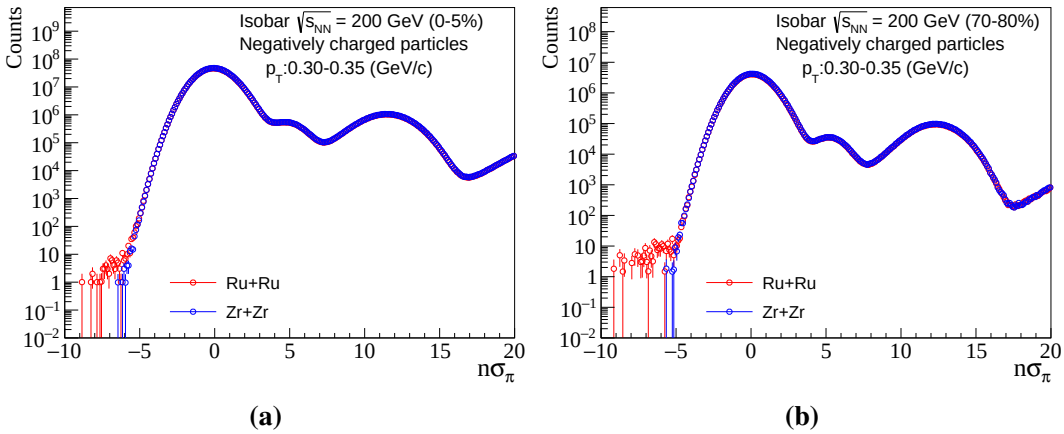

(a) **(b)**

Figure 4.3 **(a) $n\sigma_\pi$ distributions of negatively charged particles in 0-5% most central Ru+Ru and Zr+Zr collisions at $\sqrt{s_{NN}}$ = 200 GeV. (b) Same as (a) but for peripheral collisions (70-80%).**

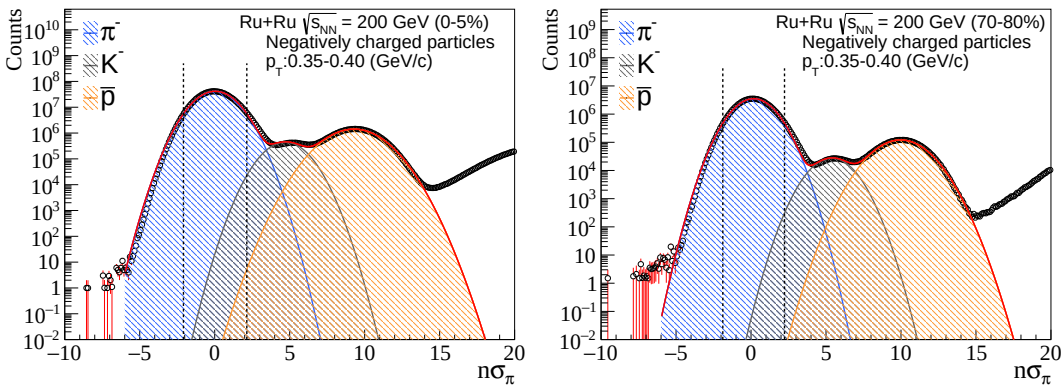

(a) **(b)**

Figure 4.4 **The $n\sigma_\pi$ distribution for the range of $0.35 < p_T < 0.4$ GeV/c in both 0-5% (a) and 70-80% (b) centrality intervals for Ru+Ru collisions at $\sqrt{s_{NN}}$ = 200 GeV. The red curves represent the fitting functions, while the shaded areas in blue, grey, and orange represent the contributions from pion, kaon, and proton, respectively.**

due to imperfect calibration. Their values in each p_T bin are extracted by performing a multi-Gaussian fit to the $n\sigma_x$, with a rapidity selection of $|y_x| < 0.5$, where y_x is calculated using the mass of the particle of interest. One Gaussian function describes the particle of interest while the other two represent the background. The raw yield is determined using the bin counting method. This involves integrating the $n\sigma_x$ distribution within a range of $(-2\sigma, 2\sigma)$, and then correcting for the counting efficiency defined as $\frac{\int_{-2\sigma}^{2\sigma} f(n\sigma_x)dn\sigma_x}{\int_{-\infty}^{\infty} f(n\sigma_x)dn\sigma_x}$, where $f(n\sigma_x)$ represents the Gaussian fit function for the particle species under study. σ denotes the width of $f(n\sigma_x)$, and the counting range $(-2\sigma, 2\sigma)$ is slightly adjusted if they do not coincide with the bin boundaries. The background is estimated using the other two Gaussian functions integrated over the same counting range and is subsequently subtracted from the raw yield value.

The bin counting method relies on accurate μ and σ values derived from fits to set

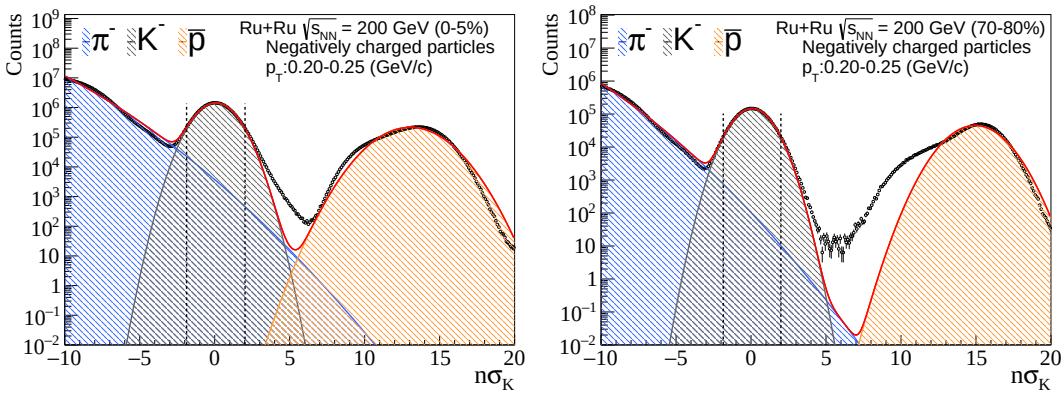

(a) **(b)**

Figure 4.5 The $n\sigma_K$ distribution for the range of $0.20 < p_T < 0.25$ GeV/c in both 0-5% (a) and 70-80% (b) centrality intervals for Ru+Ru collisions at $\sqrt{s_{NN}}$ = 200 GeV. The red curves represent the fitting functions, while the shaded areas in blue, grey, and orange represent the contributions from pion, kaon, and proton, respectively.

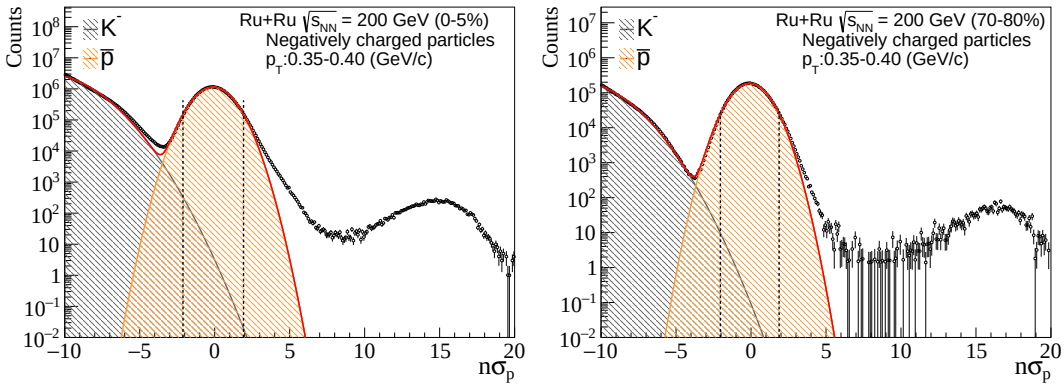

(a) **(b)**

Figure 4.6 The $n\sigma_p$ distribution for the $0.35 < p_T < 0.40$ GeV/c range in both 0-5% (a) and 70-80% (b) centrality intervals for Ru+Ru collisions at $\sqrt{s_{NN}}$ = 200 GeV. The red curves represent the fitting functions, while the shaded areas in grey, and orange represent the contributions from kaon and proton, respectively.

the integration window appropriately and evaluate the counting efficiency. The fitting quality relies on the initial parameters provided to the fit functions when the peaks in the $n\sigma_\pi$ distribution start to merge as p_T increases. To address this, the width parameters set at higher p_T are extrapolated from their values determined at low p_T regions, where the peaks of pions, kaons, and protons are distinctly separated, and thus the extraction of the width parameters is reliable. This allows for extraction and analysis of particle yields in various centrality classes and p_T ranges.

To reduce uncertainties arising from differences in fitting, it is advantageous to use the same parameters for the fit functions for positively and negatively charged particles, as well as for Ru+Ru and Zr+Zr collisions. In this context, it is important to compare the shape of the $n\sigma_x$ distributions between different charges and collision systems within the

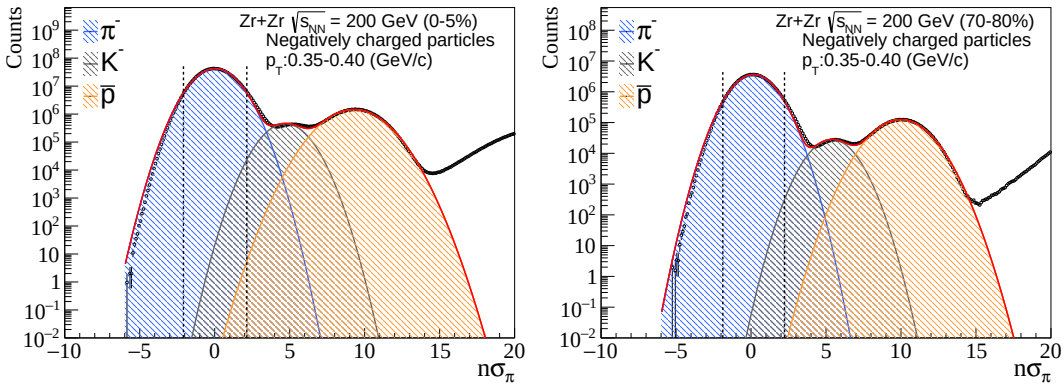

(a) **(b)**

Figure 4.7 Same as Fig. 4.4, but for Zr+Zr collisions at $\sqrt{s_{NN}}$ = 200 GeV.

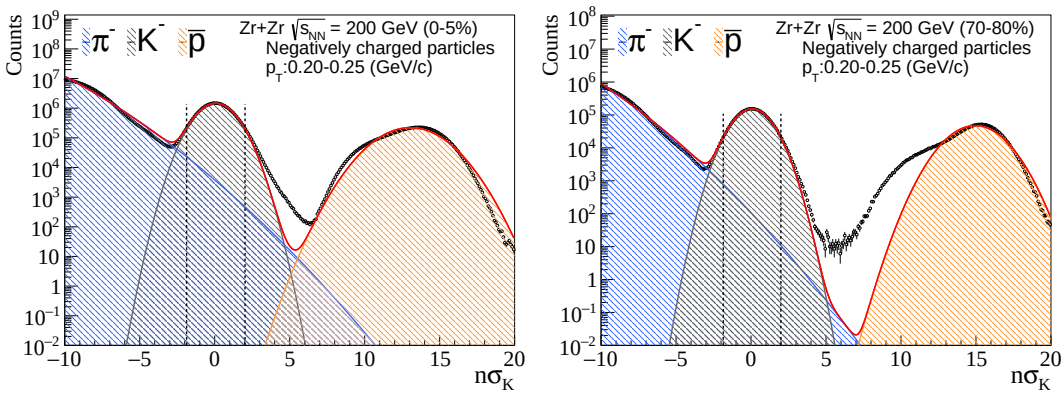

(a) **(b)**

Figure 4.8 Same as Fig. 4.5, but for Zr+Zr collisions at $\sqrt{s_{NN}}$ = 200 GeV.

same p_T range. To draw a comparison of the $n\sigma_\pi$ distribution between different charges in both central and peripheral Ru+Ru collisions, Fig. 4.2 is presented. The main peaks of pion, kaon, and proton agree well for positive and negative particles. Furthermore, Fig. 4.3 illustrates the comparison of the $n\sigma_\pi$ distribution between Ru+Ru and Zr+Zr collisions for negatively charged particles. Notable similarities in the pion, kaon, and proton peaks can be observed. Consequently, once $n\sigma_x$ distributions for the negatively charged particles in Ru+Ru collisions are fitted, their mean and width parameters are utilized to fix those in the multi-Gaussian fits for positively charged particles in Ru+Ru collisions as well as for particles of both charges in Zr+Zr collisions.

The multi-Gaussian fits to $n\sigma_\pi$, $n\sigma_K$, and $n\sigma_p$ distributions for both 0-5% central and 70-80% peripheral Ru+Ru (Zr+Zr) collisions are shown as red curves in Fig. 4.4 (Fig. 4.7), Fig. 4.5 (Fig. 4.8), and Fig. 4.6 (Fig. 4.9), respectively. The contributions from pion, kaon, and proton are represented by shaded areas in blue, grey, and orange, respectively. The $n\sigma_\pi$ distribution for 0-5% central Zr+Zr collisions at $0.50 < p_T < 0.55$ GeV/c is shown in Fig. 4.10, where the multi-Gaussian fit indi-

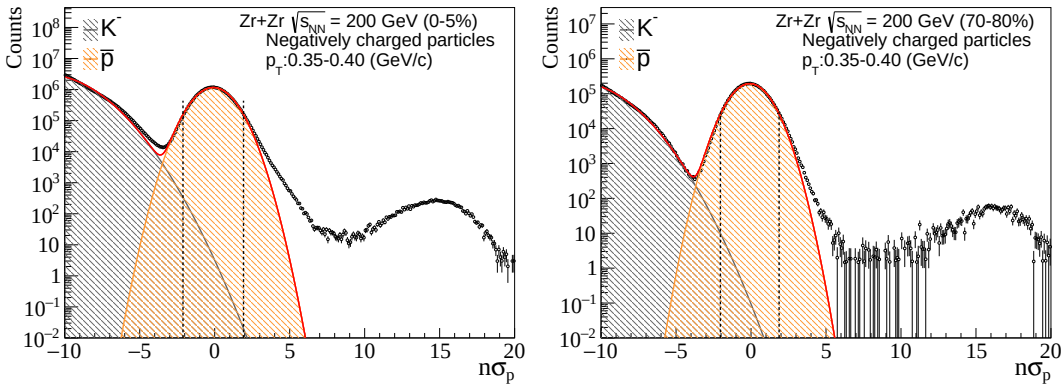

(a) **(b)**

Figure 4.9 Same as Fig. 4.6, but for Zr+Zr collisions at $\sqrt{s_{NN}}$ = 200 GeV.

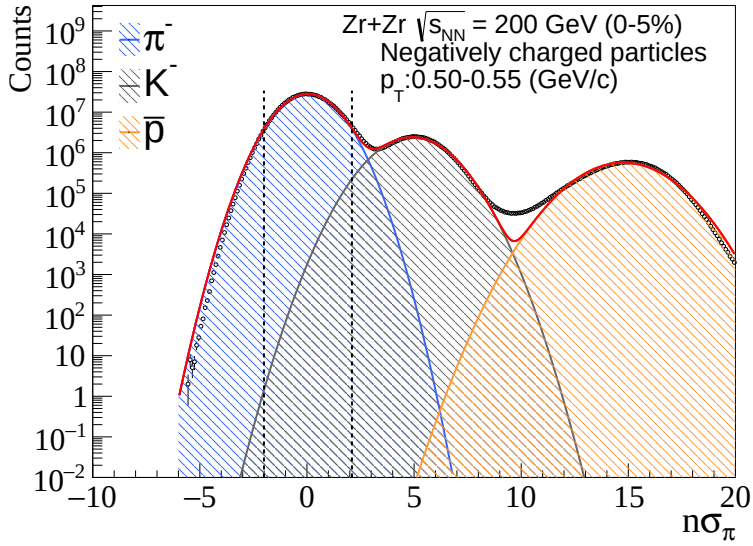

Figure 4.10 The $n\sigma_\pi$ distribution for $0.50 < p_T < 0.55$ GeV/c, in 0-5% central Zr+Zr collisions at $\sqrt{s_{NN}}$ = 200 GeV. The red curves represent the fitting functions, while the shaded areas in grey, and orange represent the contributions from kaon and proton, respectively.

cates that the overlapping region of pion and kaon peaks is significant. Therefore, TOF information is used for kaon identification starting from 0.25 GeV/c, as aforementioned.

4.1.2 Particle identification by m^2

As mentioned earlier, the PID capability of the TPC is limited to low momenta. Employing time of flight information from the TOF detector allows for the extension of particle identification to relatively higher momenta. To extract raw yields utilizing the TOF detector, the mass-square (m^2) variable is commonly used. As previously mentioned, the m^2 can be calculated utilizing Eq. 2.2. The m^2 distribution vs. rigidity is shown in Figure 4.11, where distinct bands for $\pi^-(\pi^+)$, $K^-(K^+)$, and $\bar{p}(p)$ are visible, even at higher p_T. The black dashed lines correspond to the expected m^2 values of pions, kaons, and protons.

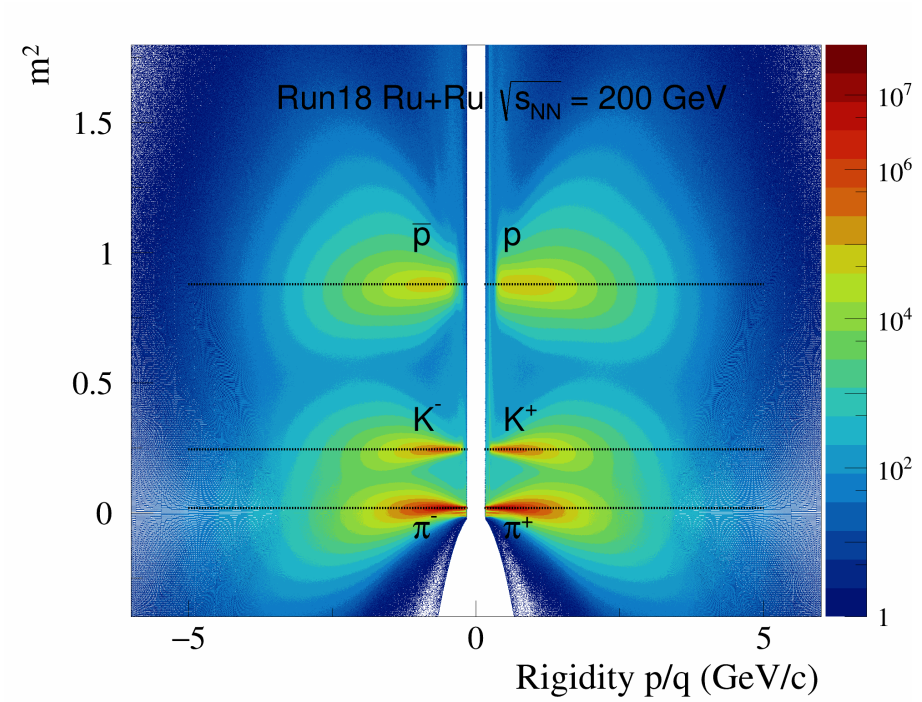

Figure 4.11 Mass-square (m^2) vs. rigidity (momentum/electric charge) in isobar collisions at $\sqrt{s_{NN}}$ = 200 GeV. The dashed lines represent the expected m^2 values for different particles[127].

The yields of $\pi^-(\pi^+)$, $K^-(K^+)$, and $\bar{p}(p)$ are obtained from the simultaneous fit of the m^2 distribution using a multi-Students't function, which is shown in Eq. 4.2.

$$\begin{aligned} f(x) = A_\pi \times & \frac{\Gamma(\frac{\nu_\pi+1}{2})}{\sqrt{\nu_\pi \pi}\Gamma(\frac{\nu_\pi}{2})\sigma_\pi}(1+\frac{((x-\mu_\pi)/\sigma_\pi)^2}{\nu_\pi})^{-(\nu_\pi+1)/2} \\ + A_K \times & \frac{\Gamma(\frac{\nu_K+1}{2})}{\sqrt{\nu_K K}\Gamma(\frac{\nu_K}{2})\sigma_K}(1+\frac{((x-\mu_K)/\sigma_K)^2}{\nu_K})^{-(\nu_K+1)/2} \\ + A_p \times & \frac{\Gamma(\frac{\nu_p+1}{2})}{\sqrt{\nu_p p}\Gamma(\frac{\nu_p}{2})\sigma_p}(1+\frac{((x-\mu_p)/\sigma_p)^2}{\nu_p})^{-(\nu_p+1)/2}, \end{aligned} \tag{4.2}$$

where the parameters A, μ, ν, and σ represent the normalization factor, peak position, degrees of freedom, and width, respectively. The subscripts π, K, and p indicate different particle species.

Figure 4.12 compares the m^2 distribution for positively and negatively charged particles in both central and peripheral Ru+Ru collisions, while Fig. 4.13 compares the negatively charged particle m^2 distribution between Ru+Ru and Zr+Zr collisions. In these distributions, the peak centered around 0 represents pions, the one centered around 0.2 represents kaons, and the one centered around 0.8 signifies protons (anti-protons). As both figures demonstrate, the pion, kaon, and proton peaks in the m^2 distributions maintain similar shapes across different charges and collision systems. Therefore, similar to

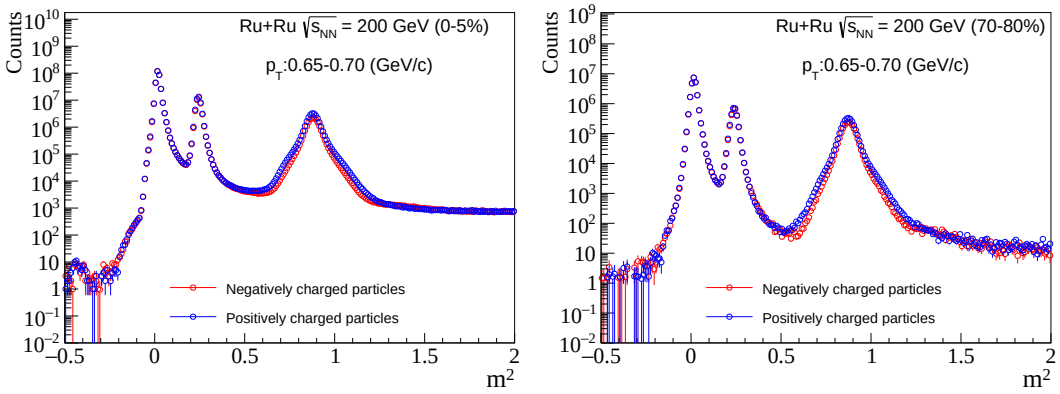

(a) **(b)**

Figure 4.12 (a) The m^2 distribution comparison between positively and negatively charged particles in most central collisions (0-5%), at $0.65 < p_T < 0.70$ GeV/c, of Ru+Ru collisions at $\sqrt{s_{NN}}$ = 200 GeV. (b) The same comparison in peripheral collisions (70-80%).

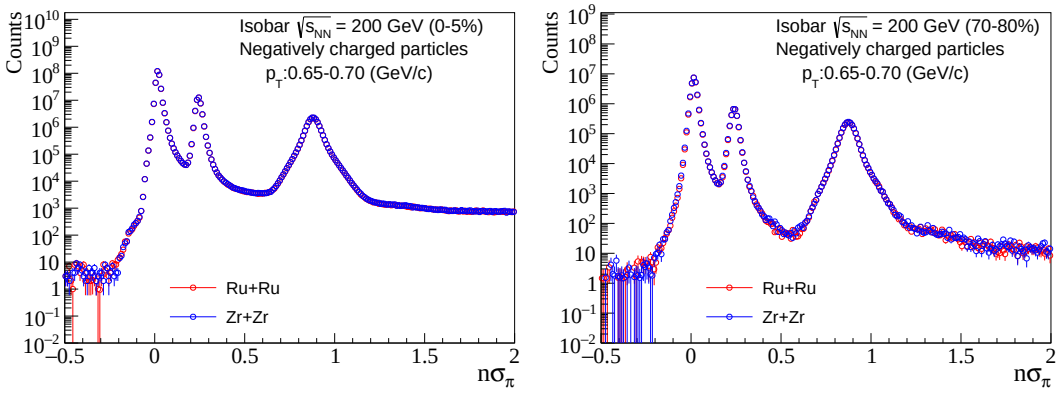

(a) **(b)**

Figure 4.13 (a) The m^2 distribution comparison of negatively charged particles between Ru+Ru and Zr+Zr collisions in most central collisions (0-5%), at $0.65 < p_T < 0.7$ GeV/c. (b) The same comparison in peripheral collisions (70-80%).

the fitting procedure used for $n\sigma_x$ distributions, after fitting the m^2 distribution for negatively charged particles in Ru+Ru collisions, the peak positions, widths, and degrees of freedom of the π^-, K^- and $\bar{p}$ peaks are utilized to fix the corresponding parameters in the fitting for π^+, K^+ and p in Ru+Ru collisions as well as for particles of both charges in Zr+Zr collisions.

The multi-students' t fits to m^2 distributions for both central (0-5%) and peripheral (70-80%) Ru+Ru and Zr+Zr collisions are shown as red curves in Fig. 4.14 and Fig. 4.15, respectively. The contributions from pion, kaon, and proton are represented by shaded areas in blue, grey, and orange.

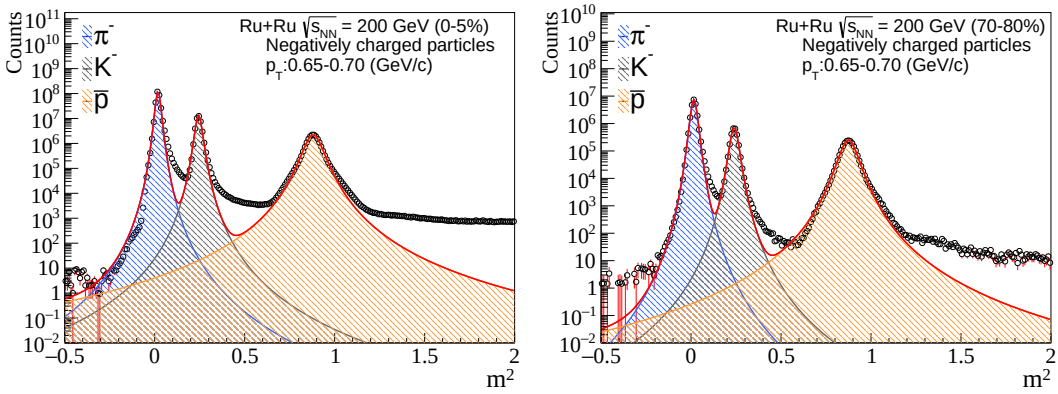

(a) (b)

Figure 4.14 The m^2 distribution for the $0.65 < p_T < 0.70$ GeV/c range in both 0-5% (a) and 70-80% (b) centrality intervals for Ru+Ru collisions at $\sqrt{s_{NN}}$ = 200 GeV. The red curves represent the fitting functions, while the shaded areas in blue, grey, and orange represent the contributions from pion, kaon, and proton, respectively.

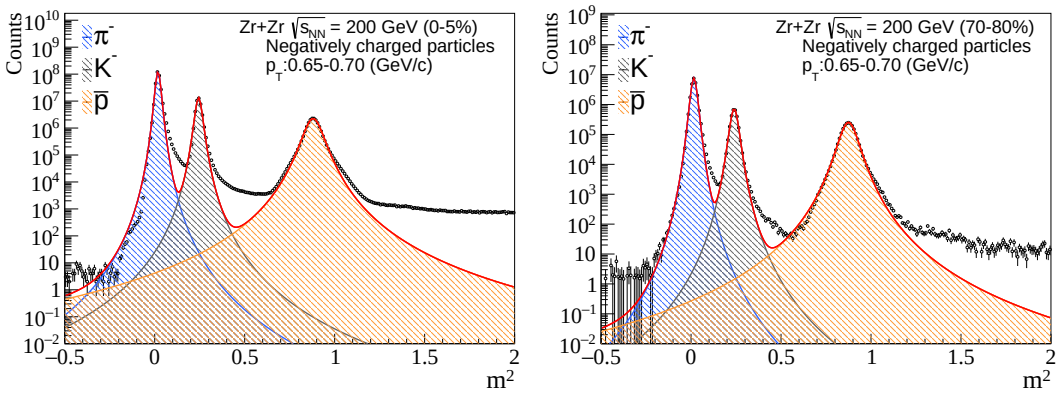

(a) (b)

Figure 4.15 Same as Fig. 4.14, but for Zr+Zr collisions.

4.1.3 Uncorrected p_T spectra

The raw yields of $\pi^+(\pi^-)$, $K^+(K^-)$, p, and $\bar{p}$ can be represented mathematically using the equation 4.3.

$$\frac{d^2N_{raw}}{2\pi p_T dp_T dy} = \frac{1}{N_{events}} \frac{N_{raw}}{2\pi p_T \Delta p_T \Delta y}, \tag{4.3}$$

where N_{events} represents the number of events within a specific centrality interval, N_{raw} is the particle yield within a certain p_T and centrality interval, Δp_T is the p_T interval and $\Delta y = 1$. Figures 4.16 and 4.17 depict the raw yields for $\pi^+(\pi^-)$, $K^+(K^-)$ and $p(\bar{p})$ as a function of p_T at mid-rapidity ($|y| < 0.5$) in Ru+Ru and Zr+Zr collisions, respectively, across nine distinct centrality intervals, ranging from 0-5% to 70-80%. The pion spectra display a pronounced drop around 0.5 GeV/c, while the proton spectra, similar drops are noticed at around 0.25 and 0.7 GeV/c, respectively. This distinct feature can be attributed to the impact of TOF utilized in the analysis. At lower momenta, the TOF

matching efficiency is around 70%, leading to the observed drop in the spectra. The p_T coverage of the spectra for different particles is determined by the detector capability. The pion spectra coverage ranges from 0.20 to 2.50 GeV/c, whereas the kaon spectra have a slightly narrower coverage, ranging from 0.30 to 2.5 GeV/c. Protons, being heavier particles, have a different spectral shape and are measured over the p_T range from 0.50 to 2.50 GeV/c.

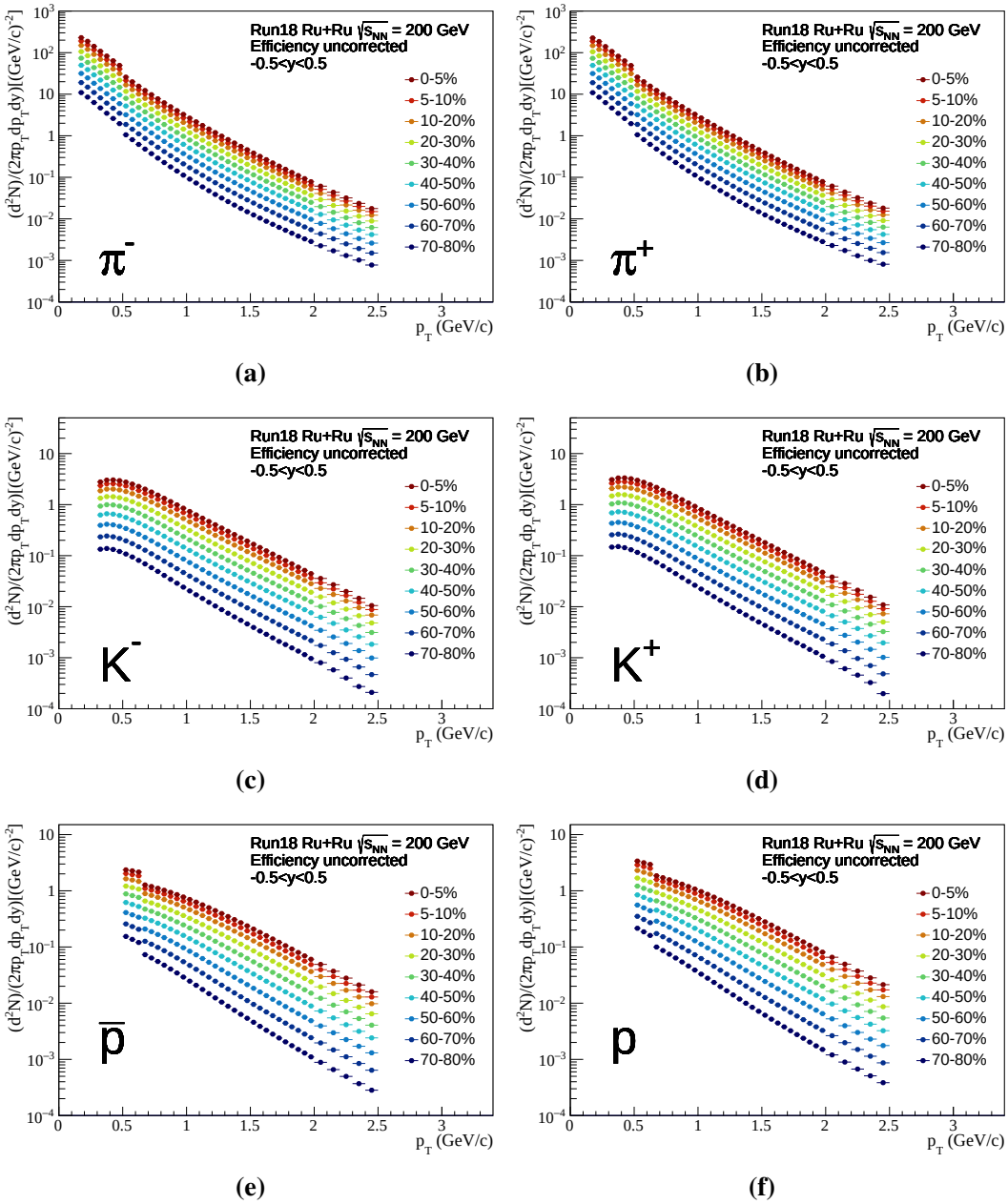

Figure 4.16 Uncorrected p_T spectra for $\pi^-(\pi^+)$, $K^-(K^+)$ and $\bar{p}(p)$ within $|y| < 0.5$ in different centrality intervals of 200 GeV Ru+Ru collisions. Error bars around the data points, smaller than the marker size, represent statistical errors.

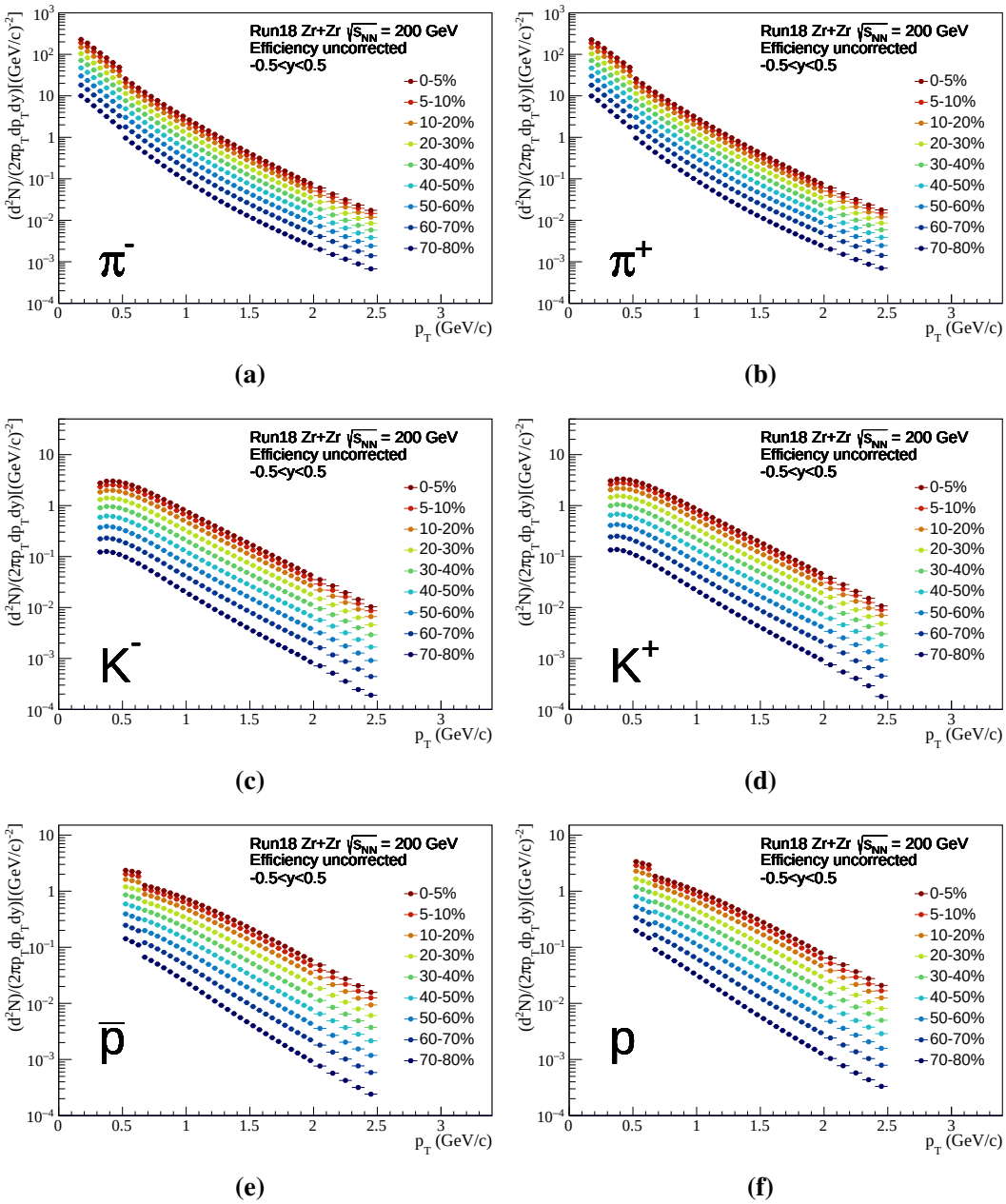

Figure 4.17 Same as Fig. 4.16, but for Zr+Zr collisions.

4.2 Corrections

Real-life detectors have finite acceptance, resolution, and efficiency, which need to be corrected for in the measurements of identified particle spectra and yields. The main detectors used in this analysis are the TPC and TOF. The combined correction factors can be expressed as the following:

$$\epsilon_{\text{Total}} = \epsilon_{\text{TPC}} \times \epsilon_{\text{TOF}}. \tag{4.4}$$

In the low p_{T} region, where TOF is not used, $\epsilon_{\text{TOF}} = 100\%$. The correction procedure for protons is different from that for pions and kaons. There are protons present in detector material and beam pipe which can be knocked out by particles produced in collisions.

These knock-out protons also contribute to the measured proton yields and need to be subtracted. Hence, the total correction factor for protons is shown as follows.

$$\epsilon_{\mathrm{TotalProton}} = \epsilon_{\mathrm{TPC}} \times \epsilon_{\mathrm{TOF}} \times \epsilon_{\mathrm{Knock-out}}. \tag{4.5}$$

The TPC correction factors (ϵ_{TPC}) include the TPC acceptance, tracking efficiency, momentum resolution, and energy loss, all of which are obtained using the Monte-Carlo embedding technique. On the other hand, the TOF matching efficiency (ϵ_{TOF}) and the knock-out proton background fraction ($\epsilon_{\mathrm{Knock-out}}$) are extracted using a data-driven method.

4.2.1 Monte-Carlo embedding at STAR

The embedding technique is used in STAR to study the TPC response. Monte-Carlo (MC) tracks of known species are generated with uniform p_{T}, η, and ϕ distributions using the so-called single-particle gun. The uniform kinematic distributions are used in order to maintain similar statistical precision across all p_{T}, η, and ϕ bins. If one would follow the particle's natural spectrum which falls steeply with increasing p_{T}, the probability to generate high-p_{T} tracks will be too small to achieve sufficient precision to be comparable or better than real data. To rectify this, a p_{T} weighting factor is applied, which adjusts the generated spectra to more accurately reflect reality.

After generation, these MC tracks are propagated through a simulated representation of the STAR detector using GEANT3[128-129], a simulation software designed to mimic the interactions of particles with matter. To generate detailed TPC information at the pad level, a TPC Response Simulator (TRS)[130] is employed. The TRS accounts for all TPC resolution effects, from electron transport within the gas to signal processing in the readout electronics. Subsequently, these MC tracks are embedded into real data at the raw detector signal level. The mixed data are processed using the standard STAR algorithm to produce reconstructed (RC) tracks, as for the real data. To avoid a significant impact on the TPC occupancy which dictates the tracking efficiency, the fraction of embedded MC tracks is capped at 5% of the event multiplicity. To evaluate the detector response, a map between MC and RC tracks is built, with the criteria of requiring more than 50% of the hits used to reconstruct a RC track to be from the matched MC track. There could be the case that more than one RC track is matched to the same MC track due to the track splitting. Those RC tracks are also included in the matching map since such cases could also happen in real data.

4.2.2 TPC related correction factors

TPC related corrections can be divided into two parts as the following:

$$\epsilon_{\mathrm{TPC}} = \epsilon_{\mathrm{Tracking}} \times \epsilon_{\mathrm{EnergyLoss}}, \tag{4.6}$$

where $\epsilon_{\mathrm{Tracking}}$ includes the TPC acceptance and track finding efficiency, while $\epsilon_{\mathrm{EnergyLoss}}$ accounts for momentum resolution and energy loss. Unless specified, the term "tracking efficiency" includes the effects of both the TPC acceptance and the track finding efficiency.

The tracking efficiency is defined as the fraction of MC tracks that can be matched to RC tracks passing all track quality cuts, as illustrated by Eq. 4.7:

$$\epsilon_{\mathrm{Tracking}} = \frac{dN^{\mathrm{MC(matched)}}/dp_{\mathrm{T}}}{dN^{\mathrm{MC(input)}}/dp_{\mathrm{T}}}. \tag{4.7}$$

Because of their similar masses, muons from pion decays can be potentially misidentified as primary pions originating from the collision vertex. Since these decaying primary pions are part of the pion yield we aim to measure, the misidentified muons are also included in RC tracks when calculating the tracking efficiency for pions.

The resulting TPC tracking efficiencies for negatively and positively charged particles as a function of MC p_{T} in 10-20% central Ru+Ru collisions are shown in Figs. 4.18 and 4.19, respectively. The error bar on each data point stands for the statistical error, which is calculated based on the Bayesian method since in the tracking efficiency definition the numerator is a subset of the denominator[131].

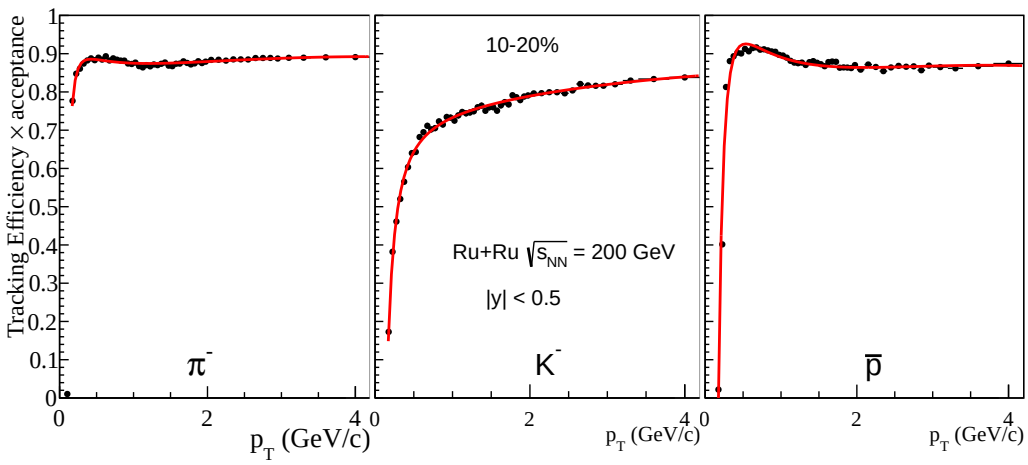

Figure 4.18 Tracking efficiency for π^-, K^- and $\bar{p}$ within $|y| < 0.5$ in 10-20% Ru+Ru collisions at $\sqrt{s_{\mathrm{NN}}}$ = 200 GeV. The solid curves are fits to the distributions.

To minimize the statistical fluctuations of the efficiency, the tracking efficiencies are fitted with a polynomial function given by $\epsilon_{\mathrm{Tracking}} = p0 + p1 \times p_{\mathrm{T}}^2 + p2 \times p_{\mathrm{T}} +$

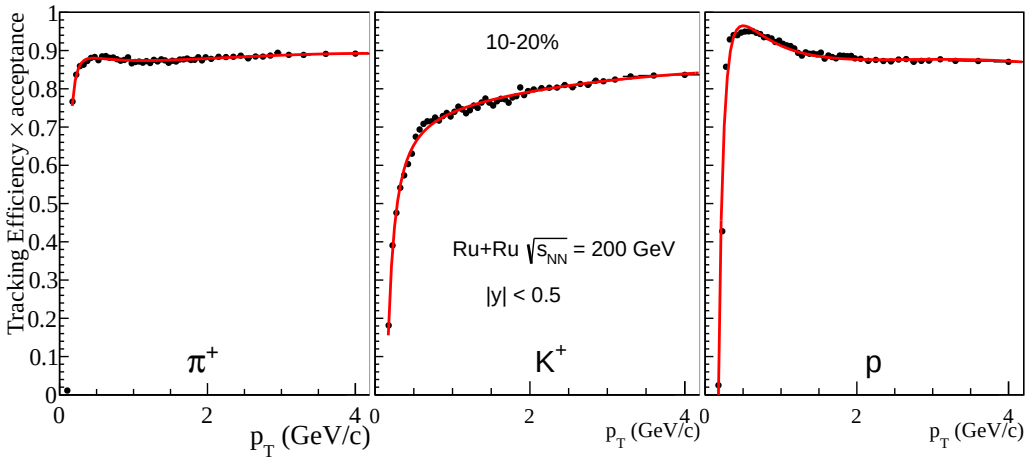

Figure 4.19 Tracking efficiency for π^+, K^+ and p within $|y| < 0.5$ in 10-20% Ru+Ru collisions at $\sqrt{s_{NN}}$ = 200 GeV. The solid curves are fits to the distributions.

$p3 \times p_T^{-1} + p4 \times p_T^{-2}$, where $p0$, $p1$, $p2$, $p3$, and $p4$ are free parameters. The fit results are shown as red curves in Figs. 4.18 and 4.19. The 68% confidence interval from fitting is used as the statistical uncertainty which is smaller than the line width shown in the figures.

Comparing the distributions in Fig. 4.18 and Fig. 4.19, one can see that the tracking efficiencies for positively and negatively charged particles of the same species are quite similar. It is also worth noting that the tracking efficiency for kaons is much smaller than that of pions at low p_T and has a much slower turn-on curve, which is attributable to kaon decays. Furthermore, the tracking efficiency for anti-protons is smaller than that of protons at low p_T due to the annihilation process.

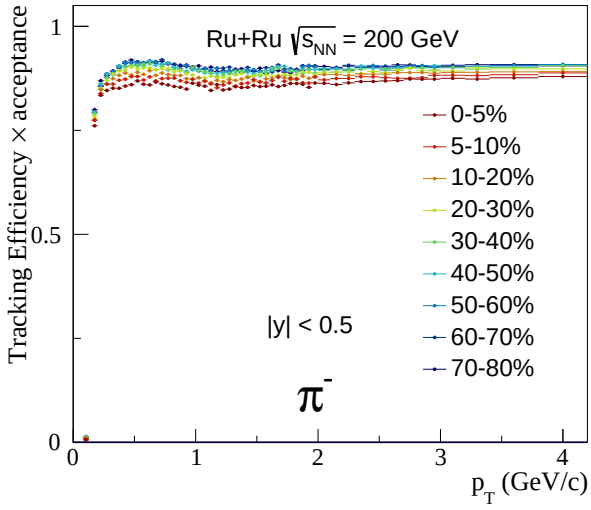

Figure 4.20 Comparison of the tracking efficiency for π^- within $|y| < 0.5$ in different centrality intervals. The error bars indicate the statistical uncertainties.

Figure 4.20 shows a comparison of the π^- tracking efficiency for different cen-

trality classes in Ru+Ru collisions. The efficiency increases from central to peripheral collisions, which is consistent with the expected impact of the TPC occupancy, *i.e.*, the smaller multiplicity in peripheral collisions leads to a lower TPC occupancy and thus a higher tracking efficiency.

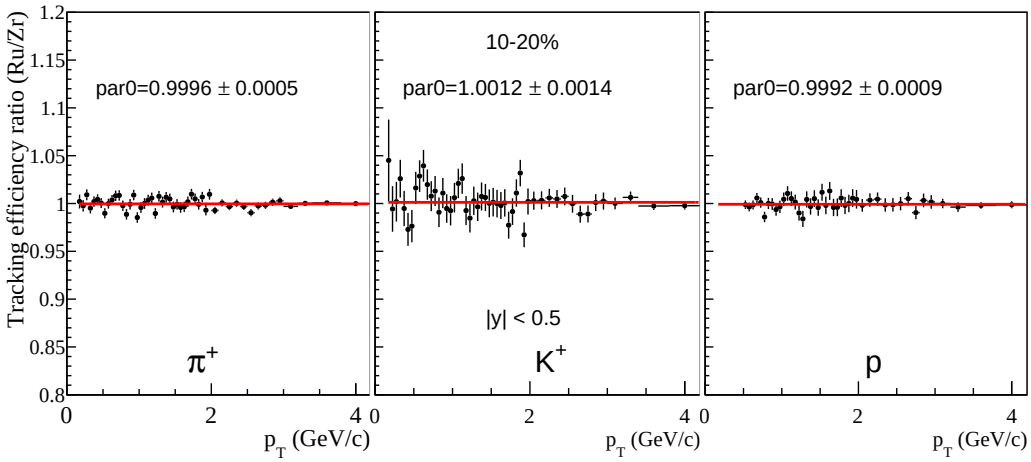

Figure 4.21 The tracking efficiency ratios of π^+_{Ru}/π^+_{Zr}, K^+_{Ru}/K^+_{Zr} and p_{Ru}/p_{Zr} for 10-20% centrality within $|y| < 0.5$. Error bars represent statistical uncertainties. The red lines are fitting results to the ratios with a zeroth-order polynomial function.

The tracking efficiencies in Ru+Ru and Zr+Zr collisions are also compared to check their consistency. Figure 4.21 shows the tracking efficiency ratios of Ru+Ru over Zr+Zr collisions for π^+, K^+ and p. A constant is used to fit the ratios, and the fitting results are consistent with unity, which indicates that the tracking efficiencies in the two collision systems are consistent. This is in line with the expectation since the beam conditions of the two collision systems were kept as identical as possible during data taking. Nevertheless, the tracking efficiency corrections are still evaluated and applied separately for the analyses of Ru+Ru and Zr+Zr events.

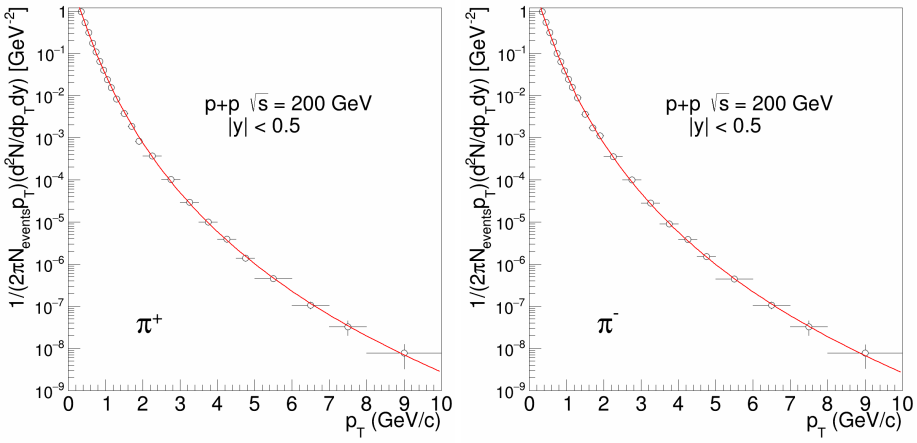

(a) **(b)**

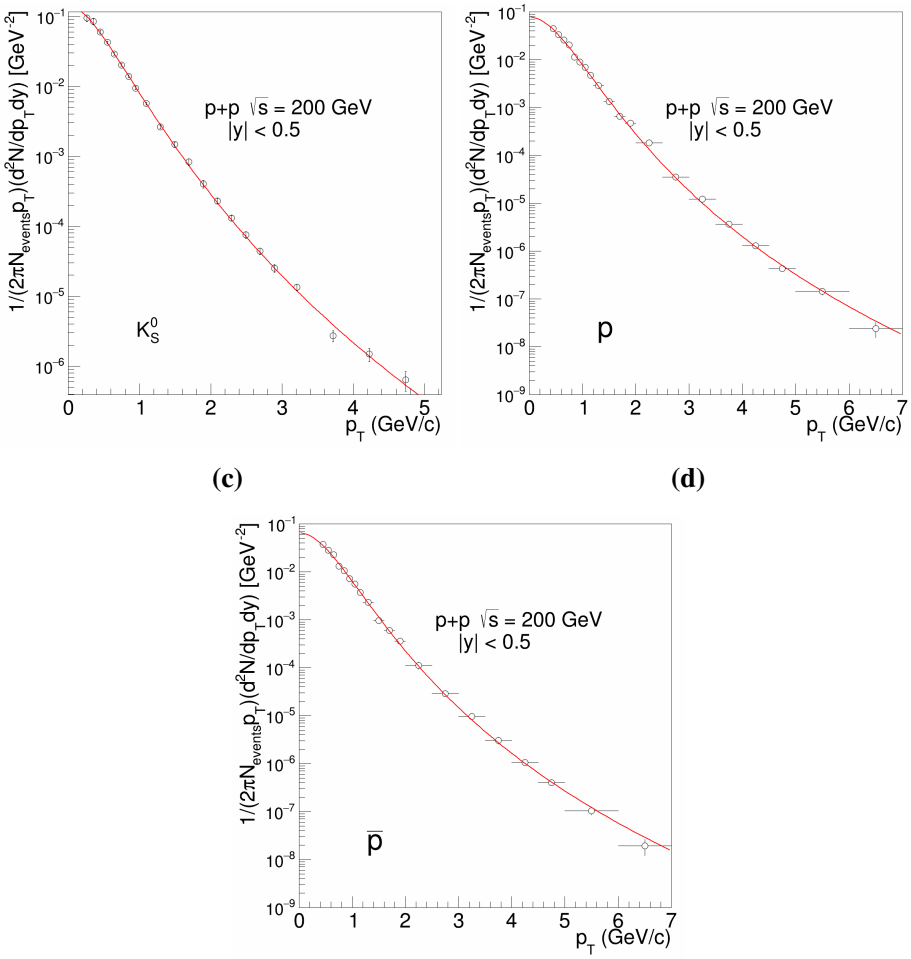

(c) (d)

(e)

Figure 4.22 Lévy fits to particle spectra in p+p collisions at $\sqrt{s}$ = 200 GeV[132-133]. The open circles are the data points and the red curves represent the fitting results.

The second part of the correction regards the energy loss and momentum resolution. Charged particles can lose energy in the detector material via scattering and ionization when passing through them. Since the reconstructed momentum refers to what a particle possesses at the collision vertex, those energy losses need to be accounted for. In the track reconstruction algorithm, such energy losses are evaluated and corrected for assuming pion mass since their identities are not known beforehand. However, particles with larger mass at low p_T are expected to lose more energy[134] than those of smaller mass. Therefore, this correction scheme of assuming pion mass results in a large discrepancy of the reconstructed momentum with respect to the true value for heavy particles at low p_T. Additional corrections are needed to account for the residual energy loss. Furthermore, the finite resolution of the reconstructed momentum, which can alter the measured spectrum shape, also needs to be taken into account in the spectrum analysis.

In former STAR analyses[9], the energy loss correction factor is evaluated as the

p_{T} difference between matched RC and MC tracks, $p_{\mathrm{T}}^{\mathrm{RC}} - p_{\mathrm{T}}^{\mathrm{MC}}$, as a function of $p_{\mathrm{T}}^{\mathrm{RC}}$, where $p_{\mathrm{T}}^{\mathrm{RC}}$ is the RC track p_{T}. No additional correction factor is applied to account for the finite momentum resolution, even though its effect is expected to be small at low p_{T}. Nevertheless, in this analysis, the correction factor is defined as a ratio shown in Eq. 4.8:

$$\epsilon_{\mathrm{EnergyLoss}} = \frac{dN/dp_{\mathrm{T}}^{\mathrm{RC(reconstructed)}}}{dN/dp_{\mathrm{T}}^{\mathrm{MC(reconstructed)}}}, \tag{4.8}$$

which includes the effects from both the residual energy loss and finite momentum resolution.

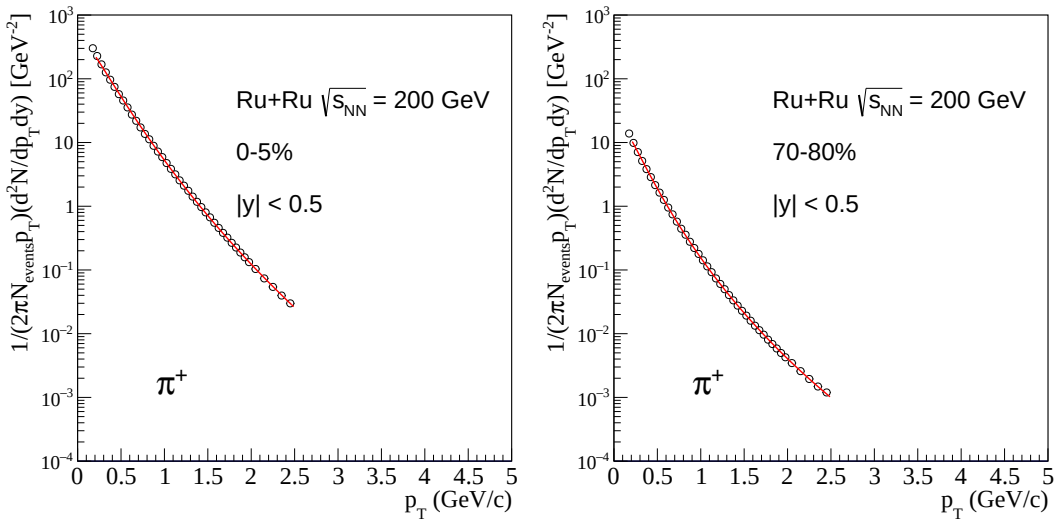

(a) **(b)**

Figure 4.23 Lévy fits to π^+ spectra in 0-5% and 70-80% Ru+Ru collisions at $\sqrt{s_{\mathrm{NN}}}$= 200 GeV. The open circles are data points and the red curves represent the fitting results.

Since the energy loss correction, as defined by Eq. 4.8, depends on the spectrum shape and as aforementioned a flat p_{T} distribution is used in the embedding to enhance the statistics at high p_{T}, ideally one needs to use the true spectrum shapes for different particle species in isobar collisions to weight the embedding sample. However, these true distributions are to be measured and are not readily available. Instead, the $\pi^+(\pi^-)$, K_s^0 and $p(\bar{p})$ spectra in p+p collisions at the same center-of-mass energy of $\sqrt{s}$ = 200 GeV[132-133] are used. Here, the K_s^0 spectra are used as a substitution for $K^+(K^-)$ spectra. These p_{T} spectra are parameterized using the Lévy function[135-136], defined as:

$$\frac{d^2N}{2\pi p_{\mathrm{T}} dp_{\mathrm{T}} dy} = \frac{dN}{dy}\frac{(n-1)(n-2)}{nC(nC+m_0(n-2))}(1+\frac{m_T-m_0}{nC})^{-n}, \tag{4.9}$$

and the fitting results are shown in Fig. 4.22. The m_0 in Eq. 4.9 is the rest mass of particle, while m_T is the transverse mass, defined as $m_T = \sqrt{p_{\mathrm{T}}^2 + m_0^2}$. To account for the fact that non-ideal spectrum shapes are used, an iterative procedure is employed. After

obtaining the spectra in isobar collisions with energy loss corrections extracted using spectrum shape in p+p collisions, these spectra are fitted using a Lévy function. Figure 4.23 shows the examples of Lévy fits to the π^+ spectra in both central and peripheral Ru+Ru collisions. Subsequently, the energy loss correction is recalculated using the fits to the spectra in isobar collisions, and this process is continued until the isobar spectra reach convergence.

Figure 4.24 shows the energy loss correction factors, evaluated in the first iteration using p+p spectrum shape, as a function of p_T for protons within $|y| < 0.5$ in different centrality intervals of 200 GeV Ru+Ru collisions. No significant centrality dependence is seen, and therefore statistics from all centrality bins are combined for evaluating the energy loss correction factors, which are used for individual centrality classes.

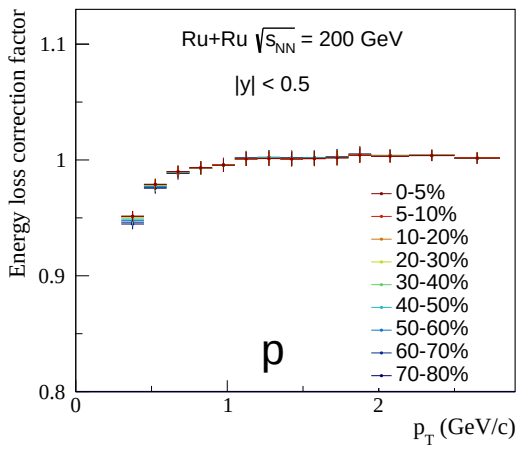

Figure 4.24 Energy loss correction factors as a function of p_T for protons within $|y| < 0.5$ in different centrality intervals of 200 GeV Ru+Ru collisions. Error bars around the data points represent statistical uncertainties.

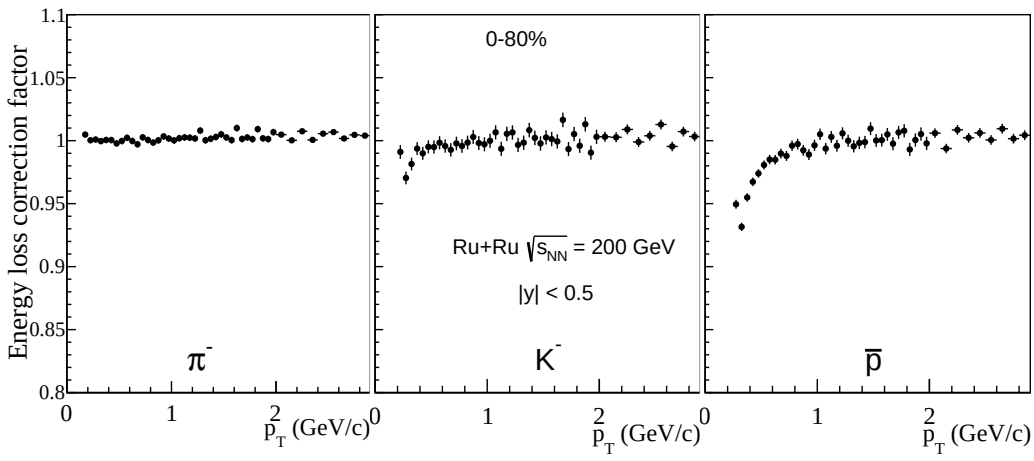

Figure 4.25 Energy loss correction factors as a function of p_T for π^-, K^- and $\bar{p}$ at mid-rapidity ($|y| < 0.5$) in 0-80% Ru+Ru collisions at $\sqrt{s_{NN}}$ = 200 GeV. Error bars shown around the data points are statistical uncertainties.

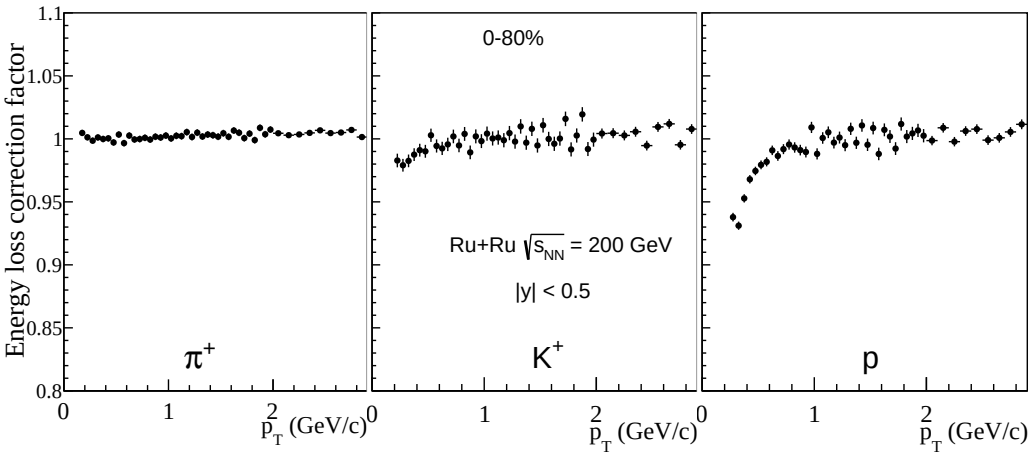

Figure 4.26 Energy loss correction factors as a function of p_T for π^+, K^+ and p at mid-rapidity ($|y| < 0.5$) in 0-80% Ru+Ru collisions at $\sqrt{s_{NN}}$ = 200 GeV. Error bars shown around the data points are statistical uncertainties.

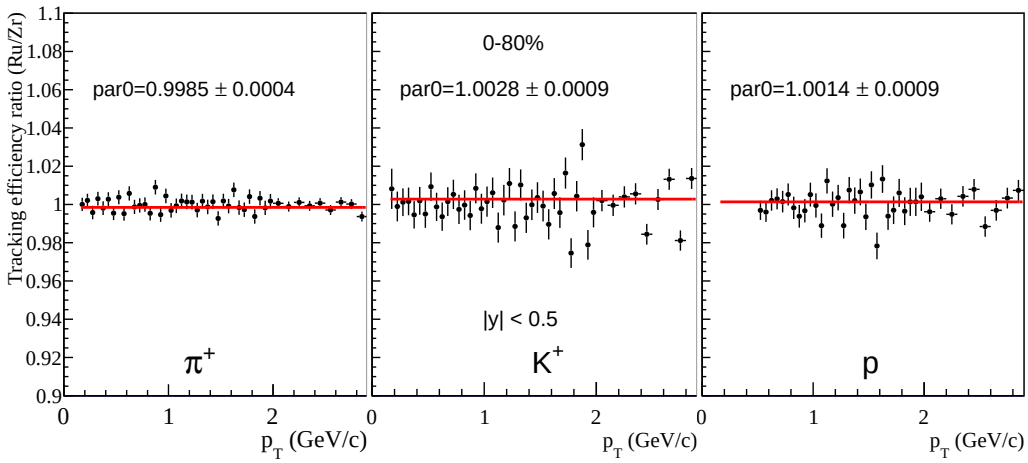

Figure 4.27 Ratios of energy loss correction factors in Ru+Ru to those in Zr+Zr collisions for π^+, K^+ and p as a function of p_T. The red lines are fitting results by a constant.

Figure 4.25 (4.26) presents the energy loss corrections for $\pi^-(\pi^+)$, $K^-(K^+)$ and $\bar{p}(p)$ as a function of p_T in 0-80% Ru+Ru collisions. As expected, the correction factor is very close to unity for pions since the pion mass is assumed to account for the energy loss during track reconstruction. On the other hand, the magnitude of the correction increases towards low p_T and for heavier particles, which highlights the necessity for such corrections.

Figure 4.27 compares the energy loss corrections between Ru+Ru and Zr+Zr collisions by taking the ratios of the correction factors as a function of p_T for π^+, K^+ and p. These ratios are fitted with a constant, and the fitting results are listed in the figure. It is clear that the correction factors are quite consistent between the two collision species as expected. Nevertheless, the energy loss corrections are still evaluated and applied to

raw spectra in Ru+Ru and Zr+Zr collisions separately.

4.2.3 TOF matching efficiency correction

The TOF matching efficiency needs to be taken into account when tracks are required to match TOF for particle identification. The TOF matching efficiency is evaluated using a data-driven method and is defined as follows:

$$\epsilon_{\mathrm{TOF}} = \frac{dN^{\mathrm{TOFMatched}}/dp_{\mathrm{T}}}{dN^{\mathrm{TPC}}/dp_{\mathrm{T}}}, \tag{4.10}$$

where dN^{TPC}/dp_{T} represents the track p_{T} distribution in the TPC after quality cuts, whereas $dN^{TOFMatched}/dp_{\mathrm{T}}$ refers to the distribution after the tracks have been matched to the TOF. The requirements of the TOF matching are listed below:

- TOF matching indication: $btofMatchFlag > 0$
- particle velocity: $\beta > 0$
- TOF pad local position limit: $|btofYLocal| < 1.8$ cm

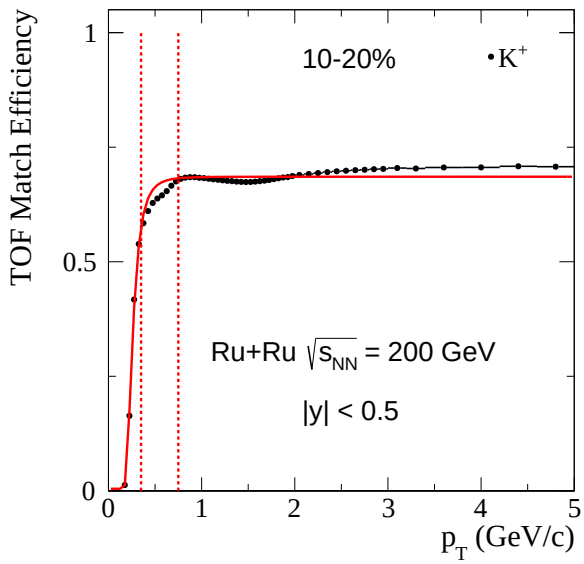

Figure 4.28 TOF matching efficiency as a function of p_{T} for K^+ in 10-20% central Ru+Ru collisions at $\sqrt{s_{\mathrm{NN}}}$ = 200 GeV. The solid red curve is the fitting function used for extrapolation, and the two vertical dashed red lines indicate the extrapolation p_{T} region.

Due to the decay process and energy loss, particles of different species are expected to have different TOF matching efficiencies, which therefore need to be evaluated separately for π, K, and p. To select enriched samples for specific particle species, tight cuts on the ionization energy loss ($n\sigma$) measured in the TPC are used, *i.e.*, $|n\sigma_{\pi}| < 0.3$ for pion, $|n\sigma_{K}| < 0.3$ for kaon and $|n\sigma_{p}| < 0.3$ for proton and anti-proton.

Figure 4.28 shows the TOF matching efficiency for K^+ in 10-20% Ru+Ru collisions. As one can see, there is a drop in the TOF match efficiency around p_{T} =

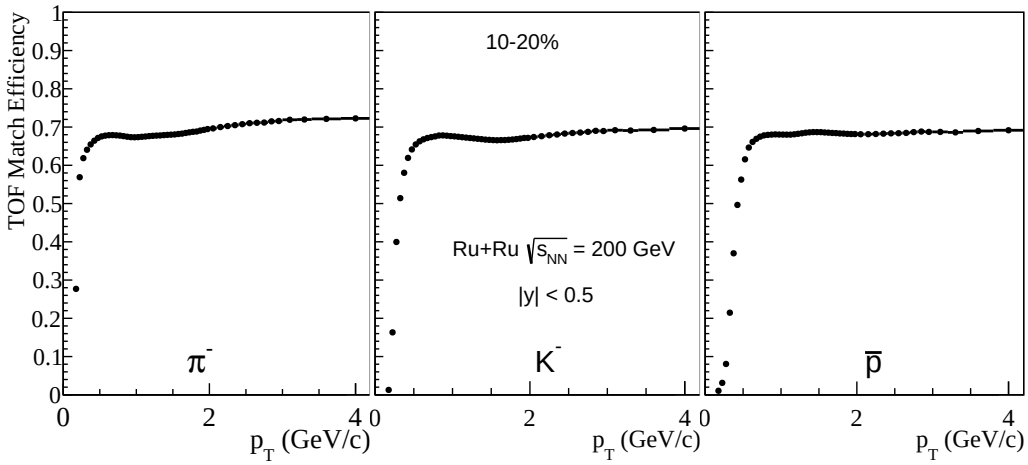

Figure 4.29 TOF matching efficiency as a function of p_T for π^-, K^- and $\bar{p}$ within $|y| < 0.5$ in 10-20% Ru+Ru collisions. The error bars represent statistical uncertainties.

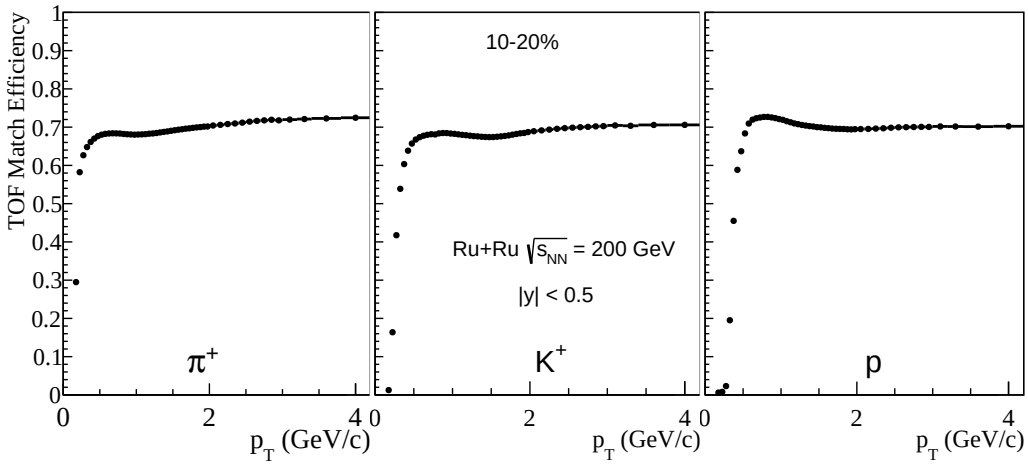

Figure 4.30 TOF matching efficiency as a function of p_T for π^+, K^+ and p within $|y| < 0.5$ in 10-20% Ru+Ru collisions. The error bars represent statistical uncertainties.

0.5 GeV/c. Such a drop has been studied using HIJING+GEANT simulations[74], and it was found that this is due to the pion contamination in the enriched kaon sample despite the tight cut on $|n\sigma_K|$. These background pions, which dominantly originate from pions with worse dE/dx resolution, exhibit low track quality, resulting in a reduced TOF matching efficiency. To overcome this issue, the kaon TOF matching efficiency is fit with the functional form shown in Eq. 4.11, with the fit range of $0.2 < p_T < 0.4$ GeV/c, $0.8 < p_T < 0.95$ GeV/c and $p_T > 2.8$ GeV/c.

$$\epsilon^{K}_{TOF} = p0 \times e^{-p1/p_T^{p2}} + p3, \tag{4.11}$$

where $p0, p1, p2$ and $p3$ are free parameters. The fit function, shown as the solid red curve in Fig. 4.28, is used for the TOF matching efficiency in the range of $0.35 < p_T < 0.75$ GeV/c, while the data points are used elsewhere. It is of course possible that kaons

can also contaminate the pion sample. However, since the pion yield is much larger than that of kaon at the same p_T, the effect of background kaons in the pion sample is negligible.

Figure 4.29 (4.30) shows the TOF matching efficiencies for $\pi^-(\pi^+)$,$K^-(K^+)$ and $\bar{p}(p)$ at mid-rapidity in 10-20% Ru+Ru collisions. Due to decaying during flight, kaons have a smaller efficiency than pions at low p_T, as seen in the TPC tracking efficiency. On the other hand, the TOF matching efficiency for anti-protons is smaller than that of protons at low p_T due to the annihilation process. At high p_T, matching efficiencies for different particles become compatible.

Figure 4.31 shows the TOF matching efficiency for π^- in different centrality classes of Ru+Ru collisions. A clear centrality dependence that the TOF matching efficiency increases from 0-5% central to 70-80% peripheral events is seen. Ratios of the TOF

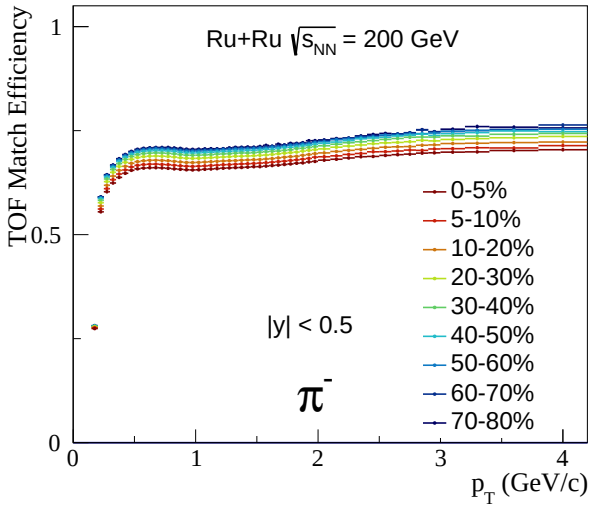

Figure 4.31 TOF matching efficiency for π^- within $|y| < 0.5$ in different centrality intervals of Ru+Ru collisions.

matching efficiencies for Ru+Ru over Zr+Zr collisions are shown in Fig. 4.32, which agree with unity very well. Again, this is due to the almost identical running conditions for the two datasets. A constant function is used to fit the ratios, which confirms the good agreement. As for the cases of TPC tracking efficiency and energy loss correction, the TOF matching efficiency is also evaluated separately for Ru+Ru and Zr+Zr collisions.

4.2.4 Knock-out proton background correction

The measured proton sample contains background protons knocked out from the beam pipe or detector material by high-energy particles, such as pions. These knock-out protons tend to have low p_T and large DCA since the production points are far away from the collision vertex. One needs to remove the knock-out contribution from the proton

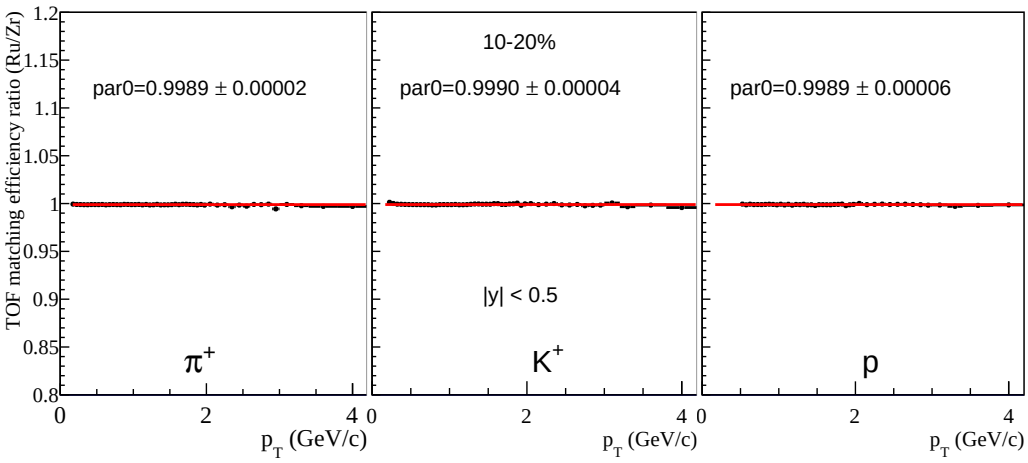

Figure 4.32 Ratios of TOF matching efficiencies in Ru+Ru to those in Zr+Zr for π^+, K^+ and p within $|y| < 0.5$ as a function of p_T. The red lines are fitting results to the ratios with a constant.

sample to obtain the proton spectrum.

Taking advantage of the different DCA shapes for primary and knock-out protons, one can perform a template fit to the DCA distribution of inclusive protons in order to statistically separate the primary protons from the knock-out background[9,11]. One can use the DCA distribution of anti-protons as the template for the primary protons since there is no knock-out contamination to the anti-proton production. On the other hand, the DCA distribution for knock-out protons can be well described by an exponential function as the following:

$$p_{bkg}(\mathrm{DCA}) \propto [1 - exp(-\mathrm{DCA}/\mathrm{DCA}_0)]^{\alpha}, \tag{4.12}$$

where DCA_0 and α are free parameters. Consequently, the inclusive proton DCA distributions can be fitted with two components:

$$p(\mathrm{DCA}) = \bar{p}(\mathrm{DCA})/r_{\bar{p}/p} + A \times p_{bkg}(\mathrm{DCA}). \tag{4.13}$$

Here $r_{\bar{p}/p}$ represents the anti-proton to proton ratio, and A is a free parameter.

To obtain enriched samples of inclusive protons and anti-protons, primary tracks are used with a cut of $|n\sigma_p| < 1$. For those protons and anti-protons identified by TOF, TOF matching is required and a TOF PID cut of $|1/\beta_{measured} - 1/\beta_{expected}| < 0.03$ is applied, where $\beta_{measured}$ is the particle velocity divided by the speed of light (c) using the flight time measured by the TOF, and $\beta_{expected}$ is the expected particle velocity over c calculated based on the track momentum measured in the TPC and mass of the particle. In the analysis, a DCA cut of 3 cm is used to select primary tracks, and therefore the knock-out background fraction within DCA < 3 cm is estimated and corrected for.

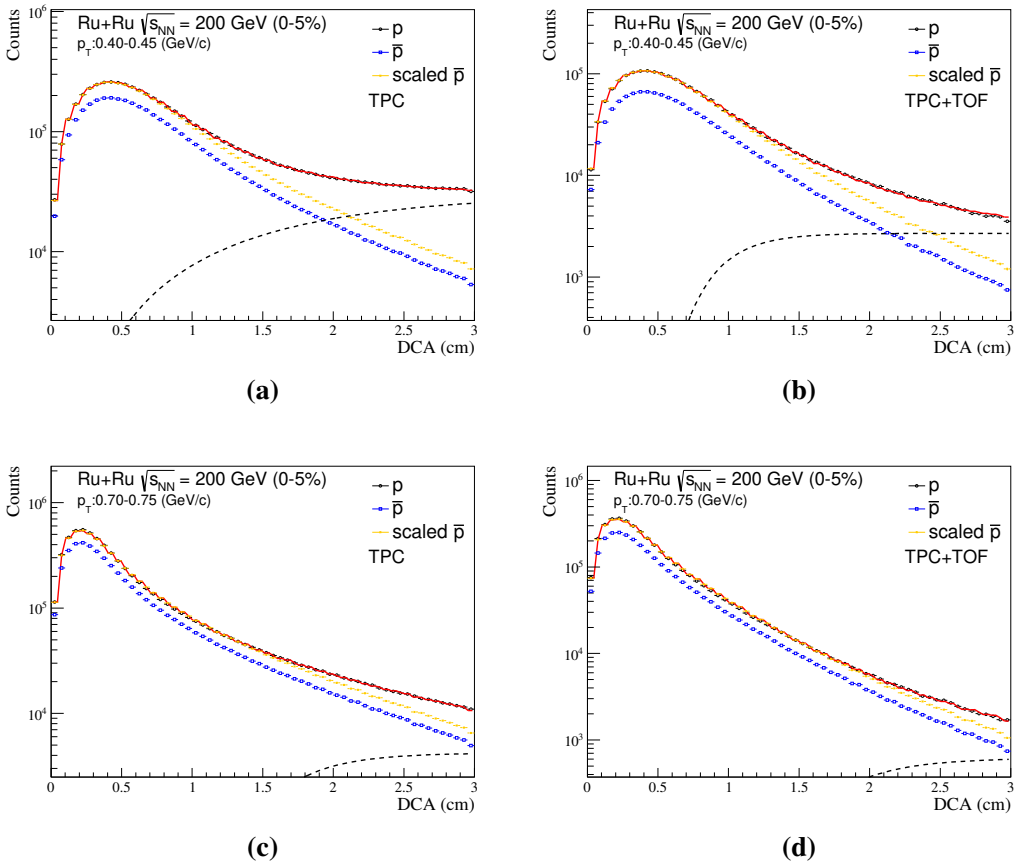

Figure 4.33 DCA distributions of protons (black) and anti-protons (blue) for $0.40 < p_T < 0.45$ GeV/c (top) and $0.70 < p_T < 0.75$ GeV/c (bottom) in 0-5% central Ru+Ru collisions at $\sqrt{s_{NN}}$ = 200 GeV. The panels (a) and (c) show the DCA distributions of p and $\bar{p}$ identified by the TPC only, while panels (b) and (d) present the DCA distributions for those identified by TPC and TOF. The solid red curves are fits to the inclusive proton DCA distributions by Eq. 4.13, while the yellow histograms are the $\bar{p}$ DCA distributions scaled up by the factor $1/r_{\bar{p}/p}$. The dashed black curves represent the knock-out proton contribution.

The left panels of Fig. 4.33 show the fitting results to DCA distributions of inclusive protons identified by TPC alone at two different p_T regions ($0.40 < p_T < 0.45$ GeV/c (top) and $0.70 < p_T < 0.75$ GeV/c) in 0-5% central Ru+Ru collisions, while the right panels show the similar results for protons identified by TPC and TOF. The black (blue) data points are for DCA distributions of inclusive protons (anti-protons). The solid red curves are the fits to inclusive proton DCA distributions by Eq. 4.13, and the dashed curves show the fits to background proton DCA distributions by Eq. 4.12. Yellow markers illustrate the scaled $\bar{p}$ DCA distributions by $1/r_{\bar{p}/p}$. Similar results are shown in Figs. 4.34 and 4.35 for 70-80% peripheral Ru+Ru and central 0-5% Zr+Zr collisions.

The fractions of knock-out protons in the measured inclusive proton sample are shown in Figs. 4.36 and 4.37 as a function of p_T for different centrality classes of Ru+Ru and Zr+Zr collisions. The background fraction drops fast as p_T increases, which is con-

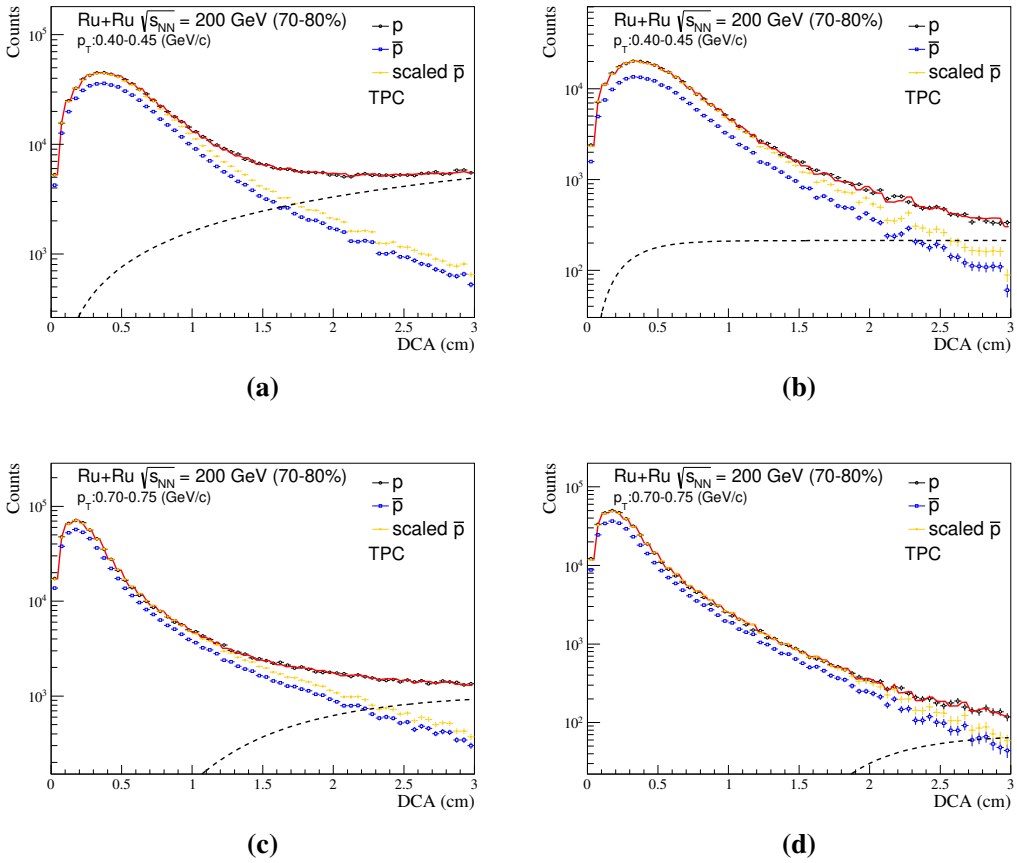

Figure 4.34 Same as Fig. 4.33 but for 70-80% peripheral Ru+Ru collisions.

sistent with the expectation that the knock-out protons mostly concentrate at low p_T. One can also see that the knock-out proton contribution is significantly suppressed for TPC&TOF compared to the case of TPC only due to that the TOF matching requirement can greatly reject non-primary tracks. Since the ratio of the proton multiplicity to the total multiplicity of particles interacting with detector material varies somewhat with centrality, and the particle kinematics also changes with centrality, a non-negligible centrality dependence of the knock-out proton fraction is seen. In the work, the knock-out proton fractions are evaluated and applied to Ru+Ru and Zr+Zr analyses separately.

4.2.5 Pion background correction

The obtained pion spectra include feed-down contributions from weak decays. For the measurement of charge stopping, these contributions are desirable since the total net-charge is to be measured. On the other hand, the weak decay contributions need to be subtracted when extracting the QGP's bulk properties since primordial pions are of interest in this case. The weak decay contributions are estimated from MC simulations of heavy-ion collisions with the HIJING event generator[137], incorporating the

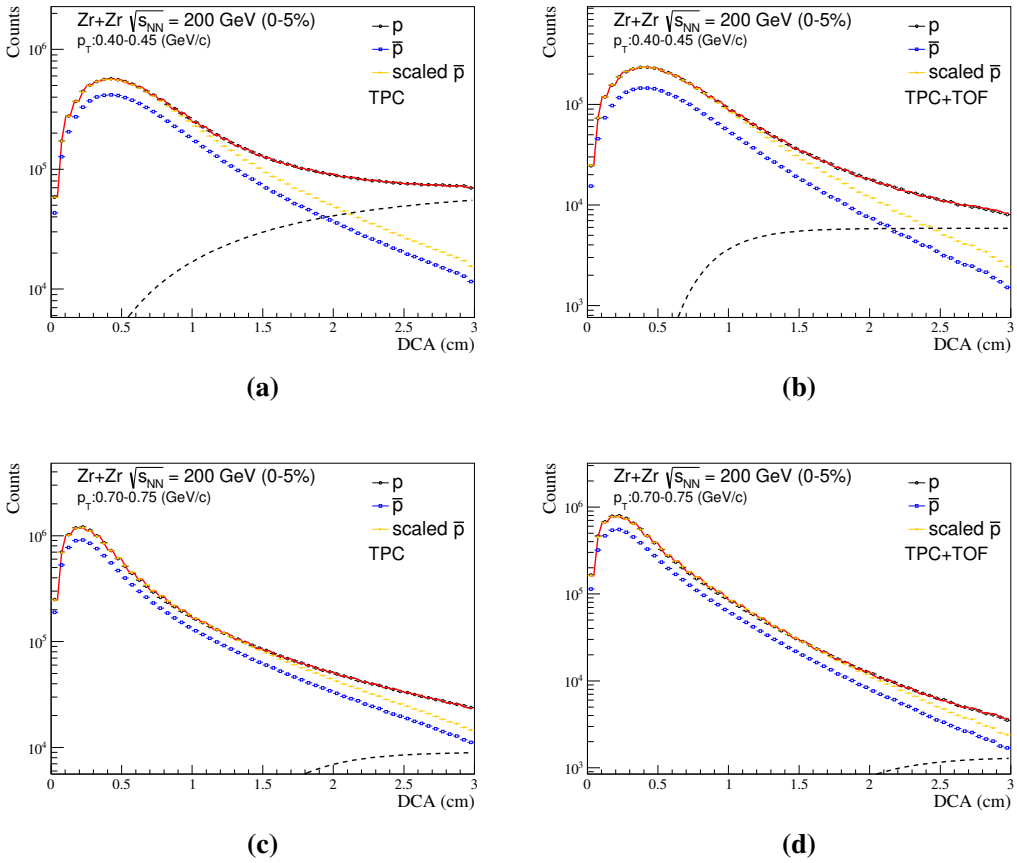

Figure 4.35 Same as Fig. 4.33 but for 0-5% central Zr+Zr collisions.

STAR geometry and realistic modeling of the detector's response. These simulated events are processed in the same manner as real data. The weak-decay daughter pions mainly originate from K_s^0 and Λ, and their identification is based on the parent particle information, which is obtainable from the simulation. Figure 4.38 shows the pion background fraction (open squares) as a function of p_T in 200 GeV d+Au collisions from reference[9]. The pion background contribution from weak decays decreases with increasing p_T. Since the weak decay contribution is found to be independent of event multiplicity[9], its fraction evaluated in 200 GeV d+Au collisions can be used for different centrality intervals of isobar collisions.

4.2.6 Corrections to double ratios

In order to estimate the charge stopping difference between Ru+Ru and Zr+Zr collisions, the double ratios for pions ($R_{2\pi}$), kaons (R_{2K}) and protons (R_{2p}) are used[56]. The definition of $R_{2\pi}$ is as follows:

$$R_{2\pi} = \frac{(N_{\pi^+}/N_{\pi^-})_{Ru}}{(N_{\pi^+}/N_{\pi^-})_{Zr}}. \tag{4.14}$$

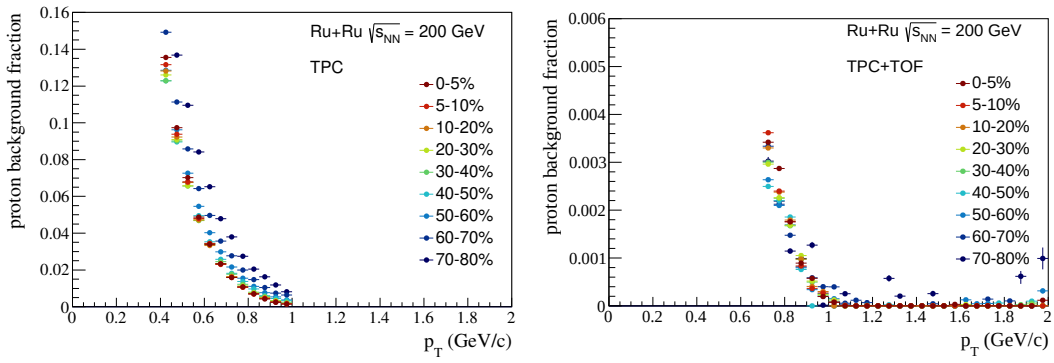

(a) **(b)**

Figure 4.36 Fraction of knock-out proton background in the inclusive proton sample as a function of p_T Ru+Ru collisions for different centrality classes. The left panel shows the background fractions for protons identified by TPC, and the right panel shows the background fractions for protons selected by TPC and TOF.

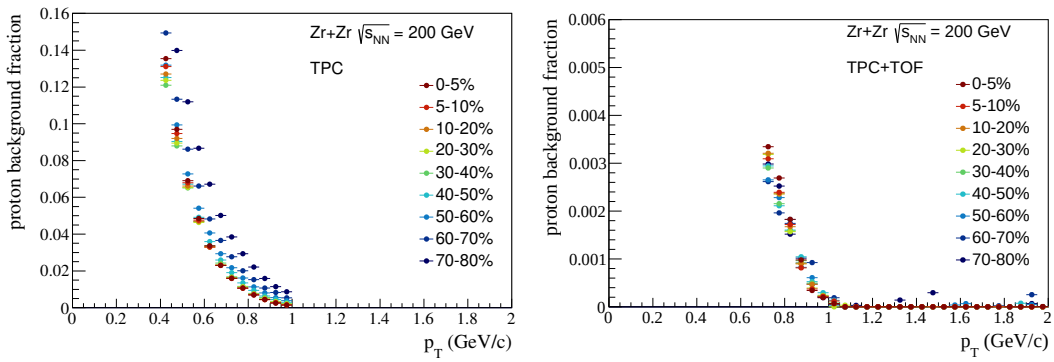

(a) **(b)**

Figure 4.37 Fraction of knock-out proton background in the inclusive proton sample as a function of p_T in Zr+Zr collisions for different centrality classes. The left panel shows the background fractions for protons identified by TPC, and the right panel shows the background fractions for protons selected by TPC and TOF.

The definitions of R_{2K} and R_{2p} are similar to that of $R_{2\pi}$. Figures 4.39, 4.40 and 4.41 show different correction factors for double ratios. These correction factors are fitted using constant functions, which are in agreement with unity. Therefore, no corrections are applied to $R_{2\pi}$, R_{2K} and R_{2p}. Also, systematic uncertainties cancel out in the double ratios.

4.3 Systematic uncertainties on transverse momentum spectra

Several sources of systematic uncertainties are considered for the corrected particle spectra.

- Track selection cuts variation
- Signal extraction
- Knock-out proton background

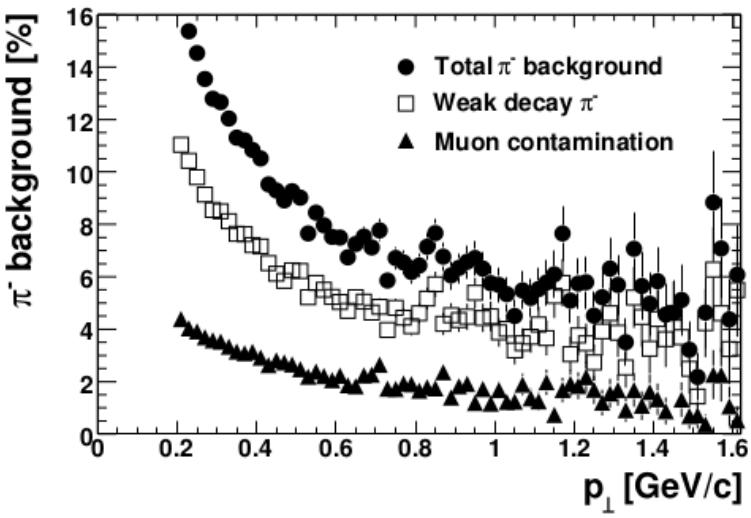

Figure 4.38 Pion background fraction from weak decays (open squares) as a function of p_T in $d + Au$ collisions at $\sqrt{s_{NN}}$ = 200 GeV. The background contribution from muon contamination is not used in this work. The plot is taken from[9].

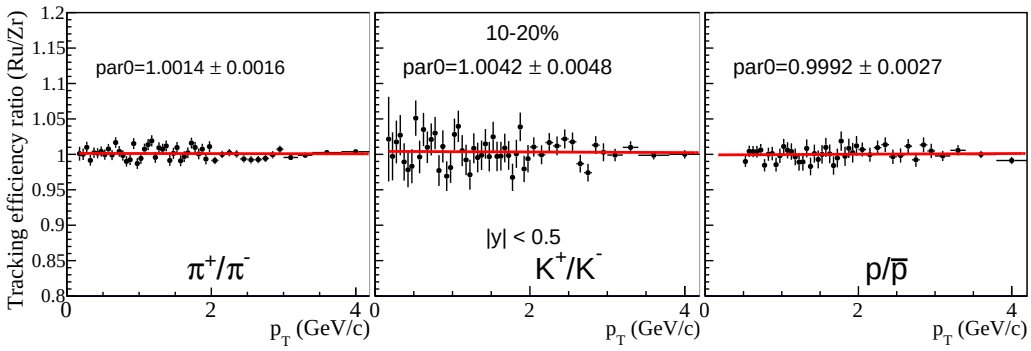

Figure 4.39 Tracking efficiencies for double ratios. The red lines are fits to the distributions.

- 5% in the tracking efficiency

The first three sources of uncertainties are treated as point-to-point uncertainties, i.e., they do not correlate among p_T or centrality bins, while the 5% overall uncertainty in the tracking efficiency is applied as the global uncertainty across all p_T and centrality intervals.

To evaluate the uncertainties related to how well the embedding sample reproduces data, two sets of alternative track quality cuts for $nHitsFit$, $nHitsDedx$, and DCA are tried, and the whole analysis procedure is repeated. The alternative cut values are listed in Table 4.1.

Table 4.1 Comparison between the default and varied cuts.

Physical quantities	Default cut	Varied cut 1	Varied cut 2
$nHitsFit$	≥15	≥20	≥15
$nHitsDedx$	≥10	≥15	≥10
DCA	DCA < 3 cm	DCA < 3 cm	DCA < 2 cm

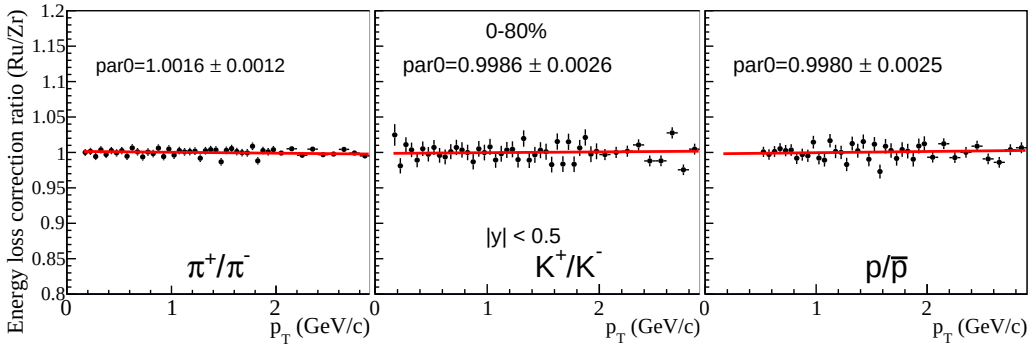

Figure 4.40 Energy loss correction factors for double ratios. The red lines are fits to the distributions.

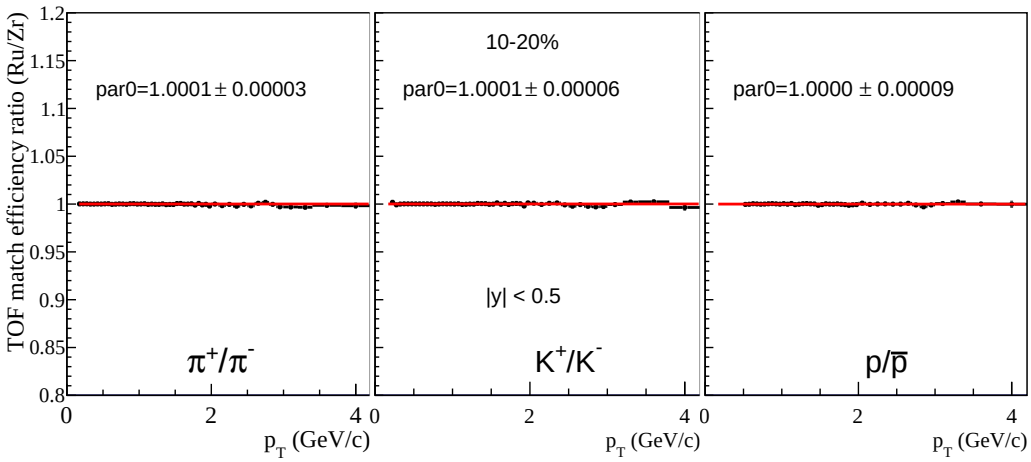

Figure 4.41 TOF matching efficiencies for double ratios. The red lines are fits to the distributions.

To estimate the systematic uncertainty brought by signal extraction, the following variations in the signal extraction procedure are tried:

- Fit $n\sigma_x$ and m^2 distributions in Zr+Zr collisions, and use the obtained fitting parameters to fix the corresponding fitting parameters for signal extraction in Ru+Ru collisions, instead of fixing the fitting in Zr+Zr collisions using the parameters obtained in Ru+Ru collisions
- Increase the parameter limits to two times the original ranges when fitting negative particles in Ru+Ru collisions
- Decrease the parameter limits to half of the original ranges when fitting negative particles in Ru+Ru collisions

The systematic uncertainty related to the knock-out proton background is estimated by using a different fitting function shown in Eq. 4.15, and changing the proton PID cuts.

$$p_{bkg}(\mathrm{DCA}) \propto Aexp(-[ln(\mathrm{DCA}) - B]^2/2C^2), \tag{4.15}$$

where A, B and C are free parameters. The ionization energy loss cut used for proton identification is changed to $|n\sigma_p| < 0.3$ to obtain enriched samples of inclusive protons and anti-protons, while the TOF PID cut remains the same.

The systematic uncertainty of a certain source is determined using the method outlined in reference[138], to account for statistical fluctuations. Specifically, the calculation of systematic uncertainties is performed in the following manner:

- Extract the difference in the corrected spectra between the default case and i^{th} variation. This difference is expressed in Eq. 4.16.

$$\Delta s = s_{i^{th}sys} - s_{def}. \tag{4.16}$$

- The quadratic difference between the statistical uncertainties on spectra in default case and i^{th} variation is calculated based on Eq. 4.17.

$$\Delta\sigma_{stat} = \sqrt{|(\sigma_{stat})^2_{i^{th}sys} - (\sigma_{stat})^2_{def}|}. \tag{4.17}$$

- If $|\Delta s| > \Delta\sigma_{stat}$, the systematic uncertainty brought by the ith variation is taken as:

$$(\sigma_{sys})_i = \sqrt{(\Delta s)^2 - (\Delta\sigma_{stat})^2}. \tag{4.18}$$

  Otherwise, the systematic uncertainty is assigned as 0.
- The final systematic uncertainty for a certain source is taken as the root mean square of all the variations, as shown in Eq. 4.19.

$$\sigma_{sys} = \sqrt{\frac{\sum_{i=1}^{N}(\sigma_{sys})_i^2}{N}}, \tag{4.19}$$

  where N is the total number of variations.

The point-to-point systematic uncertainties from each source are added in quadrature to derive the total systematic uncertainties for pion, kaon, proton, and anti-proton spectra in Ru+Ru and Zr+Zr collisions, as illustrated in Figs. 4.42 and 4.43.

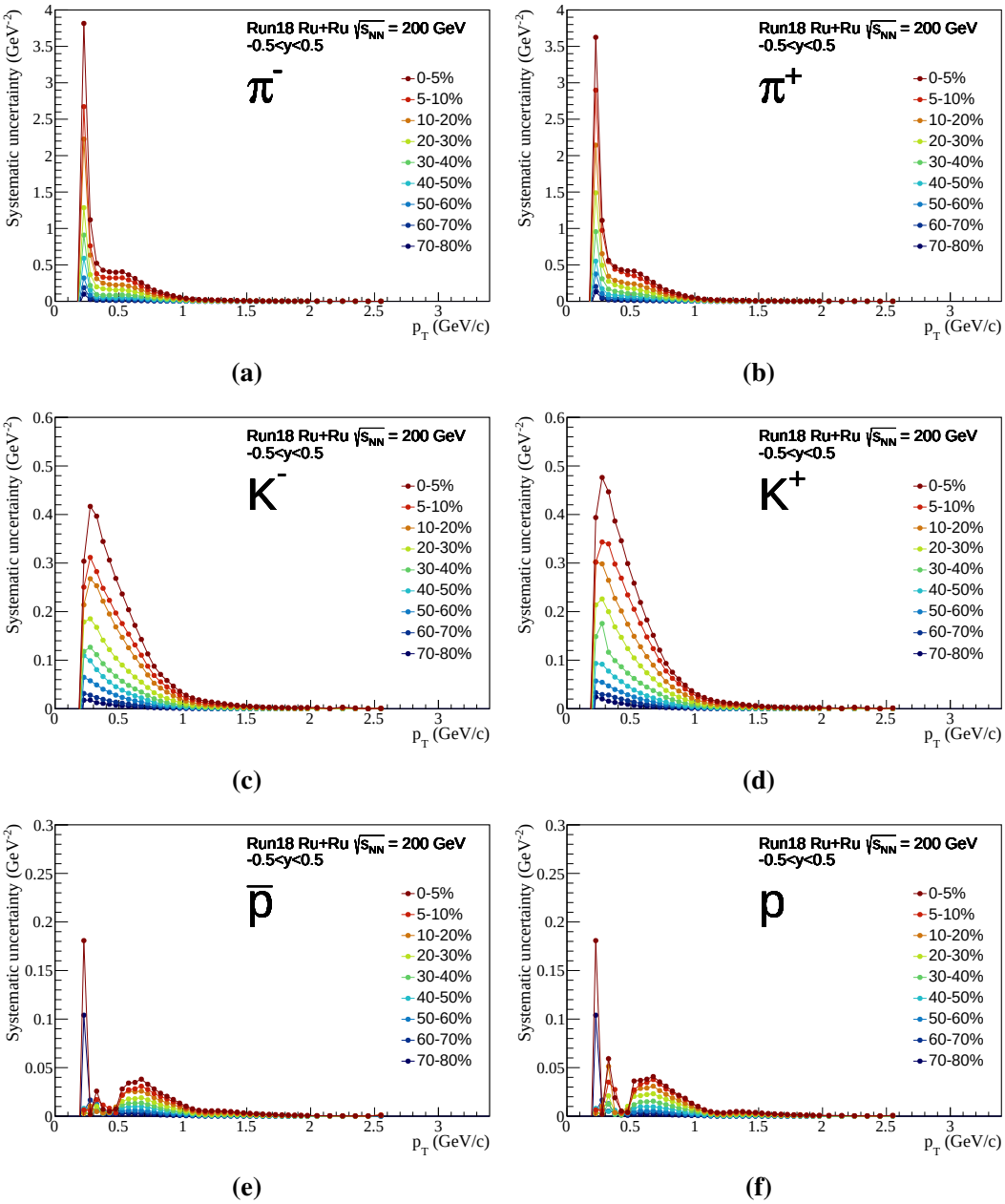

Figure 4.42 Absolute systematic uncertainties of invariant yield for $\pi^-(\pi^+)$, $K^-(K^+)$ and $\bar{p}(p)$ within $|y| < 0.5$ as a function of p_T in different centrality intervals of 200 GeV Ru+Ru collisions.

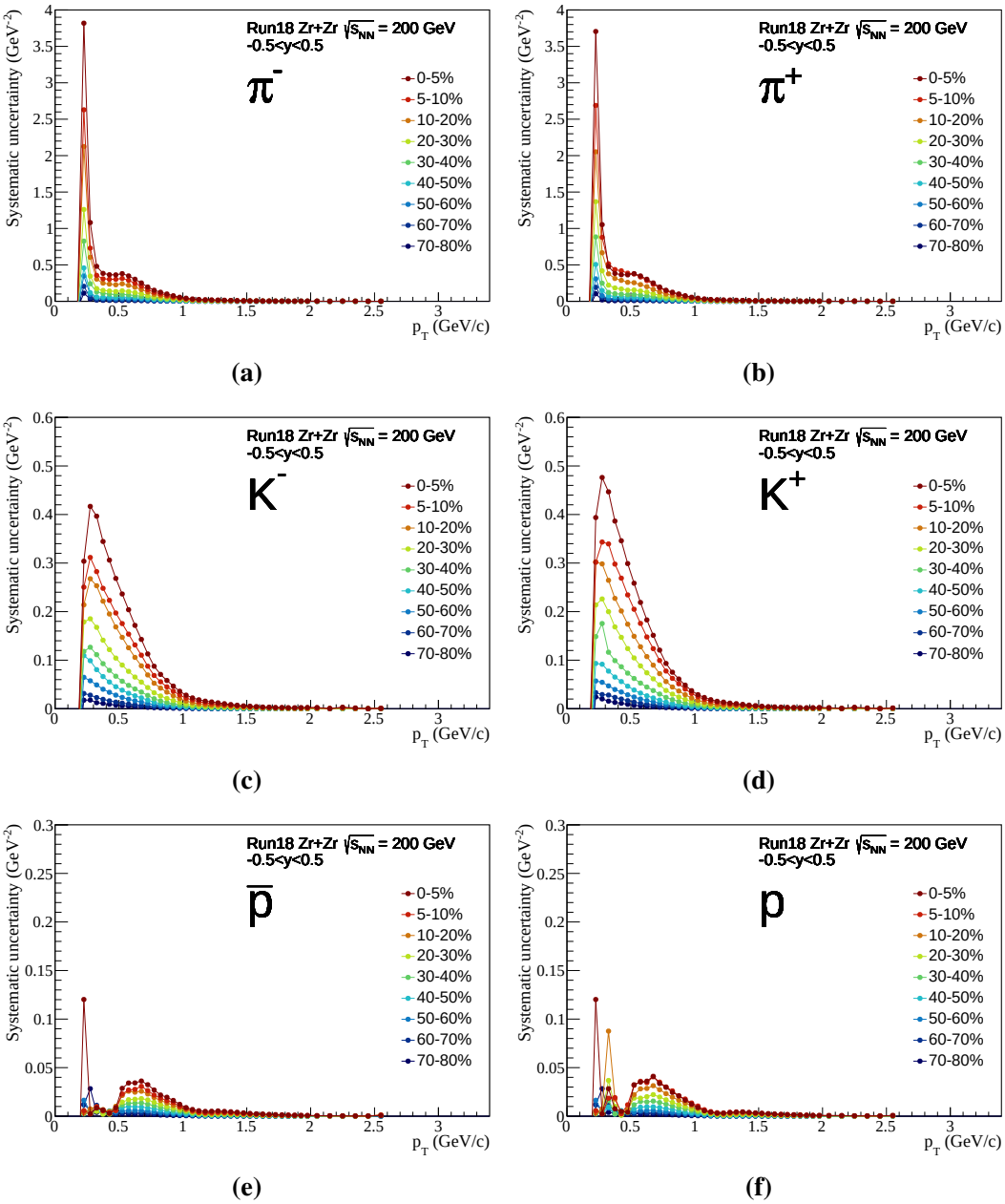

Figure 4.43 Absolute systematic uncertainties of invariant yield for $\pi^-(\pi^+)$, $K^-(K^+)$ and $\bar{p}(p)$ within $|y| < 0.5$ as a function of p_T in different centrality intervals of 200 GeV Zr+Zr collisions.

Chapter 5 Results and discussions

5.1 Corrected spectra

After implementing all of the aforementioned corrections to the raw yields, the corrected spectra are obtained and expressed as Eq. 5.1.

$$\frac{d^2N}{2\pi p_{\mathrm{T}} dp_{\mathrm{T}} dy} = \frac{1}{\epsilon}\frac{d^2N_{raw}}{2\pi p_{\mathrm{T}} dp_{\mathrm{T}} dy}, \tag{5.1}$$

where N_{raw} is the raw particle yield within a certain p_{T} and centrality interval. The term ϵ represents a correction factor that accounts for the energy loss and tracking efficiency of the TPC, as well as the matching efficiency of the TOF detector. For π^+ and π^-, contributions from weak decays are subtracted out when extracting bulk properties but retained for measuring charge stopping. For protons, additional corrections are applied to remove knock-out protons, but weak decay corrections are included in the measured p and $\bar{p}$ spectra.

Figures 5.1 and 5.2 present the final p_{T} spectra for $\pi^+(\pi^-)$, $K^+(K^-)$ and $p(\bar{p})$ in 9 centrality classes, ranging from 0-5% to 70-80%, in Ru+Ru and Zr+Zr collisions at $\sqrt{s_{\mathrm{NN}}}$ = 200 GeV. The p_{T} range for pion spectra is within $0.2 < p_{\mathrm{T}} < 2.5$ GeV/c, while for kaons and protons, the p_{T} ranges are slightly narrowed to $0.3 < p_{\mathrm{T}} < 2.5$ GeV/c and $0.5 < p_{\mathrm{T}} < 2.5$ GeV/c, respectively. As anticipated, the yields of particles increase from peripheral to central collisions. The spectral shapes for both particles and antiparticles across all species exhibit similarity within each centrality bin. However, a noticeable dependence on the particle mass is observed in the slopes of the particle spectra. For the pion spectra, with decreasing p_{T}, the slopes steepens more rapidly, which can be attributed to the significant contribution from resonance decays. The proton spectra exhibit an increasingly more concave shape from peripheral to central collisions, indicating stronger radial flow effects. The common radial velocity boosts heavier particles to higher p_{T} more significantly, which is why such an effect is more readily to be seen in the proton spectra than those of pion and kaon.

5.2 Bulk properties

Assessing bulk properties of the QGP produced in Ru+Ru and Zr+Zr collisions requires knowledge of the total particle yield at mid-rapidity ($|y| < 0.5$). As shown in Figs. 5.1 and 5.2, identified particle spectra are only measured in limited p_{T} ranges

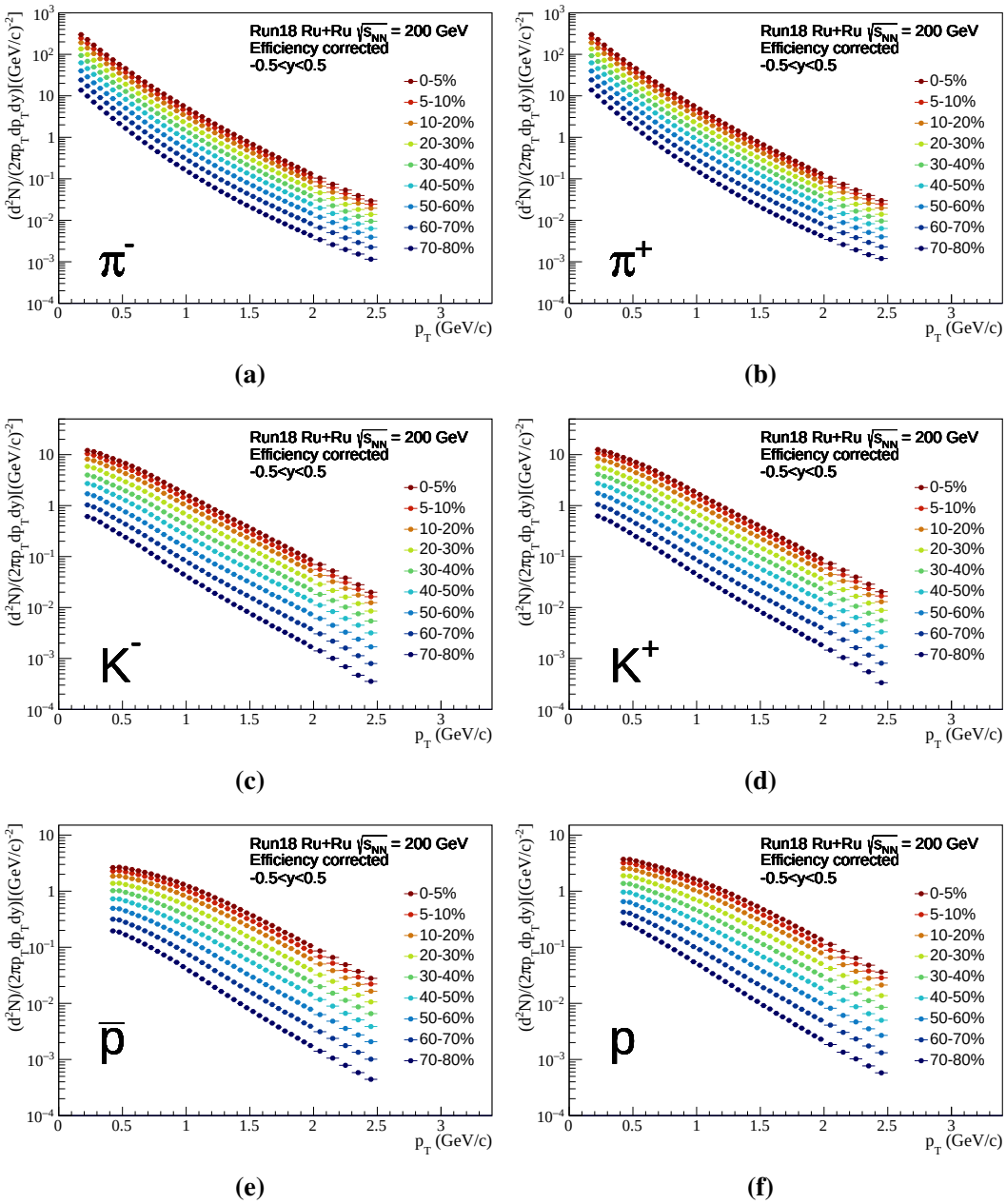

Figure 5.1 Corrected p_{T} spectra for $\pi^{-}(\pi^{+})$, $K^{-}(K^{+})$ and $\bar{p}(p)$ within $|y| < 0.5$ in different centrality intervals of 200 GeV Ru+Ru collisions. Error bars around the data points, smaller than the marker size, represent statistical uncertainties and systematic uncertainties added in quadrature.

due to finite detector acceptance. Consequently, measured spectra are parameterized for being extrapolated to unmeasured regions down to $p_{\mathrm{T}} = 0$ GeV/c.

Assuming a hard-sphere uniform density particle source with a kinetic freeze-out temperature T_{kin} and a transverse radial flow velocity β, the particle's p_{T} spectrum can be expressed with the Blast-Wave model[43]:

$$\frac{dN}{p_{\mathrm{T}} dp_{\mathrm{T}}} \propto \int_0^R r dr m_T I_0(\frac{p_{\mathrm{T}} \sinh \rho}{T_{kin}}) K_1(\frac{m_T \cosh \rho}{T_{kin}}), \tag{5.2}$$

where $\rho = \tanh^{-1} \beta$, I_0 and K_1 are the modified Bessel functions. The velocity profile

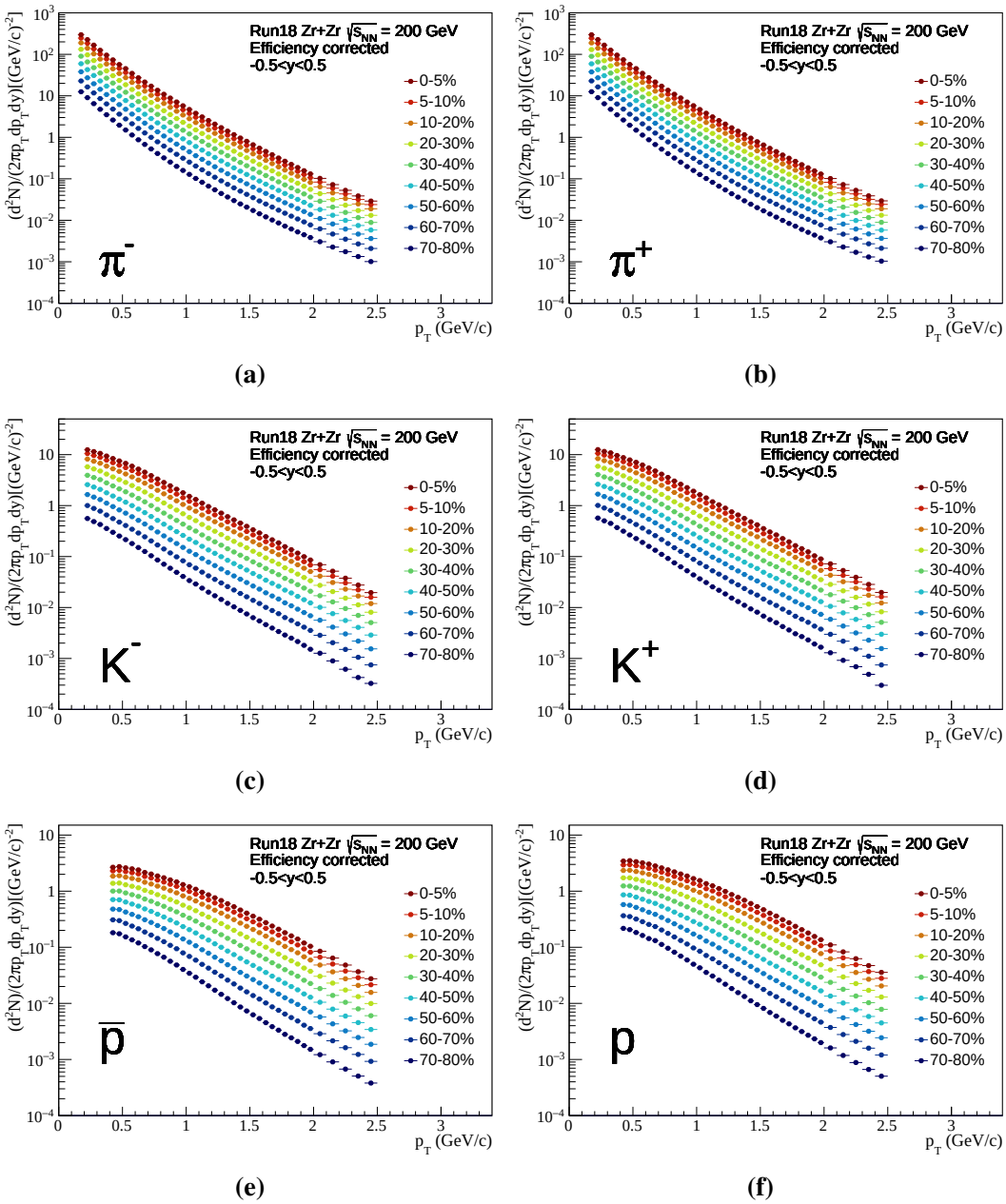

Figure 5.2 Same as Fig.5.1, but for Zr+Zr collisions.

of the flow can be expressed by the equation 5.3:

$$\beta = \beta_S (r/R)^n, \tag{5.3}$$

where β_S denotes the surface velocity and r/R represents the relative radial position within the thermal source. The choice of the value of R has no impact on the model. For kaons and protons, the Blast-Wave model is used for the extrapolation.

Due to the significant contribution of resonance decays to the pion spectra at $p_{\mathrm{T}} < 0.5$ GeV/c, the pion spectra are fitted using the Bose-Einstein distribution (Eq. 5.4):

$$\frac{dN}{m_{\mathrm{T}} dm_{\mathrm{T}}} \propto 1/[exp(m_{\mathrm{T}}/T_{BE}) - 1], \tag{5.4}$$

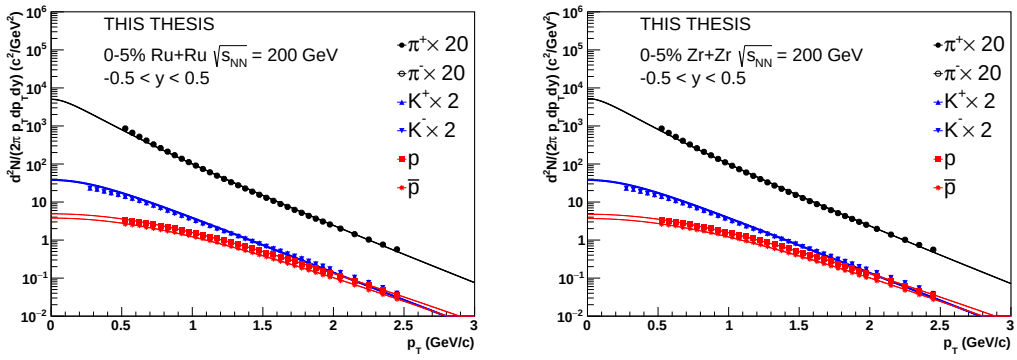

(a) **(b)**

Figure 5.3 The Blast-Wave model is simultaneously fit to the spectra of π^-, π^+, K^-, K^+, p, and $\bar{p}$ in (a) Ru+Ru and (b) Zr+Zr collisions within the 0-5% centrality interval. The errors displayed in the plot represent the quadratic sum of statistical and systematic uncertainties.

where T_{BE} is a free fit parameter, and $m_{\mathrm{T}} = \sqrt{m_0^2 + p_{\mathrm{T}}^2}$ represents the transverse mass.

The point-to-point systematic uncertainties are added in quadrature with the statistical uncertainties, and thereby included in the fits. The systematic uncertainty of the extrapolation procedure is determined by using alternative fit functions. A list of these fit functions is provided below.

$$p_{\mathrm{T}}\ exponential\ :\ \frac{dN}{p_{\mathrm{T}} dp_{\mathrm{T}}} \propto exp(-p_{\mathrm{T}}/T_{p_{\mathrm{T}}}), \tag{5.5}$$

$$p_{\mathrm{T}}\ Gaussian\ :\ \frac{dN}{p_{\mathrm{T}} dp_{\mathrm{T}}} \propto exp(-p_{\mathrm{T}}^2/T_{p_{\mathrm{T}}}^2), \tag{5.6}$$

$$p_{\mathrm{T}}^3\ exponential\ :\ \frac{dN}{p_{\mathrm{T}} dp_{\mathrm{T}}} \propto exp(-p_{\mathrm{T}}^3/T_{p_{\mathrm{T}}}^3), \tag{5.7}$$

$$m_{\mathrm{T}}\ exponential\ :\ \frac{dN}{m_{\mathrm{T}} dm_{\mathrm{T}}} \propto exp(-m_{\mathrm{T}}/T_{m_{\mathrm{T}}}), \tag{5.8}$$

$$Boltzmann\ :\ \frac{dN}{m_{\mathrm{T}} dm_{\mathrm{T}}} \propto m_T exp(-m_T/T_B), \tag{5.9}$$

where $T_{m_{\mathrm{T}}}$, $T_{p_{\mathrm{T}}}$ and T_B are fit parameters. For pion spectra, the alternative p_{T} exponential function is tried. For kaon spectra, its extrapolation uncertainty is estimated using the m_{T} exponential and Boltzmann functions. Meanwhile, the p_{T} Gaussian and p_{T}^3 exponential functions are utilized to evaluate the systematic uncertainty for the proton. These variations are selected based on the previous spectra analysis[9]. Additionally, the 5% global uncertainty in the tracking efficiency is added in quadrature to the total uncertainty of the integrated particle yield ($\mathrm{d}N/\mathrm{d}y$). It does not affect the results of $\langle p_{\mathrm{T}} \rangle$ which is only determined by the spectrum shape, and particle ratios where the global uncertainty cancels.

5.2.1 Integrated particle yields

The integrated particle yield ($\mathrm{d}N/\mathrm{d}y$) can be used to infer the total energy or entropy generated in the collision. In this analysis, it is obtained by integrating the particle spectra over p_{T}, as demonstrated in equation 5.10.

$$\frac{dN}{dy} = \int_0^a 2\pi p_{\mathrm{T}} f(p_{\mathrm{T}}) dp_{\mathrm{T}} + \int_a^{2.5} 2\pi p_{\mathrm{T}} h(p_{\mathrm{T}}) dp_{\mathrm{T}} + \int_{2.5}^{\infty} 2\pi p_{\mathrm{T}} f(p_{\mathrm{T}}) dp_{\mathrm{T}}, \quad (5.10)$$

where $f(p_{\mathrm{T}})$ denotes the function used to fit the p_{T} spectra, while $h(p_{\mathrm{T}})$ represents the measured spectra. The parameter a signifies the edge for extrapolation. In the p_{T} range of $0 < p_{\mathrm{T}} < a$ and $2.5 < p_{\mathrm{T}} < \infty$, the fit function is used for integration, while within the range of $a < p_{\mathrm{T}} < 2.5$, the measured spectra are used to calculate the yield. For pion spectra, the value of a is 0.2 GeV/c, whereas, for kaon and proton spectra, the values are 0.3 and 0.5 GeV/c, respectively.

Figures 5.4 and 5.5 exhibit the $\mathrm{d}N/\mathrm{d}y$ and $\mathrm{d}N/\mathrm{d}y$ normalized by N_{part} at mid-rapidity for pions, kaons, and protons. They are plotted against the function of $\langle N_{\mathrm{part}} \rangle$ within Ru+Ru and Zr+Zr collision environments. For comparison, measurements from Cu+Cu[47] and Au+Au[9] collisions are also shown. Because of their distinct system sizes, the different collision systems cover various N_{part} ranges. The normalized yields decrease from central to peripheral collisions for pions, while the centrality dependences of normalized yields for kaons and protons are weak. The $\mathrm{d}N/\mathrm{d}y$ for each species rise steadily from peripheral to central collisions, with the isobar data aligning with the Cu+Cu and Au+Au data at similar N_{part} values, suggesting that it's the average energy density (or N_{part}) that steers the collision dynamics.

5.2.2 Average transverse momentum

The average transverse momentum ($\langle p_{\mathrm{T}} \rangle$) of hadrons in relativistic heavy-ion collisions is indicative of the intensity of the expansion of the hot, dense QCD medium that forms during these events. Under the same total entropy (energy), a more concentrated initial state would trigger a more rapid expansion, subsequently leading to a more substantial radial flow and larger $\langle p_{\mathrm{T}} \rangle$ values[139-140]. The magnitude of $\langle p_{\mathrm{T}} \rangle$ reflects the medium's transverse dynamics. Therefore, examining $\langle p_{\mathrm{T}} \rangle$ as a function of charged hadron multiplicity offers an additional perspective on the properties of QGP. The $\langle p_{\mathrm{T}} \rangle$

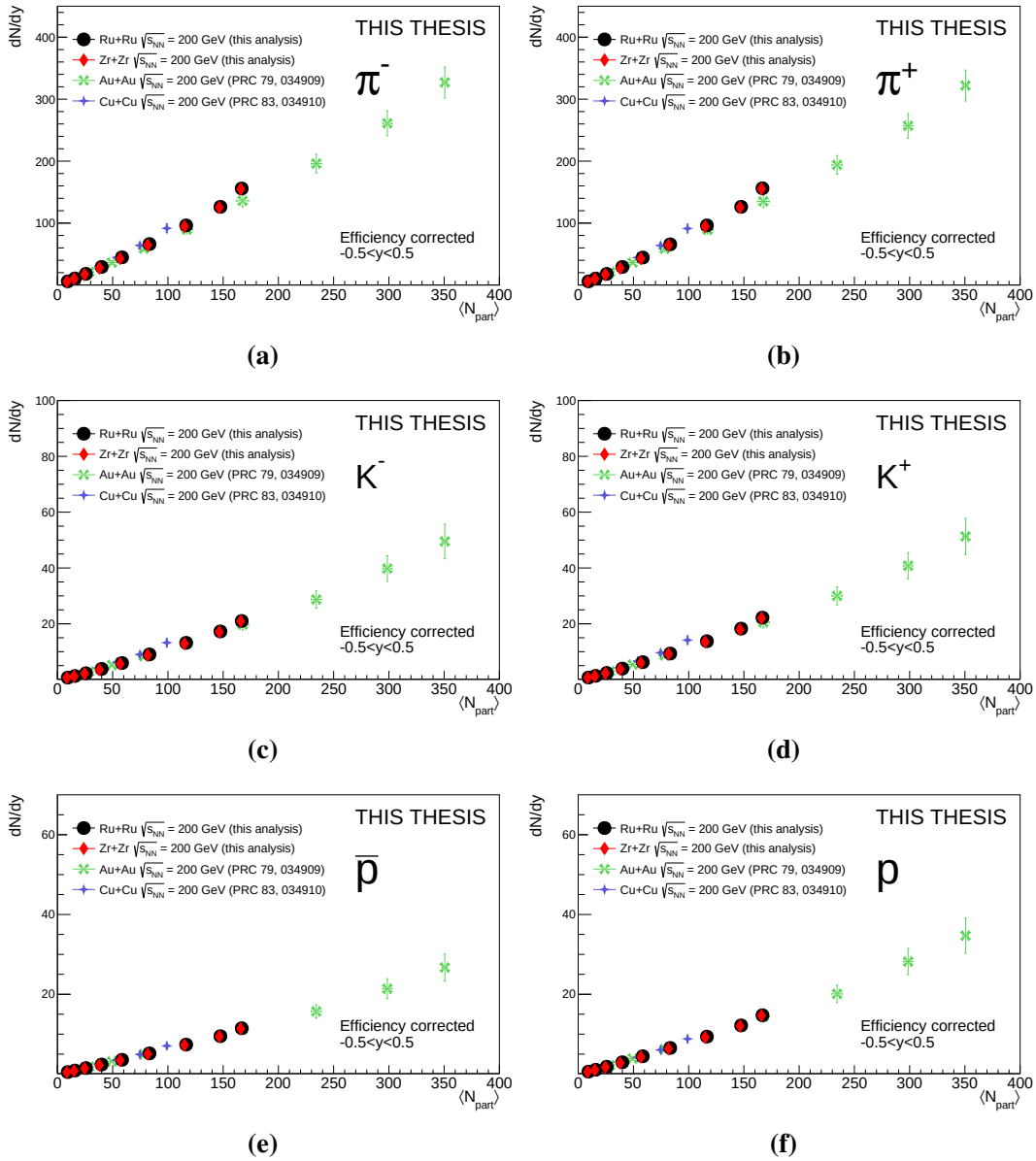

Figure 5.4 The integrated yield ($\mathrm{d}N/\mathrm{d}y$) **of** $\pi^+(\pi^-)$, $K^+(K^-)$, $p(\bar{p})$ **as a function of** $\langle N_{\mathrm{part}}\rangle$ **for Ru+Ru and Zr+Zr collisions at** $\sqrt{s_{\mathrm{NN}}}$ **= 200 GeV, and compared to similar results from Cu+Cu and Au+Au collisions at the same energy. The errors displayed in the plot represent the quadratic sum of statistical and systematic uncertainties.**

can be computed using Eq. 5.11.

$$\langle p_{\mathrm{T}}\rangle = \frac{\int_0^a p_{\mathrm{T}} 2\pi p_{\mathrm{T}} f(p_{\mathrm{T}}) dp_{\mathrm{T}} + \int_a^{2.5} p_{\mathrm{T}} 2\pi p_{\mathrm{T}} h(p_{\mathrm{T}}) dp_{\mathrm{T}} + \int_{2.5}^{\infty} p_{\mathrm{T}} 2\pi p_{\mathrm{T}} f(p_{\mathrm{T}}) dp_{\mathrm{T}}}{\int_0^a 2\pi p_{\mathrm{T}} f(p_{\mathrm{T}}) dp_{\mathrm{T}} + \int_a^{2.5} 2\pi p_{\mathrm{T}} h(p_{\mathrm{T}}) dp_{\mathrm{T}} + \int_{2.5}^{\infty} 2\pi p_{\mathrm{T}} f(p_{\mathrm{T}}) dp_{\mathrm{T}}}, \tag{5.11}$$

where $f(p_{\mathrm{T}})$ denotes the function used to fit the p_{T} spectra, while $h(p_{\mathrm{T}})$ represents the measured spectra. The parameter a indicates the edge for extrapolation. The values of a and the integration procedure employed are identical to those used for $\mathrm{d}N/\mathrm{d}y$ measurement.

Figure 5.6 displays the relationship between $\langle p_{\mathrm{T}}\rangle$ and N_{part} in Ru+Ru and Zr+Zr

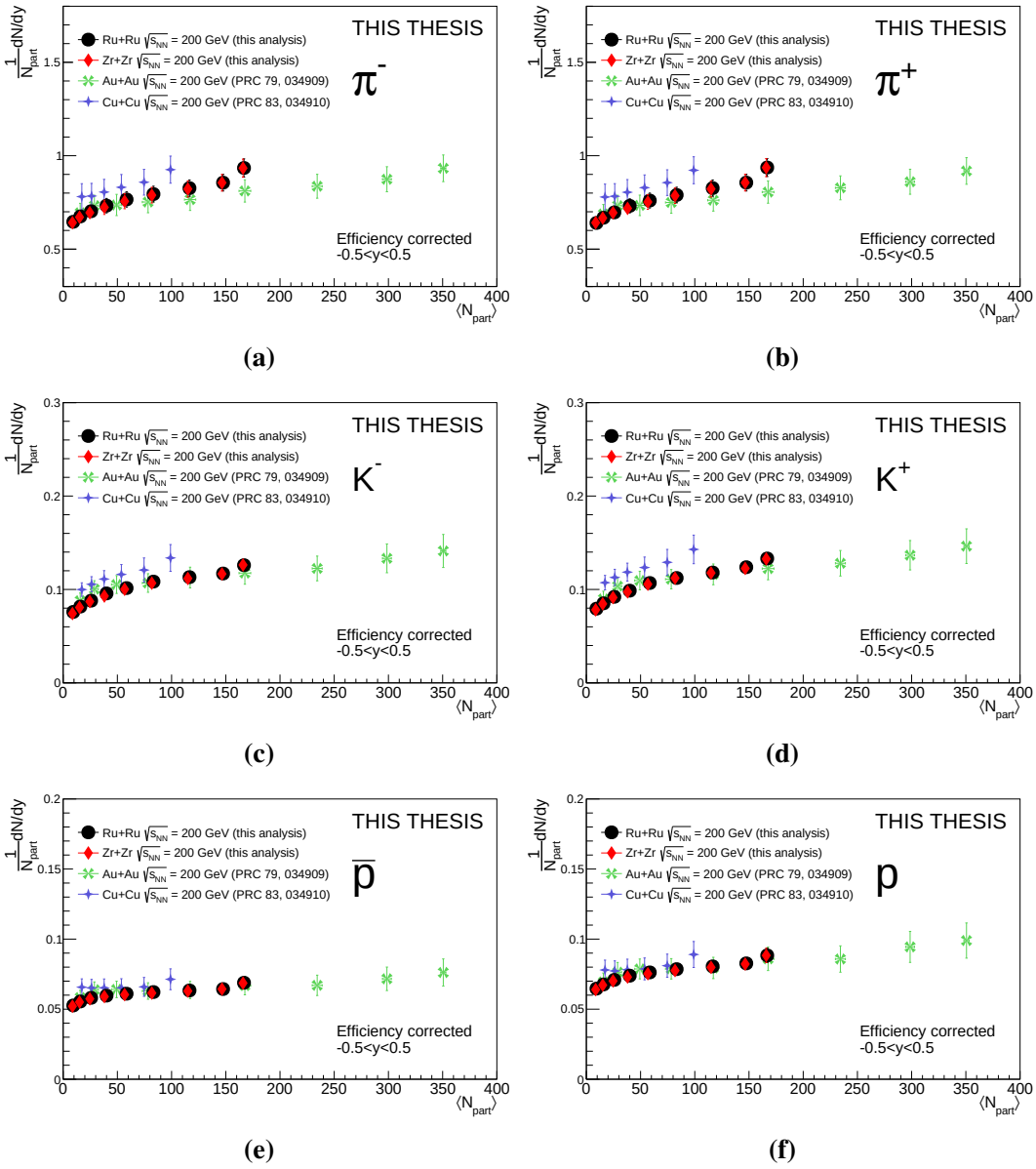

Figure 5.5 The integrated yield ($\mathrm{d}N/\mathrm{d}y$) normalized by N_{part} of $\pi^+(\pi^-)$, $K^+(K^-)$, $p(\bar{p})$ as a function of $\langle N_{\mathrm{part}}\rangle$ for Ru+Ru and Zr+Zr collisions at $\sqrt{s_{\mathrm{NN}}}$ = 200 GeV, and compared to similar results from Cu+Cu and Au+Au collisions at the same energy. The errors displayed in the plot represent the quadratic sum of statistical and systematic uncertainties.

collisions, compared to similar measurements from Au+Au[9] and Cu+Cu[47] collisions. For $\pi^+(\pi^-)$, $\langle p_{\mathrm{T}}\rangle$ is around 0.45 GeV/c, and almost independent of centrality. For $K^+(K^-)$ and $p(\bar{p})$, the $\langle p_{\mathrm{T}}\rangle$ increases with increasing N_{part} or centrality, indicating an increasing radial flow effect from peripheral to central collisions. $\langle p_{\mathrm{T}}\rangle$ also increases from pions to kaons and to protons, consistent with the expectation that heavier particles are more strongly affected by collective flow than lighter particles. The behaviors of $\langle p_{\mathrm{T}}\rangle$ as a function of $\langle N_{\mathrm{part}}\rangle$ for all three particle species in Ru+Ru and Zr+Zr collisions are similar to those observed in 200 GeV Au+Au and Cu+Cu collisions, within uncertainties.

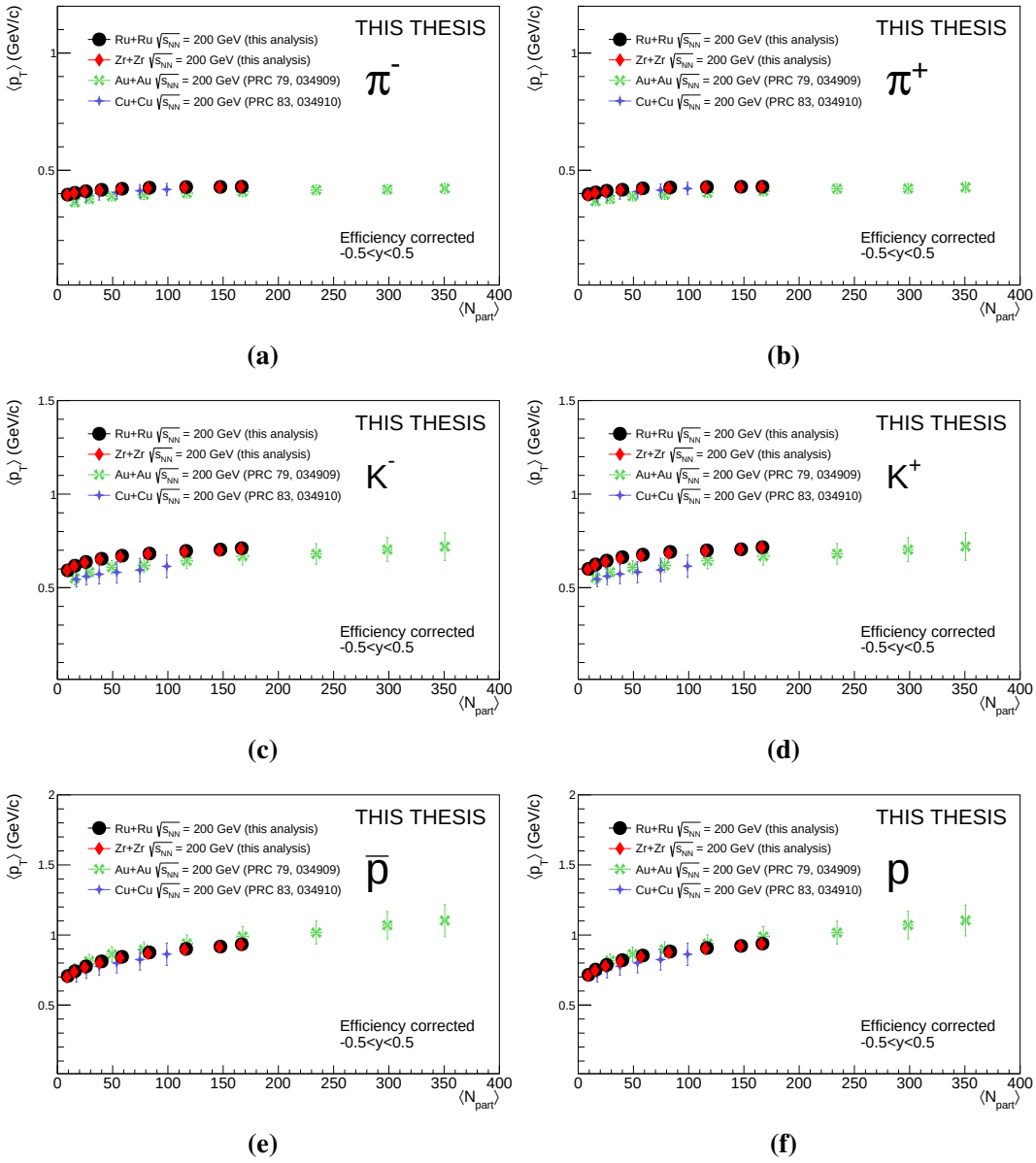

Figure 5.6 Same as Fig. 5.4, but for $\langle p_{\mathrm{T}} \rangle$ measurements.

5.2.3 Antiparticle-to-particle ratios

Ratios of particle yields can be calculated by dividing the integrated $\mathrm{d}N/\mathrm{d}y$ values of different particles and used to study the particle production mechanism. The 5% global cancels in the ratios.

Figure 5.7 illustrates the antiparticle-to-particle ratios (π^-/π^+, K^-/K^+ and $\bar{p}/p$) as a function of N_{part} in Ru+Ru and Zr+Zr collisions at $\sqrt{s_{\mathrm{NN}}}$ = 200 GeV, along with data from Au+Au[9] and Cu+Cu[47] collisions at the same energy. The ratio π^-/π^+ is observed to be roughly unity across all analyzed collision systems, and independent of the centrality. This implies that the production of positive and negative pions is approximately equal. The K^-/K^+ ratios hover around 0.95 (below 1) across all collision

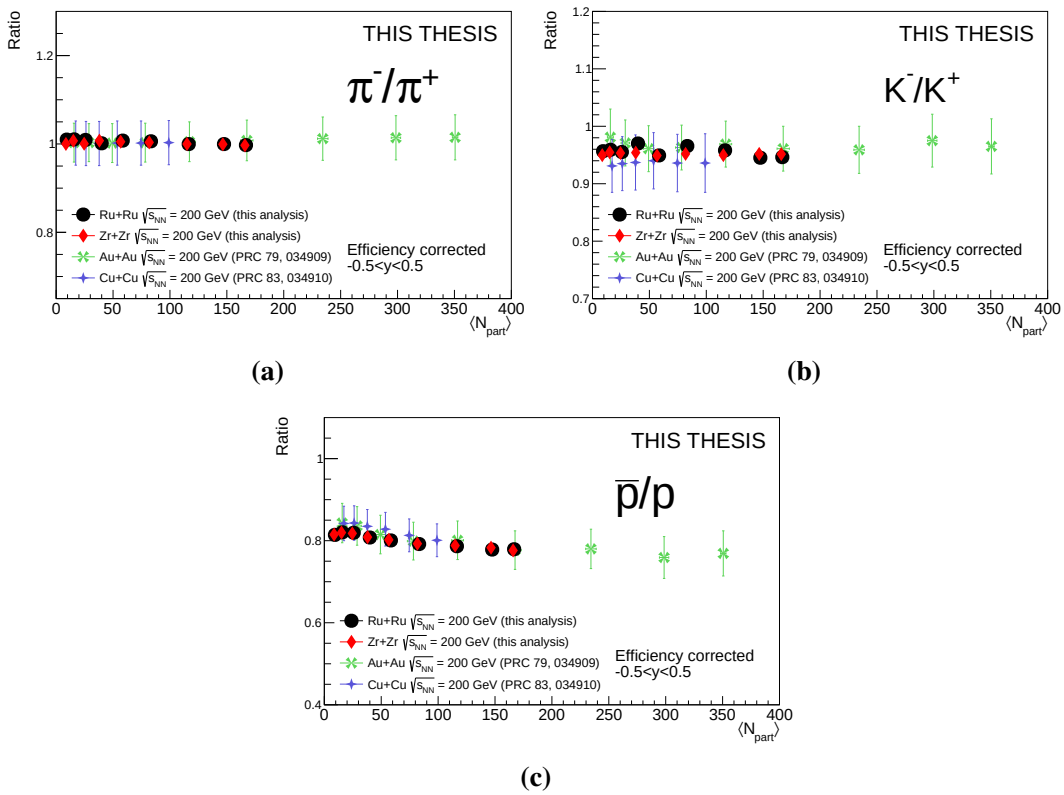

Figure 5.7 The antiparticle-to-particle ratios (π^-/π^+, K^-/K^+ and $\bar{p}/p$) as a function of $\langle N_{\text{part}}\rangle$ for Ru+Ru, Zr+Zr, Cu+Cu and Au+Au collisions at 200 GeV. The errors displayed for results in Ru+Ru and Zr+Zr collisions are statistical uncertainties, while those for Cu+Cu and Au+Au are quadratic sums of statistical and systematic uncertainties.

systems, albeit with large uncertainties. This could be attributed to the production of K^+ in conjunction with the Λ hyperons[9]. The $\bar{p}/p$ ratios are similar across different collision systems at similar $\langle N_{\text{part}}\rangle$, with a slight decreasing trend toward central collisions in all cases. Notably, $\bar{p}$ particles are produced solely through pair production, whereas p particles can either be produced or transported from the colliding nuclei. This drop in the $\bar{p}/p$ ratio is consistent with a larger baryon stopping in central collisions.

It's worth emphasizing that the $\mathrm{d}N/\mathrm{d}y$, $\langle p_{\mathrm{T}}\rangle$, and anti-particle-to-particle ratios all exhibit similar trends in isobar, Cu+Cu, and Au+Au collisions. The observation of consistent behavior across these different collision systems suggests that the driving force behind the collision dynamics and global characteristics of the QGP is primarily the average energy, rather than the specific geometry of the collision. This emphasizes the universal nature of QGP properties.

5.2.4 Kinetic freeze-out parameters

At kinetic freeze-out, elastic interactions among particles cease and their p_{T} spectra are fixed. The Blast-Wave model is used to fit all the identified particle spectra (π^+, π^-,

K^+, K^-, p and $\bar{p}$) simultaneously within a certain centrality interval. Figure 5.3 displays the simultaneous fit of the Blast-Wave model to the spectra of π^-, π^+, K^-, K^+, p, and $\bar{p}$ in the 0-5% most central Ru+Ru and Zr+Zr collisions. The Blast-Wave model provides a good fit for the spectra. The kinetic freeze-out temperature T_{kin}, the average transverse flow velocity $\langle\beta\rangle$, and the exponent of the assumed flow velocity profile n are the free parameters in this model. The fit excludes the low momentum regions of the pion spectra where $p_{\mathrm{T}} < 0.5$ GeV/c. This is due to the Blast-Wave model's inability to accurately describe the pion spectra in this p_{T} region, primarily due to the substantial contributions from resonance decays.

While T_{kin} and $\langle\beta\rangle$ are the primary factors that determine the spectra, the flow velocity profile's shape also has some effect on the spectra due to non-linearity in the spectral shape's dependence on the flow velocity. To evaluate the systematic uncertainty resulting from this effect, the spectra are fitted with the flow velocity profile exponent n fixed at unity instead. The fit quality is significantly degraded for some of the spectra when n is fixed, but still, changes in the fit parameters are used as conservative estimates of the systematic uncertainties.

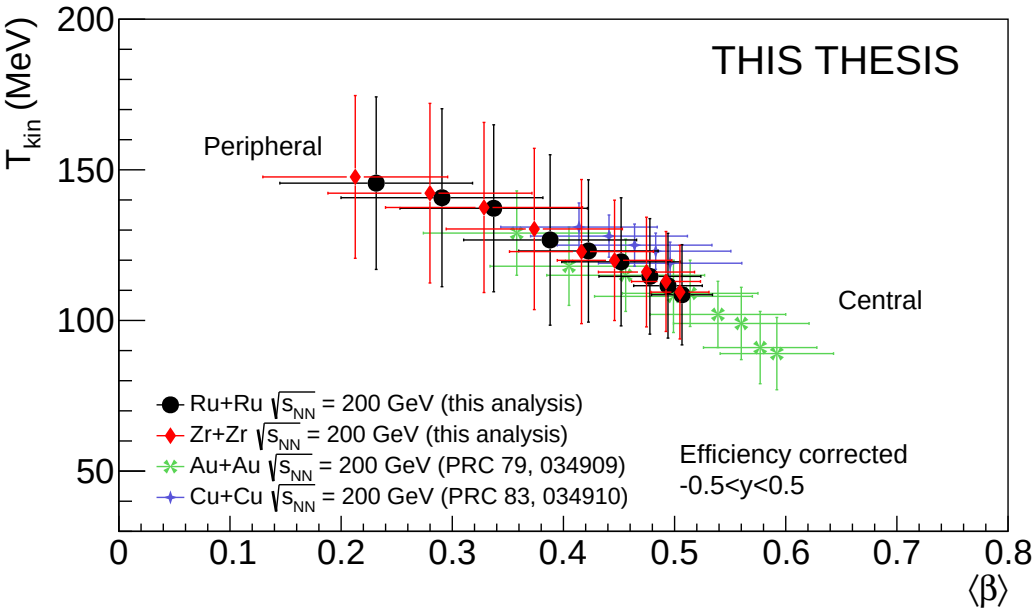

Figure 5.8 The relationship between T_{kin} and $\langle\beta\rangle$ for different collision systems and centrality intervals. For a given system, the centrality increases from left to right. Data points, excluding isobar collisions, are obtained from references[9,47]. The uncertainties presented in the graph represent the combined systematic and statistical uncertainties.

In Fig. 5.8, the variation of T_{kin} with $\langle\beta\rangle$ is shown for different collision systems and centrality intervals. The value of $\langle\beta\rangle$ increases from peripheral to central collisions, suggesting more rapid expansion in central collisions. Conversely, T_{kin} decreases from peripheral to central collisions, consistent with the expectation of a shorter-lived fireball,

and thus higher temperature at freeze-out, in peripheral collisions[141]. Additionally, the parameters demonstrate a two-dimensional anti-correlation band, indicating that higher values of T_{kin} correspond to lower values of $\langle\beta\rangle$, and vice versa. A common trend is seen among all four collision systems (Ru+Ru, Zr+Zr, Au+Au, and Cu+Cu at $\sqrt{s_{\mathrm{NN}}}$ = 200 GeV). While the uncertainties are substantial, the $\langle\beta\rangle$ is systematically higher in Ru+Ru collisions compared to that in Zr+Zr collisions.

5.2.5 Particle yield ratio of Ru+Ru to Zr+Zr collisions

Figure 5.9 presents the ratios of $(dN/dp_{\mathrm{T}})_{\mathrm{Ru+Ru}}/(dN/dp_{\mathrm{T}})_{\mathrm{Zr+Zr}}$ for π^-, K^-, and $\bar{p}$. It is clear that these ratios exceed 1 in all centrality intervals, indicating a higher particle production rate in Ru+Ru collisions compared to Zr+Zr collisions in the same centrality. All of these ratios exhibit an increase as p_{T} increases, and additionally, there is an upward trend from central to peripheral collisions. The centrality dependence appears to be similar for all particle species. Furthermore, for a given centrality, the particle ratio rises more rapidly with an increase in particle mass, suggesting the possible influence of different radial flows in the two collision systems as shown in Fig. 5.10. These could likely be attributed to the differences in nuclear size and structure between Ru and Zr nuclei as shown in Table. 3.2.

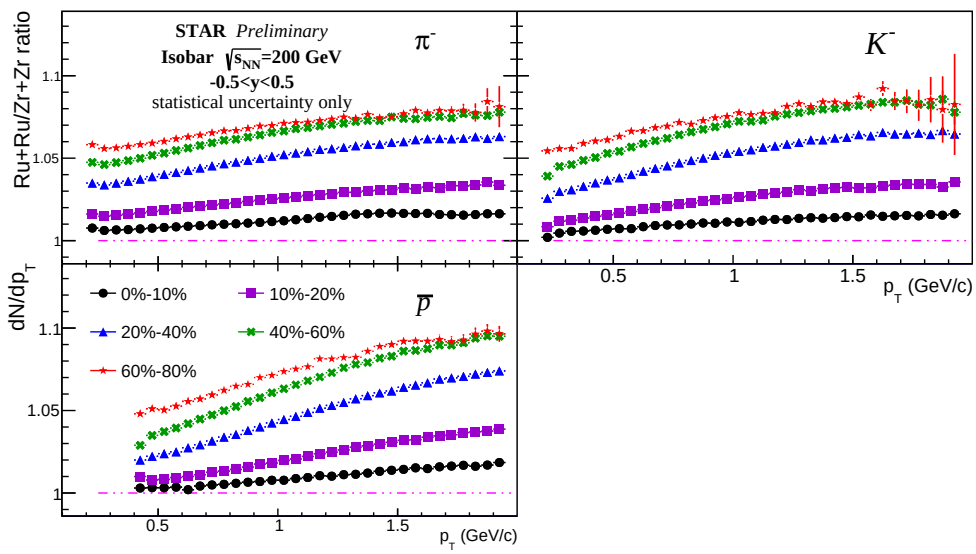

Figure 5.9 Ratios of π^-, K^- and $\bar{p}$ in Ru+Ru/Zr+Zr collisions. The dashed magenta lines are at unity.

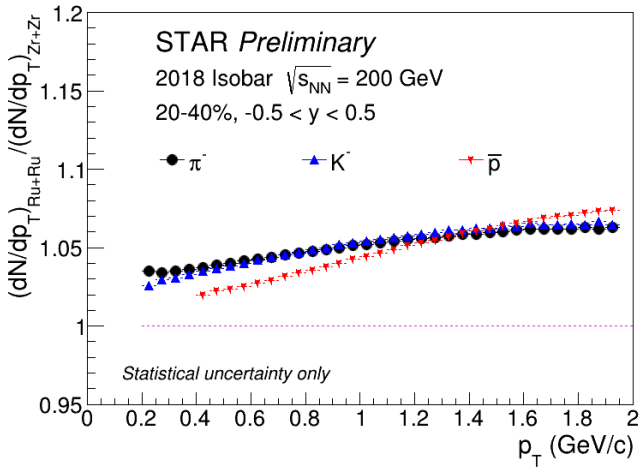

Figure 5.10 Comparison of ratios for π^-, K^- and $\bar{p}$ in 20-40% Ru+Ru/Zr+Zr collisions. The dashed magenta lines are at unity.

5.3 Charge stopping vs. baryon stopping in isobar collisions

As aforementioned, charge stopping and baryon stopping at mid-rapidity can be compared to distinguish different models of baryon number carriers. If valence quarks carry the baryon number, the ratio of net-baryon number (B) to net-charge difference between Ru+Ru and Zr+Zr collisions should be close to $A/\Delta Z$ = 96/4. Otherwise, if the baryon junction carries the baryon number, $B/\Delta Q > A/\Delta Z$ due to enhanced baryon stopping. Since pions, kaons, and protons (as well as anti-protons) constitute the majority of particles produced in heavy-ion collisions, the net charge Q can be expressed as Eq. 5.12.

$$Q = (N_{\pi^+} + N_{K^+} + N_p) - (N_{\pi^-} + N_{K^-} + N_{\bar{p}}). \tag{5.12}$$

The net-charge difference (ΔQ) between Ru+Ru and Zr+Zr collisions is:

$$\begin{aligned}
\Delta Q &= (Q_{Ru} - Q_{Zr}) \\
&= [(N_{\pi^+} + N_{K^+} + N_p) - (N_{\pi^-} + N_{K^-} + N_{\bar{p}})]_{Ru} \\
&- [(N_{\pi^+} + N_{K^+} + N_p) - (N_{\pi^-} + N_{K^-} + N_{\bar{p}})]_{Zr} \\
&= [(N_{\pi^+} - N_{\pi^-})_{Ru} - (N_{\pi^+} - N_{\pi^-})_{Zr}] \\
&+ [(N_{K^+} - N_{K^-})_{Ru} - (N_{K^+} - N_{K^-})_{Zr}] \\
&+ [(N_p - N_{\bar{p}})_{Ru} - (N_p - N_{\bar{p}})_{Zr}].
\end{aligned} \tag{5.13}$$

Here we introduce the double ratio of particle yields between Ru+Ru and Zr+Zr

collisions. Equation 5.14 is an example of the pion double ratio:

$$\begin{aligned} R2_\pi &= \frac{(N_{\pi^+}/N_{\pi^-})_{Ru}}{(N_{\pi^+}/N_{\pi^-})_{Zr}} \\ &= \frac{[1+(N_{\pi^+}-N_{\pi^-})/N_{\pi^-}]_{Ru}}{[1+(N_{\pi^+}-N_{\pi^-})/N_{\pi^-}]_{Zr}} \\ &\approx \frac{[1+(N_{\pi^+}-N_{\pi^-})/N_{\pi}]_{Ru}}{[1+(N_{\pi^+}-N_{\pi^-})/N_{\pi}]_{Zr}} \\ &= \frac{1+\Delta R_\pi^{Ru}}{1+\Delta R_\pi^{Zr}} \approx 1+\Delta R_\pi^{Ru}-\Delta R_\pi^{Zr}, \end{aligned} \tag{5.14}$$

where $N_\pi = (N_{\pi^+} + N_{\pi^-})/2$. Double ratios of kaon and proton are defined similarly. Then the net-charge difference (ΔQ) can be calculated based on the double ratios of particle yields:

$$\begin{aligned} \Delta Q &\approx N_\pi(R2_\pi - 1) + N_K(R2_K - 1) + N_p(R2_p - 1) \\ &= N_\pi[(R2_\pi - 1) + \frac{N_K}{N_\pi}(R2_K - 1) + \frac{N_p}{N_\pi}(R2_p - 1)], \end{aligned} \tag{5.15}$$

where the average values of N_π, N_K and N_p between Ru+Ru and Zr+Zr collisions are used for the net-charge difference calculation.

The net-baryon B can be calculated approximately as:

$$B = (N_p - N_{\bar{p}}) + (N_n - N_{\bar{n}}). \tag{5.16}$$

As neutrons are charge-neutral particles, their yields cannot be directly measured at STAR. Hence, yields of deuterons and anti-deuterons are used to estimate the neutron yields.

Within the framework of the statistical thermal model[48,142], Eq. 5.17 gives the particle multiplicity from a source with volume V and chemical freeze-out temperature T.

$$N_i = \frac{g_i V}{\pi^2} m_i^2 T K_2(m_i/T) exp(\mu_i/T). \tag{5.17}$$

The equation includes variables such as g_i, m_i, and μ_i, which represent the degeneracy, particle mass, and chemical potential of a specific particle species i, respectively. The chemical potential of a particle species i can be expressed as the sum of the products of the baryon number, strangeness, and charge of that species, with their corresponding chemical potentials μ_B, μ_S, and μ_Q, respectively. Consequently, multiplicities of protons (anti-protons), deuterons (anti-deuterons), and neutrons (anti-neutrons) can be described in terms of conserved quantum numbers and their associated chemical poten-

tials. We also make the assumption that protons and neutrons share the same mass.

$$
\begin{aligned}
N_d &= \frac{g_d V}{\pi^2} m_d^2 T K_2(m/T) exp(2\mu_B + \mu_Q), \\
N_{\bar{d}} &= \frac{g_{\bar{d}} V}{\pi^2} m_{\bar{d}}^2 T K_2(m/T) exp(-2\mu_B - \mu_Q), \\
N_p &= \frac{g_p V}{\pi^2} m_p^2 T K_2(m/T) exp(\mu_B + \mu_Q), \\
N_{\bar{p}} &= \frac{g_{\bar{p}} V}{\pi^2} m_{\bar{p}}^2 T K_2(m/T) exp(-\mu_B - \mu_Q), \\
N_n &\approx \frac{g_n V}{\pi^2} m_p^2 T K_2(m/T) exp(\mu_B), \\
N_{\bar{n}} &\approx \frac{g_{\bar{n}} V}{\pi^2} m_p^2 T K_2(m/T) exp(-\mu_B).
\end{aligned}
\tag{5.18}
$$

The expressions of N_n and $N_{\bar{n}}$ can be further derived as Eq. 5.19.

$$
\begin{aligned}
N_n &= N_{\bar{p}} \sqrt{\frac{N_d}{N_{\bar{d}}}}, \\
N_{\bar{n}} &= N_p \sqrt{\frac{N_{\bar{d}}}{N_d}}.
\end{aligned}
\tag{5.19}
$$

As a result, the net-baryon yield can be computed using Eq. 5.20, where the N_d and $N_{\bar{d}}$ values are from a separate analysis.

$$
B = (N_p - N_{\bar{p}}) + N_{\bar{p}} \sqrt{\frac{N_d}{N_{\bar{d}}}} - N_p \sqrt{\frac{N_{\bar{d}}}{N_d}}, \tag{5.20}
$$

where the average values of N_p, $N_{\bar{p}}$, N_d and $N_{\bar{d}}$ between Ru+Ru and Zr+Zr collisions are used for the calculation.

Figure 5.11 illustrates the double ratios $R2_\pi$, $R2_K$, and $R2_p$ between Ru+Ru and Zr+Zr collisions as a function of p_{T} for different centrality intervals. The magenta dotted lines represent the baseline at 1. The double ratios for pion and proton take a value around 1.001, while it is consistent with 1 for kaon. They are extrapolated to the unmeasured p_{T} region using a linear function. The Blast-Wave models are used to fit the corrected spectra for $\pi^+(\pi^-)$, $K^+(K^-)$, $p(\bar{p})$, and $d(\bar{d})$ in Ru+Ru and Zr+Zr collisions at corresponding centrality intervals are shown in Figure 5.12 and 5.13, represented by dashed curves, in order to extrapolate to unmeasured regions. It is worth noting that the fit is done separately for different particle species, unlike the case of extracting the freeze-out parameters. No feed-down corrections for weak decays have been applied to the corrected spectra, as we aim to retain all the particles produced in the collisions

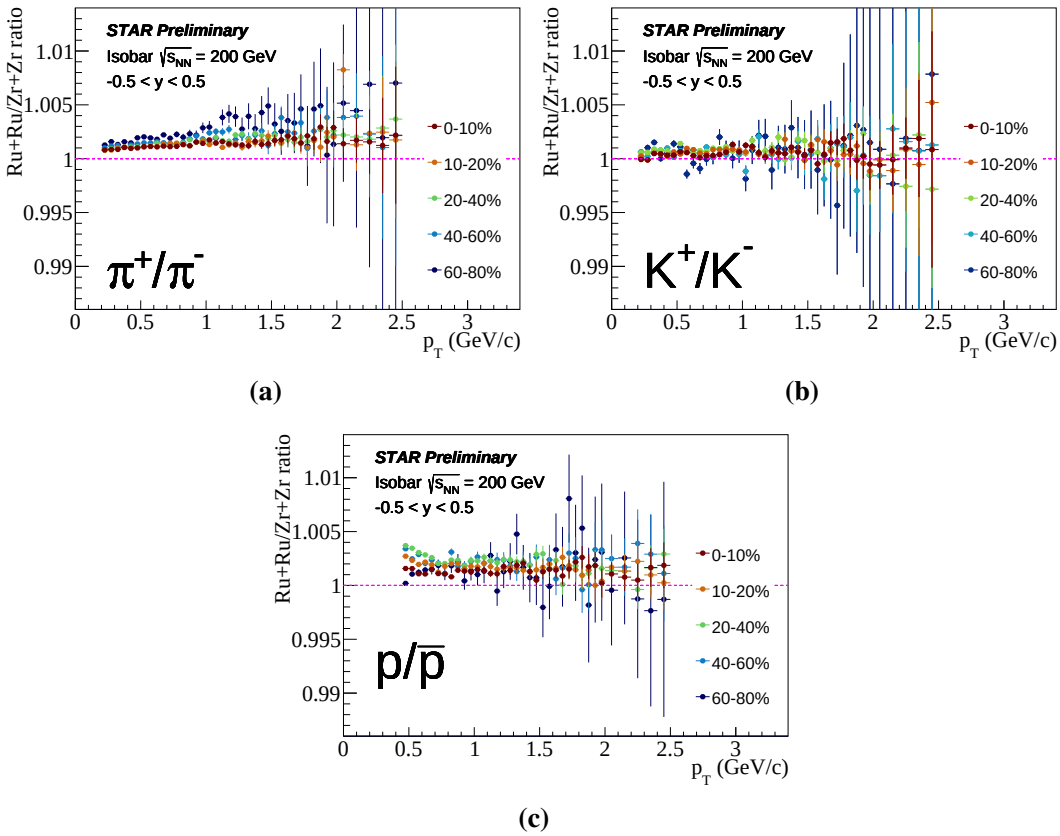

Figure 5.11 Double ratios for π^+/π^-, K^+/K^- and $p/\bar{p}$ as a function of p_T within $|y| < 0.5$ in Ru+Ru/Zr+Zr collisions at different centrality intervals.

for studying baryon and charge stopping. Finally, the ΔQ and B are first evaluated as a function of p_T and then integrated over p_T. The statistical uncertainties on B and ΔQ are evaluated based on the statistical uncertainties on double ratios and the spectra using a Monte-Carlo sampling method.

Figure 5.14 depicts the ratio of B to ΔQ scaled by $\Delta Z/A$ (4/96) plotted against $\langle N_{part} \rangle$. The data points with systematic uncertainties are represented by solid red circles with rectangular boxes. The $B/\Delta Q$ ratio between the two colliding systems is found to be approximate twice the ratio of mass number to atomic number differences (i.e. 96/4) in central collisions, indicating a strong enhancement of baryon stopping. The $B/\Delta Q$ ratio also shows a centrality dependence, with the value decreasing as $\langle N_{\text{part}} \rangle$ decreases. Calculations from Ultra-relativistic Quantum Molecular Dynamics (UrQMD) model[144-146] for isobar collisions and the HERWIG event generator[147-148] for p+p collisions at 200 GeV are shown as hatched band and open star, respectively, in Fig. 5.14 for comparison. Neither of the models implements the baryon junction mechanism, and their predictions are significantly below the measurement.

Additionally, the intriguing centrality dependence observed in the $B/\Delta Q$ ratio could be attributed to different neutron skin thickness in the two isobaric nuclei[143,149].

Despite the isospin symmetry of the strong force in the nucleus, heavy nuclei typically demand more neutrons than protons for their stability, as Coulomb interactions become significant. This results in the root-mean-square radius of the neutron distribution in heavy nuclei being larger than that of the proton distribution, leading to a disparity known as the neutron skin thickness $\Delta r_{\mathrm{np}} = r_{\mathrm{n}} - r_{\mathrm{p}}$[150]. Here, r_{n} and r_{p} represent the root-mean-square radii of the neutron and proton distributions, respectively. Figure 5.15 shows the dependence of the proton fraction (q_{AA}) among participating nucleons at the initial stage of the collision on the charged hadron multiplicity (N_{ch}), calculated based on the Trento model[151]. The dashed curves represent the results from Ru+Ru collisions, while the solid curves depict those from Zr+Zr collisions. The dotted and short dashed lines indicate the overall values of 44/96 and 40/96, corresponding to the fraction of protons in the entire Ru and Zr nuclei, respectively. The values of q_{AA} are calculated with four sets of nuclear densities derived from the density functional theory (DFT). The first set is based on the standard Skyrme-Hartree-Fock (SHF) model using the well-established interaction set SLy4. The other three sets are obtained from the extended SHF (eSHF) model, using three different sets of interaction parameters, denoted as Lc47, Lc20, and Lc70. These labels correspond to L_c values of 47.3, 20, and 70 MeV, respectively, for different neutron skin depths[143]. The curves obtained from different parameter sets exhibit an increase with rising multiplicity, and the differences between these curves decrease from peripheral to central collisions. Using the parameter sets Lc20 and Lc70, the $B/\Delta Q$ value, multiplied by 4/96, as a function of centrality from the Trento model is shown in Fig. 5.14 as the solid band. The numbers of nucleons and protons in the interaction zone are used to calculate B and ΔQ, respectively. A similar decreasing trend with centrality is seen as that observed in data, suggesting its origin to be the difference in the neutron skin depths between the two isobars. Even when taking into account the neutron skin thickness, the Trento calculations are still significantly below the measurements. This observation supports the baryon junction hypothesis, which predicts an enhanced interaction cross section and a different distribution function compared to valence quarks.

Figures 5.16 and 5.17 provide additional insight by comparing separately the net-baryon number between Ru+Ru and Zr+Zr collisions and net-charge difference to the UrQMD calculations. The solid red circles with rectangular boxes indicate the experimental data with the box height representing the systematic uncertainties, while the hatched bands represent predictions from the UrQMD model. In Fig. 5.16, the average net-baryon yields in Ru+Ru and Zr+Zr collisions are consistent with the UrQMD results,

especially in central collisions. This is likely due to that the UrQMD has been tuned to reproduce baryon production at mid-rapidity since a wealth of data is available. On the other hand, Fig. 5.17 reveals that the simulated net-charge difference between Ru+Ru and Zr+Zr collisions in UrQMD is almost a factor 3 higher than the measurement in central collisions. Since there are no measurements of charge stopping at mid-rapidity to date, UrQMD could not be tuned previously. The larger charge stopping predicted by UrQMD than that observed in data is likely due to that a large number of quarks are forced to be stopped at mid-rapidity in order to match the baryon yield, resulting in an overprediction of the charge stopping.

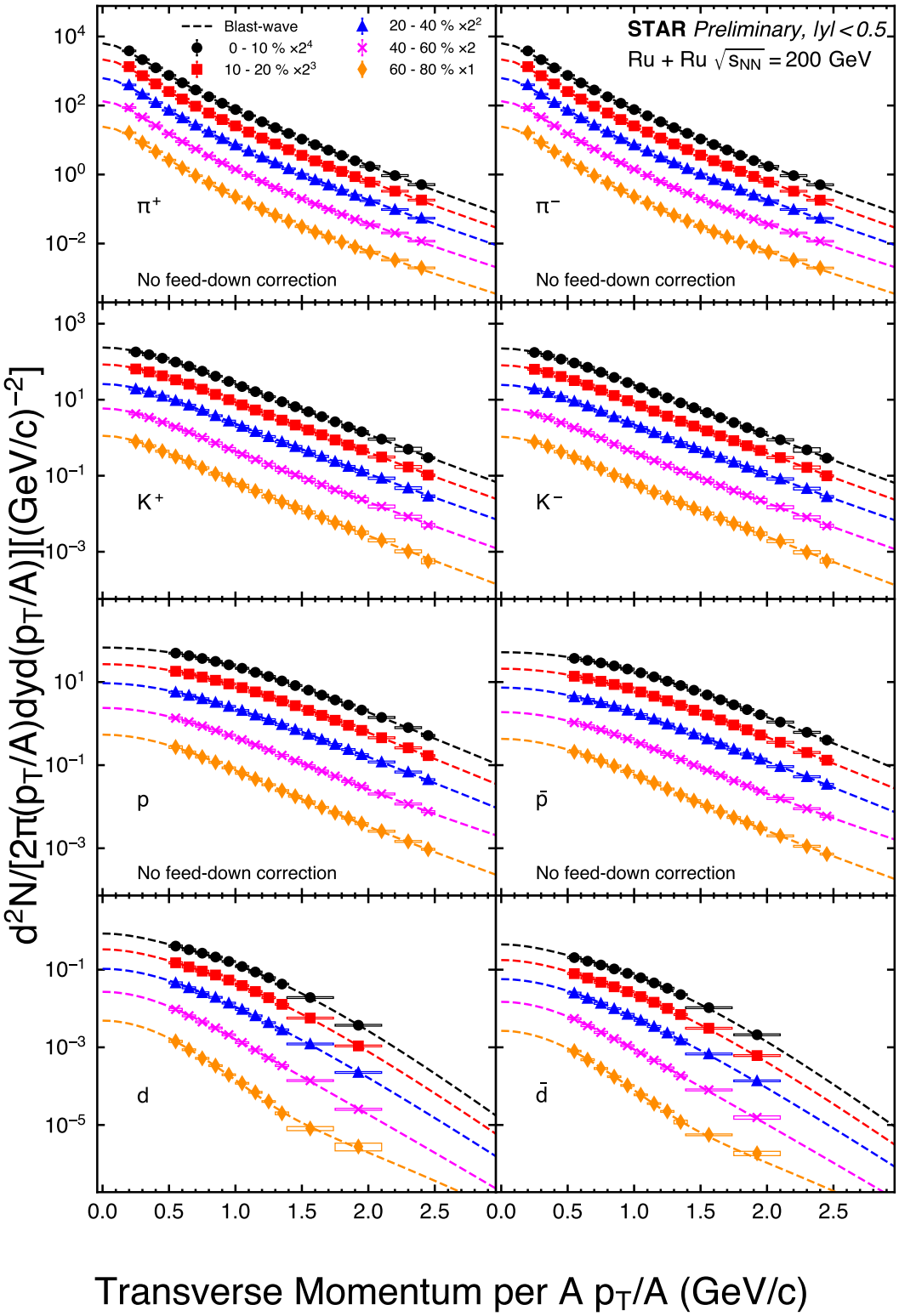

Figure 5.12 **Identified particle spectra in mid-rapidity region ($|y| < 0.5$) for Ru+Ru collisions at $\sqrt{s_{NN}}$ = 200 GeV, separated into five centrality bins: 0-10%, 10-20%, 20-40%, 40-60%, and 60-80%. The box around each data point represents the systematic uncertainty, while the statistical uncertainties are smaller than the marker size. The dashed curves represent fits of the Blast-Wave model to the spectra, and arbitrary scale factors, listed in the figure, are applied for better clarity.**

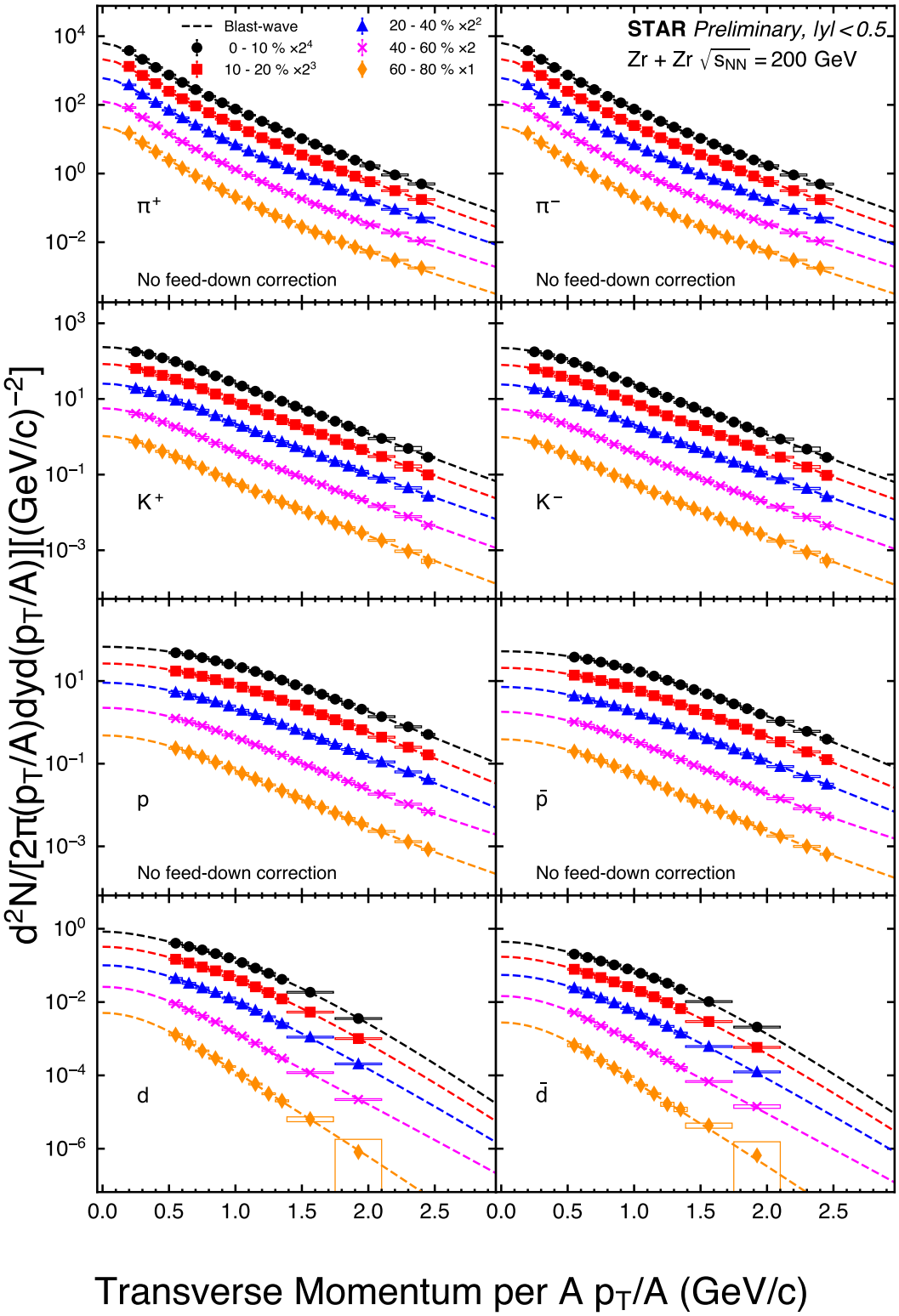

Figure 5.13 **Same as Fig. 5.12, but for Zr+Zr collisions.**

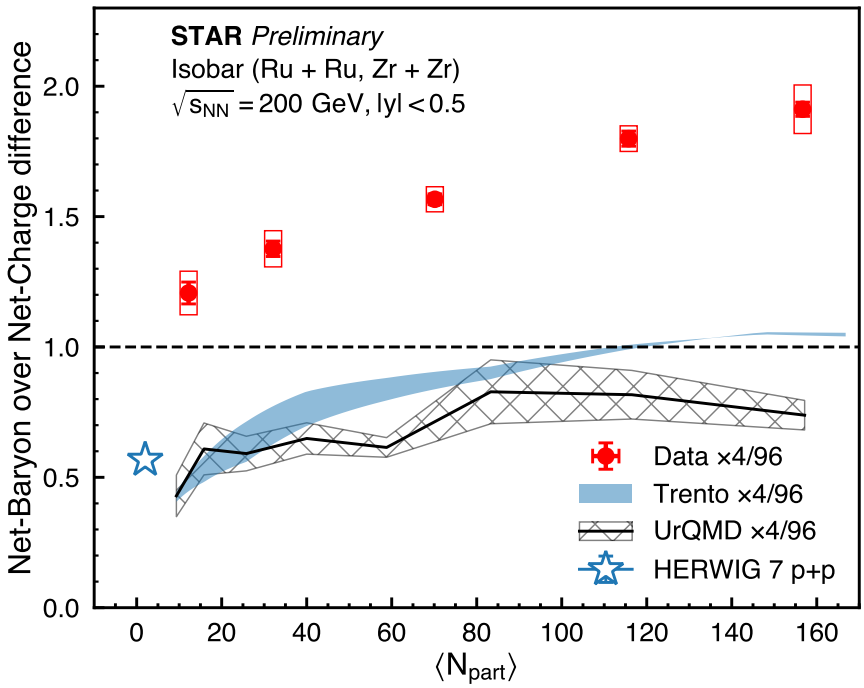

Figure 5.14 The ratio of net-baryon to net-charge difference between Ru+Ru and Zr+Zr collisions as a function of $\langle N_{\text{part}} \rangle$, scaled by 4/96 = $\Delta Z/A$. The solid circles with rectangular boxes represent data with box heights representing systematic uncertainties. Calculations from UrQMD, HERWIG, and Trento are shown as the hatched band, open star, and solid band for comparison.

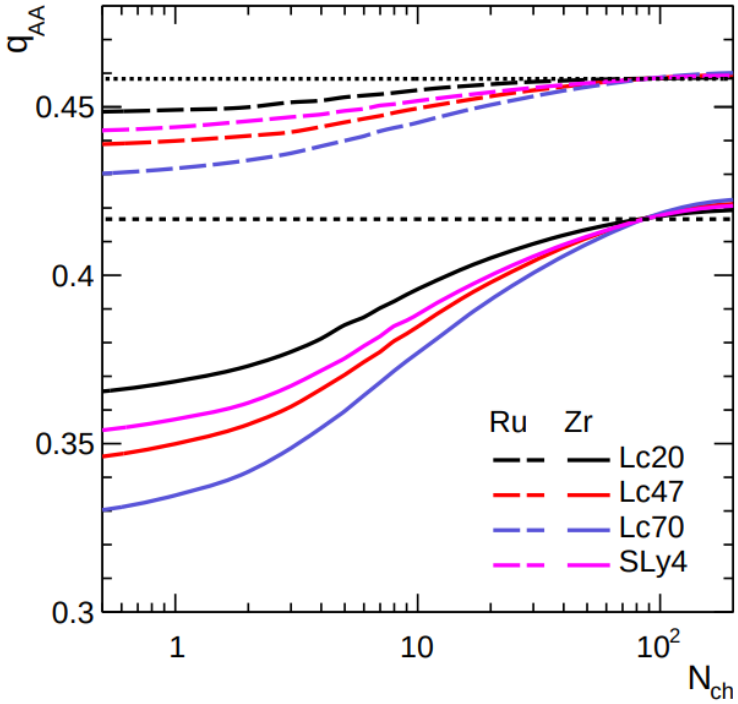

Figure 5.15 The proton fractions q_{AA} in the participating nucleons as a function of charged hadron multiplicity N_{ch} calculated using the Trento model with nuclear densities from eSHF (Lc20, Lc47, Lc70) and SHF (SLy4) for $^{96}_{44}$Ru and $^{96}_{40}$Zr. The overall values of 44/96 and 40/96 for the entire Ru and Zr nuclei are indicated by the dotted and dashed lines. Figure is taken from [143]

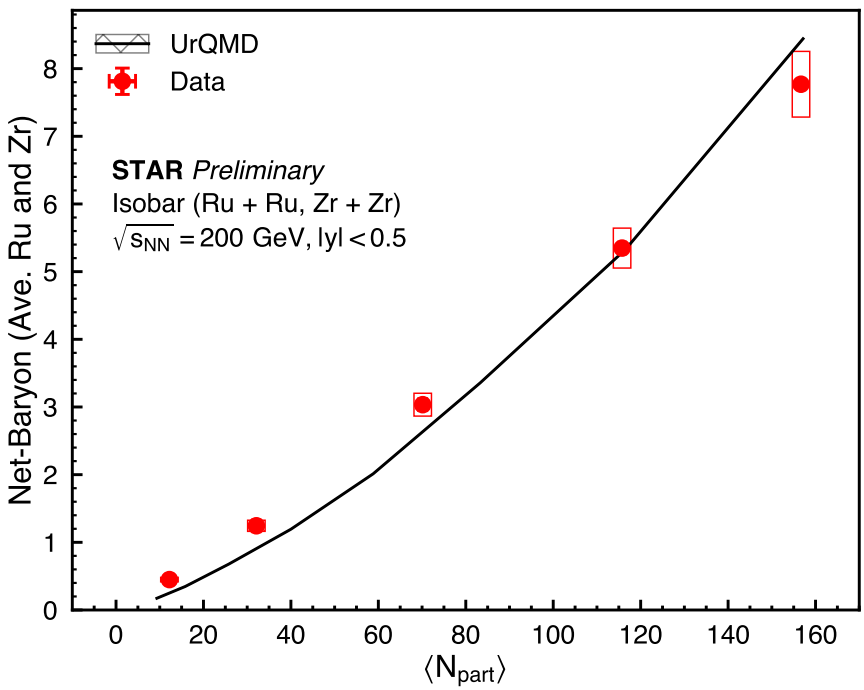

Figure 5.16 Average net-baryon yield in Ru+Ru and Zr+Zr collisions as a function of $\langle N_{part} \rangle$. The solid circles with rectangular boxes depict data with box heights representing systematic uncertainties. The hatched band denotes predictions from UrQMD model.

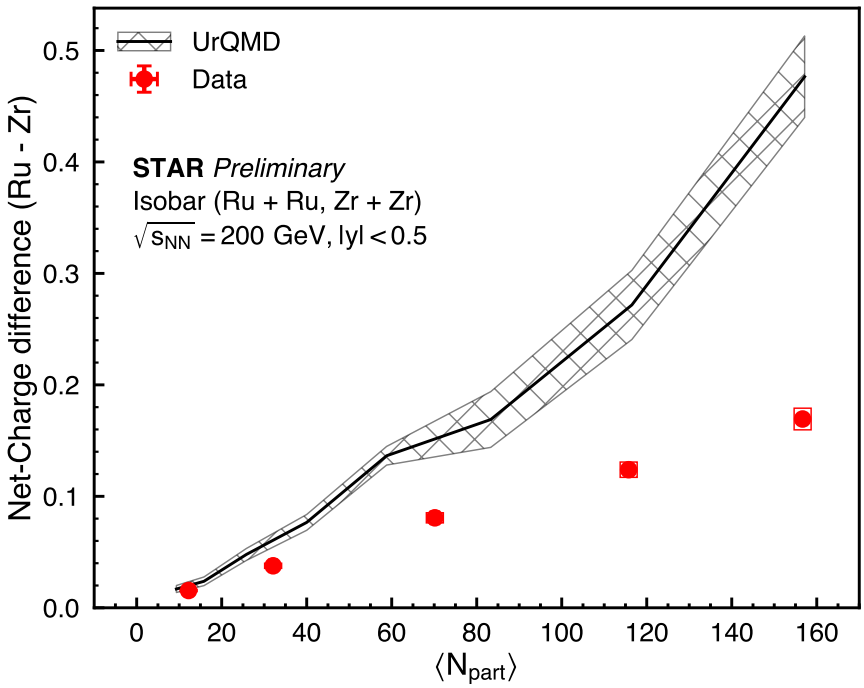

Figure 5.17 The variation of net-charge difference between Ru+Ru and Zr+Zr collisions as a function of $\langle N_{\text{part}} \rangle$. The solid circles with rectangular boxes represent data with box heights representing systematic uncertainties. The hatched band denotes predictions from UrQMD model.

Chapter 6 Summary and outlook

The thesis presents the first measurements of identified particle spectra, including positively and negatively charged pion, kaon and proton, at mid-rapidity ($|y| < 0.5$) in Ru+Ru and Zr+Zr collisions at $\sqrt{s_{\mathrm{NN}}}$ = 200 GeV using the STAR detector at RHIC. These spectra are obtained from the raw yields extracted based on the energy loss and flight time information for particle identification, and corrected for detector effects evaluated using both data-driven and simulation methods. The final pion spectra are obtained within the p_{T} range of $0.2 < p_{\mathrm{T}} < 2.5$ GeV/c. For kaons and protons, the ranges are $0.3 < p_{\mathrm{T}} < 2.5$ GeV/c and $0.5 < p_{\mathrm{T}} < 2.5$ GeV/c, respectively.

The transverse momentum spectra are extrapolated to unmeasured regions using a hydrodynamics-inspired Blast-Wave model for kaons and protons, and a Bose-Einstein function for pions. This extrapolation allows for calculating integrated particle multiplicity density ($\mathrm{d}N/\mathrm{d}y$), average transverse momenta ($\langle p_{\mathrm{T}} \rangle$), and the anti-particle-to-particle ratio. These results are subsequently reported. The $\mathrm{d}N/\mathrm{d}y$ measured in Ru+Ru, Zr+Zr, Cu+Cu, and Au+Au collisions is seen to follow a command trend as a function of N_{part}, indicating that the average energy density (or N_{part}) primarily governs the collision dynamics. The average transverse momentum ($\langle p_{\mathrm{T}} \rangle$) increases both with particle mass within each collision system and with centrality for each particle species. This trend can be attributed to the radial flow effect, which is known to intensify with increasing particle mass and collision centrality. The π^-/π^+ ratio is close to unity in all collision systems, hinting at a slight excess due to the isospin effect. The K^-/K^+ ratio is around 0.95, possibly due to associated K^+ production with Λ hyperons. The $\bar{p}/p$ ratio shows a mild decline in central collisions, consistent with larger baryon stopping[9]. The $\mathrm{d}N/\mathrm{d}y$, $\langle p_{\mathrm{T}} \rangle$, and anti-particle-to-particle ratios show consistent trends across isobar, Cu+Cu, and Au+Au collisions, implying that the QGP's properties are primarily influenced by average energy and not collision geometry, highlighting the universality of QGP characteristics. The kinetic freeze-out temperature, determined from the Blast-Wave fit to the transverse momentum spectra of all six particle species simultaneously, decreases from peripheral to central collisions. Meanwhile, the radial flow velocity of the system at kinetic freeze-out exhibits a substantial increase toward central collisions. The anti-correlations between T_{kin} and $\langle \beta \rangle$ for Ru+Ru and Zr+Zr collisions closely resemble each other and are in line with the previous measurements from Au+Au and Cu+Cu collisions.

More importantly, a novel method is employed to measure the net-charge difference at mid-rapidity between Ru+Ru and Zr+Zr collisions, based on the double ratios of the antiparticle to particle and Ru+Ru to Zr+Zr to study the baryon stopping. Since the Ru+Ru and Zr+Zr data were taken with almost identical collider and detector conditions, the double ratios can be measured with high precision despite their small values. The net-charge difference can be compared to the average baryon number in Ru+Ru and Zr+Zr collisions within the same rapidity range for testing what carries the baryon number. In isobar collisions, it is observed that there is more baryon stopping than charge stopping compared to the expectation of valence quarks carrying the baryon number. The results are consistent with the predictions of the baryon junction hypothesis, which suggests a Y-shaped configuration of low-momentum gluons carrying the baryon number. The baryon junction is more likely to be stopped at mid-rapidity than valence quarks due to its smaller momentum. Previous measurements in γ+Au collisions have shown significant baryon stopping in these processes, and the slope of the net-proton yield as a function of rapidity is significantly smaller than the model calculation with valence quarks carrying the baryon number. Furthermore, the dependences of net-proton yields on rapidity loss in hadronic Au+Au collisions are consistent among different centrality intervals and can be explained by the baryon junction hypothesis. Put these together, all three independent measurements collectively disfavor the scenario where valence quarks carry the baryon number, and are consistent with the baryon junction mechanism.

For the future study of bulk properties, chemical freeze-out parameters can be obtained by examining particle yields, and the properties of QGP can be further explored through other probes, such as fully reconstructed jets. Additionally, it is possible to probe the initial geometries of isobar nuclei by utilizing the average transverse momentum ratio, $R_{\langle p_{\mathrm{T}} \rangle} = \frac{\langle p_{\mathrm{T}} \rangle_{Ru+Ru}}{\langle p_{\mathrm{T}} \rangle_{Zr+Zr}}$, between Ru+Ru and Zr+Zr collisions. This ratio is unaffected by bulk evolution, and thus sensitive to subtle variances in the initial nuclear structure, such as neutron skin and deformation, of the Ru and Zr nuclei[140].

There are also numerous future opportunities for further investigations of charge and baryon stopping. One possibility is to analyze photo-nuclei events across various collision systems and energies. Another avenue is to compare charge stopping and baryon stopping in Au+Au and O+O collisions at $\sqrt{s_{\mathrm{NN}}}$ = 200 GeV and U+U collisions at $\sqrt{s_{\mathrm{NN}}}$ = 193 GeV. This can be achieved by constructing double ratios between the two collisions at the same multiplicity. Measuring charge stopping vs. rapidity using d+Au collisions at 200, 62.4, 39, and 20 GeV can shed new light on the underlying

mechanism. One can tag the neutron from the incoming deuteron in the ZDC for peripheral d+Au collisions, which should be dominated by cases of one nucleon from the deuteron interacting with the Au. If one sees a neutron in the ZDC, it is effectively a p+Au collision. If not, it is more like a n+Au collision. One can construct double ratios between p+Au and n+Au collisions, and explore charge stopping against δy for different beam energies. Moreover, with the upcoming Electron-Ion Collider, a wealth of new opportunities will emerge to explore the baryon-stopping mechanism in great detail. In particular, one might be able to measure the baryon junction distribution in the nucleon, similar to the well-known parton distribution function, with the Electron Ion Collider[152].

Bibliography

[1] Standard model[EB/OL]. https://en.wikipedia.org/wiki/Standard_Model.

[2] HIGGS P W. Broken symmetries, massless particles and gauge fields[J/OL]. Phys. Lett., 1964, 12: 132-133. DOI: 10.1016/0031-9163(64)91136-9.

[3] HIGGS P W. Broken Symmetries and the Masses of Gauge Bosons[J/OL]. Phys. Rev. Lett., 1964, 13: 508-509. DOI: 10.1103/PhysRevLett.13.508.

[4] AAD G, et al. Observation of a new particle in the search for the Standard Model Higgs boson with the ATLAS detector at the LHC[J/OL]. Phys. Lett. B, 2012, 716: 1-29. DOI: 10.1016/j.physletb.2012.08.020.

[5] CHATRCHYAN S, et al. Observation of a New Boson at a Mass of 125 GeV with the CMS Experiment at the LHC[J/OL]. Phys. Lett. B, 2012, 716: 30-61. DOI: 10.1016/j.physletb.2012.08.021.

[6] WORKMAN R L, et al. Review of Particle Physics[J/OL]. PTEP, 2022, 2022: 083C01. DOI: 10.1093/ptep/ptac097.

[7] WILSON K G. Confinement of Quarks[J/OL]. Phys. Rev. D, 1974, 10: 2445-2459. DOI: 10.1103/PhysRevD.10.2445.

[8] BAZAVOV A, et al. Chiral crossover in QCD at zero and non-zero chemical potentials[J/OL]. Phys. Lett. B, 2019, 795: 15-21. DOI: 10.1016/j.physletb.2019.05.013.

[9] ABELEV B I, et al. Systematic Measurements of Identified Particle Spectra in pp, d+Au and Au+Au Collisions from STAR[J/OL]. Phys. Rev. C, 2009, 79: 034909. DOI: 10.1103/PhysRevC.79.034909.

[10] LEE T D. Abnormal nuclear states and vacuum excitation[J]. Reviews of Modern Physics, 1975, 47(2): 267.

[11] ADAMCZYK L, et al. Bulk Properties of the Medium Produced in Relativistic Heavy-Ion Collisions from the Beam Energy Scan Program[J/OL]. Phys. Rev. C, 2017, 96(4): 044904. DOI: 10.1103/PhysRevC.96.044904.

[12] AOKI Y, ENDRODI G, FODOR Z, et al. The Order of the quantum chromodynamics transition predicted by the standard model of particle physics[J/OL]. Nature, 2006, 443: 675-678. DOI: 10.1038/nature05120.

[13] BAZAVOV A, et al. The chiral and deconfinement aspects of the QCD transition[J/OL]. Phys. Rev. D, 2012, 85: 054503. DOI: 10.1103/PhysRevD.85.054503.

[14] BELLWIED R, BORSANYI S, FODOR Z, et al. The QCD phase diagram from analytic continuation[J/OL]. Phys. Lett. B, 2015, 751: 559-564. DOI: 10.1016/j.physletb.2015.11.0

11.

[15] BORSANYI S, FODOR Z, GUENTHER J N, et al. QCD Crossover at Finite Chemical Potential from Lattice Simulations[J/OL]. Phys. Rev. Lett., 2020, 125(5): 052001. DOI: 10.1103/PhysRevLett.125.052001.

[16] FUKUSHIMA K, HATSUDA T. The phase diagram of dense QCD[J/OL]. Rept. Prog. Phys., 2011, 74: 014001. DOI: 10.1088/0034-4885/74/1/014001.

[17] LUO X, SHI S, XU N, et al. A Study of the Properties of the QCD Phase Diagram in High-Energy Nuclear Collisions[J/OL]. Particles, 2020, 3(2): 278-307. DOI: 10.3390/particles3 020022.

[18] BZDAK A, ESUMI S, KOCH V, et al. Mapping the Phases of Quantum Chromodynamics with Beam Energy Scan[J/OL]. Phys. Rept., 2020, 853: 1-87. DOI: 10.1016/j.physrep.2020 .01.005.

[19] LUO X, XU N. Search for the QCD Critical Point with Fluctuations of Conserved Quantities in Relativistic Heavy-Ion Collisions at RHIC : An Overview[J/OL]. Nucl. Sci. Tech., 2017, 28(8): 112. DOI: 10.1007/s41365-017-0257-0.

[20] ABELEV B I, et al. Experimental Study of the QCD Phase Diagram and Search for the Critical Point: Selected Arguments for the Run-10 Beam Energy Scan at RHIC[J/OL]. STAR Internal Note, SN-0493, 2009. https://drupal.star.bnl.gov/STAR/system/files/BES-Short-v8 .3_0.pdf.

[21] BAZAVOV A, et al. Skewness and kurtosis of net baryon-number distributions at small values of the baryon chemical potential[J/OL]. Phys. Rev. D, 2017, 96(7): 074510. DOI: 10.1103/ PhysRevD.96.074510.

[22] BAZAVOV A, DING H T, HEGDE P, et al. QCD equation of state to $\mathcal{O}(\mu_B^6)$ from lattice QCD [J/OL]. Phys. Rev. D, 2017, 95: 054504. https://link.aps.org/doi/10.1103/PhysRevD.95.054 504.

[23] MATTIA. Evolution of collisions and QGP[EB/OL]. https://particlesandfriends.wordpress. com/2016/10/14/evolution-of-collisions-and-qgp/.

[24] APOLINÁRIO L, LEE Y J, WINN M. Heavy quarks and jets as probes of the QGP[J/OL]. Prog. Part. Nucl. Phys., 2022, 127: 103990. DOI: 10.1016/j.ppnp.2022.103990.

[25] CONNORS M, NATTRASS C, REED R, et al. Review of jet measurements in heavy ion collisions[Z]. 2017.

[26] LIU T. System size dependence of high-p_{T} hadron yield modification in the QGP with $\sqrt{s_{\mathrm{NN}}}$ = 200 GeV isobar collisions at STAR[J]. Hot Quarks 2022, 2022.

[27] MATSUI T, SATZ H. J/ψ Suppression by Quark-Gluon Plasma Formation[J/OL]. Phys. Lett. B, 1986, 178: 416-422. DOI: 10.1016/0370-2693(86)91404-8.

[28] ADAM J, et al. Measurement of inclusive J/ψ suppression in Au+Au collisions at $\sqrt{s_{NN}}$ = 200 GeV through the dimuon channel at STAR[J/OL]. Phys. Lett. B, 2019, 797: 134917. DOI: 10.1016/j.physletb.2019.134917.

[29] ABELEV B B, et al. Centrality, rapidity and transverse momentum dependence of J/ψ suppression in Pb-Pb collisions at $\sqrt{s_{\mathrm{NN}}}$=2.76 TeV[J/OL]. Phys. Lett. B, 2014, 734: 314-327. DOI: 10.1016/j.physletb.2014.05.064.

[30] ADARE A, et al. J/ψ Production in $\sqrt{s_{\mathrm{NN}}}$ = 200 GeV Cu+Cu Collisions[J/OL]. Phys. Rev. Lett., 2008, 101: 122301. DOI: 10.1103/PhysRevLett.101.122301.

[31] ADAMCZYK L, et al. J/ψ production at low p_{T} in Au+Au and Cu+Cu collisions at $\sqrt{s_{\mathrm{NN}}}$ = 200 GeV with the STAR detector[J/OL]. Phys. Rev. C, 2014, 90(2): 024906. DOI: 10.1103/PhysRevC.90.024906.

[32] $\psi(2S)$ suppression in Pb-Pb collisions at the LHC[A]. 2022. arXiv: 2210.08893.

[33] ZHAO X, RAPP R. Transverse Momentum Spectra of J/ψ in Heavy-Ion Collisions[J/OL]. Phys. Lett. B, 2008, 664: 253-257. DOI: 10.1016/j.physletb.2008.03.068.

[34] YAN L, ZHUANG P, XU N. J/ψ production in quark-gluon plasma[J]. Physical review letters, 2006, 97(23): 232301.

[35] YANG G. Measurement of the Υ production in heavy-ion collisions at the top RHIC energy with the STAR detector[J/OL]. ATHIC 2023, 2023. https://indico.cern.ch/event/1176274/contributions/5323519/attachments/2635503/4559394/Athic_Upsilon_Production.pdf.

[36] GALE C, JEON S, SCHENKE B. Hydrodynamic Modeling of Heavy-Ion Collisions[J/OL]. Int. J. Mod. Phys. A, 2013, 28: 1340011. DOI: 10.1142/S0217751X13400113.

[37] BASS S, BLEICHER M, CASSING W, et al. Last call for RHIC predictions[J]. Nuclear Physics A, 1999, 661(1-4): 205-260.

[38] ADAMCZYK L, et al. Global Λ hyperon polarization in nuclear collisions: evidence for the most vortical fluid[J/OL]. Nature, 2017, 548: 62-65. DOI: 10.1038/nature23004.

[39] VOLOSHIN S, ZHANG Y. Flow study in relativistic nuclear collisions by Fourier expansion of Azimuthal particle distributions[J/OL]. Z. Phys. C, 1996, 70: 665-672. DOI: 10.1007/s002880050141.

[40] ADAMCZYK L, et al. Centrality and transverse momentum dependence of elliptic flow of multistrange hadrons and ϕ meson in Au+Au collisions at $\sqrt{s_{NN}}$ = 200 GeV[J/OL]. Phys. Rev. Lett., 2016, 116(6): 062301. DOI: 10.1103/PhysRevLett.116.062301.

[41] DONG X, ESUMI S, SORENSEN P, et al. Resonance decay effects on anisotropy parameters [J]. Physics Letters B, 2004, 597(3-4): 328-332.

[42] ABDALLAH M, et al. Search for the chiral magnetic effect with isobar collisions at $\sqrt{s_{NN}}$=200 GeV by the STAR Collaboration at the BNL Relativistic Heavy Ion Collider

[J/OL]. Phys. Rev. C, 2022, 105(1): 014901. DOI: 10.1103/PhysRevC.105.014901.

[43] SCHNEDERMANN E, SOLLFRANK J, HEINZ U W. Thermal phenomenology of hadrons from 200-A/GeV S+S collisions[J/OL]. Phys. Rev. C, 1993, 48: 2462-2475. DOI: 10.1103/PhysRevC.48.2462.

[44] RETIERE F, LISA M A. Observable implications of geometrical and dynamical aspects of freeze-out in heavy ion collisions[J]. Physical Review C, 2004, 70(4): 044907.

[45] ABELEV B I, et al. Energy and system size dependence of phi meson production in Cu+Cu and Au+Au collisions[J/OL]. Phys. Lett. B, 2009, 673: 183-191. DOI: 10.1016/j.physletb.2009.02.037.

[46] SORENSEN P. Elliptic Flow: A Study of Space-Momentum Correlations In Relativistic Nuclear Collisions[M/OL]. 2010: 323-374. DOI: 10.1142/9789814293297_0006.

[47] AGGARWAL M M, et al. Scaling properties at freeze-out in relativistic heavy ion collisions [J/OL]. Phys. Rev. C, 2011, 83: 034910. DOI: 10.1103/PhysRevC.83.034910.

[48] WHEATON S, CLEYMANS J. THERMUS: A Thermal model package for ROOT[J/OL]. Comput. Phys. Commun., 2009, 180: 84-106. DOI: 10.1016/j.cpc.2008.08.001.

[49] BEARDEN I G, et al. Nuclear stopping in Au+Au collisions at $\sqrt{s_{\mathrm{NN}}}$ = 200 GeV[J/OL]. Phys. Rev. Lett., 2004, 93: 102301. DOI: 10.1103/PhysRevLett.93.102301.

[50] ABELEV B, et al. Centrality dependence of π, K, p production in Pb-Pb collisions at $\sqrt{s_{NN}}$ = 2.76 TeV[J/OL]. Phys. Rev. C, 2013, 88: 044910. DOI: 10.1103/PhysRevC.88.044910.

[51] ARTRU X. String Model with Baryons: Topology, Classical Motion[J/OL]. Nucl. Phys. B, 1975, 85: 442-460. DOI: 10.1016/0550-3213(75)90019-X.

[52] ROSSI G C, VENEZIANO G. A Possible Description of Baryon Dynamics in Dual and Gauge Theories[J/OL]. Nucl. Phys. B, 1977, 123: 507-545. DOI: 10.1016/0550-3213(77)90178-X.

[53] ROSSI G, VENEZIANO G. I. Theoretical aspects of baryonium physics[J]. Physics Reports, 1980, 63(3): 153-200.

[54] KHARZEEV D. Can gluons trace baryon number?[J/OL]. Phys. Lett. B, 1996, 378: 238-246. DOI: 10.1016/0370-2693(96)00435-2.

[55] LEWIS N. Talk: Search for baryon junctions in photonuclear processes and heavy-ion collisions at STAR[J/OL]. 30th International Workshop on Deep Inelastic Scattering, 2023. https://indico.cern.ch/event/1199314/contributions/5189836/attachments/2620560/4532611/DIS2023_smallx1.pdf.

[56] BRANDENBURG J D, LEWIS N, TRIBEDY P, et al. Search for baryon junctions in photonuclear processes and isobar collisions at RHIC[A]. 2022. arXiv: 2205.05685.

[57] ABBAS E, et al. Mid-rapidity anti-baryon to baryon ratios in pp collisions at $\sqrt{s}$ = 0.9, 2.76 and 7 TeV measured by ALICE[J/OL]. Eur. Phys. J. C, 2013, 73: 2496. DOI: 10.1140/epjc/s

10052-013-2496-5.

[58] AAMODT K, et al. Midrapidity antiproton-to-proton ratio in pp collisions at $\sqrt{s} = 0.9$ and 7~TeV measured by the ALICE experiment[J/OL]. Phys. Rev. Lett., 2010, 105: 072002. DOI: 10.1103/PhysRevLett.105.072002.

[59] LEWIS N. Flash talk and poster: Identified hadron spectra and baryon stopping in γ+Au collisions at STAR[J/OL]. Quark Matter 2022, 2022. https://indico.cern.ch/event/895086/contributions/4824032/.

[60] HARRISON M, LUDLAM T, OZAKI S. RHIC project overview[J/OL]. Nucl. Instrum. Meth. A, 2003, 499: 235-244. DOI: 10.1016/S0168-9002(02)01937-X.

[61] HARRISON M, PEGGS S G, ROSER T. The RHIC accelerator[J/OL]. Ann. Rev. Nucl. Part. Sci., 2002, 52: 425-469. DOI: 10.1146/annurev.nucl.52.050102.090650.

[62] ADAMS J, et al. Experimental and theoretical challenges in the search for the quark gluon plasma: The STAR Collaboration's critical assessment of the evidence from RHIC collisions [J/OL]. Nucl. Phys. A, 2005, 757: 102-183. DOI: 10.1016/j.nuclphysa.2005.03.085.

[63] BACK B B, et al. The PHOBOS perspective on discoveries at RHIC[J/OL]. Nucl. Phys. A, 2005, 757: 28-101. DOI: 10.1016/j.nuclphysa.2005.03.084.

[64] ARSENE I, et al. Quark gluon plasma and color glass condensate at RHIC? The Perspective from the BRAHMS experiment[J/OL]. Nucl. Phys. A, 2005, 757: 1-27. DOI: 10.1016/j.nuclphysa.2005.02.130.

[65] ADCOX K, et al. Formation of dense partonic matter in relativistic nucleus-nucleus collisions at RHIC: Experimental evaluation by the PHENIX collaboration[J/OL]. Nucl. Phys. A, 2005, 757: 184-283. DOI: 10.1016/j.nuclphysa.2005.03.086.

[66] ACCARDI A, et al. Electron Ion Collider: The Next QCD Frontier: Understanding the glue that binds us all[J/OL]. Eur. Phys. J. A, 2016, 52(9): 268. DOI: 10.1140/epja/i2016-16268-9.

[67] RHIC Complex at Brookhaven National Laboratory[EB/OL]. https://www.flickr.com/photos/brookhavenlab/7979381212/in/album-72157613690851651/.

[68] ALESSI J, BARTON E, BEEBE E, et al. Electron beam ion source pre-injector project (EBIS) conceptual design report[EB/OL]. 2023. DOI: 10.2172/15020507.

[69] BERGSMA F, et al. The STAR detector magnet subsystem[J/OL]. Nucl. Instrum. Meth. A, 2003, 499: 633-639. DOI: 10.1016/S0168-9002(02)01961-7.

[70] WIEMAN H, et al. STAR TPC at RHIC[J/OL]. IEEE Trans. Nucl. Sci., 1997, 44: 671-678. DOI: 10.1109/23.603731.

[71] ACKERMANN K H, et al. STAR detector overview[J/OL]. Nucl. Instrum. Meth. A, 2003, 499: 624-632. DOI: 10.1016/S0168-9002(02)01960-5.

[72] QIU H. STAR heavy flavor tracker[J/OL]. Nuclear Physics A, 2014, 931: 1141-1146. https:

//www.sciencedirect.com/science/article/pii/S0375947414003157. DOI: https://doi.org/10.1016/j.nuclphysa.2014.08.056.

[73] ADAMCZYK L, et al. Measurement of D^0 Azimuthal Anisotropy at Midrapidity in Au+Au Collisions at $\sqrt{s_{NN}}$=200 GeV[J/OL]. Phys. Rev. Lett., 2017, 118(21): 212301. DOI: 10.1103/PhysRevLett.118.212301.

[74] ADAM J, et al. Centrality and transverse momentum dependence of D^0-meson production at mid-rapidity in Au+Au collisions at $\sqrt{s_{\rm NN}}$ = 200 GeV[J/OL]. Phys. Rev. C, 2019, 99(3): 034908. DOI: 10.1103/PhysRevC.99.034908.

[75] ADAM J, et al. First measurement of Λ_c baryon production in Au+Au collisions at $\sqrt{s_{\rm NN}}$ = 200 GeV[J/OL]. Phys. Rev. Lett., 2020, 124(17): 172301. DOI: 10.1103/PhysRevLett.124.172301.

[76] ABDALLAH M S, et al. Evidence of Mass Ordering of Charm and Bottom Quark Energy Loss in Au+Au Collisions at RHIC[J/OL]. Eur. Phys. J. C, 2022, 82(12): 1150. DOI: 10.1140/epjc/s10052-022-11003-7.

[77] KAJIMOTO K. A large area time of flight detector for the STAR experiment at RHIC[M]. The University of Texas at Austin, 2009.

[78] BEDDO M, et al. The STAR barrel electromagnetic calorimeter[J/OL]. Nucl. Instrum. Meth. A, 2003, 499: 725-739. DOI: 10.1016/S0168-9002(02)01970-8.

[79] YANG C, et al. Calibration and performance of the STAR Muon Telescope Detector using cosmic rays[J/OL]. Nucl. Instrum. Meth. A, 2014, 762: 1-6. DOI: 10.1016/j.nima.2014.05.075.

[80] RUAN L, et al. Perspectives of a Midrapidity Dimuon Program at RHIC: A Novel and Compact Muon Telescope Detector[J/OL]. J. Phys. G, 2009, 36: 095001. DOI: 10.1088/0954-3899/36/9/095001.

[81] ADAMCZYK L, et al. Suppression of Υ production in d+Au and Au+Au collisions at $\sqrt{s_{NN}}$=200 GeV[J/OL]. Phys. Lett. B, 2014, 735: 127-137. DOI: 10.1016/j.physletb.2014.06.028.

[82] ADLER C, DENISOV A, GARCIA E, et al. The RHIC zero-degree calorimeters[J/OL]. Nucl. Instrum. Meth. A, 2003, 499: 433-436. DOI: 10.1016/j.nima.2003.08.112.

[83] WHITTEN C A. The beam-beam counter: A local polarimeter at STAR[J/OL]. AIP Conf. Proc., 2008, 980(1): 390-396. DOI: 10.1063/1.2888113.

[84] LLOPE W J, et al. The STAR Vertex Position Detector[J/OL]. Nucl. Instrum. Meth. A, 2014, 759: 23-28. DOI: 10.1016/j.nima.2014.04.080.

[85] BULTMANN S, et al. Double Spin Asymmetries A_{NN} and A_{SS} at $\sqrt{s}$ = 200 GeV in Polarized Proton-Proton Elastic Scattering at RHIC[J/OL]. Phys. Lett. B, 2007, 647: 98-103. DOI:

10.1016/j.physletb.2007.01.067.

[86] BRAIDOT E. Two Particle Correlations at Forward Rapidity in STAR[J/OL]. Nucl. Phys. A, 2011, 854: 168-174. DOI: 10.1016/j.nuclphysa.2011.01.016.

[87] BRAIDOT E. Looking forward for Color Glass Condensate signatures[J/OL]. Nucl. Phys. A, 2009, 830: 603C-606C. DOI: 10.1016/j.nuclphysa.2009.09.050.

[88] ADAM J, et al. Measurement of transverse single-spin asymmetries of π^0 and electromagnetic jets at forward rapidity in 200 and 500 GeV transversely polarized proton-proton collisions [J/OL]. Phys. Rev. D, 2021, 103(9): 092009. DOI: 10.1103/PhysRevD.103.092009.

[89] JUDD E G, et al. The evolution of the STAR Trigger System[J/OL]. Nucl. Instrum. Meth. A, 2018, 902: 228-237. DOI: 10.1016/j.nima.2018.03.070.

[90] BIESER F S, et al. The STAR trigger[J/OL]. Nucl. Instrum. Meth. A, 2003, 499: 766-777. DOI: 10.1016/S0168-9002(02)01974-5.

[91] LANGE J S, et al. The STAR level 3 trigger system[J/OL]. Nucl. Instrum. Meth. A, 2000, 453: 397-404. DOI: 10.1016/S0168-9002(00)00664-1.

[92] KE H. Beam Energy, Collision Centrality and Charge Asymmetry Dependence of the Pion Event Anisotropy in Au+Au Collisions at RHIC[J/OL]. STAR Graduate Thesis, 2013. https://drupal.star.bnl.gov/STAR/files/PhDthesis_kehw.pdf.

[93] ABELEV B I, et al. Identified particle production, azimuthal anisotropy, and interferometry measurements in Au+Au collisions at $\sqrt{s_{\mathrm{NN}}}$ = 9.2 GeV[J/OL]. Phys. Rev. C, 2010, 81: 024911. DOI: 10.1103/PhysRevC.81.024911.

[94] ABELEV B I, et al. Studying the Phase Diagram of QCD Matter at RHIC[J/OL]. STAR BES-II White Paper, 2014. https://drupal.star.bnl.gov/STAR/system/files/BES_WPII_ver6.9_Cover.pdf.

[95] YANG C. The STAR beam energy scan phase II physics and upgrades[J/OL]. Nucl. Phys. A, 2017, 967: 800-803. DOI: 10.1016/j.nuclphysa.2017.05.042.

[96] YANG Q. The STAR BES-II and Forward Rapidity Physics and Upgrades[J/OL]. Nucl. Phys. A, 2019, 982: 951-954. DOI: 10.1016/j.nuclphysa.2018.10.029.

[97] SHEN F, WANG S, YANG C, et al. MWPC prototyping and testing for STAR inner TPC upgrade[J/OL]. JINST, 2017, 12(06): C06008. DOI: 10.1088/1748-0221/12/06/C06008.

[98] YANG C, CHEN J, MA Y, et al. Inner TPC upgrade at RHIC – STAR[J]. SCIENTIA SINICA Physica, Mechanica & Astronomica, 2019.

[99] ABELEV B I, et al. A proposal for STAR inner TPC sector upgrade (iTPC)[J/OL]. STAR Internal Note, SN-0619, 2015. https://drupal.star.bnl.gov/STAR/system/files/STAR_iTPC_proposal_06_09_2015.pdf.

[100] ADAMS J, et al. The STAR Event Plane Detector[J/OL]. Nucl. Instrum. Meth. A, 2020, 968:

163970. DOI: 10.1016/j.nima.2020.163970.

[101] An Event Plane Detector for STAR[J/OL]. STAR Internal Note, 2016. https://drupal.star.bnl.gov/STAR/files/Construction_Proposal_0.pdf.

[102] Physics Program for the STAR/CBM eTOF Upgrade[A]. 2016. arXiv: 1609.05102.

[103] LANDGRAF J M, LEVINE M J, LJUBICIC A, et al. An overview of the STAR DAQ system [J/OL]. Nucl. Instrum. Meth. A, 2003, 499: 762-765. DOI: 10.1016/S0168-9002(02)01973-3.

[104] ASCHENAUER E C, et al. The RHIC Cold QCD Program[A]. 2023. arXiv: 2302.00605.

[105] BRANDENBURG J. STAR Forward Rapidity Upgrade[J/OL]. PoS, 2021, HardProbes2020: 179. DOI: 10.22323/1.387.0179.

[106] ASCHENAUER E C, et al. The RHIC Cold QCD Plan for 2017 to 2023: A Portal to the EIC [A]. 2016. arXiv: 1602.03922.

[107] SEKHNIAIDZE G. Construction and performance of the sTGC and MicroMegas chambers for ATLAS NSW upgrade[J/OL]. JINST, 2017, 12(03): C03020. DOI: 10.1088/1748-0221/12/03/C03020.

[108] ZHAO X, ZHANG D, LI W, et al. Cosmic test of sTGC detector prototype made in China for ATLAS experiment upgrade[J/OL]. Nucl. Instrum. Meth. A, 2019, 927: 257-261. DOI: 10.1016/j.nima.2019.02.061.

[109] KOTCHENDA L, KOZLOV S, KRAVTSOV P, et al. STAR TPC gas system[J/OL]. Nucl. Instrum. Meth. A, 2003, 499: 703-712. DOI: 10.1016/S0168-9002(02)01967-8.

[110] ANDERSON M, et al. The STAR time projection chamber: A Unique tool for studying high multiplicity events at RHIC[J/OL]. Nucl. Instrum. Meth. A, 2003, 499: 659-678. DOI: 10.1016/S0168-9002(02)01964-2.

[111] ABELE J, BERKOVITZ J, BOEHM J, et al. The laser system for the STAR time projection chamber[J]. Nuclear Instruments and Methods in Physics Research Section A: Accelerators, Spectrometers, Detectors and Associated Equipment, 2003, 499(2-3): 692-702.

[112] NORMAN B, et al. STAR Integrated Tracker Guide[J/OL]. STAR Internal Note, 2002. https://www.star.bnl.gov/public/comp/meet/ITTFReviewSept2002/IttfDocumentation.pdf.

[113] LLOPE W J. The large-area time-of-flight (TOF) upgrade for the STAR detector[J/OL]. AIP Conf. Proc., 2009, 1099(1): 778-781. DOI: 10.1063/1.3120153.

[114] BONNER B, CHEN H, EPPLEY G, et al. A single Time-of-Flight tray based on multigap resistive plate chambers for the STAR experiment at RHIC[J/OL]. Nuclear Instruments and Methods in Physics Research Section A: Accelerators, Spectrometers, Detectors and Associated Equipment, 2003, 508(1): 181-184. https://www.sciencedirect.com/science/article/pii/S0168900203013470. DOI: https://doi.org/10.1016/S0168-9002(03)01347-0.

[115] SHAO M, RUAN L J, CHEN H F, et al. Beam test results of two kinds of multi-gap resistive plate chambers[J/OL]. Nucl. Instrum. Meth. A, 2002, 492: 344-350. DOI: 10.1016/S0168-9002(02)01355-4.

[116] LLOPE W J. Multigap RPCs in the STAR experiment at RHIC[J/OL]. Nucl. Instrum. Meth. A, 2012, 661: S110-S113. DOI: 10.1016/j.nima.2010.07.086.

[117] MARR G, et al. Ion Collider Precision Measurements With Different Species[C/OL]//10th International Particle Accelerator Conference. 2019: MOZPLS2. DOI: 10.18429/JACoW-IPAC2019-MOZPLS2.

[118] GARG P, MISHRA D K. Higher moments of net-proton multiplicity distributions in a heavy-ion event pile-up scenario[J/OL]. Phys. Rev. C, 2017, 96(4): 044908. DOI: 10.1103/PhysRevC.96.044908.

[119] AAIJ R, et al. Centrality determination in heavy-ion collisions with the LHCb detector[J/OL]. JINST, 2022, 17(05): P05009. DOI: 10.1088/1748-0221/17/05/P05009.

[120] BRONIOWSKI W, FLORKOWSKI W. Geometric relation between centrality and the impact parameter in relativistic heavy ion collisions[J/OL]. Phys. Rev. C, 2002, 65: 024905. DOI: 10.1103/PhysRevC.65.024905.

[121] SWEGER Z, ZHANG Y, NONAKA T, et al. Centrality for isobars: status report[J/OL]. STAR Centrality Working Group Presentation, 2021. https://drupal.star.bnl.gov/STAR/system/files/CentralityForIsobars_20211217.pdf.

[122] MILLER M L, REYGERS K, SANDERS S J, et al. Glauber modeling in high energy nuclear collisions[J/OL]. Ann. Rev. Nucl. Part. Sci., 2007, 57: 205-243. DOI: 10.1146/annurev.nucl.57.090506.123020.

[123] WOODS R D, SAXON D S. Diffuse Surface Optical Model for Nucleon-Nuclei Scattering [J/OL]. Phys. Rev., 1954, 95: 577-578. DOI: 10.1103/PhysRev.95.577.

[124] DENG W T, HUANG X G, MA G L, et al. Test the chiral magnetic effect with isobaric collisions[J/OL]. Phys. Rev. C, 2016, 94: 041901. DOI: 10.1103/PhysRevC.94.041901.

[125] XU H J, LI H, WANG X, et al. Determine the neutron skin type by relativistic isobaric collisions[J/OL]. Phys. Lett. B, 2021, 819: 136453. DOI: 10.1016/j.physletb.2021.136453.

[126] BICHSEL H. A method to improve tracking and particle identification in TPCs and silicon detectors[J/OL]. Nucl. Instrum. Meth. A, 2006, 562: 154-197. DOI: 10.1016/j.nima.2006.03.009.

[127] ZYLA P A, et al. Review of Particle Physics[J/OL]. PTEP, 2020, 2020(8): 083C01. DOI: 10.1093/ptep/ptaa104.

[128] BRUN R, HAGELBERG R, HANSROUL M, et al. Geant: Simulation Program for Particle Physics Experiments. User Guide and Reference Manual[Z]. 1978.

[129] FINE V, FISYAK Y V, PEREVOZCHIKOV V, et al. The STAR offline framework[C]//11th International Conference on Computing in High-Energy and Nuclear Physics. 2000: 196-200.

[130] ADLER C, et al. Midrapidity Λ and $\bar{\Lambda}$ production in Au+Au collisions at $\sqrt{s_{\mathrm{NN}}}$ = 130 GeV [J/OL]. Phys. Rev. Lett., 2002, 89: 092301. DOI: 10.1103/PhysRevLett.89.092301.

[131] ULLRICH T, XU Z. Treatment of errors in efficiency calculations[M/OL]. arXiv, 2007. https://arxiv.org/abs/physics/0701199. DOI: 10.48550/ARXIV.PHYSICS/0701199.

[132] ADAMS J, et al. Identified hadron spectra at large transverse momentum in p+p and d+Au collisions at $\sqrt{s_{\mathrm{NN}}}$ = 200 GeV[J/OL]. Phys. Lett. B, 2006, 637: 161-169. DOI: 10.1016/j.physletb.2006.04.032.

[133] ABELEV B I, et al. Strange particle production in p+p collisions at $\sqrt{s_{\mathrm{NN}}}$ = 200 GeV[J/OL]. Phys. Rev. C, 2007, 75: 064901. DOI: 10.1103/PhysRevC.75.064901.

[134] YAO W M, et al. Review of Particle Physics[J/OL]. J. Phys. G, 2006, 33: 1-1232. DOI: 10.1088/0954-3899/33/1/001.

[135] WILK G, WŁODARCZYK Z. Interpretation of the nonextensivity parameter q in some applications of tsallis statistics and lévy distributions[J/OL]. Phys. Rev. Lett., 2000, 84: 2770-2773. https://link.aps.org/doi/10.1103/PhysRevLett.84.2770.

[136] ADAMS J, et al. K(892)* resonance production in Au+Au and $p+p$ collisions at $\sqrt{s_{\mathrm{NN}}}$ = 200 GeV at STAR[J/OL]. Phys. Rev. C, 2005, 71: 064902. DOI: 10.1103/PhysRevC.71.064902.

[137] WANG X N, GYULASSY M. HIJING: A Monte Carlo model for multiple jet production in p+p, p+A and A+A collisions[J/OL]. Phys. Rev. D, 1991, 44: 3501-3516. DOI: 10.1103/PhysRevD.44.3501.

[138] BARLOW R. Systematic errors: Facts and fictions[C]//Conference on Advanced Statistical Techniques in Particle Physics. 2002: 134-144.

[139] GIACALONE G, GARDIM F G, NORONHA-HOSTLER J, et al. Correlation between mean transverse momentum and anisotropic flow in heavy-ion collisions[J]. Physical Review C, 2021, 103(2): 024909.

[140] XU H J, ZHAO W, LI H, et al. Probing nuclear structure with mean transverse momentum in relativistic isobar collisions[A]. 2021. arXiv: 2111.14812.

[141] HEINZ U W. Concepts of heavy ion physics[C]//2nd CERN-CLAF School of High Energy Physics. 2004: 165-238.

[142] ADAM J, et al. Beam energy dependence of (anti-)deuteron production in Au + Au collisions at the BNL Relativistic Heavy Ion Collider[J/OL]. Phys. Rev. C, 2019, 99(6): 064905. DOI: 10.1103/PhysRevC.99.064905.

[143] XU H J, LI H, ZHOU Y, et al. Measuring neutron skin by grazing isobaric collisions[J/OL]. Phys. Rev. C, 2022, 105(1): L011901. DOI: 10.1103/PhysRevC.105.L011901.

[144] BLEICHER M, et al. Relativistic hadron hadron collisions in the ultrarelativistic quantum molecular dynamics model[J/OL]. J. Phys. G, 1999, 25: 1859-1896. DOI: 10.1088/0954-3899/25/9/308.

[145] BASS S A, et al. Microscopic models for ultrarelativistic heavy ion collisions[J/OL]. Prog. Part. Nucl. Phys., 1998, 41: 255-369. DOI: 10.1016/S0146-6410(98)00058-1.

[146] PETERSEN H, STEINHEIMER J, BURAU G, et al. A Fully Integrated Transport Approach to Heavy Ion Reactions with an Intermediate Hydrodynamic Stage[J/OL]. Phys. Rev. C, 2008, 78: 044901. DOI: 10.1103/PhysRevC.78.044901.

[147] BELLM J, et al. Herwig 7.0/Herwig++ 3.0 release note[J/OL]. Eur. Phys. J. C, 2016, 76(4): 196. DOI: 10.1140/epjc/s10052-016-4018-8.

[148] BAHR M, et al. Herwig++ Physics and Manual[J/OL]. Eur. Phys. J. C, 2008, 58: 639-707. DOI: 10.1140/epjc/s10052-008-0798-9.

[149] LIU L M, ZHANG C J, ZHOU J, et al. Probing neutron-skin thickness with free spectator neutrons in ultracentral high-energy isobaric collisions[J/OL]. Phys. Lett. B, 2022, 834: 137441. DOI: 10.1016/j.physletb.2022.137441.

[150] BROWN B A. Neutron radii in nuclei and the neutron equation of state[J/OL]. Phys. Rev. Lett., 2000, 85: 5296-5299. DOI: 10.1103/PhysRevLett.85.5296.

[151] MORELAND J S, BERNHARD J E, BASS S A. Alternative ansatz to wounded nucleon and binary collision scaling in high-energy nuclear collisions[J/OL]. Phys. Rev. C, 2015, 92(1): 011901. DOI: 10.1103/PhysRevC.92.011901.

[152] CEBRA D, SWEGER Z, DONG X, et al. Backward-angle (u-channel) production at an electron-ion collider[J]. Physical Review C, 2022, 106(1): 015204.

Acknowledgements

First and foremost, I would like to convey my deepest appreciation to my advisors, Zebo Tang, Lijuan Ruan, and Rongrong Ma, for their indispensable guidance and consistent support throughout my Ph.D. journey. Zebo, whose mentorship was instrumental in my introduction to the field of heavy ion physics, has been pivotal in shaping my understanding of physics analysis and particle detectors. His teachings have significantly contributed to my academic advancement. Lijuan's meticulous guidance, coupled with her nurturing care for my life and studies at BNL, has truly inspired me. Rongrong has enlightened me with his insightful discussions on physics and analysis techniques, and his expertise and advice have been immensely beneficial. I am also particularly grateful to Zhangbu Xu for the invigorating ideas and insights in physics, which have made my work more engaging. I wish to express special thanks to Rongrong for being a part of my wedding ceremony, a cherished milestone in my life.

The journey at USTC has been enriched by the support and camaraderie of my peers, including Long Zhou, Zhen Liu, Guannan Xie, Yuanjing Ji, Shenghui Zhang, Pengfei Wang, Kaifeng Shen, Ziyang Li, Ziwei Li, Xinjian Wang, Jian Zhou, and Yitao Wu. Your unwavering enthusiasm, dedication, and passion for science have served as a source of inspiration, and I value the friendships we have fostered. A special acknowledgment goes to Yu Hu, Xiaoxuan Chu, Zhen Wang, Baoshan Xi, Yufu Lin, and Ding Chen, who I met at BNL. You all have added color to my days, and I am grateful for the memories we have created together. The friendship and support you have provided have been immeasurable, and I will cherish them always.

My heartfelt gratitude goes to my parents, who have been the cornerstone of my life. They have provided me with unwavering love, support, and education. The value of hard work, guidance, and advice they instilled in me have been influential in shaping my character. Although I lost my father and grandfather last year, I seize this moment to honor them and express my deep appreciation for their immense contributions to my life. Their memory continues to inspire me every day.

I am also deeply grateful to my wife, Jiaxin, who always stood by my side. It was difficult for me to know about my father's passing during my thesis preparation, but her unwavering support and presence brought light into my life. Her encouragement, patience, and understanding have been invaluable to me, and I am truly grateful for everything she has done. Jiaxin, you complete my soul.

Finally, I wish to express my appreciation for the constructive discussions with Chun Yuen Tsang, Nicole Lewis, Hui Liu, and Jia Chen. Their insightful feedback and perspectives were invaluable to the successful completion of my work, and I am grateful for the opportunity to have collaborated with them.

Publications

Published papers

1. STAR Collaboration (Yang Li is one of the Principal Authors). Search for the chiral magnetic effect with isobar collisions at $\sqrt{s_{\mathrm{NN}}}$= 200 GeV by the STAR Collaboration at the BNL Relativistic Heavy Ion Collider. Phys. Rev. C, 2022, 105(1): 014901. DOI: 10.1103/PhysRevC.105.014901.
2. Yang Li, Kun Jiang, Zebo Tang, et al. High dynamic range base design and characterization of an 8-inch photomultiplier tube CR365-02-2 for the LHAASO-MD experiment. Nucl. Instrum. Meth. A, 2022, 1025: 166190. DOI: 10.1016/j.nima.2021.166190.
3. Kun Jiang, Zebo Tang, Yang Li, et al. Qualification tests of 997 8-inch photomultiplier tubes for the water Cherenkov detector array of the LHAASO experiment. Nucl. Instrum. Meth. A, 2021, 995: 165108. DOI: 10.1016/j.nima.2021.165108.

Paper in preparation

1. STAR Collaboration (Yang Li is one of the Principal Authors), Tracking the baryon number with heavy-ion collisions, under STAR internal review (Target journal: Science).